



High-content imaging and proteostasis deregulation study in dilated cardiomyopathy associated with myofibrillar myopathy due to a desmin mutation (DES E439K)

Vivien Batoumeni

► To cite this version:

Vivien Batoumeni. High-content imaging and proteostasis deregulation study in dilated cardiomyopathy associated with myofibrillar myopathy due to a desmin mutation (DES E439K). Cellular Biology. Sorbonne Université, 2024. English. NNT : 2024SORUS043 . tel-04575955

HAL Id: tel-04575955

<https://theses.hal.science/tel-04575955>

Submitted on 15 May 2024

HAL is a multi-disciplinary open access archive for the deposit and dissemination of scientific research documents, whether they are published or not. The documents may come from teaching and research institutions in France or abroad, or from public or private research centers.

L'archive ouverte pluridisciplinaire **HAL**, est destinée au dépôt et à la diffusion de documents scientifiques de niveau recherche, publiés ou non, émanant des établissements d'enseignement et de recherche français ou étrangers, des laboratoires publics ou privés.

THÈSE DE DOCTORAT DE SORBONNE UNIVERSITÉ

Spécialité

Physiologie, physiopathologie et thérapeutique
(École doctorale ED394)

Présentée par

Vivien BATOUMENI

Pour obtenir le grade de

DOCTEUR DE SORBONNE UNIVERSITÉ

High-content imaging and proteostasis deregulation study in dilated cardiomyopathy associated with myofibrillar myopathy due to a desmin mutation (*DES* ^{E439K})

Soutenue le 29 Janvier 2024, devant le jury composé de :

Dr. VILQUIN Jean-Thomas	Président du Jury
Dr. BATONNET-PICHON Sabrina	Rapporteur
Dr. GACHE Vincent	Rapporteur
Dr. CIENIEWSKI-BERNARD Caroline	Examinateur
Pr. CHARBONNIER Frederic	Examinateur
Pr. VARTANIAN Jean-Pierre	Examinateur
Dr. JOANNE Pierre	Co-Encadrant de Thèse
Pr. AGBULUT Onnik	Directeur de Thèse

Remerciements

Tout d'abord je souhaiterai remercier les membres du jury: Dr. Jean-Thomas VILQUIN, Dr. Sabrina BATONNET-PICHON, Dr. Vincent GACHE, Dr. Caroline CIENIEWSKI-BERNARD, Pr. Frederic CHARBONNIER, Pr. Jean-Pierre VARTANIAN d'avoir accepté de juger ce travail. Merci pour votre temps et votre disponibilité.

Je tiens à remercier le Pr. Onnik AGBULUT et le Dr. Pierre JOANNE qui m'ont encadré en tant que directeur de thèse et co-encadrant. Je vous remercie pour la confiance que vous m'avez accordé tout au long de cette expérience. Malgré les emplois du temps chargés, la distance pendant de longue période, vous avez toujours su vous montrer disponible, bienveillant et de bons conseils. J'ai énormément appris à vos côtés et je vous en suis très reconnaissant.

Je tiens à remercier l'association Ksilink qui a permis la réalisation de ce projet en partenariat. Un grand merci au Dr. Laurent BRINO pour sa disponibilité et son investissement, j'aurai adoré travailler plus longtemps à ses côtés. Merci également au Dr. Konstantinos GKATZIS pour son accompagnement sur la dernière année. Je tiens à mentionner le Dr. Peter SOMMER, bien que pas directement impliqué dans mon encadrement, il a toujours su m'apporter les conseils scientifiques me permettant de mieux aborder ma problématique, Merci.

Je remercie chaleureusement tous les membres de l'équipe Ksilink pour ses moments passés ensemble et pour votre soutien tout au long de ce projet. Plus particulièrement, ceux avec qui nos relations se sont développées bien au-delà d'une simple relation de travail : Léa, Amandine, Aurore, Amélie, Thomas, David, Béné, Marion, Kayhan, Carole, Zahra, Karen et François. J'ai aimé rire, boire, manger avec vous. Votre bonne humeur au quotidien m'a aidé à tenir dans les moments les plus compliqués. De nombreux souvenirs construits ensemble m'accompagneront tout au long de ma vie « Ksilinker un jour ksilinker toujours ».

J'adresse également mes remerciements à l'ensemble de l'équipe CARTHER qui m'a toujours faire sentir que j'y avais ma place malgré la fréquence de mes allers et venues au laboratoire. Merci à Gaelle et Alexandre de m'avoir accueilli et de m'avoir aidé dans des missions à distance, en particulier toi Alex, ton aide a vraiment été précieuse. Une immense reconnaissance et beaucoup d'amour pour mes co-thésards et collègues proches en

particulier Mélanight, J-S, Den's et Cat-Cat avec qui on a partagé nos joies, nos peurs, nos moments « philosophie ». Sincèrement merci de m'avoir donné la sensation que je n'étais pas seul dans cette aventure. Je garde chaleureusement avec moi ses souvenirs dans les divers congrès qu'on a pu partager. Minh, Brice, Gabi, Laura, je suis également content de vous avoir rencontré et d'avoir partagé certes beaucoup moins mais tout de même ces moments précieux.

Enfin, je souhaiterai remercier mes proches pour leur indéfectible soutien et leur présence dans les moments personnels les plus difficiles, me permettant de continuer à donner le maximum dans ce projet de thèse. Mes parents et ma sœur qui ont toujours été disponibles au moindre « coup de mou », au moindre doute et qui malgré leur non expertise dans les sciences ont toujours été d'excellents conseillers. Merci à vous. Le Parrot Gang, ils se reconnaîtront, merci d'être vous et toujours présents dans mes différentes aventures. Merci à toi Booboo, je ne te l'ai pas assez dit mais ton soutien au quotidien surtout dans la dernière ligne droite a été incommensurable et précieux.

A mon Grand-père,

A mon Amie.

Abstract

Myofibrillar myopathies linked to desmin, also known as desminopathies, are rare genetic diseases caused by mutations in the *DES* gene primarily characterized by the progressive appearance of muscle weakness. In many cases, these pathologies are also associated with dilated cardiomyopathy, leading to heart failure, which is a major cause of death in these patients. Indeed, in addition to the disorders of cardiac contractility common to all dilated cardiomyopathies, those induced by a *DES* gene mutation are characterized by the presence of protein aggregates, mitochondrial dysfunction and myofibril disorganization. To date, no effective treatment, pharmacological or surgical approach, can reverse this progressive and disabling heart disease. The purpose of this PhD was first to highlight pathophysiological mechanisms involved in the establishment and maintenance of the disease. Then to better shed light on the cellular *DES*^{E439K} morphological phenotypes, with the aim of modulating them by treatment with annotated compounds. These assays allow us to deduce and validate biological targets previously identified, in order to open the way toward new therapeutic approaches. In this context, the precise aim was to focus on the state of proteostasis and protein quality control systems (PQC).

To reach these objectives, this study exclusively used *in vitro* models of *DES*^{E439K} mutation-induced dilated cardiomyopathy based on cardiomyocyte derived from human induced pluripotent stem cells (iPSC-CM) cultured as 2D monolayers or as engineered human myocardium (EHM). Thus, after validation that the models recapitulated the hallmarks of dilated cardiomyopathy, it was shown that in a *DES*^{E439K} mutation context, cellular proteostasis was disrupted and PQC activated, notably the autophagy process. A high-content imaging approach was then implemented to better characterize and quantify the phenotypic properties of iPSC-CM carrying the DES E439K mutation. This method allowed us to quantify the effects of annotated small compounds and to select those capable of reversing the cellular phenotype. The identification of the mechanisms of action of these compounds confirmed the involvement of mitochondrial and endoplasmic reticulum stress response processes in the establishment of pathological phenotypes.

In conclusion, this study highlights the importance of regulating cellular proteostasis and mitochondrial homeostasis in dilated cardiomyopathy caused by the *DES* gene mutation, which could represent an interesting therapeutic approach.

Résumé

Les myopathies myofibrillaires liées à la desmine, également appelées desminopathies, sont des maladies génétiques rares causées par des mutations du gène *DES* qui se caractérisent principalement par l'apparition progressive d'une faiblesse musculaire. Dans de nombreux cas, ces pathologies sont également associées à une cardiomyopathie dilatée, conduisant à une insuffisance cardiaque, qui est une cause majeure de décès chez ces patients. En effet, outre les troubles de la contractilité cardiaque communs à toutes les cardiomyopathies dilatées, celles induites par une mutation du gène *DES* se caractérisent par la présence d'agrégats protéiques, de dysfonction mitochondriale et de désorganisation des myofibrille. À ce jour, aucun traitement efficace, qu'il soit pharmacologique ou chirurgical, ne peut inverser cette maladie cardiaque progressive. L'objectif de cette thèse est d'abord de mettre en évidence les mécanismes physiopathologiques impliqués dans l'émergence et le maintien de la maladie. Puis de mettre en avant les phénotypes morphologiques cellulaires *DES^{E439K}*, dans le but de les moduler par un traitement avec des composés annotés. Ces essais permettent de déduire et de valider des cibles biologiques préalablement identifiées, afin d'ouvrir la voie vers de nouvelles approches thérapeutiques. Dans ce contexte, l'objectif précis était de se focaliser sur l'état de la protéostasie et des systèmes de contrôle de la qualité protéique (PQC).

Pour atteindre ces objectifs, cette étude a utilisé exclusivement des modèles *in vitro* de cardiomyopathie dilatée induite par la mutation *DES^{E439K}*, se reposant sur des cardiomyocytes dérivés de cellules souches pluripotentes induites humaines (iPSC-CM) cultivées en monocouches 2D ou en myocarde humain (EHM). Ainsi, après avoir validé que les modèles récapitulaient les caractéristiques de la cardiomyopathie dilatée, il a été montré que dans un contexte de mutation *DES^{E439K}*, la protéostasie cellulaire était perturbée et la PQC activée, notamment le processus d'autophagie. Une approche d'imagerie à haut contenu a ensuite été mise en œuvre pour mieux caractériser et quantifier les propriétés phénotypiques des iPSC-CM porteurs de la mutation *DES^{E439K}*. Cette méthode nous a permis de quantifier les effets de composés chimiques annotés et de sélectionner ceux capables d'inverser le phénotype cellulaire. L'identification des mécanismes d'action de ces composés a confirmé l'implication des processus de réponse au stress mitochondrial et du réticulum endoplasmique dans l'établissement des phénotypes pathologiques.

En conclusion, cette étude met en évidence l'importance de la régulation de la protéostasie cellulaire et de l'homéostasie mitochondriale dans les cardiomyopathie dilatée causée par la mutation du gène *DES*, ce qui pourrait représenter une approche thérapeutique intéressante.

Contents

I.	Introduction	6
I.1.	Myofibrillar Myopathy	6
I.2.	Dilated Cardiomyopathy.....	7
I.3.	Desmin related to (cardio)myopathy, Desminopathy.....	9
I.3.1.	Desmin.....	10
I.3.2.	Pathophysiological mechanisms caused by a <i>DES</i> mutation.....	14
I.3.3.	Proteostasis and cardiac diseases.....	16
I.3.4.	Therapeutic approaches for desminopathies.....	21
I.4.	Disease Modeling	22
I.4.1.	Animal models.....	23
I.4.2.	<i>In vitro</i> 2D	25
I.4.3.	<i>In vitro</i> 3D	29
I.5.	High content imaging	31
I.5.1.	Principle.....	31
I.5.2.	Image-based profiling.....	34
I.5.3.	Image-based profiling in drug discovery.....	42
II.	Objective.....	46
III.	Materials and Methods	48
III.1.	Cardiomyocytes derived from induced pluripotent stem cells	48
III.1.1.	Induced pluripotent stem cells and genomic editing	48
III.1.2.	Cardiomyocyte derived induced pluripotent stem cells (iPSC-CM) .	49
III.1.3.	Thawing iPSC-CM	52
III.1.4.	iPSC-CM Culture Media	52
III.1.5.	iPSC-CM staining and image acquisition.....	54
III.2.	Engineering Human myocardium (Myrtissues)	55

III.3.	Seahorse	56
III.4.	Transcriptomic Analysis	56
III.4.1.	RNA extraction	56
III.4.2.	Reverse transcription cDNA	56
III.4.3.	RNA sequencing	57
III.4.4.	RT-qPCR.....	58
III.5.	Protein expression analysis	59
III.5.1.	Protein extraction	59
III.5.2.	Western blot	59
III.6.	Image analysis and Data mining	60
III.7.	Statistical analysis	65
III.8.	Tool compounds treatment.....	65
IV.	Results	67
IV.1.	Functional impairment associated with dilated cardiomyopathy due to a Desmin mutation (<i>DES</i> ^{E439K})	67
IV.1.1.	Functional contraction in EHM 3D model.....	67
IV.1.2.	Functional mitochondrial respiration in iPSC-CM	70
IV.1.3.	Desmin aggregation and autophagic flux in iPSC-CM.....	72
IV.2.	Transcriptomic study on EHM models	75
IV.2.1.	Transcriptomic exploration using RNAseq.....	75
IV.2.2.	Transcriptomic validation RT-qPCR	80
IV.3.	Optimization of iPSC-CM modeling dilated cardiomyopathy caused by <i>DES</i> ^{E439K} mutations for High content imaging	85
IV.3.1.	Developing cell imaging tools on 384 well plate.....	85
IV.3.2.	Optimization Cell culture condition on 384 well plate format.....	90
IV.4.	Implementation of a high-content imaging assay for screening	97
IV.4.1.	Read out identification	97
IV.4.2.	Cell profiling classification model	106

IV.4.3. Tool compounds identification	123
V. Discussion.....	147
V.1. Disease modeling: a perspective on opportunities and limitations.....	147
V.1.1. Immaturity of iPSC-CM	147
V.1.2. Isogenic pairs CRISPR/Cas9 and Monogenic disease	150
V.1.3. Engineered human myocardium limited for high-throughput phenotypic studies	152
V.2. Characterization of phenotypes associated with <i>DES</i> ^{E439K} mutation..	152
V.2.1. <i>DES</i> ^{E439K} induced Desmin aggregation, Mitochondria alteration and Sarcomere defect	152
V.2.2. Proteostasis response to aggregate protein and dysfunctional mitochondrial stress.....	153
V.2.3. <i>DES</i> ^{E394K} impairs cardiac development	159
V.3. High-content imaging and screening strategies.....	159
V.3.1. Phenotypic characterization using HCI and image-based profiling	159
V.3.2. Screening and tool compounds.....	161
VI. Conclusion and perspective	164
VII. Bibliographie	166
VIII. Annexes	188

Abbreviations

- MFM:** Myofibrillar myopathy
- DCM:** Dilated cardiomyopathy
- ER/SR:** Endoplasmic reticulum/Sarcoplasmic reticulum
- Hsp:** Heat shock proteins
- PTM:** Post translational modification
- PAO:** Preamyloid oligomers
- PQC:** Protein quality control
- UPS:** Ubiquitin proteasome system
- ER:** Endoplasmic reticulum
- 2D:** Two dimensional
- 3D:** Three dimensional
- iPSC:** Induced pluripotent stem cell
- CM:** Adult human cardiomyocytes
- iPSC-CM:** Cardiomyocyte derived from iPSC
- hEHT:** Human engineered heart tissue
- EHM:** Engineered human myocardium
- HCI:** High Content Imaging
- HCS:** High content screening
- HCA:** High content analysis
- AI:** Artificial intelligence
- ML:** Machine learning
- LDA:** Linear Discriminant Analysis
- TBDD:** Target-based drug discovery
- PDD:** Phenotypic drug discovery
- T3:** Thyroid hormone triiodothyronine
- Dex:** Glucocorticoid dexamethasone
- NT:** not treated
- Chlq:** Chloroquine
- DEG:** Differentially expressed genes
- GO:** Gene Ontology
- cTnT:** Troponin T
- ROI:** Region of interest
- D10:** 10 days cell culture

D20: 20 days cell culture

I. INTRODUCTION

I.1. Myofibrillar Myopathy

Myofibrillar myopathy (MFM) is a rare neuromuscular disease characterized by the onset of progressive muscle weakness. In the 1990s, a number of myopathies were grouped together under the term MFM, on the basis of common characteristics. These muscular pathologies presented the same histopathological patterns, as well as myofibrillar dissolution associated with the accumulation of myofibrillar degradation products. In addition, ectopic expression of multiple Z-disc-derived proteins was observed (Béhin et al., 2015).

MFM is a heterogeneous group of hereditary diseases. According to rare disease databases (OMIM and Orphanet) the main genes known to be associated with MFM are *DES* (coded for Desmin), *CRYAB* (coded for α -B-crystallin), *MYOT* (coded for Myotilin), *LDB3* (coded for LIM domain binding 3), *FLNC* (coded for Filamin C), *BAG3* (coded for BAG cochaperone 3), *FHL1* (coded for Four and a half LIM domains 1), *TTN* (coded for Titin) and *DNAJB6* (coded for DnaJ heat shock protein family (Hsp40) member B6). The majority of hereditary mutations are autosomal dominant, a few mutations follow autosomal recessive mode, and few others are present as sporadic forms. The underlying mechanisms of these disorders are not yet fully understood. They may differ from one type of disorder to another, depending on the causal mutations in a single gene. Actually, some pathologies such as laminopathy or selenopathies have the same histopathological features as MFM, but are not classified in the same group. In fact, these disorders have quite distinct pathophysiological mechanisms (D'Amico et al., 2005; Ferreiro et al., 2004).

The clinical spectrum of MFM is large, in addition to the progressive development of proximal and/or distal limb muscle weakness; limb-girdle and scapuloperoneal phenotypes may be observed, as well as involvement of muscles of the hand, face and pharynx (Schröder & Schoser, 2009). Cardiomyopathy, peripheral neuropathy, respiratory failure and cataracts are frequently associated clinical perturbations (Ferrer & Olivé, 2008). The diagnosis of these pathologies can be established by muscle biopsy showing abnormal fibers containing amorphous material of irregular shape and size or the positivity test into

the aggregate structure for several proteins, including α -B-crystallin, desmin and myotilin (Cannone et al., 2023).

MFM and more specifically those caused by pathogenic variants in the *DES* gene are associated with a high risk for arrhythmogenic dilated cardiomyopathy, characterized by a high risk for (1) severe heart failure due to left ventricular systolic dysfunction and restrictive filling pattern and (2) arrhythmic complications including complete atrioventricular block and sustained ventricular tachyarrhythmias (Wahbi et al., 2012a).

1.2. Dilated Cardiomyopathy

Cardiomyopathies are a group of heart disorders characterized by structural or functional alterations of the heart muscle, without an external cause such as coronary disease or arterial hypertension being responsible for these abnormalities. As a result, the heart is no longer able to perform its role of pumping blood efficiently. Cardiomyopathies are a major source of cardiovascular morbidity and mortality worldwide (Brieler et al., 2017). There are several types of cardiomyopathy, including restrictive cardiomyopathy, hypertrophic cardiomyopathy or dilated cardiomyopathy (DCM) (McNally EM, 2017). DCM is one of the most common forms of cardiomyopathy. It manifests as abnormal dilatation of the heart's chambers, principally the left ventricle, leading to loss of contractile function and heart failure. The diagnostic tests for all patients with known or suspected DCM include clinical history, laboratory tests, electrocardiogram (ECG), and cardiac imaging. Classically, a diagnosis of DCM requires the identification of both ventricular dilation and systolic dysfunction (Heymans et al., 2023).

There are several direct causes of DCM: pathogenic gene variants, infections, autoimmunity, toxins (ethanol, recreational drugs and cancer treatments), endocrinopathies and tachyarrhythmias. In 30-40% of cases, DCM is due to a genetic cause. The mode of inheritance of familial DCM is typically autosomal dominant, suggesting a monogenic or mendelian cause, although X-linked, autosomal recessive and mitochondrial inheritance can also be observed (Khan et al., 2022). Over fifty genes have been characterized as inducing DCM, however, evidence of causality is often incomplete (Mazzarotto et al., 2020). Previous studies using a contemporary variant classification have highlighted the importance of some twenty genes for which pathogenic or probable pathogenic variants have been shown to be more or less causative of DCM. These genes code for proteins involved in different mechanisms of cardiac contractility (Figure 1).

Myofibril contractile dysfunction plays a central role in the initiation and progression of DCM. The sarcomere is composed of numerous proteins, and mutations in several of them have been associated with DCM, including actin α -cardiac muscle 1 (encoded by *ACTC1*), myosin C binding protein cardiac type (encoded by *MYBPC3*), myosin chains (encoded by *MYL2*, *MYL3*, *MYH6* and *MYH7*) and the α 1 chain of tropomyosin (encoded by *TPM1*). Mutations in genes encoding cardiac troponins (encoded by *TNNT2*, *TNNC1* and *TNNI3*) are also directly linked to disordered force generation (Willott et al., 2010). Mutations in TTN which encodes the giant titin protein that connects myosin to the Z-discs, are found in approximately 25% of patients with DCM (Ware & Cook, 2018). Mutations in genes encoding proteins that are not directly related to the sarcomere have also been described to be involved in the development of DCM. For example, mutations in other non-contractile proteins (a co-chaperone for heat shock protein 70 (*HSP70*) encoded by *BAG3*) can induce defects in cellular signaling pathways that alter cardiac response (Knezevic et al., 2015). Moreover, mutations in phospholamban (encoded by *PLN*), a key calcium signaling protein, have been directly linked to abnormal contractility (G. S. Liu et al., 2015). It was also reported that desmosomal protein variants, notably, desmocollin 2 (encoded by *DSC2*), desmoglein 2 (encoded by *DSG2*), desmoplakin (encoded by *DSP*) and plakophilin 2 (encoded by *PKP2*) are most commonly associated with arrhythmogenic right ventricular cardiomyopathy, but mutations in these genes have also been implicated in DCM (Sen-Chowdhry et al., 2008). In addition, in some patients with genetic DCM, a particular genetic defect may be suggested by cardiac conduction abnormalities. In particular, variants of lamin A/C (encoded by *LMNA*) a protein structure linked to the inner nuclear membrane are associated with high rates of conduction system disease, ventricular arrhythmias and sudden cardiac death (Japp et al., 2016).

Finally, the cytoskeleton which provides an important intracellular scaffold for the transmission of force from the sarcomere to the extracellular matrix and for the protection of the myocyte against external mechanical stress could also be associated to DCM. Indeed, defects in cytoskeletal proteins such as desmin (encoded by *DES*) could predispose to DCM by reducing force transmission and/or resistance to mechanical stress (Wahbi et al., 2012b).

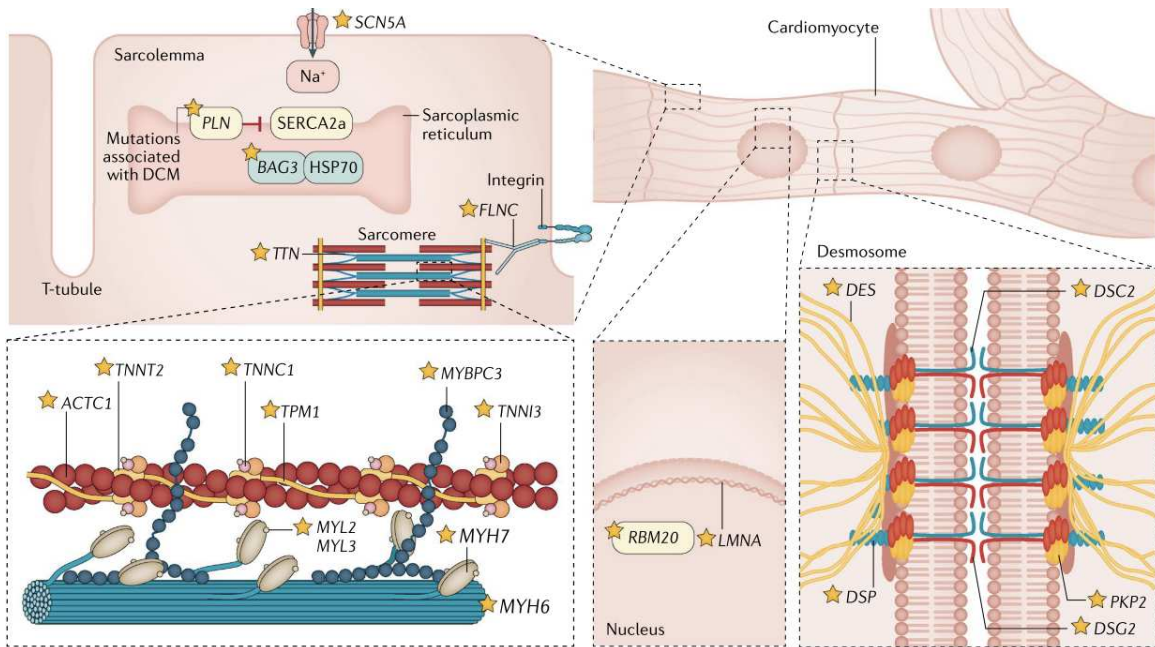


Figure 1 : Genetic causes of dilated cardiomyopathy. Stars represent genes whose mutation is likely to induce dilated cardiomyopathy from (Schultheiss et al., 2019)

1.3. Desmin related to (cardio)myopathy, Desminopathy

Desminopathy refers to diseases caused by disruption of the desmin protein, such as MFM and DCM. Morphologically, desminopathies are often characterized by protein aggregation of the desmin and disruption of the myofibrillar network (Selcen, 2011). In addition, abnormalities in the intercalated discs and mainly in mitochondria are observed (Goldfarb & Dalakas, 2011). Initially, desminopathy was associated with progressive distal limb myopathy, but other studies have shown that desminopathy can be considered as part of the MFM family (Béhin et al., 2015). Cardiac manifestations may precede, co-occur or follow skeletal muscle manifestations. They take the form of cardiomyopathy leading to cardiac conduction disorders or arrhythmias. Patients carrying *DES* mutations are also at risk of developing respiratory and ocular diseases such as cataracts conduction (Capetanaki et al., 2015).

Desminopathies are rare diseases with a prevalence of 5/10000, due to mutation in *DES* encoding desmin. These diseases are found in both men and women. However, it has been observed that men carrying the heterozygous mutation are more likely prone to develop cardiac manifestations. The average age of manifestation is quite variable, ranging from the first to the eighth decade of life. However, it appears that the majority of patients manifests the disease between their 2nd and 4th decade of life (Clemen et al., 2013).

More than 70% of *DES* mutations induce heterogenous cardiac manifestations (Van Spaendonck-Zwarts et al., 2011), which are the main cause of premature death in this type of patients (Figure 2).

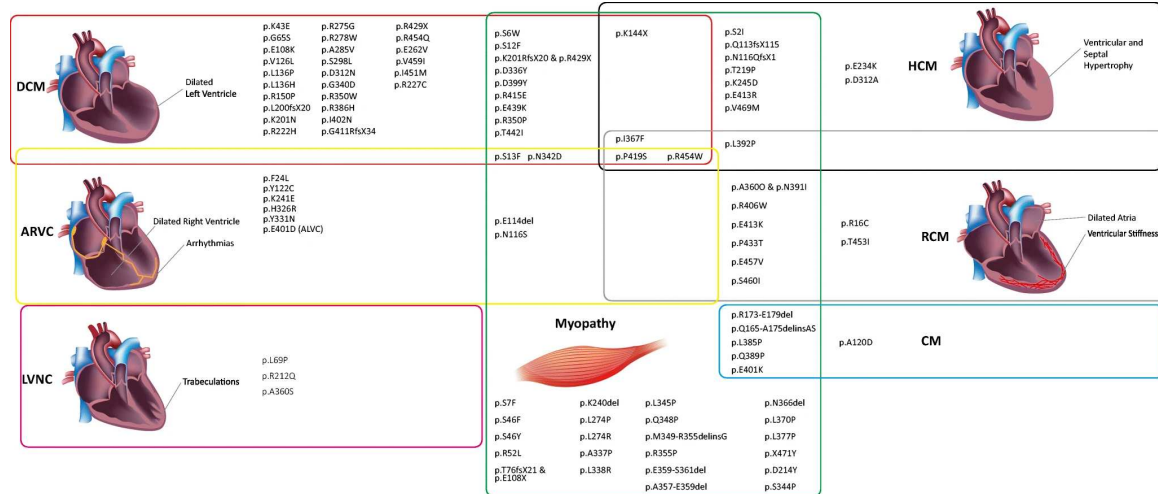


*Figure 2 : Venn diagram indicating the different cardiac and skeletal phenotypes of *DES* mutation carriers. Of note, the associated clinical phenotypes of different mutations overlap significantly. DCM = dilated cardiomyopathy, HCM = hypertrophic cardiomyopathy, ARVC = arrhythmogenic right ventricular cardiomyopathy, RCM = restrictive cardiomyopathy, LVNC = left ventricular cardiomyopathy, CM = atypical or unknown cardiomyopathy from (Brodehl et al., 2018)*

I.3.1. Desmin

In eukaryotic cells, three filamentous systems form the cytoskeleton. First, actin filaments ensure the structural integrity and stability of almost all mammalian cells, in (cardio)myocytes, these structures also compose the sarcomeric filaments. Next, microtubules are composed of α and β -tubulin and are required for kinesin-mediated vesicle transport. Lastly, intermediate filaments ("IF") are formed by highly flexible, non-globular protein units, composed mainly of α -helices. IF proteins are nanomolecular springs that offer structural flexibility. There are over 73 different IF proteins, classified into six groups on the basis of similarities between their amino acid sequences (Hnia et al., 2015). In cardiac tissue, the cytoskeletal IF proteins expressed are:

- type III: desmin, vimentin, paranemin and sycoilin
- type IV: symenin and nestin
- type V: nuclear lamins

Desmin is the muscle-specific IF protein and the most abundant IF protein expressed in cardiomyocytes, it is also found in skeletal and smooth muscle cells.

Desmin is a 470 amino acid protein with a molecular weight of 53.5 kDa. Like all IF proteins, desmin is fibrous in nature and has a tripartite structure with a central, predominantly α -helical. This domain, known as the "rod", is surrounded by non- α -helical amino-terminal ("head") and carboxy-terminal ("tail") domains. The central rod domain contains four alpha-helical regions (1A, 1B, 2A, 2B) separated by three non-helical junctions (Figure 3).

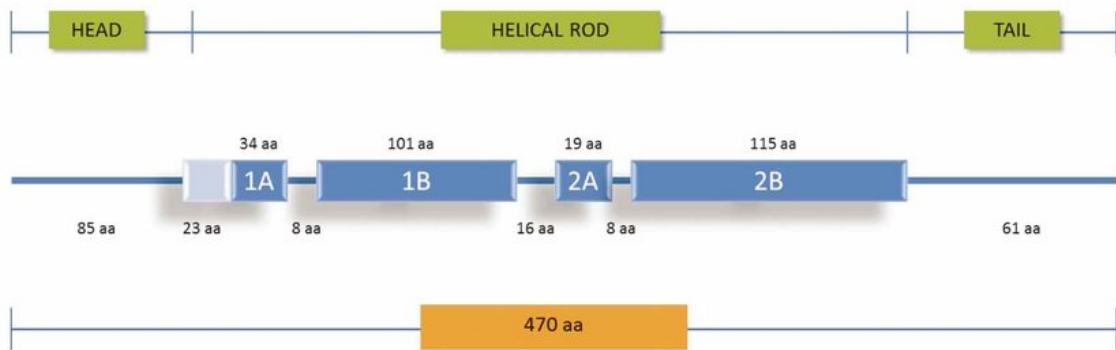


Figure 3 : Schematic representation of desmin protein. Amino acid (aa) from (Marzuca-Nassr et al., 2018)

The human desmin gene (*DES*), located on chromosome 2q35, is a single-copy gene spanning approximately 8.3 kb and comprising nine exons encoding for desmin. Nearly 70 mutations in the *DES* gene have been identified as inducing desminopathy (Van Spaendonck-Zwarts et al., 2011). The vast majority of familial desminopathies follow an autosomal dominant mode of inheritance. The most frequent *DES* mutations are missense mutations leading to single amino acid substitutions (Clemen et al., 2013).

Desmin is one of the first muscle-specific proteins to appear during embryonic development, where it is transiently expressed along with vimentin, nestin and keratins (Kuisk et al., 1996). Studies have shown that amino-terminal mutations in desmin interfere with cardiogenesis by altering important cardiogenic regulators such as brachyury, goosecoid, nkx2.5 and mef2 (Hofner et al., 2007). Indeed, desmin appears to play a regulatory role during myogenic and cardiogenic commitment and differentiation (Höllrigl et al., 2007).

Desmin and its multiple binding partners form a 3D scaffold that spans the entire diameter of the cardiomyocyte, surrounding the Z-discs linking the contractile apparatus to the costamers and intercalated discs of the plasma membrane, as well as to most membrane-bound cellular organelles, including mitochondria, the sarcoplasmic reticulum and the nucleus (Capetanaki et al., 2007).

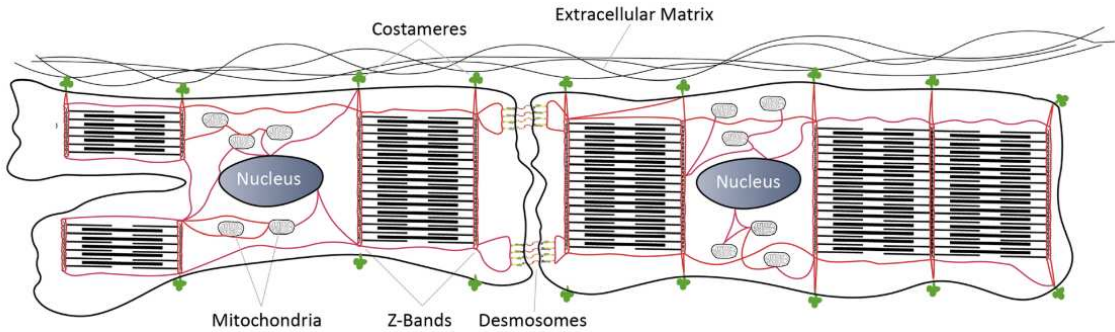


Figure 4 : Schematic overview about the localization of desmin filaments (red) in cardiomyocytes. Of note, desmin filaments connect several protein-protein complexes (e.g., desmosomes) and cell organelles (mitochondria, nuclei) to the cytoskeletal network from (Brodehl et al., 2018)

First, desmin were described to be responsible for the lateral alignment of myofibrils and the integrity of the contractile apparatus (Granger & Lazarides, 1980). However, in *DES*^{-/-} mice model (Z. Li et al., 1996), overexpression of Bcl-2, a mitochondrial anti-apoptotic protein, has been shown to restore correct Z-disk alignment in the absence of desmin (Weisleder et al., 2004). Still, desmin is important to ensure the stability of these structures, as illustrated by some studies where the interaction of nebulin and nebulette with desmin induced stabilization of actin filaments in sarcomeres (Hernandez et al., 2016).

Studies involving a desmin-deficient mice model (*DES*^{-/-}) have highlighted the importance of the interaction between desmin and mitochondria (Milner et al., 2000). (Cardio)muscular homeostasis requires a close link between energy production and demand. Therefore, mitochondrial abnormalities are a common pathological feature of desmin-related cardiomyopathies. Indeed, the earliest and most prominent features of *DES*^{-/-} mice are mitochondrial structural disturbances, appearing before any other cardiac dysfunction (Milner et al., 2000). Mitochondrial defects include loss of proper morphology followed by cardiomyocyte death, inflammation, fibrosis and calcification. This cascade of events leads to myocardial degeneration, DCM and heart failure (Fountoulakis et al., 2005). Desmin appears to be important for cristae structure, respiratory function, activation of the mitochondrial permeability transition pore (mPTP), sensitivity to oxidative stress and appropriate mitochondrial membrane potential ($\Delta\psi_m$) (Diokmetzidou et al., 2016). Indeed, the desmin network could keep mitochondria close to myofibrils and facilitate the sensing and transfer of energy requirements, thus coupling mechanochemical signaling to metabolism. Moreover, desmin would also promote mitochondrial interactions with other organelles such as the endoplasmic reticulum/sarcoplasmic reticulum (ER/SR) (Tsikitis et al., 2018). Indeed, it has been shown that desmin is localized in contact sites between the

SR and mitochondria (MAMs, mitochondria-associated membranes), structures that are important for multiple cellular processes, including Ca^{2+} and metabolite transfer, lipid metabolism, regulation of mitochondrial shape, the formation of autophagosomes and inflammasomes (Eisner et al., 2013). This association could be mediated by the voltage-dependent anion channel (VDAC), present in both mitochondria and SRs, which has been shown to interact directly with desmin (H. Li et al., 2016). The importance of desmin in mitochondrial function is reinforced by the discovery of desmin associating with various mitochondrial proteins like the MICOS (mitochondrial contact site and cristae organizing system) complex, the mitochondrial outer membrane Sam50 and OPA1 involved in fusion and ATP synthase β (Diokmetzidou et al., 2016). Furthermore, a recently demonstrated association of RyR2a with myospryn desmin-associated protein (CMY45, cardiomyopathy-associated 5), a novel protein of the tripartite motif (TRIM) family, demonstrated an indirect pathway for desmin association with the SR of cardiomyocytes (Agnetti et al., 2022).

Interestingly, studies have shown that desmin can be associated with proteins involved in vesicle trafficking and control of endo/lysosomal compartments. This promotes the appropriate biogenesis and distribution of lysosomes in cardiomyocytes, and potentially the appropriate formation of autophagosomes/autophagophores (X. Wang & Robbins, 2014).

Two heat shock proteins have been described as interacting with desmin at multiple sites: Hsp25 (Hsp27) and α -B-crystallin (HspB5) (Wettstein et al., 2012). The desmin- α -B-crystallin interaction appears to play an important role in the pathology of cardiomyopathies. Mutations in this hsp cause the same desmin-related DCM and heart failure with similar mitochondrial defects (Goldfarb & Dalakas, 2011). α -B-crystallin and desmin are notably localized in mitochondria-SR contact sites (MAMs) and their correct interaction has mitoprotective and cardioprotective effects (Ganguly et al., 2014). It has been illustrated that overexpression of α -B-crystallin in desmin-deficient hearts improves all mitochondrial defects and cardiac function (X. Wang et al., 2001). Mechanisms involving hsp will be described later in the manuscript.

Post-translational modifications of desmin include phosphorylation, ADP-ribosylation, ubiquitination, glycation, oxidation and nitration and have implicated in the pathogenesis of desmin-related muscle diseases (Claeyssen et al., 2023; D. L. Winter et al.,

2014). Most post-translational modifications result in the disassembly of the desmin network, with the exception of ubiquitination, which leads to its degradation.

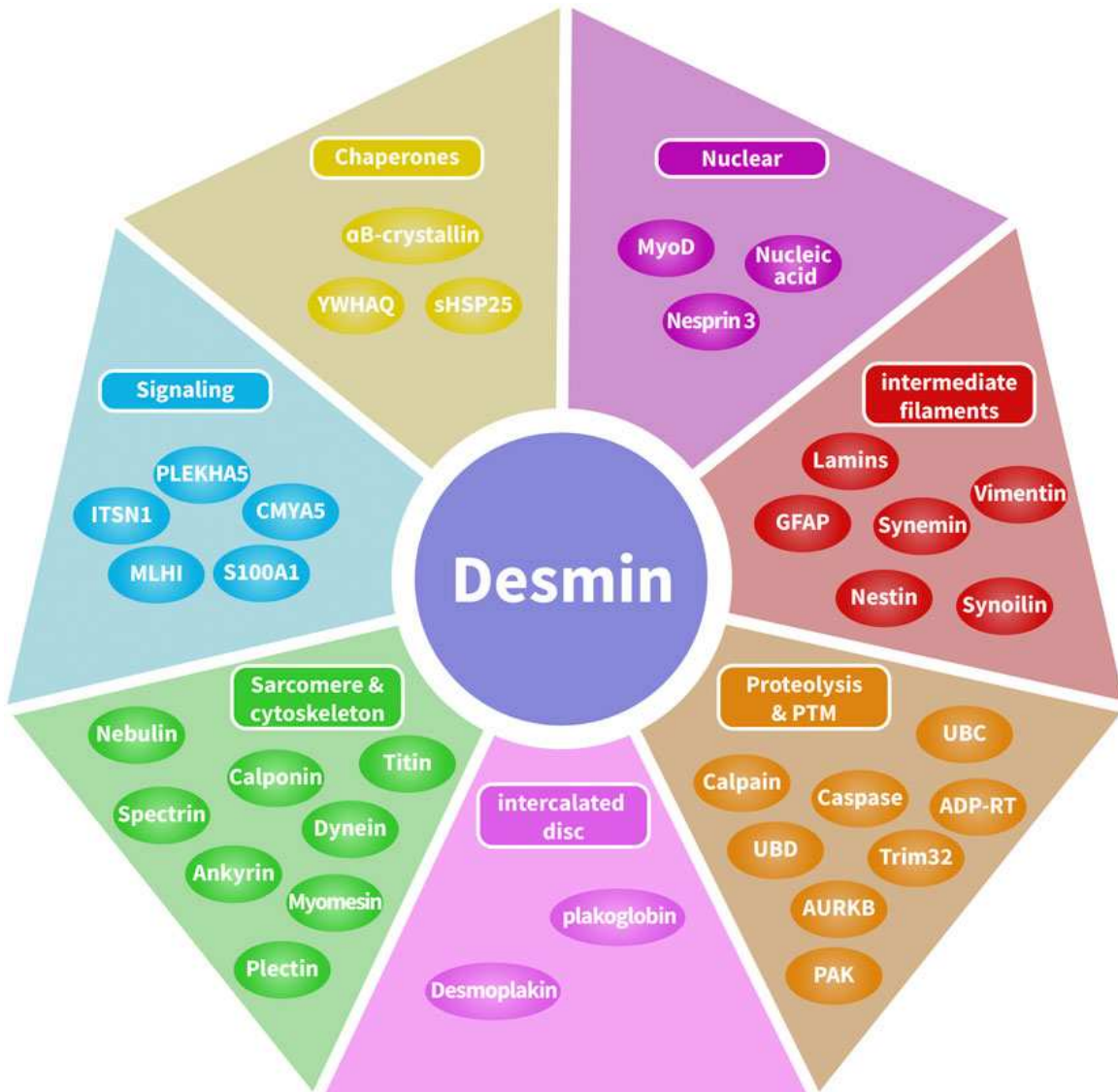


Figure 5 : Desmin interactome map (Su et al., 2022)

I.3.2. Pathophysiological mechanisms caused by a *DES* mutation

As already mentioned *DES* mutations are characterized by the appearance of abnormal cytoplasmic aggregates of desmin in (cardio)myocytes, this phenomenon could be considered as a histopathological hallmark for desminopathies (Bär et al., 2004). Nevertheless, it is still not clear what the main cause of cardiomyocyte degeneration is between the appearance of toxic aggregates and the loss of function of the desmin network (Capetanaki et al., 2015).

Considering the multiple interactions of desmin with other cell constituents, it's not surprising that a *DES* mutation induces a variety of pathophysiological mechanisms that

can lead to cell death. First, the aggregation formation could not be composed only of desmin misfolded protein but by its binding partners that could also co-aggregate (Quinlan et al., 2013). These aggregates can lead to apoptosis, like it was observed in a study where abnormal protein aggregates caused by the *CRYAB* p.R120G mutation (a mutation in the gene encoding for α -B-crystallin considered to induce desminopathy) lead to increased apoptosis, mediated by caspase-3 activation, in transgenic mice (Maloyan et al., 2007). It has also been shown that desmin filaments can be substrates for apoptosis-promoting caspases (Chen et al., 2003). Furthermore, formation of these protein aggregates may be accompanied by the generation of toxic oligomers with amylopathic potential (Sanbe et al., 2004), similar with the ones observed in many neurodegenerative diseases. Many post translational modification are responsible for initiating the nucleation process that leads to the toxic formation of preamyloid oligomers (PAO). A study showed that specific expression of an exogenous peptide capable of adopting a PAO conformation in cardiomyocytes was sufficient to induce heart failure leading to mortality in a transgenic mice model (Pattison & Robbins, 2008). Although the exact mechanism of cellular toxicity induced by protein aggregates in the heart is a subject of debate, studies have shown that PAO cause a disruption of Ca^{2+} transients (S. R. Singh & Robbins, 2018).

A study showed that actin filaments can also be affected by a *DES* mutation (Conover et al., 2008). This may be explained by the existence of cross-linked between IF system and cytoskeletal components. Consequently, (cardio)myoblast force of contraction and full cell elasticity can be impaired by *DES* mutations (Charrier & Jamme, 2016)(Even et al., 2017).

Interestingly, several studies have reported structural or functional alteration of mitochondria by *DES* mutations (Henderson et al., 2013; McCormick et al., 2015; Smolina et al., 2020; Lilli Winter et al., 2016). Desmin deficiency compromises interaction with α -B-crystallin, which appears to be necessary for proper targeting of proteins to mitochondria and SR. It disturbs the assembly and stabilization of mitochondrial and SR complexes. This disruption affects the dialogue between these organelles as well as mitochondrial biogenesis and function (S. Singh et al., 2020). The desmin network also ensures the proper functioning of costamers and intercalated discs. Disruption of the network therefore leads to dysfunction of these structures which can no longer support cell adhesion, cell-cell communication and electrical conductivity. These various disturbances will induce a proteostasis imbalance and lead to decreased contractile function observed in heart failure (Figure 6).

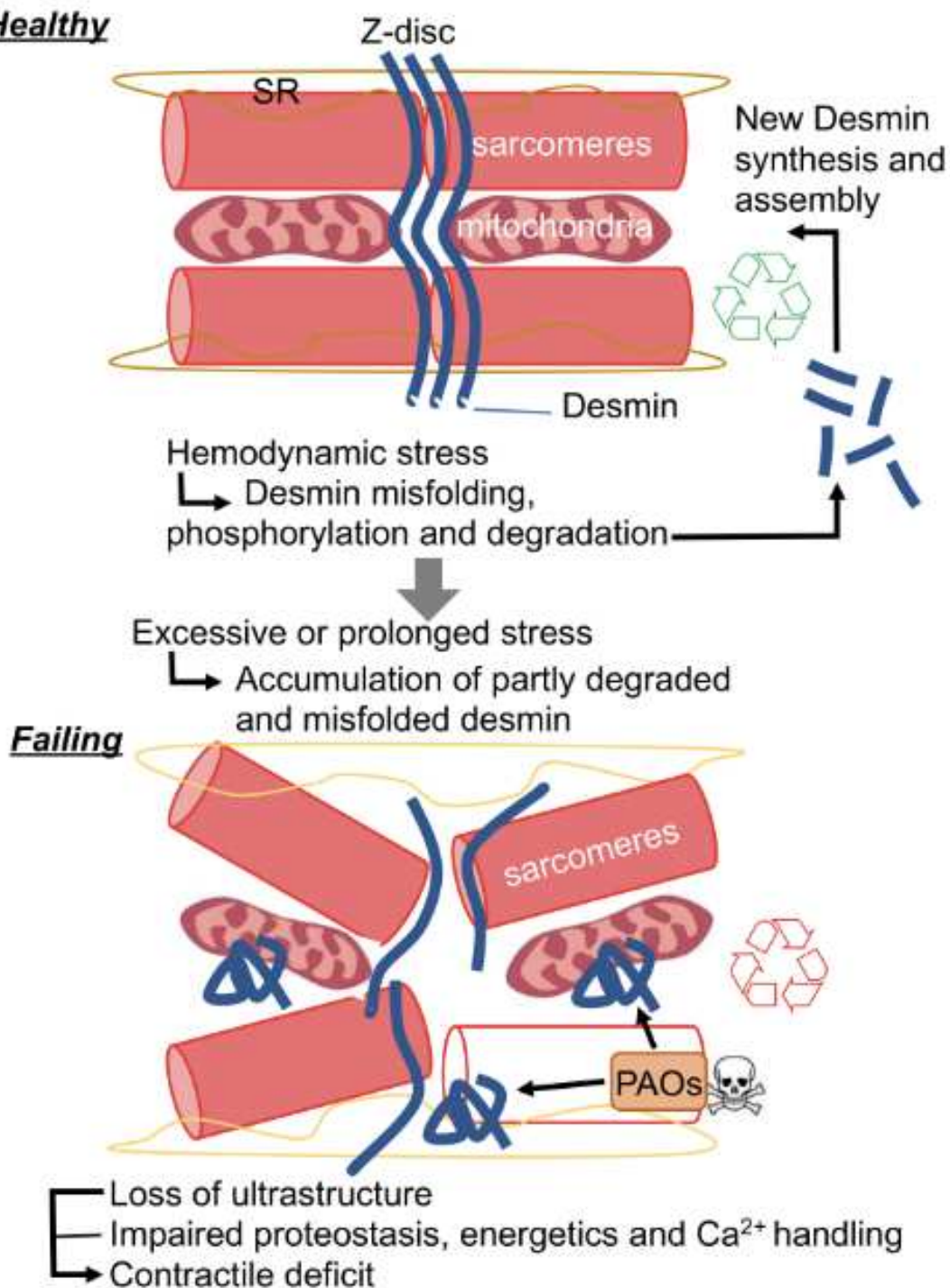


Figure 6 : New proposed mechanism for desmin pathophysiological function in cardiac disease. SR, sarcoplasmic reticulum; preamyloid-oligomers (PAO) from (S. Singh et al., 2020)

I.3.3. Proteostasis and cardiac diseases

Cellular proteostasis refers to the dynamic balance between protein synthesis, maintenance and degradation within the cell. This balance is essential for proper cell function, particularly in post-mitotic cells such as cardiomyocytes. Proteostasis therefore plays an essential role in maintaining a healthy heart (Maejima, 2020). There are a number

of elements involved in maintaining proteostasis, including protein quality control (PQC) systems mainly composed of heat shocks protein system, ubiquitin-proteasome process and autophagic system. PQC ensure the degradation of misfolded proteins and protein aggregates (Figure 7).

Firstly, chaperones, also known as heat shock proteins (hsp), help to induce the correct conformation of proteins by assisting proper folding and repair damaged proteins. Chaperone proteins also prevent the formation of protein aggregates. These specialized proteins help to guide misfolded proteins to the appropriate degradation systems. There are different types of hsp: HSPA (HSP70), HSPB (small HSPs), HSPC (HSP90), HSPD and HSPE (chaperonin families HSP60 and HSP10, respectively), HSPH (HSP110), and DNAJ (HSP40). These groups of chaperones have different roles and are specifically localized in cellular compartments. These proteins can be expressed constitutively or in response to stress. In cardiomyocytes, high levels of specific members like the small HSP families (HSPBs), are observed. These are HSPB1 (HSP27), HSPB5 (α -B-crystallin), HSPB6 (HSP20), HSPB7 (cardiovascular HSP) and HSPB8 (HSP22), which are considered to protect cardiomyocytes from proteotoxicity by stabilizing the contractile apparatus. α -B-crystallin is the specific chaperone of the desmin protein. α -B-crystallin is essential for the assembly and formation of the desmin network. α -B-crystallin also interacts with desmin to inhibit its aggregation. In addition to promoting the assembly and stabilization of desmin IFs, the interaction between desmin and α -B-crystallin is involved in mitochondrial homeostasis and cell viability (Claeyssen et al., 2023). It should be noted that studies have shown that a mutation in the *CRYAB* ^{R120G} gene induces the same characteristics as desminopathy and can therefore be considered as a desmin related myopathy (Bova et al., 1999). An increased levels of α -B-crystallin and Hsp27 in skeletal muscle tissue derived from homozygous *DES*^{R349P} desmin knock-in mice and in desminopathy myotubes models has been observed (L. Winter et al., 2019).

The ubiquitin proteasome system (UPS) is a system that degrades misfolded proteins down to a certain size. This system begins with a process of ubiquitination, whereby small ubiquitin molecules are bound to the misfolded target protein. The ubiquitylation machinery involves the ubiquitin-activating enzyme (E1), ubiquitin-conjugating enzymes (E2) and ubiquitin ligases (E3). The misfolded ubiquitinated proteins are then directed to the proteasome, which degrades the target proteins into peptides that can be reused for the synthesis of new proteins. Unfolded proteins in the endoplasmic reticulum (ER) are

removed by the ER-associated degradation system (ERAD) (Henning & Brundel, 2017b). ERAD induces translocation of unfolded proteins from the ER to the cytosol, where they are eliminated by the UPS. In a model of muscular atrophy, a study showed that desmin was subject to ubiquitylation by the ubiquitin ligase Trim2, favoring degradation by the proteasome. This ubiquitylation was induced by GSK3b phosphorylation of desmin. (Cohen et al., 2012). It appears that misfolded desmin prior to aggregate formation is recognized and guided to proteasomal degradation by the MTM1-UBQLN2 complex. (Gavriilidis et al., 2018). It has been shown in the immortalized myotube model carrying a *DES*^{R349P} mutation an increase of the overall activity of the UPS (L. Winter et al., 2019). Besides, the overexpression of *DES* p.Arg¹⁷³ Glu^{179del} in cultured neonatal rat ventricular myocytes led to the formation of desmin-positive protein aggregates and inhibited the function of the UPS in a dose-dependent manner (J. Liu et al., 2006). It should be noted that this system also plays an important role in mitochondrial homeostasis. Two predominant mechanisms by which the UPS protects mitochondria from the accumulation and toxic effects of abnormal proteins could be mentioned: Ubiquitin-mediated activation of mitochondria-specific autophagy (mitophagy) with ubiquitin ligase Parkin (Rakovic et al., 2019), and a direct ubiquitination and proteasomal degradation mediated removal of abnormal mitochondrial proteins involving the E3 ubiquitin ligase MITOL/MARCH5 (Karbowski et al., 2022).

If the misfolded proteins cannot be maintained, repaired or degraded by the first lines of defense of chaperones and the UPS system, the misfolded proteins may form protein aggregates which will be degraded by the autophagic system (Wiersma et al., 2016). The autophagic system begins with an initiation phase, with the formation of a phagophore. The phagophore then expands to form the autophagosome, a double-membrane vesicle that expands to encompass the cellular components to be degraded, such as misfolded proteins or defective organelles. Finally, the autophagosome fuses with a lysosome, a cellular structure containing digestive enzymes, to form an autolysosome. The enclosed components are then degraded, recycled for the synthesis of new proteins or used as a source of energy (Sciarretta et al., 2018). An increase in the activity of autophagic systems has been demonstrated in mouse hearts with transgenic overexpression of a desminopathy-linked mutant desmin (Q. Zheng et al., 2011). Moreover, the *DES*^{p.Arg¹⁷³ Glu^{179del} desmin mouse had been crossed with an autophagy reporter mouse model expressing a GFP-LC3 fusion protein and show an increase of autophagic activity. Interestingly, mitophagy, which}

mediates the selective elimination of dysfunctional mitochondria, is essential for cardiac homeostasis, it is regulated mainly by PTEN-induced putative kinase protein-1 (PINK1)/parkin pathway (Turkieh et al., 2022).

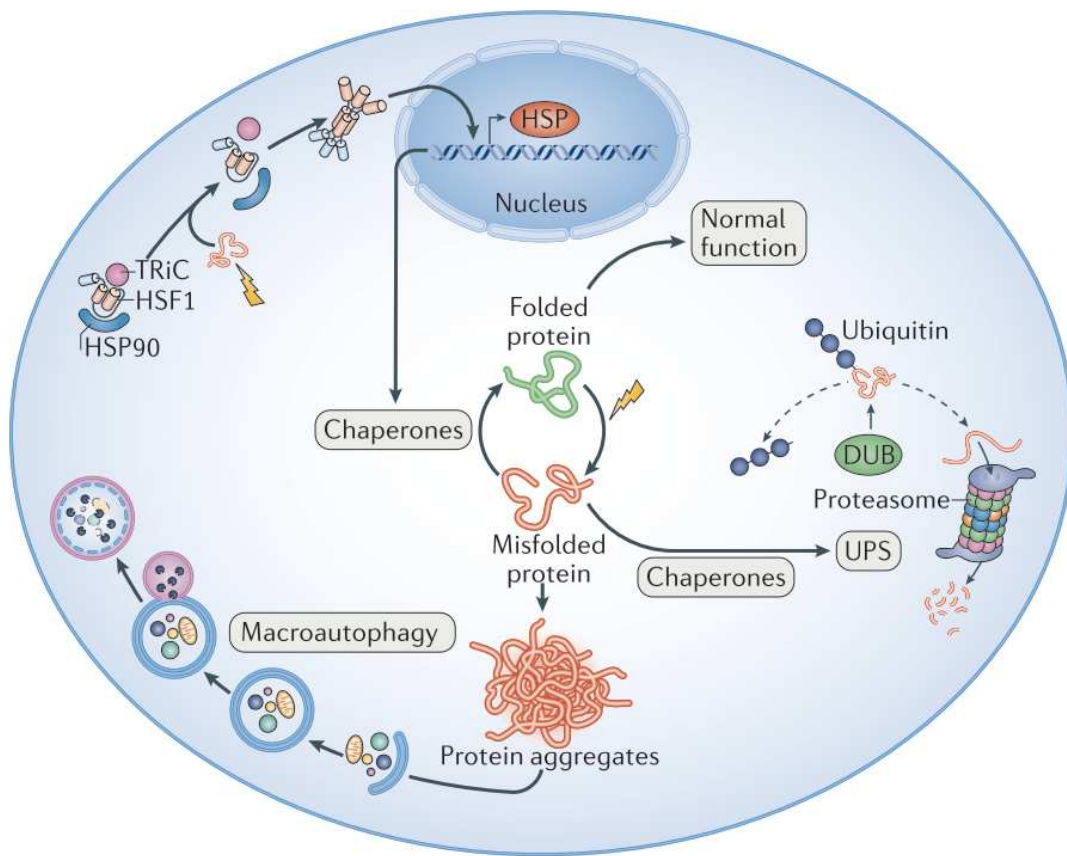


Figure 7 : Overview of the protein quality control system from (Henning & Brundel, 2017b)

It is also important to highlight the importance of cytoskeletal networks in maintaining proteostasis, particularly in cardiomyocytes. The cytoskeleton, composed of actin filaments, microtubule fibers and intermediate filaments, enables communication and maintenance of equilibrium between the components of the proteostasis network (Sequeira et al., 2014). This complex system plays an important role in signal transmission and the transport of ubiquitinated proteins within PQC systems. In particular, microtubules are of vital importance in this network and are in contact with the sarcoplasm/ER and mitochondria; loss of contact leads to Ca^{2+} overload in organelles, unfolded protein response in the ER and mitochondrial dysfunction.

Activation of PQC under diverse conditions of cardiac stress can be seen as a positive compensatory response to maintain proteostasis. This may be particularly true in the case of DCM due to a desmin mutation, where protein aggregation may be the mechanism responsible for the disease. In this case, the accumulation of protein aggregates may impair

PQC function by overloading its components, including chaperone proteins, the UPS system and autophagy. This could lead to increased levels of protein aggregates, exacerbating disease progression. These observations have also been noted in other studies of DCM due to mutations in genes encoding sarcomeric proteins (Dorsch et al., 2019). In this context, three scenarios are currently being debated. Firstly, the mutation has a direct effect on the PQC, which induces further cellular dysfunction. Secondly, the PQC initially compensates for the mutation-induced disruption, until its derailment leads to further cellular dysfunction. Finally, the mutation induces a compensation of the PQC systems which, weakened, will not be able to respond to other environmental stress, promoting the development of the disease (Figure 8).

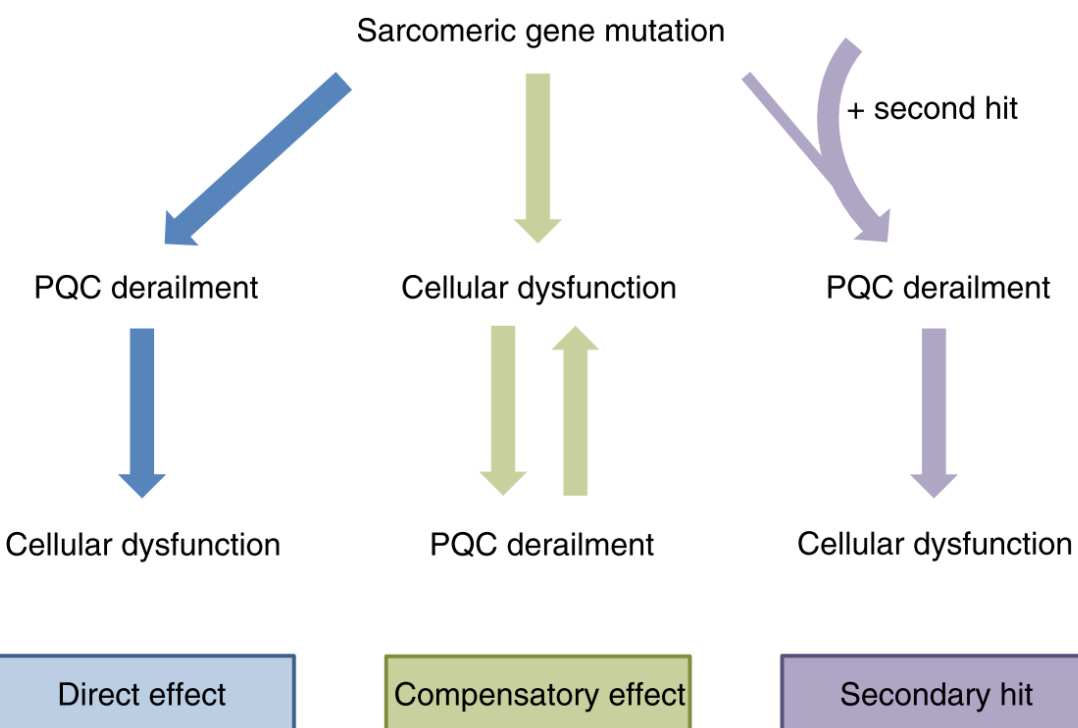


Figure 8 : Effects of sarcomeric gene mutations on the protein quality control (PQC) system from (Dorsch et al., 2019)

In conclusion, desminopathies were characterized by the production of abnormal desmin protein and its loss of function. This leads to structural defects in the cardiomyocyte, but also to altered mitochondrial positioning and function. As a result, oxidative stress can be generated (Lilli Winter et al., 2016). Secondly, aberrant proteins and organelles are detected by the PQC. Thus, PQC systems, hsp, UPS and autophagic degradation systems, will attempt to restore cellular proteostasis. Furthermore, the accumulation of protein aggregates can promote the formation of amyloid oligomers, leading to the generation of

beta-amyloid fibers, which are toxic to cells (Maejima, 2020). These events can ultimately lead to apoptosis or necrosis (Dunlop et al., 2009).

I.3.4. Therapeutic approaches for desminopathies

Taking into account observations of pathophysiological mechanisms involving desmin aggregates and mitochondrial disruption, stimulation of PQC systems has mainly been explored as a therapeutic approach for desminopathies (Batonnet-Pichon et al., 2017).

Firstly, induction of the HSP system is a strategy notably used in neurodegenerative pathologies also associated with proteinopathy due to protein aggregation (Hauser et al., 2000). Thus, α -B-crystallin activity has been identified as cardioprotective against the aggregation effects of mutant desmin. It has been shown that HSP27 (HSPB1) may also have a beneficial effect against toxicity mediated by misfolded proteins (Arrigo et al., 2007). Finally, a transgenic line expressing cardiac-specific HSP22 (HSPB8) also demonstrates a slowing of cardiomyopathy progression compared with *CRYAB* p.R120G mice. Indeed, a study showed that the non-toxic HSP inducer geranyl acetone, can inhibit desmin-related cardiomyopathy progression (Sanbe et al., 2009). Moreover, the chemical chaperone compound 4-phenyl-butyrate appeared to induce a reduction in protein aggregation in primary myotubes and plectin-deficient mice models displaying abnormal desmin aggregation (Lilli Winter et al., 2014).

Secondly, as previously mentioned, desminopathies are characterized by mitochondrial dysfunction, which can lead to oxidative stress as well as apoptotic processes. In this context, a mitochondrial ATP-sensitive potassium channel opener has been shown to induce a reduction in mitochondrial disruption and apoptotic death in *CRYAB* p.R120G transgenic mice (Sanbe et al., 2011). Secondly, a precursor of NAD⁺ involved in the acetylation of mitochondrial proteins and subsequently regulates mitochondrial function (R. Zhang et al., 2017) has been described as maintaining cardiac mitochondrial homeostasis and prevents heart failure.

Finally a pharmacological studies in C2C12 myoblastic cells expressing mutant *DES* found that a combination of inhibitor of the Rac1 pathway (a G protein signaling pathway involved in diverse cellular processes), antioxidant treatment and stimulation of macroautophagy reduced protein aggregation by up to 75% (Cabet et al., 2015). This confirms that combining strategies such as oxidative stress reduction and stimulation of

autophagy may be considered as an interesting therapeutic approach in the context of desminopathy.

In parallel with curative treatments, studies on *CRYAB* pR120G mouse models have shown that strategies involving preventive treatment, inhibiting the formation of protein aggregates, could be a solution. For example. Doxycycline administered to *CRYAB* pR120G transgenic mice reduces the formation of protein aggregates and prolongs the survival of transgenic mice (H. Zheng et al., 2010). Long-term voluntary exercise in *CRYAB* pR120G mice was shown to induce a significant reduction in beta-amyloid oligomers, with a concomitant increase in survival time (Maloyan et al., 2007).

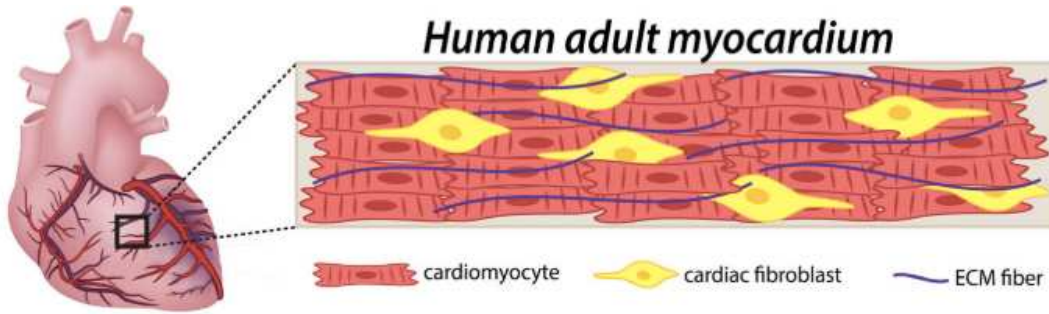
Despite this, there are no clear and effective treatment methods or drugs for impaired desmin-induced DCM. Nevertheless, concerning the consequences of cardiac arrhythmias, conduction defects and heart failure, there is some treatments. Thus, angiotensin-converting enzyme inhibitors (or angiotensin receptor blockers) and β-blockers are, for example, some of the standard drugs to treat heart failure caused by DCM (Schultheiss et al., 2019).

In conclusion, several therapeutic approaches are currently being explored for the treatment of patients suffering from desminopathies inducing notably DCM. An important element of this type of research is the use of disease modeling (Batonnet-Pichon et al., 2017). At the moment, there are a number of strategies with different advantages.

I.4. Disease Modeling

Disease modeling is a research approach focusing on reproducing and studying the characteristics of a disease in an experimental model. These models can be used to better understand pathophysiological mechanisms and to test potential therapies. There are different types of model (Veldhuizen et al., 2019). Firstly, animal models allow the study of complex diseases in a living organism (Figure 9). Secondly, *in vitro* models correspond to less complex cellular or tissue systems. However, they can have the advantage of being human models, with characteristics closer to those observed in patients (Figure 9). Lastly, 3D *in vitro* models, organoids resembling mini-organs, are often generated from stem cells (Figure 9).

With regard to disease modeling of desminopathy and DCM, there are different types of study models, ranging from animal models to organoid tissue or induced pluripotent stem cells.



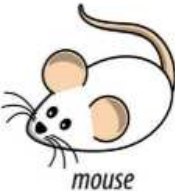
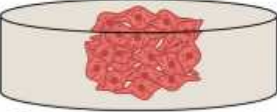
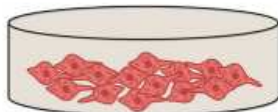
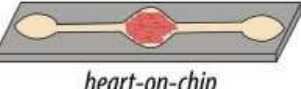
<i>in vivo models</i>	<i>3D assays</i>	<i>3D micromodels</i>
 <i>mouse</i>		
2D assays	 <i>spheroid</i>	 <i>muscular thin film</i>
 <i>culture dish</i>	 <i>hydrogel-encapsulated</i>	 <i>engineered heart tissue</i>
		 <i>heart-on-chip</i>

Figure 9 : Schematic of healthy adult myocardium and examples of the different platforms implemented for cardiac tissue modeling from (Veldhuizen et al., 2019)

I.4.1. Animal models

In the 1990s, *Des*^{-/-} knockout mice were generated by homologous recombination (Capetanaki et al., 1997; Z. Li et al., 1997). These mice were viable, fertile, and developed disturbances in all three types of muscle. Homozygous *DES*^{-/-} mice developed severe cardiomyopathy including hemorrhages, extensible fibrosis and calcification of the ventricular septum, whereas heterozygous *DES*^{+/+} mice were unaffected by these symptoms. Despite these interesting results, *DES*^{-/-} mice have certain limitations, as only a few *DES*^{-/-} mutations have been described in humans, indeed the majority of *DES* mutations induce aggregation dominated by functional alterations.

Different transgenic and knock-in mouse models expressing mutated desmin have been developed and characterized (Figure 10). One successful example is a *DES*^{P.R350P} knock-in mouse model, in which the development of DCM associated with cardiac arrhythmia and cardiac conduction disorder was observed (Clemen et al., 2015). Another

successful model has been recently implemented, the *DES*^{R405W}-desmin knock-in mice develop both a myopathy and a cardiomyopathy (Herman et al., 2023).

These symptoms were comparable to the clinical phenotypes of human patients with this desmin mutation. A transgenic mouse model with specific cardiac overexpression of mutant α-B-crystallin (*CRYAB*^{P.R120G}) was developed to study desminopathy. These mice are characterized by high mortality in early adulthood, toxic aggregates, increased cardiomyocyte apoptosis and oxidative stress (X. Wang et al., 2001). A study of transverse aortic constriction in mice demonstrated that toxic PAO containing cleaved desmin species accumulate in this model, inducing heart failure (Rainer et al., 2018).

Studies on a zebrafish model have also been performed (Figure 10). This model contains two different desmin genes, *desma* and *desmb*, which are 81% and 83% homologous to human *DES* respectively (Kayman Kürekçi et al., 2021). Using antisense oligonucleotides, studies were able to reduce the expression of *desma* and *desmb* by 50%. The embryos then developed cardiac edema and showed reduced swimming activity due to disorganized muscles. Further studies in this model, with aggregates introduced, showed the development of embryonic cardiac defects such as altered cardiac fractional shortening, disturbed cardiac biomechanics and altered Ca²⁺ signaling (Mei Li et al., 2013; Ramspacher et al., 2015).

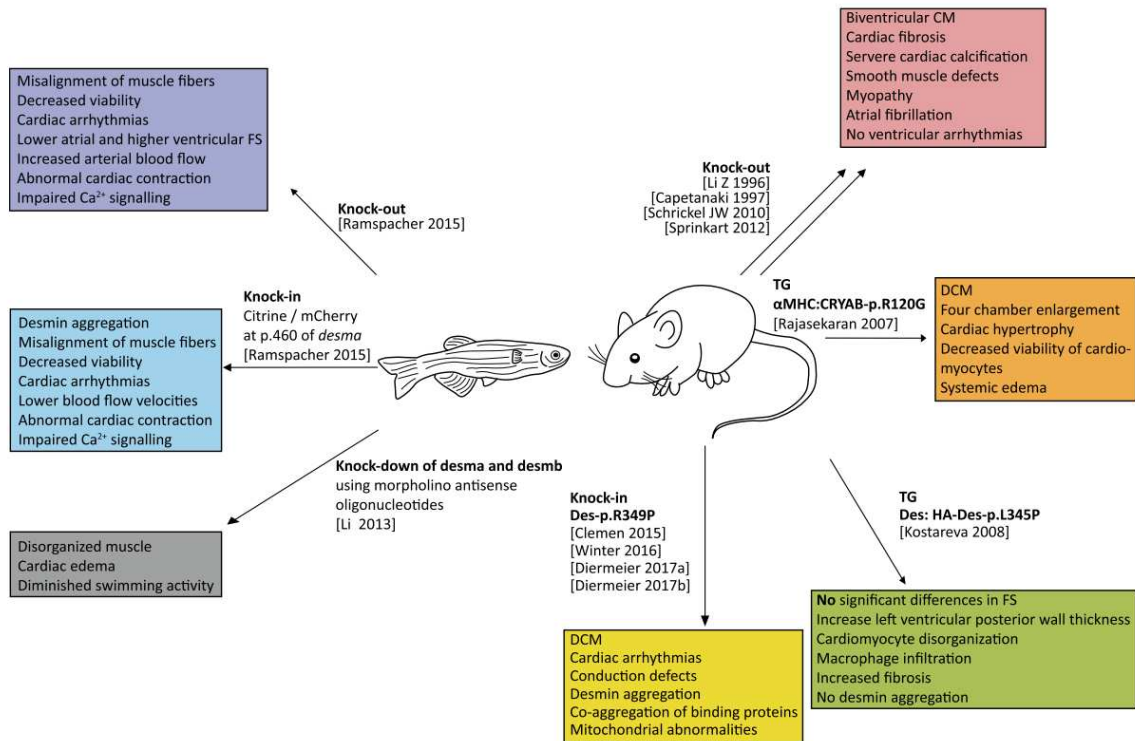


Figure 10 : Overview of animal models used for modeling desminopathies. CM = cardiomyopathy, DCM = dilated cardiomyopathy from (Brodehl et al., 2018)

I.4.2. In vitro 2D

2D *in vitro* culture refers to cell models. This approach involves cell culture methods on different surfaces, often in culture dishes or plates. This modeling can be conducted on animal or human cells. Culture conditions such as medium composition, temperature and oxygen concentration can be controlled by the researcher. These models are ideal for studying cellular responses to perturbation or evaluating potential treatments (Veldhuizen et al., 2019). Due to the difficulties inherent in isolating adult human cardiomyocytes (CM), their use in *in vitro* modeling has been limited.

Since 2006, it has been possible to generate induced pluripotent stem cells (iPSCs) from somatic cells using reprogramming factors that activate cell reprogramming: Oct-4, Sox2, c-Myc and Klf4 (Takahashi et al., 2007; Yamanaka & Takahashi, 2006). Oct-4 is a homeodomain transcription factor controlling the maintenance and differentiation of pluripotent stem cells. Sox2 plays a crucial role in controlling Oct-4 expression (Masui et al., 2007). Together with Nanog, Oct-4 and Sox2 constitute the key transcriptional network for pluripotency. c-Myc is a proto-oncogene associated with the cause of various cancers, it recruits chromatin-modifying proteins, leading to widespread transcriptional activation (Nakagawa et al., 2010). Klf4 acts as a context-dependent oncprotein or tumor suppressor,

is a downstream target of leukemia inhibitory factor and activates Sox2 (Niwa et al., 2009). Although the precise mechanisms have not been fully elucidated, the coordination of these reprogramming factors leads to the reprogramming of somatic cells into pluripotent cells.

The pluripotency of human iPSCs can be confirmed by the ability to differentiate into three embryonic leaflets (Endoderm, Ectoderm and Mesoderm). iPSCs can be generated from several cell types by different methods, which can lead to genetic aberrations and diverse epigenetic profiles. This effect may explain why differentiation from different human iPSCs lines or clones is not equally efficient. Several factors affecting differentiation capacity have been reported. The residual DNA methylation signature transmitted by parental cells, known as epigenetic memory; genetic differences between individual donors; or the appearance of genetic aberration during the reprogramming process. Comprehensive profiling of iPSCs lines is therefore essential to identify which are suitable for biomedical application (Yoshida & Yamanaka, 2017).

Next, it was shown that iPSCs could be differentiated into cardiomyocytes (iPSC-CM) by mimics the sequential stages of embryonic cardiac development (Mummery et al., 2012).

Three families of protein growth factors have been described as responsible for the early stages of mesoderm formation and cardiogenesis: bone morphogenetic proteins (BMPs), which are members of the transforming growth factor β superfamily; Wingless/INT proteins (WNTs); and fibroblast growth factors (FGFs). These factors and their inhibitors are found in the endoderm. Wnt factors have a complex activity, and can either inhibit or promote differentiation depending on the spatio-temporal context and activation of the canonical (acting via β -catenin/GSK3 to repress cardiogenesis) or non-canonical (acting via PKC/JNK to promote cardiogenesis) signaling pathway. Once forward-migrating mesodermal cells have received the appropriate signals, they activate a highly conserved combination of cardiac-specific transcription factors establishing the cardiac transcriptional program. Initially, mesodermal precursor cells in the primitive streak express transcription factors such as the T-box factor Brachyury (T) and the homeodomain protein Mix11. Then, before migrating out of the streak, these cells transiently activate the basic helix-loop-helix transcription factor posterior mesoderm 1 (Mesp1) to enter a "precardiac" stage of mesoderm development (Bondu et al., 2011; Wu, 2008). A subset of the Mesp1+ cell population then begins to express the homeodomain transcription factor Nkx2-5, the T-box protein Tbx5 and Isl1, a LIM homeodomain transcription factor. These

proteins are early markers of the cardiac lineage. Nkx2-5 and Tbx5 then associate with members of the GATA family of zinc-finger transcription factors (GATA4/5/6) and serum response factor (SRF) to activate cardiac structural genes such as actin, myosin light chain, myosin heavy chain (MHC), troponins and desmin. Tbx5 can also cooperate with Nkx2-5 to activate expression of ANF and the junctional protein connexin 40. GATA4, which plays an early role in heart tube formation by regulating extra-embryonic endoderm and embryo folding (Molkentin et al., 1997), is essential for proepicardial formation and muscle development (Pu et al., 2004). Specific ablation of GATA4 in cardiomyocytes results in myocardial hypoplasia (Zeisberg et al., 2005). GATA6 also plays a key role in myogenesis. Embryos lacking GATA4 and 6 do not develop cardiac tissue (Zhao et al., 2008). Members of the myocyte enhancer factor 2 (MEF2) family of transcription factors also play a key role in cardiomyocyte differentiation by regulating the structural genes of cardiac muscle. Thus, multiple complex interactions between these highly conserved gene regulatory networks control the initial differentiation, proliferation and maturation of cardiomyocytes. In addition to their functional role, many of these factors can be used as markers of emerging cardiomyocytes in iPSC differentiation cultures (Figure 11). The sequential activation of transcription factors leading to the formation of the precardiac mesoderm, determining the fate of cardiac cells, can be reproduced in iPSC cultures. Many protocols successfully developed to induce cardiomyogenesis in pluripotent cells are based on the activation or inhibition of these well-known signaling pathways (Talkhabi et al., 2016).

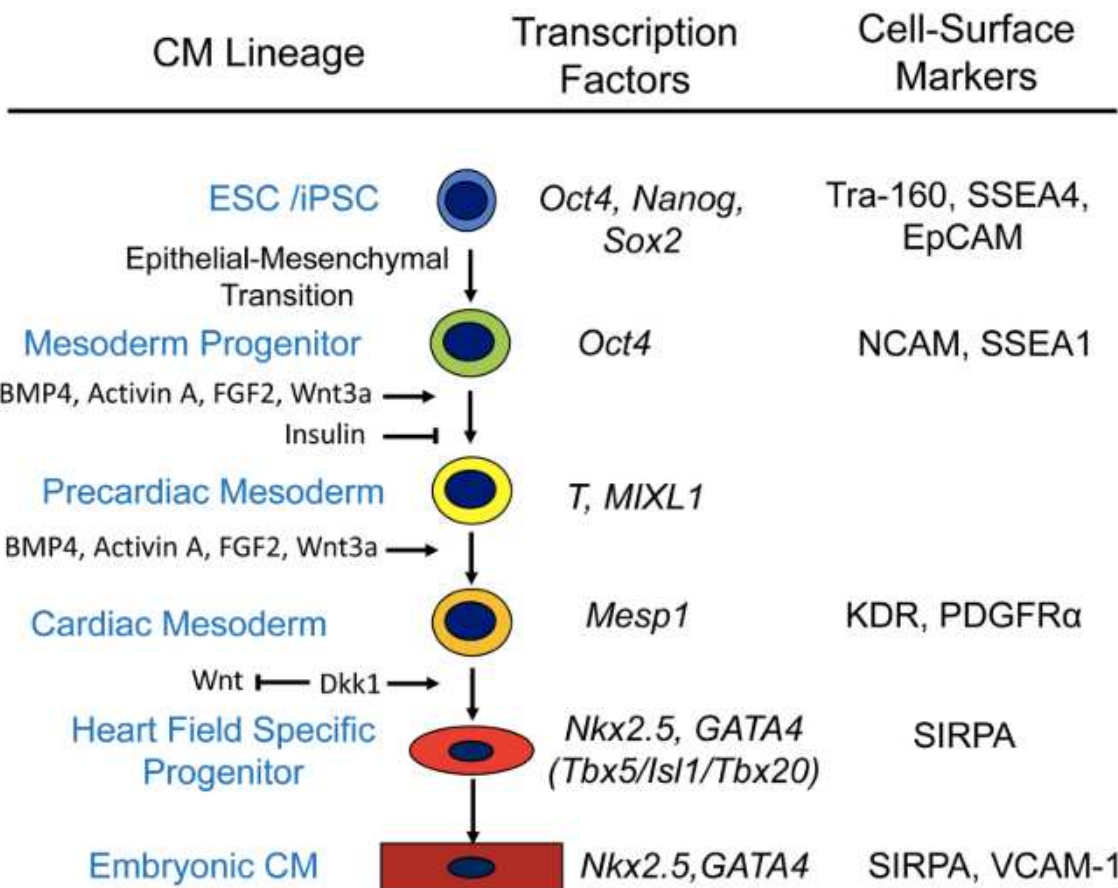


Figure 11 : Model of Differentiation of Human PSC via Sequential Progenitors to Cardiomyocytes from (Mummery et al., 2012)

iPSC-CM have characteristics similar to those of isolated fetal immature cardiomyocytes. They are generally circular in shape, their electrophysiological mechanics are immature, and their metabolic mechanism is glycolytic rather than oxidative as in adult cardiomyocytes. This is why efforts have been made to generate cardiomyocyte maturation protocols, providing a cellular model closer to the adult cardiomyocytes (Figure 12). Different strategies are available, using physical, chemical, genetic or environmental

inducers.

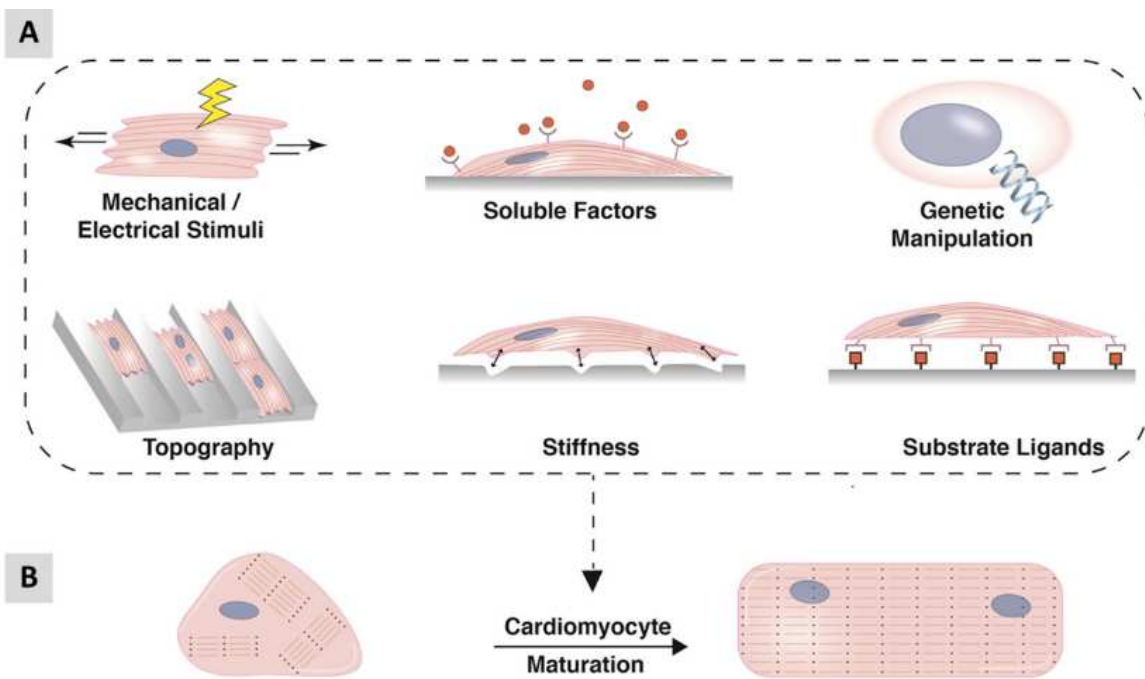


Figure 12 : Schematic of *in vitro* maturation strategies for iPSC-CM from (Denning et al., 2016)

In vitro modeling derived from iPSCs increasingly involves the use of genetic engineering techniques, notably CRISPR/Cas9, to introduce mutations into healthy cell lines or to correct cell lines with mutations. The advantage of this approach is to provide « isogenic pairs » cell lines with the same genetic background, the only difference being the mutation being studied (Bassett, 2017a). This method facilitates the study of phenotypes induced by a given mutation.

I.4.3. *In vitro* 3D

As mentioned previously, 2D models have certain limitations when compared with the complexity of tissues in living organisms. As a result, *in vitro* disease modeling is increasingly turning to 3D models. The latter attempt to reproduce more closely the microarchitecture and three-dimensional cellular interactions found in the human body (J. Cho et al., 2022). The adult heart is a complex organ, containing 30% contractile cardiomyocytes, with the remaining content composed of cardiac endothelial cells, vascular stromal cells and cardiac fibroblasts. *In vitro* 3D cardiac structures include those known as human engineered heart tissue (hEHT) or Engineered human myocardium (EHM). This type of structure involves different cell types and possibly different biomaterials. This is the case for the following hEHTs: Ring, Patch, film, heart-on-a-chip, spheroid (Figure 13).

Type	Shape	Generation	Characteristics	Applications
Strip		Compaction of cells and hydrogel around two parallel wires or posts[26, 31, 38, 46, 49-52]	Drug testing; No vasculature; Limited diffusion	Drug screening
Ring		Condensation of hydrogel with cells in circular casting mold and transfer onto silicon passive stretcher[28, 32]	Applicable for electrical pacing studies; No vasculature; Arrhythmogenic	Disease Modeling; Drug screening
Patch		Accumulation of cell layers on coated plates[53-55]	Regenerative therapies; Higher number of cells required; Low throughput; Risk of breaking; Unequal distribution of the cells	Cardiac Regeneration; Disease modeling
Film		Seeding of cells onto coated film [56, 57]	Limited cell-cell and cell-matrix interactions; Embedded electrode	Disease modeling
Microfluidic Chips		Seeding of cells onto chip (MPS)[58, 59]	Easy manipulation of the microenvironment; Realtime on-chip analysis; Limited cell-cell and cell-matrix interactions; Limited force measurement; Requiring multi-step fabrication; Unintended drug absorption	Drug screening
Spheroid		Assembly of cell mixture and hydrogel[60-65]	No requirement for expensive instruments; High-throughput drug testing; Necrosis in the core (>250) (limitation of diffusion) Not feasible for electromechanical stimulation	Disease modeling; Drug screening
Chamber		Cell seeding in agarose mold around balloon Foley catheter[66, 67]	Recapitulating 3D structure of the heart; Low throughput; No chamber specification; Catheter related complications	Disease modeling; Drug screening
Tube		Wrapping of cell sheets (CM, fibroblasts) around a hollow column[68]	Emulating the multi-layered cardiac wall; Low throughput; Medium leakage leading to the shrinkage of the tube; Requiring high percent of fibroblasts for wall stiffness	Cell-based cardiac pump

Figure 13 : different type of human engineered heart tissue (hEHT) from (J. Cho et al., 2022)

From these different 3D constructions, it is possible to provide measurements of isometric force, auxotonic force and shortening speed of the structures (J. Cho et al., 2022).

Engineered Human Myocardium (EHM) in ring form is usually suspended between two flexible supports (Goldfracht et al., 2020). Then, it could be subjected to electrical stimulation to induce synchronized heartbeats. The force of contraction of the EHM can be measured using force transducers or similar techniques. Spontaneous EHM contraction can also be studied by automated video-optical recording (Schaaf et al., 2011). These measurements can be used to assess the contractility of cardiac tissue. Under conditions of pharmacological treatment, this type of model can be used to assess beneficial or toxic effects on cardiac function (Tiburcy et al., 2017).

A study on the role of Arid1a, a subunit of the switching defective/sucrose non-fermenting (SWI/SNF) chromatin remodeling complex in cardiomyocyte maturation, showed that Arid1a overexpression had induced an increase in the force of contraction of the EHM. Thus, this study testifies of the relevance from the EHM model for functional studies of cardiac contractility and the correlation between cardiomyocyte maturity and cardiac contractility (Boogerd et al., 2023).

In conclusion, disease modeling is an ideal strategy for summarizing pathological phenotypes and investigating the pathophysiological mechanisms behind disease. Tools for measuring and investigating these phenotypes have been developed around these models, with the aim of accurately characterizing even the most complex phenotypes. This is particularly illustrated with the High Content Imaging approach.

I.5. High content imaging

I.5.1. Principle

Recent developments in optical microscopy, fluorescent cell staining and data mining based on statistical analysis have provided the basis for the emergence of High Content Imaging (HCI) (Brodin et al., 2015). This research method involves the automated acquisition and analysis of cell images to identify morphological profiles. First, HCI requires the use of cell models that may be primary cells, cells derived from induced pluripotent stem cells, and/or cells that have been genetically edited to highlight a pathological characteristic (Bickle, 2010). The interest of HCI lies in the identification of morphological differences between cells in different states. These states may differ as a result of a mutation in the cell genome inducing a morphological change, or in response to a disruptive agent such as small molecules, RNAi, or clustered regularly interspaced short palindromic repeats (CRISPR)/Cas9, applied with the goal of identifying and studying factors that control the morphological phenotypes (Haggarty et al., 2001; Wade, 2015). Fluorescent staining of cell morphological structures in different states is performed to identify morphological phenotypes. For example, a labeling technique known as "cell painting" involves six fluorescent dyes to label different components of the cell, including the nucleus, endoplasmic reticulum, mitochondria, cytoskeleton, Golgi apparatus and RNA (Bray et al., 2016). The culture and the staining of the cells could use an automated liquid handling, it will enable these steps to be completed in a standardized and repeatable way. Secondly, high-throughput microscopy technologies for automated acquisition of a large number of images from previously cultured and stained cells is required in this type of approach. Finally, an automated image analysis method for cellular features extraction, and statistical data analysis is required. This enabling the identification of precise morphological phenotypes (Figure 14).

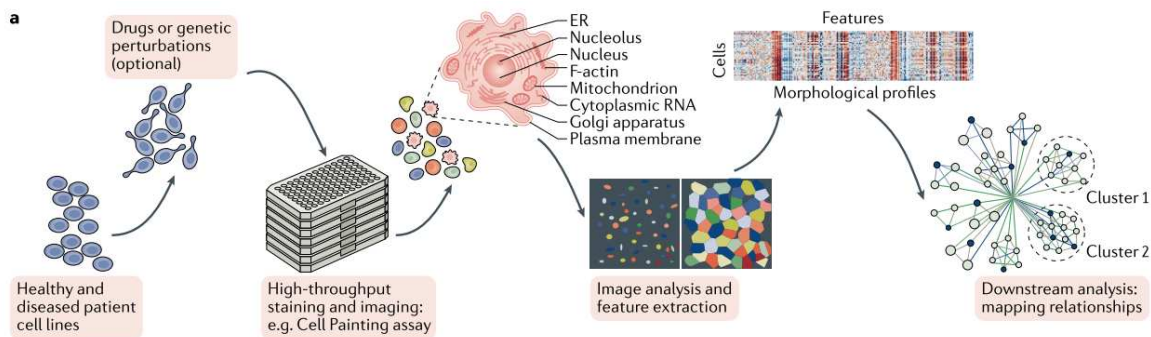


Figure 14 : Example of High content imaging workflow based on Cell painting assay from (Chandrasekaran et al., 2020)

Thus, HCI offers the opportunity to test biological questions by playing on a large number of experimental conditions, in large cell populations and in an unbiased way. It enables deep investigation of cellular phenotypic variations by not just focusing on a single selected cell characteristic, but offering great flexibility in the use of a wide range of morphological features (Ljosa & Carpenter, 2009). Indeed, most cellular phenotypes identified with a traditional microscope can be used in this kind of assay. These approaches preserve cellular integrity, provides spatial and kinetic information on biological processes, and can be multiplexed to study several phenotypes in a single experiment. Moreover, HCI combines these advantages with the generation of large-scale quantitative measurements. It is a highly versatile method in its applications. Depending on the objective, workflow design can vary, and different strategies can be adapted based on:

- The choice of the disease model
- The disruptive agents that could be employed for the modulation of the cellular phenotype
- The fluorescent markers that will be applied for the staining of the cells and the highlight of cellular phenotypes
- The image analysis strategy that will be used for data interpretation

For all these reasons, HCI has emerged as one of the tools of choice for identifying new cellular pathways involved in the establishment of human diseases, elucidating their molecular mechanisms and identifying potential therapeutic approaches (Pegoraro & Misteli, 2017).

HCI involves three more or less integrated approaches to setting up an assay: screening, profiling and deep phenotyping.

Most studies are based on high content screening (HCS) assays. This type of assay involves to screen a large number of disruptive agents (chemical compounds, RNAi, etc.) in a high-throughput process, with the objective of identifying pharmacologically active compounds. These assays could lead to understand the mechanisms of action of potential drugs and/or studying complex cellular pathways. The first disruptive agents to be used for screening were chemical compounds (Haggarty et al., 2001). Thus, large collections of chemically diverse compounds have been developed for screening in order to identify and validate active compounds. Libraries of characterized chemical compounds with known biological targets were screened to identify genes or signaling pathways involved in regulating cell phenotype. This kind of approach has been used for screening of granule dissolution stress inhibitors and has revealed mechanisms of response to a cellular stress (Wippich et al., 2013). These approaches were followed by the emergence of RNAi screening. This type of HCS provides detailed information on the effects of gene silencing at the level of morphological cellular phenotype. The results can be used to understand the physiological mechanisms which implicated the targeted genes. Based on this strategy a study performed a high-content image-based genome-wide small interfering RNA to detect genes required for the colocalization of Sindbis virus capsid protein with autophagolysosomes. Thus they identify the protein SMURF1 as a newly recognized mediator of viral autophagy (Orvedahl et al., 2011). Recently, screens based on CRISPR/Cas9-based genome-editing reagents have been used (Shalem et al., 2014; T. Wang et al., 2014). Genome-wide libraries that include multiple targeting reagents per gene have been generated. The use of CRISPR/Cas9 as a screening tool is still in its earliest stages, and further works are needed to improve this approach (Tan & Martin, 2016).

Initially, screening approaches were limited to the measurement of one or a few parameters. Thanks to its ability to generate large datasets, the profiling based on HCI enables a multi-parametric approach for cellular characterization. Image analysis is automated, relying on the extraction of image features describing the morphological phenotype acquired. These data can be used to generate cellular profiles providing a basis for analysis of cellular phenotypes. Statistical learning methods are performed to classify and cluster treatments based on the similarities of the phenotypes they induce in the cellular profile (Caicedo et al., 2016). Thus, profiling is an approach that can be used to annotate compound libraries functionally on the basis of induced effects, known as phenotypic fingerprints.

HCI enables the generation of large amounts of data at the single cell level, allowing the study of rare phenotypes, known as deep imaging (Roukos & Misteli, 2014). This type of approach goes beyond traditional phenotypic characteristics and aims to identify rare or hidden phenotypes that may not be detected by conventional methods. These phenotypes will appear 10 to 100 times on a much larger cell population, up to 10^5 . The identification of rare phenotypes can be crucial, especially in the context of complex diseases or subtle cellular responses to specific stimuli.

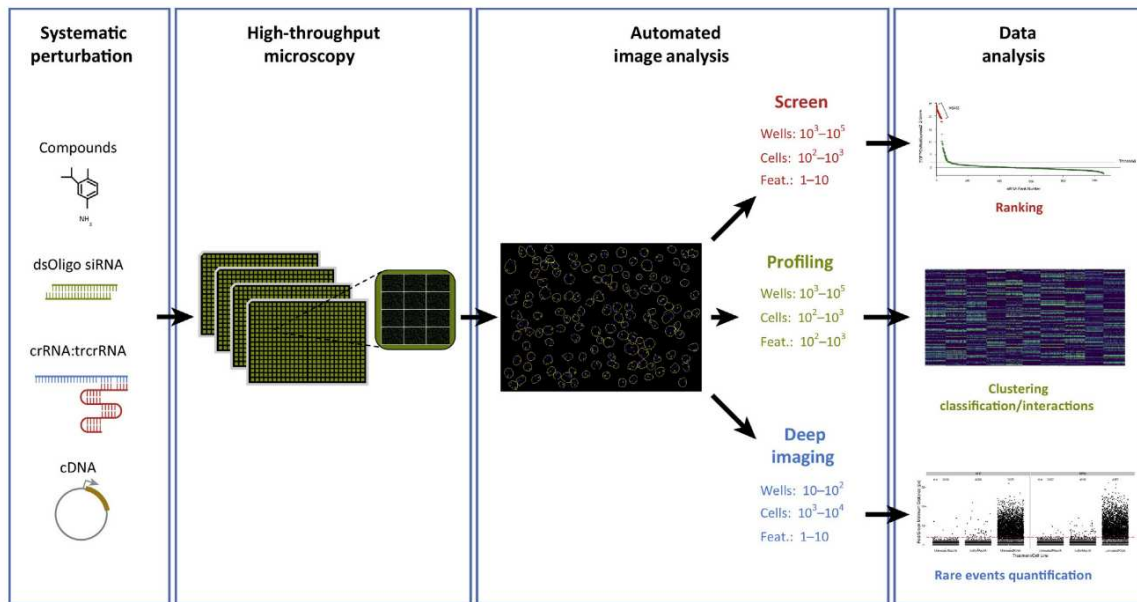


Figure 15 : Principle of High content imaging from (Pegoraro & Misteli, 2017)

I.5.2. Image-based profiling

When perturbed, cells show detectable changes in their morphological characteristics, allowing quantitative and qualitative extraction of data from microscopy images with the purpose of attributing a phenotypic fingerprint to a perturbation (Reisen et al., 2015). This analysis process is known as "image-based profiling" and relies on profiling cells subjected to different treatments in order to identify morphological changes (Scheeder et al., 2018).

Firstly, the cell model must represent the biological system under study. The identification of a disease-associated phenotype in the images is crucial. The goal is to ensure that we have a cellular model allowing identification of a cellular profile in a pathological state from a cellular profile in a healthy state. Indeed, the image-based profiling approach can be used to generate and compare profiles of these different cell states in detail (R. E. Hughes et al., 2021). There are several strategies for achieving this:

- First of all, group cells derived from patients carrying the pathology compared with group of cells derived from healthy patients. These models are a physiologically relevant choice. However, a sufficient number of independent patients in each group must be ensured (Chandrasekaran et al., 2020). This guarantees that phenotypic differences are associated with the disease and not with the morphological variability inherent in cell lines from one patient to another. As HCI can identify subtle differences, it may be subject to confounding factors. Features that appear to distinguish between healthy and diseased states could in fact reflect biases linked to age, genetics etc.
- A second strategy involves the genetic modification of cells. Genome editing is used to introduce specific genetic modifications into a cell line, to create a modified (mutant) version and an unmodified (wild-type or control) version (Bassett, 2017b). The generation of an isogenic pair thus makes it possible to obtain two cell lines that are genetically identical except for the specific modification introduced. This allows to compare the effects of genetic modification while minimizing other genetic variables.
- A third approach is the induction of the pathological state in healthy cells using gene inhibition with RNAi or CRISPR/Cas9. This strategy is particularly appropriate for the study of disorders caused by loss-of-function mutations in single genes (Gibson et al., 2015).
- A fourth approach induces the pathological state in a healthy cell by overexpressing a gene encoding a protein known to cause the disorder. The protein of interest can be labeled to examine its localization in addition to the cell's overall morphology (Rohban et al., 2017).
- A fifth approach involves comparing untreated pathological cells with pathological cells treated with existing drugs for the disease of interest. Once the profiles have been identified, they are used as references to identify new drug candidates and their mode of action (Rihel et al., 2010).

Thus, these cells can be treated with a variety of disturbing agents, depending on the study being conducted.

To enable high-throughput image acquisition with an automated microscope, cells must be cultured in microwell plates, usually 96 or 384 wells. Moreover, depending on the study, cells may need to be treated with biological compounds at different concentrations. Thus, culture and treatment steps require an automated liquid handling. This represents a set of experimental steps designed to simultaneously move a large number of liquid samples from one or more source containers, into cell culture plates using programmable, multi-channel robotic dispensing devices (Chan et al., 2005).

HCI requires the distinct cell structure or protein of interest in the cell to be identified with a fluorescent marker. The value of fluorescent staining resides in its ability to provide detailed information on the localization, distribution and intensity of targets of interest, which is essential for quantitative and qualitative cell analysis. To achieve this, there are several fluorescent marking methods. Firstly, immunostaining is a technique based on the use of antibodies that stain specific structures in the cell. Primary antibodies can be directly associated with a fluorophore that allows visualization of the structure of interest. Or they may be accompanied by a secondary antibody associated with the fluorophore and being specific to the primary antibody. Next, a fluorescent protein such as GFP can be fused to a protein of interest, so that expression of the fused protein allows visualization of the localization and dynamics of the target protein. Finally, dye-specific fluorescent probes can be used to live-stain sub-cellular organelles such as nuclei, mitochondria, endoplasmic reticulum, lysosomes etc (Karacosta, 2021).

One of the advantages of these methods is the ability to co-stain, allowing the simultaneous staining of different cell targets. In this context, a co-staining method has been developed and is attracting increasing interest in recent times. Cell painting is an approach that consists in staining a set of cellular components: nucleus, endoplasmic reticulum, mitochondria, cytoskeleton, Golgi apparatus, and RNA. This technique captures an overall view of the cell, and is particularly useful for analyzing complex cellular phenotypes, characterizing the effects of compounds and identifying potential therapeutic targets (Bray et al., 2016).

High-throughput image acquisition using an automated microscope involves capturing large-scale cell images in an automated way. First, the high-throughput

microscope must be configured for the given experiment. This involves choosing the objective, setting up filters and cameras to detect fluorescent channels, and focusing each channel to obtain high-quality images. Next, the automated acquisition plan can be programmed to determine which wells, which area of the wells and in which order the acquisition should be performed. Some systems allow simultaneous acquisition of different channels, thus reducing the total acquisition time for the whole plate.

Image analysis is a key step in the HCl process. Although fully integrated into the HCl process, this step is sometimes specifically referred to as high content analysis (HCA) (Caicedo et al., 2017). HCA involves using mathematical image processing functions to extract information and generate new knowledge about the biological processes under study. More recently, HCA has involved the use of artificial intelligence like machine learning or deep learning, which are algorithms often used when a large number of measurements per cell needs to be translated into something that is biologically interpretable. It's a tool to analyze cellular images in depth, to obtain more precise information on cellular phenotypes and responses to treatments (Malandraki-Miller & Riley, 2021).

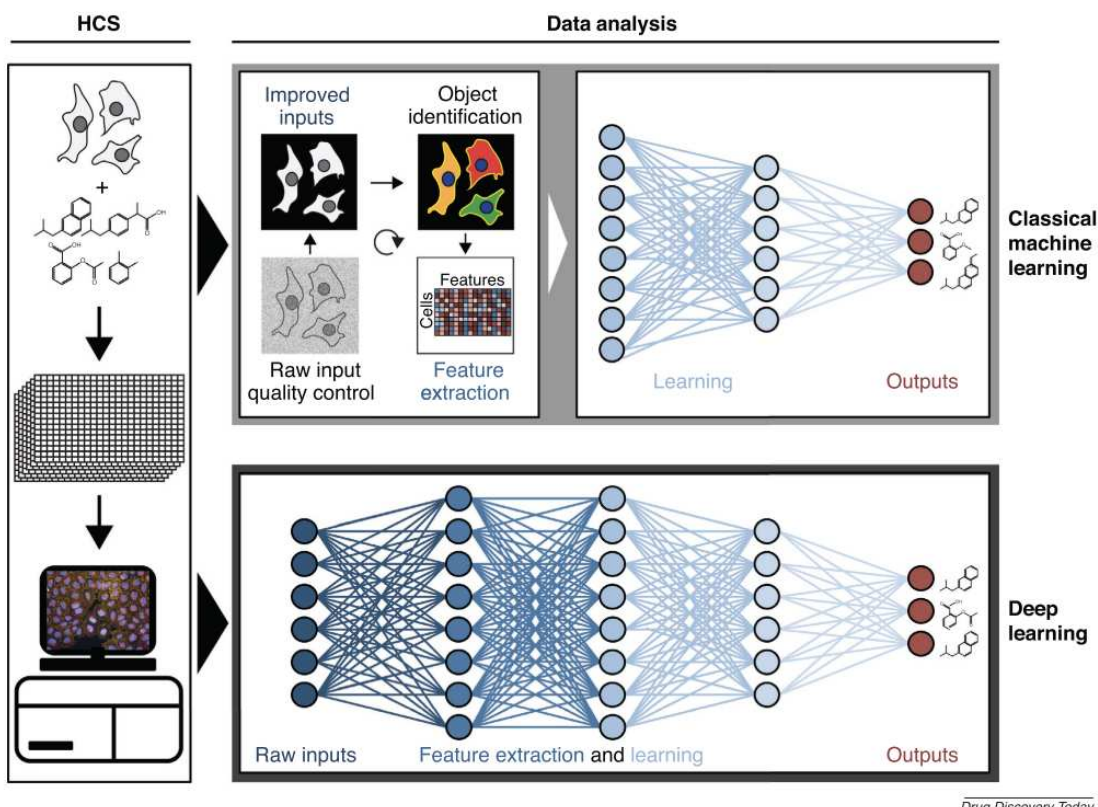


Figure 16 : High content analysis workflow used in High content screening (HCS) from (Lin et al., 2020)

Image quality assessment

In order to avoid mis-interpretation, images with excessive background noise or artifacts are first corrected and/or eliminated. Indeed, uncorrected images can potentially mislead to intensity-based measurements and severely impair the extraction of cellular characteristics. Various existing filters have been implemented in image analysis software to correct poorly illuminated or noisy images (Y. li Wang, 2007).

Segmentation

The detection and segmentation of cellular components corresponds to the identification of objects of interest. Cell segmentation establishes a framework for subsequent feature extraction. Fluorescent staining of the cell structures enables the identification of cells and their cell structures. Detection and segmentation are then established on the basis of fluorescent signals. Initially, areas such as nucleus and cytoplasm are defined, before proceeding to the identification of more complex objects. Identification of the nucleus regularly serves as an initial point for segmenting objects located near the nucleus.

Feature extraction

Following segmentation, the desired single-cell features are extracted using appropriate feature extraction algorithms. These features are mainly classified into four categories:

- average, median or maximum fluorescence intensities
- morphological characteristics, such as cell surface, length or roundness
- microenvironment and context characteristics (major axis direction, distance from neighbors), enabling extraction of the spatial relationship of the segmented object within the cell or cell population
- texture features describing the appearance of characteristic intensity patterns

These extracted features could be used to create cellular profiles that comprehensively describe cell behavior under each experimental condition. These cellular profiles are multidimensional vectors describing the features of each cell (Caicedo et al., 2017).

Machine Learning in image-based profiling

Artificial intelligence (AI) is a field of computer science that focuses on the development of systems capable of performing tasks that generally require human intelligence. AI is about creating computer programs capable of learning, reasoning and solving problems. The use of AI algorithms enables the implementation of automated analysis methods that considerably reduce the experimenter's workload, while guaranteeing the objectivity and consistency of the entire HCA (Danuser, 2011).

Machine learning (ML) is a sub-discipline of AI that focuses on the development of techniques that enable computers to learn from data. ML allows the system to analyze data examples and make conclusions, by automatically adjusting its mathematical models or algorithms according to the information received. There are three types of ML model: supervised, semi-supervised and unsupervised learning (Sommer & Gerlich, 2013). Supervised ML algorithms rely on representative data sets (training sets) of sufficient size and quality, in which features are collected. When a given feature is considered useful by the ML algorithm during the learning process, it is associated with at least one corresponding label (known output), provided by the experimenter, who has prior knowledge of the possible outcomes. The goal is to learn the relationship between inputs (data containing features) and outputs (labels) so that the model can generalize and make accurate predictions on new, unlabeled data (Figure 17).

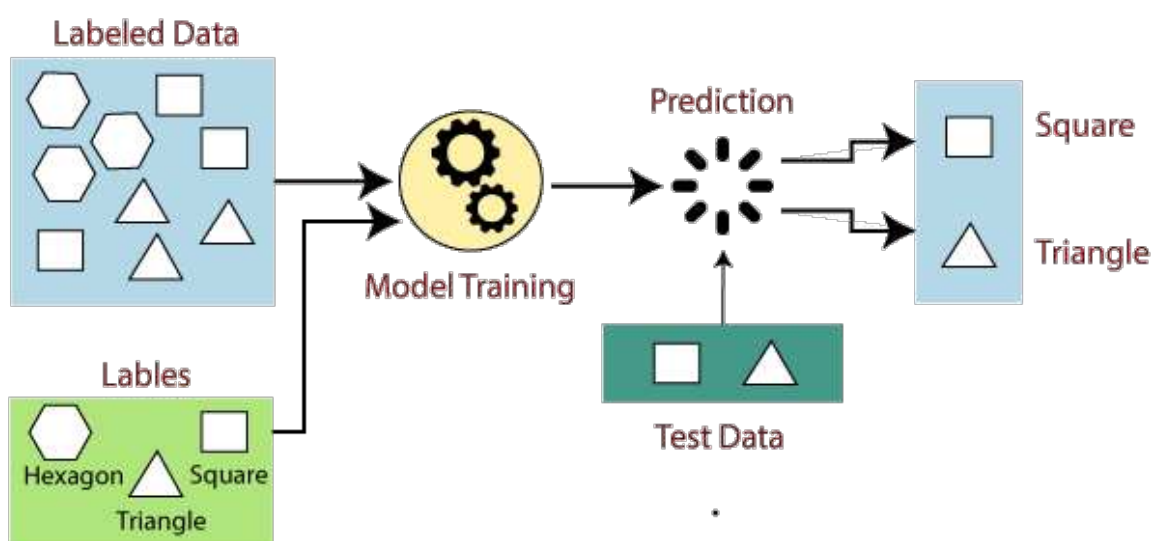


Figure 17 : Supervised machine learning model from <https://www.javatpoint.com/supervised-machine-learning>

Once trained on a sufficient quantity of training data (for example, a variety of cellular profiles per category), the ML algorithm is able to generalize. Then, starting from an unseen data set, it can attempt to predict the output on the basis of the prediction model established during the training phase. The most common types of models used in supervised learning are classification and regression models. Both require features and labels to generate a predictive model for estimating the desired outcome. However, they differ in their respective output variables: categorical (discrete) in classification and numerical (continuous) in regression models. Thus, the classification model predicts the class an observation belongs to, based on a variable taking values in discrete classes (e.g., healthy and pathological cells). The regression model predicts a numerical value based on a continuous variable that can take a value from a given range.

A crucial step in this process is the validation of an ML model to assess its performance and its ability to generalize to new data. This step relies on a set of test data used to evaluate the performance of the ML model on unseen data. The confusion matrix is an essential component in the validation stage of a machine learning model. It allows the visualization of the model's performance by comparing its predictions with the true values of the testing set. The confusion matrix is a table with four entries:

- True Positives (TP): Cases where the model correctly predicted a positive class.
- True Negatives (TN): Cases where the model correctly predicted a negative class.
- False Positives (FP): Cases where the model has incorrectly predicted a positive class.
- False Negatives (FN): Cases where the model incorrectly predicted a negative class.

The confusion matrix is used to calculate various performance metrics, such as precision, negative predictive value, recall, specificity, accuracy and F1 score (Figure 18).

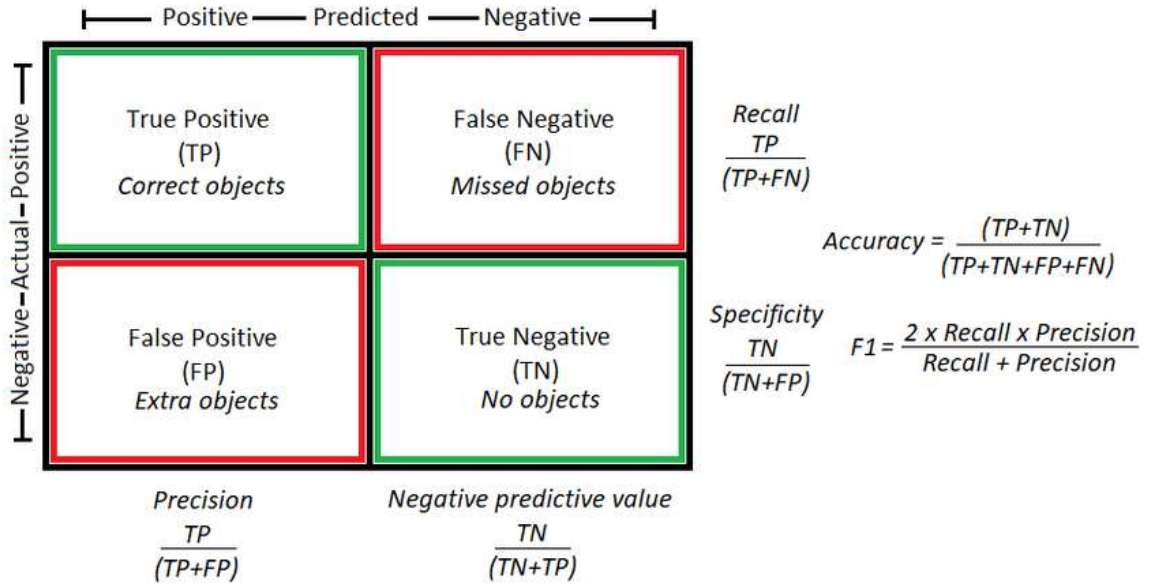


Figure 18 : Confusion matrix and performance evaluation metrics of Supervised machine learning model validation set from (Punn & Agarwal, 2021)

Within classification-based learning models, there are different methods such as SVM (Support Vector Machine), Decision Trees, Random Forest, k-Nearest Neighbors, Naive Bayes or Linear Discriminant Analysis (LDA). This thesis focused on LDA, a statistical method that finds the linear combination of features that maximizes the separation between several classes. It is often used when classes have normal distributions.

It is important to be aware of certain limitations of ML models. Firstly, ML models are highly dependent on the quality and quantity of the data on which they are trained. Data which are insufficient, biased or unrepresentative can result in unreliable models. Secondly, there can be a risk of overfitting: models can sometimes fit too closely to the training data and fail to generalize correctly on new data. This can happen if the model is too complex for the amount of data available. Finally, MLs can often identify correlations, but establishing causal relationships can be difficult. Understanding why a model makes a particular decision can be complex (Bermúdez-Chacón et al., 2015).

There are more advanced machine learning models, inspired by the way the brain works, based on neural networks with many hidden layers. These models are known as deep learning, Convolutional Neural Networks (CNN) or Recurrent Neural Networks (RNN) (Greener et al., 2022).

I.5.3. Image-based profiling in drug discovery

Drug Discovery refers to the pre-clinical identification of molecules with the potential to become pharmaceutical drugs. In recent years, the emergence of biotechnology, bioinformatics and omics technologies has led to the development of more specific approaches (J. P. Hughes et al., 2011). The initiation of a drug discovery project occurs when a pathology does not present a suitable treatment in terms of efficacy and toxicity. The classic drug discovery process begins with "basic research", where therapeutic targets for potential drugs are identified. Next comes the "lead discovery" phase, where chemical compounds or molecules are identified for their therapeutic potential. The third stage is "preclinical development", involving extensive testing in animal models to assess the safety and efficacy of drug candidates. The next phase is "clinical development", where drug candidates are tested in humans. This stage is divided into successive phases (I, II, III), each intended to provide data on the safety, dose and efficacy of the drug on increasingly large groups of participants. The final stage, FDA filing, involves submitting an application for regulatory approval to the U.S. Food and Drug Administration (FDA) or other regulatory bodies such as the European Medicines Agency (EMA) (Figure 19).

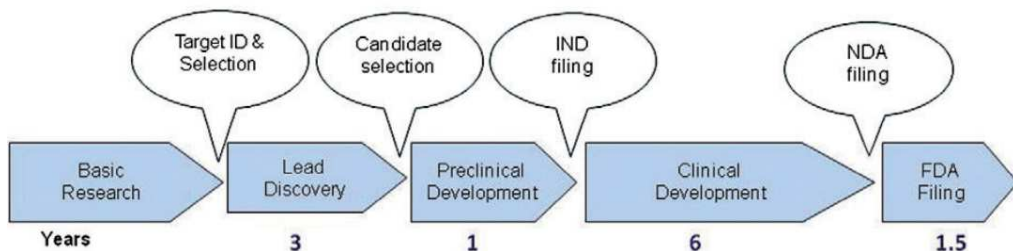


Figure 19 : Different phase in Drug discovery from (J. P. Hughes et al., 2011)

Concerning the first step of drug discovery, before the preclinical development, different strategy could be implement. A first approach, target-based drug discovery (TBDD), is based on identification and validation of a biological target implicated in the pathophysiological mechanism of the pathology of interest (Michael Hay et al., 2014). This biological target may be a protein, a gene or a signaling pathway involved in the establishment, development or maintenance of the pathology under study. Thus, the TBDD often follows fundamental research studies on the disease, enabling the identification of the therapeutic biological target. Then, a target validation assay based on biochemical assays or structure based assay is performing. The goal is to ensure that modulation of the target

is possible and will induce an effect on the disease. Finally a screening assay could be implemented based on the target, with the goal of identifying compounds capable of interacting with the target and induce a the therapeutic effects. The main advantage of the TBDD approach is that the mechanism of action is known from the beginning, which can speed up preclinical evaluation. Other advantages include the ability to facilitate lead compound optimization, given that a clear structure-activity relationship exists, which can lead to improved physicochemical properties. It is also possible to predict the safety risks and toxicity associated with the target (Bunnage et al., 2013).

However, in this type of drug, problems of cell permeability, accessibility and stability of small molecules may arise in later follow-up studies, after much investment has already been made in the drug discovery process. Although many drugs are initially designed to modulate the activity of individual targets, these often result in off-target effects that have a critical impact on the desired efficacy, while adding undesirable toxicity. The ability of one molecule to interact with several targets is called polypharmacology. The assumption that a single target is responsible for a disease phenotype underestimates the complexity of biological systems (Malandraki-Miller & Riley, 2021).

Thus a second approach has been developed, it is the phenotypic drug discovery (PDD). This strategy starts with the investigation of phenotypic perturbations in typically cell-based systems (Horvath et al., 2016). Indeed, like it was described image-based profiling could be used for cell based assay HCS. The multiparametric nature of image-based profiling enables the simultaneous identification of different cellular phenotypes and the precise study of the polypharmacological aspect of compounds. Finally, disease-driving phenotypes find in the PDD approach can be used to determine compounds that change the outcome of multiple biological pathways without prior knowledge of the molecular mechanisms of the disease. Such screens are unbiased and may identify compounds targeting completely unexpected proteins or pathways (Kouroupi et al., 2020).

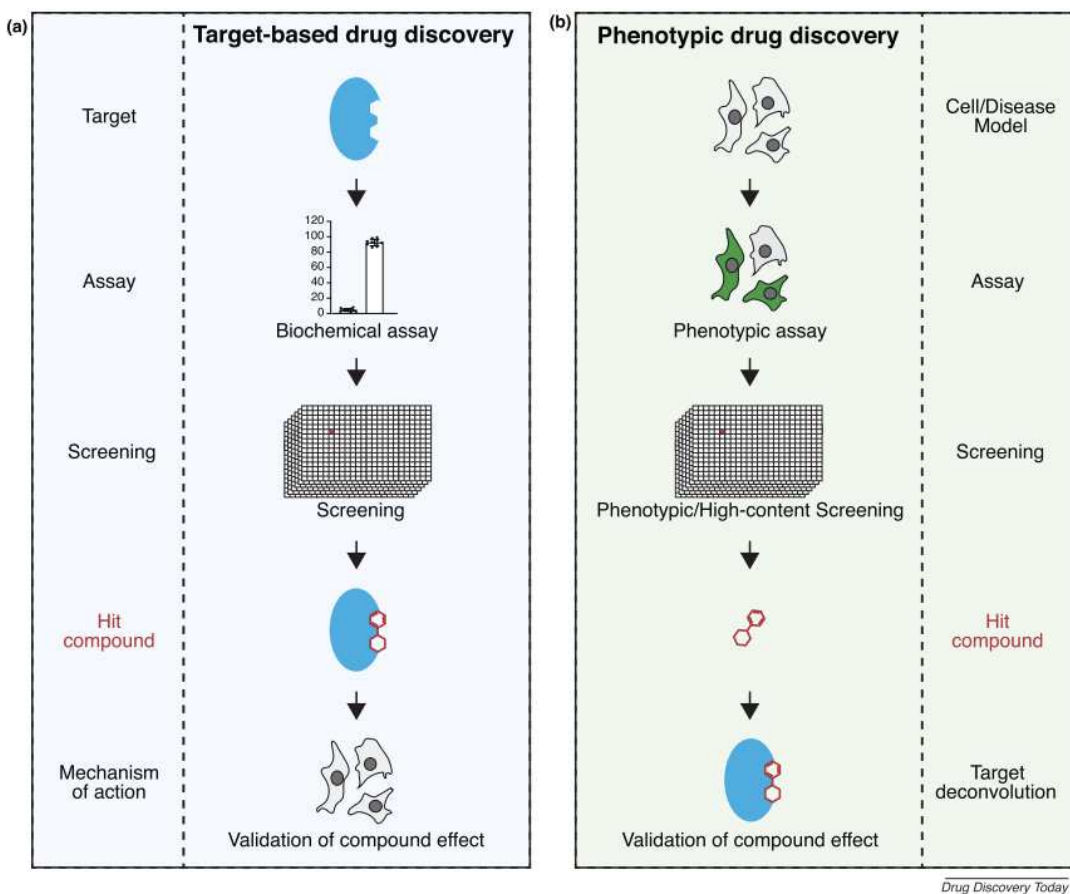


Figure 20 : Target-based drug discovery (TBDD) versus phenotypic drug discovery (PDD) (Lin et al., 2020).

In conclusion, HCI combined with Image-Based Profiling enables detailed multi-parametric analysis of cellular phenotypes by extracting complex information from cellular images. The use of technology and automated algorithms enables the identification and characterization of specific cellular signatures associated with pathological conditions and/or in response to treatments. In fact, this approach provides a better understanding of the underlying mechanisms. In addition, these approaches can be combined with HCS, facilitating the identification of promising compounds in terms of therapy, opening up new perspectives in drug discovery.

More and more studies on cardiomyopathies are relying on these technologies. One study highlighted that deep learning-based system could be useful for the evaluation of cardiomyocyte hypertrophy and drug screening, leading to the development of new treatments for heart failure (Komuro et al., 2022). Research has been conducted to develop an automated tool for characterizing the state of organization of sarcomeres in iPSC-CM based on an ML approach (Gerbin et al., 2021b). It may therefore be of interest to use these

approaches to characterize the cellular phenotypes of DCM associated with a *DES* mutation and identify new therapeutic approaches.

II. OBJECTIVE

This PhD project was carried out at the interface of fundamental research and applied research thanks to the tight collaboration between Sorbonne University and Ksilink, a private company. The ultimate goal of this project is to identify potential treatments for genetic-driven dilated cardiomyopathy, and more specifically to delineate therapeutic options for patients affected by MFM. Moreover, this study benefited from results accumulated previously by our team (Hovhannisyan et al., 2023). Thus, it was shown that patients carrying *DES*^{E439K} mutation presented DCM associated with MFM but also atrial fibrillation, right bundle branched block and respiratory insufficiency (Wahbi et al., 2012a). To better understand the pathophysiological mechanisms induced by this mutation, iPSC-CM using iPSCs from a patient carrying the heterozygous *DES*^{E439K} mutation and from healthy donors as a control were generated. An isogenic pair of these control iPSCs in which the same *DES*^{E439K} mutation has also been derived. iPSC-CM were either cultured on an anisotropic micropatterned surface (2D cultures) or as a cardiac spheroid (3D cultures), to create a micro-tissue. These models have successfully recapitulated the crucial structural changes (desmin network and sarcomeric organisation) as well as mitochondrial alterations observed in heart biopsies from a patient *DES*^{E439K}. These results highlight the relevance of these cell models to study the pathology. The data reinforce also the hypothesis that the primary disruption of the desmin network due to *DES* mutations induces mitochondrial defects and contribute to a vicious circle leading to cardiomyocyte dysfunction and subsequently to DCM. Then, the study showed the critical defects in mitochondrial architecture, respiratory capacity and metabolic activity in the iPSC-CM carrying *DES*^{E439K}. Normal mitochondria were transferred inside iPSC-CM carrying *DES*^{E439K}, inducing restoration of mitochondrial and contractile functions (Hovhannisyan et al., 2023).

To continue this work, we firstly validate the *DES*^{E439K} phenotypes in various 2D and 3D *in vitro* models. Ensuring that our model disease recapitulates the hallmarks of DCM associated with desminopathy is crucial for the identification of new therapeutic approaches. In addition, study of the underlying mechanisms, notably those involving restoration of cellular proteostasis via PQC, may provide a better characterization of the cellular response to stress induced by the initial perturbations. Finally, the implementation of HCI and image-based profiling approaches could serve to better characterize the

different cellular phenotypes associated with desminopathy (*DES*^{E439K} mutation) and this approach could be exploited in the future for the identification of potential treatments for this type of pathology. This approach could be exploited to identify chemical compounds capable of modulating cellular phenotypes. The study of the mechanisms of action of these compounds could shed light on the pathophysiological mechanisms involved in the establishment and/or maintenance of *DES*^{E439K} phenotypes. Therefore, this project has highlighted the complementarities of the two approaches with a goal of identifying relevant therapeutic approaches: On one hand, our studies focused on the molecular identification of targets involved in the establishment and maintenance of the cellular phenotype; on the other, our research sought to characterize and modulate the cellular phenotypes. Thus, these two strategies can be used to first identify and then validate new therapeutic targets. of interest.

Indeed to address these aims, the PhD work was organized into the following objectives: (i) perform a functional characterization of DCM associated with MFM due to a desmin mutation (*DES*^{E439K}) in order to better understand the pathology and its development; (ii) then, identify proteostasis deregulation and the role of the PQC in DCM due to a desmin mutation (*DES*^{E439K}) and (iii) implement a cellular phenotyping strategy based on HCI, to better address cellular pathophysiological mechanisms involved in the establishment and maintenance of the disease, and to identify new therapeutic approaches.

III. MATERIALS AND METHODS

III.1. Cardiomyocytes derived from induced pluripotent stem cells

III.1.1. Induced pluripotent stem cells and genomic editing

Reprogramming of patient blood cells into iPSCs (Figure 21) was carried out at Phenocell by a non-integrative method using a commercial kit based on the use of episomes (ThermoFischer Scientific #a15960). The various clones were then amplified in Matrigel®-coated culture dishes (Corning Life Sciences) and cultured in mTeSR™1 medium (Stem Cell Technologies), which is renewed daily.

When cell density reaches around 80%, cell passage is performed on iPSC colonies using ReLeSR (Stem Cell Technologies) for 5 min at 37°C. The cell suspension is diluted in culture medium at a ratio of 1:30, then transferred to Matrigel-coated plates. 20 passages are performed before iPSCs are cryopreserved. iPSCs are detached using ReLeSR, resuspended in freezing medium (PSC Cryomedium, Life Technologies) and transferred to cryotubes for storage in liquid nitrogen after 24h at -80°C.

Each cryotube was thawed in rapid immersion at 37°C. Once thawed, the cell suspension were diluted 1/10 in thawing medium composed of culture medium supplemented with 5 µM ROCK inhibitor Y27632. After centrifugation (200 g, 5 minutes, room temperature). The pellet is gently resuspended in thawing medium and cells are seeded at the desired density.

Generation of an isogenic pair (Figure 21). Isogenic control iPSC cultured with mTesR1 was detached using Accutase® (Stemcell Technologies) and electroporated using the Neon® electroporation system (Thermo Fisher Scientific) with 3 different plasmids diluted in resuspension RBuffer: (1) 1000 ng/µL of pCMV_AncBE4max_P2A_GFP (Koblan et al., 2018), encoding a nucleus-targeted chimeric protein composed of a cytidine deaminase and a Cas9 nickase, 2x500 ng/µL of pBlueScript-U6sgRNA (Nelles et al., 2016) encoding single guide RNA specific for *DES* or encoding single guide RNA specific for *ATPIA1* (used for a positive selection of transformed clones). The sequence of guide RNAs for *DES* to generate E439K mutation was 5'-CTcAGAACCCCTTGCTC-3' and the sequence of guide RNAs for *ATPIA1* to generate point mutation to induce resistance to ouabain was 5'-cATCCAAGCTGCTACAGAAGG-3'. Electroporation was performed at a voltage of 1300

V with 2 pulses on 150 000 cells resuspended in resuspension buffer for a 10 µl neon tip. After electroporation, the cells were transferred into pre-warmed mTeSR1 medium on Matrigel-coated plates, cultured for 3 days at which 1 µg/ml ouabain (Enzo Life Sciences) was added for clonal selection during 3 more days. The resistant cells were sequenced to confirm or deny the success of genomic editing. Single cell cloning was then performed using CloneR (Stem Cell Technologies) following the manufacturer's instructions. pCMV_AncBE4max_P2A_GFP was a gift from David Liu (Addgene plasmid #112100; <http://n2t.net/addgene:112100>; RRID:Addgene_112100) and pBluescript-U6sgRNA empty was a gift from Eugene Yeo (Addgene plasmid #74707; <http://n2t.net/addgene:74707>; RRID:Addgene_74707).

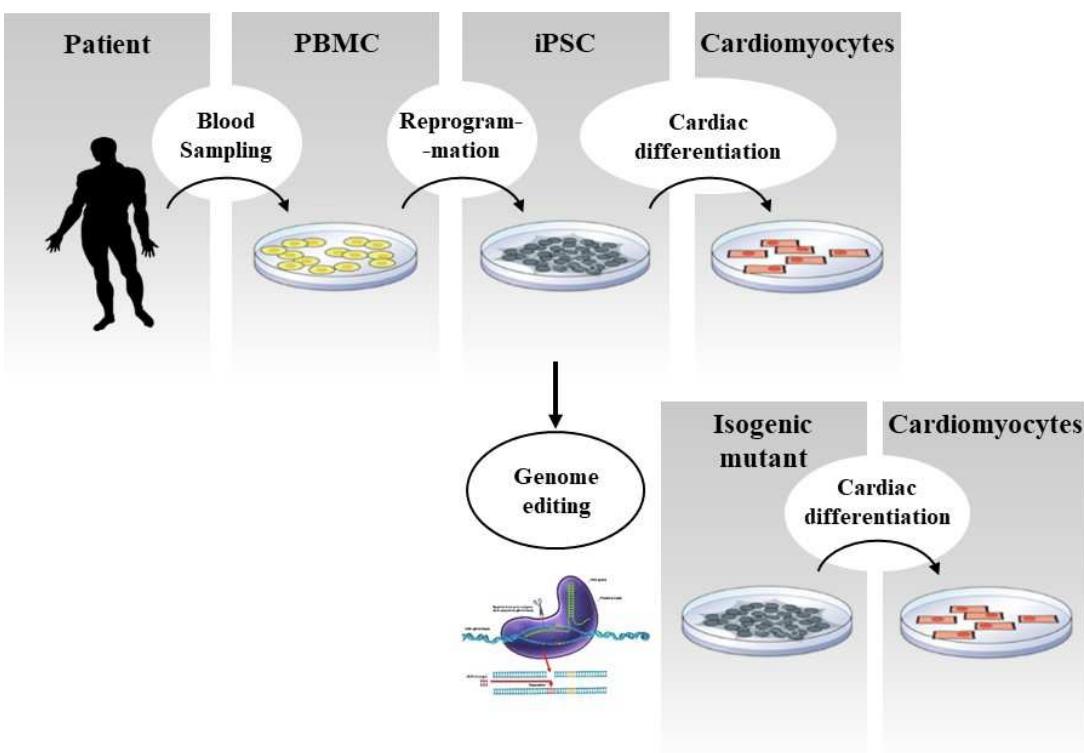


Figure 21 : Generation of Cardiomyocytes derived from iPSC (iPSC-CM)

III.1.2. Cardiomyocyte derived induced pluripotent stem cells (iPSC-CM)

Cardiac differentiation protocols

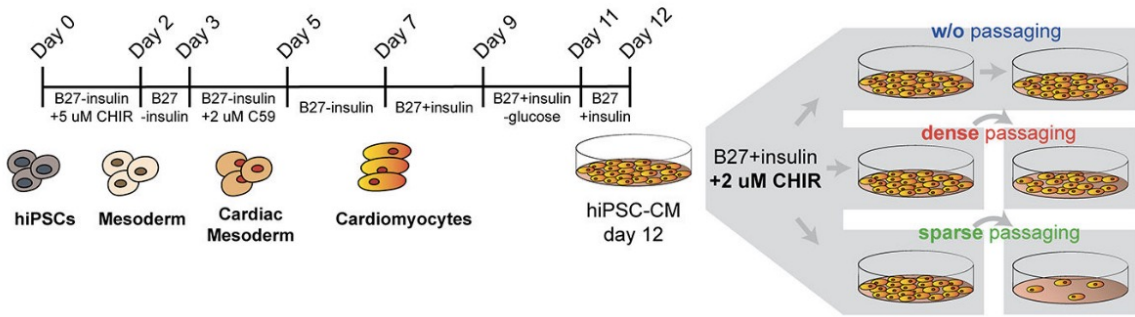
Different sources and protocols of iPSC-CM differentiation were used (Figure 22).

Source 1. Cardiac differentiation was based on the GiWi protocol published in 2012 (Lian et al., 2012). At 80% confluence, iPSCs were detached with Accutase®, counted and then seeded at optimal density. Two days later, cardiac differentiation was initiated by replacing mTeSR1 with RPMI medium (Thermo Fisher Scientific) enriched with 2%

insulin-free B27 supplement (Thermo Fisher Scientific) containing 9 μ M CHIR99021 (Selleckchem). This medium was replaced with RPMI supplemented insulin-free B27 after 24 hours. Two days later, cells were treated with RPMI enriched with insulin-free B27 and 5 μ M IWP2 (Tocris Bioscience) for 48 hours and then the medium was replaced with RPMI enriched with insulin-free B27. Two days later, the culture medium was replaced by RPMI enriched with B27 supplement and was changed every two days. At Day 12, an amplification step started by adding 2 μ M CHIR in the culture medium RPMI enriched with B27 (Buikema et al., 2020a). This procedure lead to the proliferation of the iPSC-CM. During 15 days the cells where maintain in this amplification culture medium. Each time the cells became confluent at 80%-90%, a cellular passaging was done using TrypLE Select Enzyme 1X (Invitrogen) (Thermo Fisher Scientific) (incubation at 37°C for 10 min). 15 days after amplification, iPSC-CMs were detached with TrypLE Select 1X (Thermo Fisher Scientific) (incubation at 37°C for 10 min), suspended in RPMI containing 20% fetal bovine serum (Thermo Fisher Scientific), filtered on a 70 μ m cell strainer, then centrifuged and resuspended in PSC Cryomedium (Life Technologies).

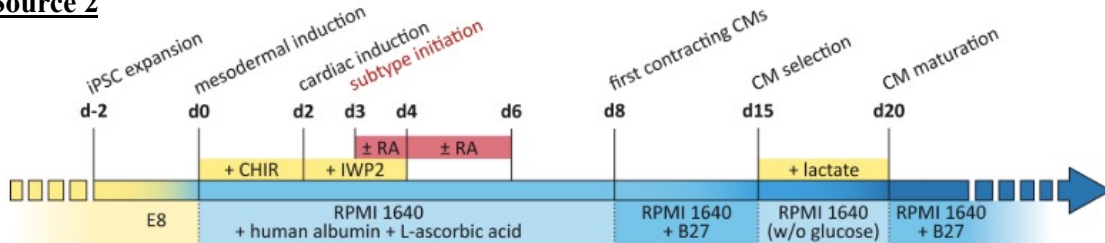
Source 2 (by Myriamed) (Cyganek et al., 2018). The iPSC-CM differentiation was initiated at 80%–90% confluence in Geltrex-coated plates with cardio differentiation medium composed of RPMI 1640 with Glutamax and HEPES (Thermo Fisher Scientific), 0.5 mg/ml human recombinant albumin, and 0.2 mg/ml L-ascorbic acid 2-phosphate and sequential treatment with 4 μ M CHIR99021 (Merck Millipore) for 48 hours and then 5 μ M IWP2 (Merck Millipore) for 48 hours. Medium was changed to cardio culture medium composed of RPMI 1640 with Glutamax, HEPES, and 2% B27 (Thermo Fisher Scientific) at day 8. For atrial subtype differentiation, 1 μ M RA (Sigma-Aldrich) was supplemented at days 3–6 during differentiation. Differentiated cultures around day 15 were digested with collagenase B (Worthington Biochemical) and 0.25% Trypsin/EDTA (Thermo Fisher Scientific) and replated at lower density (1:2 to 1:3) in Geltrex-coated plates. Metabolic iPSC-CM selection was performed using cardio selection medium composed of RPMI 1640 without glucose (Thermo Fisher Scientific), 0.5 mg/ml human recombinant albumin, 0.2 mg/ml L-ascorbic acid 2-phosphate, and 4 mM of lactate/HEPES (L4263 and 83264, Sigma-Aldrich).

Source 1



Buikema, Wu et al., (2020). Wnt Activation and Reduced Cell-Cell Contact Synergistically Induce Massive Expansion of Functional Human iPSC Derived Cardiomyocytes. *Cell Stem Cell*, 27(1), 50-63.e5. <https://doi.org/10.1016/j.stem.2020.06.001>

Source 2



Cyganek, L., Gerstenberg, K., et al., (2018). Deep phenotyping of human induced pluripotent stem cell – derived atrial and ventricular cardiomyocytes Find the latest version : Deep phenotyping of human induced pluripotent stem cell – derived atrial and ventricular cardiomyocytes. *JCI Insight*, 3(12), e99941. 10.1172/jci.insight.99941

Figure 22 : Cardiac differentiation protocols (Buikema et al., 2020a; Cyganek et al., 2018)

iPSC-CM derived from different cell line with specific genotype

Different group of iPSC-CM were generated based on different iPSC cell lines with specific genotype. There were control lines (Control 1 and Control 2) which carried no mutation associated with DCM and myofibrillar myopathy. Then there were the *DES* E439K patient lines derived from a patient carrying the *DES* E439K mutation and suffering from DCM associated with myofibrillar myopathy. From this patient two clones were isolated during reprogramming and iPSC generation, by differentiating these two clones from the same patient two lines could be generated (Patient 1 *DES* E439K and Patient 2 *DES* E439K). Finally, an isogenic pair composed of a control line (Isogenic control) and a line derived from the control line into which the *DES* E439K mutation has been introduced by CRISPR/CAS9 (Isogenic the *DES* E439K). These iPSC-CM were generated according to the two protocols (described in “Cardiac differentiation protocols”, Table 1). As the goal of this project was not to compare the two protocols, no experiments were performed in this regard. However, it was interesting to use both methods to consider inter-batch variability, particularly in control cells. Thus, the observations made during this project could be impacted on the genotype only, and not on the differentiation method (Bassett, 2017b).

Table 1 : Different Cell Lines used for the study of dilated cardiomyopathy caused by DES gene mutation

Cell Lines	Genotype (source)	Cardiac differentiation Protocol
Control 1	Wild Type (MYRIAMED)	Source 2 (Hudson et al., 2012; Tiburcy et al., 2017)
Control 2	Wild Type (healthy patient)	Source 1 (Buikema et al., 2020b; Lian et al., 2013)
Isogenic Control	Wild Type (GIBCO)	Source 1 (Buikema et al., 2020b; Lian et al., 2013)
Isogenic DES E439K	DES E439K (Isogenic Control Genome edited)	Source 1 (Buikema et al., 2020b; Lian et al., 2013)
Patient 1 DES E439K	DES E439K (DCM/MFM Patient clone 1)	Source 2 (Hudson et al., 2012; Tiburcy et al., 2017)
Patient 2 DES E439K	DES E439K (DCM/MFM Patient clone 2)	Source 2 (Hudson et al., 2012; Tiburcy et al., 2017)

III.1.3.Thawing iPSC-CM

20 day *in vitro* old iPSC-CM were thawed in a 37°C water bath for approximately 3 min. The cell suspension was then diluted 10-fold in thawing medium composed by basal medium supplemented with 10µM Y-27632 and 10% KnockOut™ Serum Replacement. The cells were centrifuged (300 g, 5 min, RT) in basal medium supplemented with ROCK inhibitor (Tocris #1254). Cell pellets were resuspended in differentiation medium supplemented with ROCK inhibitor. 384-well plates (Perkin Elmer, #6007558) were coated with 2,5 ug/mL Laminin 521 for 3 h at 37°C or overnight at 4°C followed by 1h Room Temperature incubation. Using trypan blue (Sigma, #T8154-20ML) and a Countess automated cell counter (Invitrogen), 6000 cells/well were seeded in 384-well plates. Edge wells were avoided for seeding and filled with PBS. Cells were incubated at 37°C, 5% CO2 in basal medium (RPMI1640 +B27) with media changes every two days.

III.1.4.IPSC-CM Culture Media

Different culture media have been used for iPSC-CM cultures Table 2. The first, "normal medium", is a iPSC-CM maintenance medium classically used for iPSC-CM

culture (Laco et al. 2020). The “normal medium” is composed of RPMI-1640 with Glutamax, 1% 100× penicillin/streptomycin (Thermo Fisher Scientific), 1% 100× sodium pyruvate (Thermo Fisher Scientific), 200 μ M L-ascorbic acid 2 phosphate sesquimagnesium salt hydrate (Sigma-Aldrich, USA), 2% B27 supplement (Thermo Fisher Scientific).

Then, the aim was to generate iPSC-CMs with more identifiable mature structures to distinguish the effects of Desmin mutation. Thus, two culture media were implemented. firstly, the "T3+Dex" culture medium, Thyroid and glucocorticoid hormones are critical for cardiac maturation ((Li et al. 2014),(Rog-Zielinska et al. 2015)). Many studies have shown that the combination of the thyroid hormone triiodothyronine (T3) and the glucocorticoid dexamethasone (Dex) enables the maturation of iPSC-CMs, and in particular of structures that are important for the functional competence of these cells, such as T-tubules (Parikh et al. 2017) or structures involved in electrophysiological function (Wang et al. 2021). Therefore, the "T3+Dex" culture medium was composed of the basic culture medium "Normal medium" to which was added the thyroid hormone triiodothyronine (Thermo Fisher Scientific) at 100 nM and dexamethasone (Tocris) at 1 μ M. Finally, another method for strongly inducing iPSC-CM maturation consists to provide oxidative substrates adapted to the metabolic needs of the iPSC-CMs (Yang et al. 2019). During fetal development, iPSC-CM progenitors switch from glycolytic to oxidative metabolism to support the energy demands of functional aspect (Gaspar et al. 2014). To realize it, the culture medium "maturation medium" was implemented with DMEM no Glucose (11966025, GIBCO); 1X B27 Supplement (17504-044, GIBCO); 1X NEAA (11140050, GIBCO); 250U/ml penicillin-streptomycin (15070063, GIBCO); 0,5% KnockOut Serum Replacement (10828028, GIBCO); 3mM Glucose (G7021, Sigma); 10 mM L-lactate sodium (71718, Sigma); 5mM Creatine monohydrate (C3630, Sigma); 0,5% Albumax I (11020-021, GIBCO); Vitamin B12 (V6629, Sigma); 0,82 μ M Biotin (B4639, Sigma), 2mM Taurine (T0625, Sigma), 2 mM L-Carnitine (C0283, Sigma); 0,5M Ascorbic Acid (A8960, Sigma) (Feyen et al. 2020).

Table 2 : Key ressources table for iPSC-CM culture and immunocytostaining

	Reagent	Source	Catalog number
Culture Media	RPMI 1640 Medium, GlutaMAX™ Supplement, HEPES	Gibco Life Technologies	11875119
	B-27™ Supplement (50X), serum free	Gibco Life Technologies	17504044
	L-Ascorbic Acid 2-Phosphate	Merck	A8960
	Sodium Pyruvate	GIBCO	11360039
	Pénicilline-streptomycine (5 000 U/ml)	GIBCO	15070063
	Y-27632 dihydrochloride, Rho kinase inhibitor	TOCRIS	1254
	KnockOut™ Serum Replacement	GIBCO	1082810
Antibodies / Dyes	Biolaminin-521, human recombinant protein, non-gmp, 0.1mg/ml	BIOLAMINA	LN521-05
	Hoechst 33342	Invitrogen	H7035
	Image-iT™ TMRM Reagent	Invitrogen	I34361
	Mitotracker™ Deep Red FM	Thermofisher	M22426
	FM green MitoTracker™	Thermofisher	M7514
	Anti-Cardiac Troponin T	Abcam	ab45932
	Anti Desmin	Novusbio	AF3844
	Anti α -Actinin	Sigma-Aldrich	A7811
	Donkey anti Goat IgG (H+L) 488	Invitrogen	A21042
	Donkey anti rabbit IgG(H+L) 555	Invitrogen	A31572

III.1.5. iPSC-CM staining and image acquisition

Mitotracker™ Deep Red FM (M22426, ThermoFisher) or FM green MitoTracker™ (M7514, ThermoFisher) and TMRM (I34361, Invitrogen) dyes were prepared in cell culture medium and the cells are incubated 45min at 37°C 5% CO₂, followed by 3 washes with cell culture medium. Then, the iPSC-CM were either acquired live imaging or fixed (only worked for Mitotracker). Fixation was performed in 4% ParaFormaldehyde (EMS Euromedex, #15710) for 20 min, followed by two PBS (Gibco, #14190) washes. The permeabilization and blocking were performed with 10% BSA (Bovine Serum Albumin, Merk Sigma, A9647) and 0.5% Triton X-100 (Sigma, #T9284) dissolved in PBS for 1 h. Primary antibodies, Anti-Cardiac Troponin T (ab45932, Abcam) 1:1000, Anti Desmin (AF3844, Novusbio) 1:500 are prepared in antibody dilution buffer (PBS supplemented with 1% BSA) and incubated with the cells overnight at 4°C, followed by three PBS washes. Secondary antibodies, Donkey anti Goat IgG (H+L) 488 (A21042, Invitrogen)

1:1000, Donkey anti rabbit IgG(H+L) 555 (A31572, Invitrogen) 1:1000 and Hoechst (H7035, Invitrogen) 1:1000 in antibody dilution buffer were added to the cells for 1h at Room Temperature, followed by three PBS washes. Imaging was performed on a Yokogawa CV7000 microscope in scanning confocal mode using a dual Nipkow disk. 384-well plates (Phenoplate, Perkin Elmer) were mounted on a motorized stage and images were acquired in a row-wise “zigzag” fashion at RT for fixed cells. The system’s software (CellVoyager) and solid laser lines (405/488/561/640-nm) was used to acquire 3 Z-plane ($1\mu\text{m}$ shifting) 16-bit TIFF images through a dry 40x objective lens using a cooled sCMOS camera with $2,560 \times 2,160$ pixels and a pixel size of 6.5 mm without pixel binning. The 3 Z-plane are fused with maximum projection. Nine images in a 3×3 matrix pattern were acquired from the center of each well.

III.2. Engineering Human myocardium (Myrtissues)

The engineered human myocardium (EHM) generated by MYRIAMED (Figure 23). These 3D microtissues are composed of iPSC-CM at day 60 of differentiation and human foreskin fibroblasts (ATCC) at a ratio of 70/30. They also include collagen fibers and have already been described as ideal for studying cardiac contraction (Tiburcy et al., 2017). The EHM were cultured 28 days in 48 well plate, the detail protocol is describe here: (Tiburcy et al., 2020).

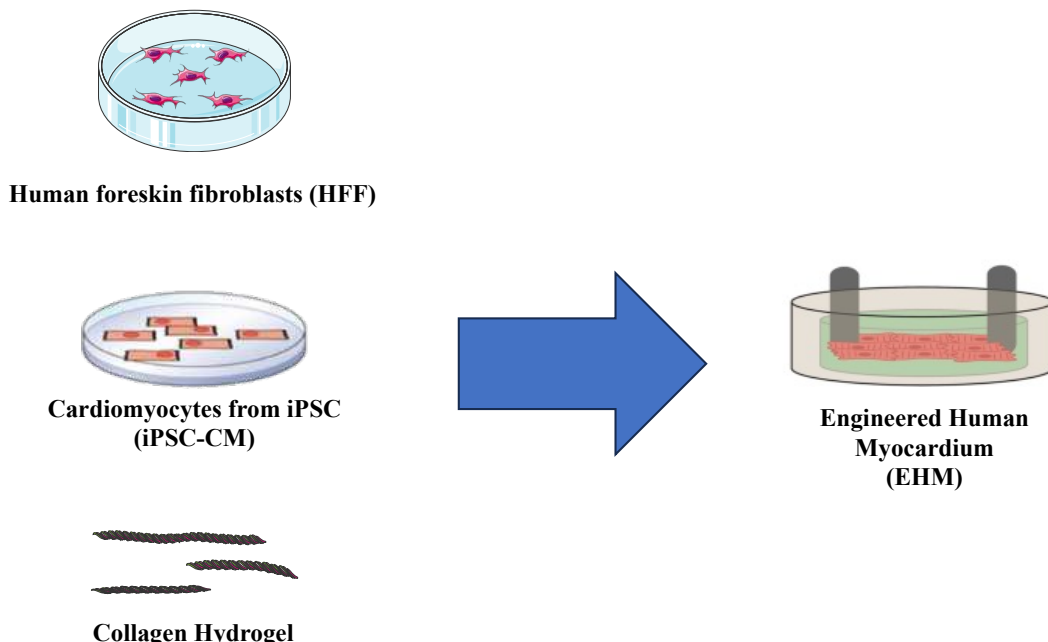


Figure 23 : Generation of *in vitro* cardiac 3D models. Generation of Engineered Human Myocardium (EHM).

III.3. Seahorse

After culture iPSC-CM were dissociated using TrypLE Select 1X and seeded on Matrigel coated test plates (Extracellular Flux Assay Kit, Agilent) at the density 25,000-50,000 cells/well and cultured for 4 days. The assay was conducted in medium composed of bicarbonate-free RPMI (pH=7.4) supplemented with glucose (4.5 g/L), sodium pyruvate (100 µM) and glutamine (200 µM). iPSC-CM were washed twice and incubated at 37°C without CO₂ in 500 µL of medium for 1 h before measurement. Concerning the Mito Stress condition, 50µL of stock solution of each drug were injected sequentially during the experiment. Stock solutions of oligomycin (10 µM), FCCP (10 µM) and rotenone + antimycin A (1 µM) were prepared in DMSO, stored at -20°C. For normalization, OCR values have been divided by the number of iPSC-CMs per well as counted after immunostaining for cardiac cTnT. Calibration to correct the plate effect has been done by dividing all the OCR values by the lowest OCR value of the plate after addition of rotenone and antimycin. Then, basal and ATP-linked respirations, maximal, reserve capacities and OCR/ECAR were calculated.

III.4. Transcriptomic Analysis

III.4.1.RNA extraction

Following cell cultures, cells were detached using TRYPLE 10X 10min at 37°C. The reaction is stopped with culture medium (1:10 dilution). The cell suspension is then centrifuged for 5min at 200g. The supernatant is discarded and the cell pellet is resuspended in Lysis Buffer RA1 (740961,MACHEREY-NAGEL) before being stored at -80°C. RNA extraction is continued using and following the protocol of the NucleoSpin RNA XS, Micro kit for RNA purification (740902, MACHEREY-NAGEL). Once the RNA samples have been obtained, determination of RNA concentration and quality is carried out using the NanoPhotometer (Implen). Samples with a 260/280 ratio of ~2 were accepted. RNA concentration was given in ng/µl. Then, the RNA sample were stored at -80°C.

III.4.2.Reverse transcription cDNA

Depending on the RNA concentration of a given sample, the volume required for a 1000ng quantity of RNA was taken. To obtain cDNA from the different samples the SuperScript™ VILO™ cDNA Synthesis Kit (11754050, ThermoFisher) was used

following the protocol. Depending on the number of samples, a pre-mix of 5X VILO™ Reaction Mix and 10X SuperScript™ Enzyme Mix was prepared and added to each sample. Once the cDNA samples have been obtained, determination of cDNA concentration and quality is carried out using the NanoPhotometer (Implen). Samples with a 260/280 ratio of ~1,8 were accepted. cDNA concentration was given in ng/ μ l. Then, the cDNA sample were stored at -80°C.

III.4.3.RNA sequencing

RNA was purified using Qiagen RNeasy microkits Plus (Qiagen). RNA was quantified using the Quant-iT RiboGreen RNA Assay Kit (Thermo Fisher Scientific) and quality control performed on a Bioanalyzer (Agilent), prior to mRNA library preparation using the Single Cell/Low Input RNA Library Prep Kit for Illumina® (New England Biolabs). Libraries were sequenced on an Illumina HiSeq 2500 V4 system. Sequencing quality control was performed using Sequence Analysis Viewer and FastQ files were generated on the Illumina BaseSpace Sequence Hub. Transcript reads were aligned to the hg18 human reference genome using Salmon v1.9.0 (Patro et al, 2017). Import and summarize transcript-level abundance to gene-level was performed with tximport package (Soneson et al, 2015). Quality control of the alignment was performed via MultiQC v1.4 . Finally, counts were normalized as counts per million. Differential gene expression analysis was performed with the DESeq2 R package (Love et al, 2014). Principal Component Analysis (PCA) was performed with factorMineR package(Lê et al, 2008) and facto extra package(Kassambara & Mundt, 2020). The differentially expressed genes with adjusted p values false discovery rate (FDR) \leq 0.05 were subjected to GSEA with GO database using the ClusterProfiler R package (Yu et al, 2012). The density plots were produced using the ggplot2 R package (Wickham, 2009). Weighted correlation network analysis (WGCNA) was applied on normalized data recovered from DESeq2 analysis. Pathways associated with each WGCNA modules were determined using METASCAPE web application (Zhou et al, 2019). WGCNA module genes were also submitted to protein-protein interactions using STRING web software (<https://string-db.org/>), and to MCODE analysis (Bader & Hogue, 2003) using Cytoscape software(Shannon et al, 2003). The heatmap was, performed with the R package pheatmap (version 1.0.12). All analysis was performed in R (v.4.2.0).

III.4.4. RT-qPCR

TAqMAN Gene expression assay

Real-time PCR was based on TaqMan Gene expression assay (Applied Biosystems) using TaqMan Fast Advanced Master Mix 1X (ThermoFisher) and TaqMan Assay specific probes (ThermoFisher) corresponding to primers customized for a given gene and associated with a fluorophore probes. Primers for PPIA gene were associated with VIC-MGB and used as reference. Whereas, gene of interest were associated with FAM-MGB. Before the Real-time PCR reaction and depending of the number of reaction, pre-MIX were prepare with 5µl/per reaction of TaqMan Fast Advanced Master Mix (2X), 0.5 µl/per reaction TaqMan Assay Primer probes (20X) and Nuclease-free Water 2.5 µl/per reaction. 8µl/per reaction of the pre-Mix were transfer to each well of a 384 well plate and 2µl/per reaction cDNA samples (50ng/sample). Then the relative quantification was performed using the QuantStudio 5 Real-Time PCR Instruments within 20s at 95°C for polymerase activation and 40 cycles of 1s at 95°C for denaturation and 20s at 60°C for annealing and extending.

SYBR Green Assay

Relative quantification of RNA expression was performed using a LightCycler® 480 (Roche PCR Instrument). Primer efficiency was assessed by preparing a cDNA mix diluted using the 1:25, 1:50, 1:100, 1:200, 1:400, 1:800 cascade dilution method. qPCR was performed in SYBR Green Master mix with 500 nM of sense and antisense primers, 1:25 cDNA sample. The qPCR conditions were as follows: 95 °C-5 min, then 40 cycles (95 °C-15 s, 60 °C-30 s, 70 °C-30s). Primer specificity was determined by the melting curve of the amplified product, and reaction efficiency by analysis of the slope of the amplification curve. To calculate relative gene expression, the $\Delta\Delta Ct$ method with *NUBP1* and *SLC4A1AP* as reference gene was used.

Primers used for RT-qPCR

Genes	Forward (5' --> 3')	Reverse (5' --> 3')	Annealing Temp (°C)
BAG3	CCCCGTTCAGGTCATCTGTC	AGGTGCAGTTCTCGATGGG	60°C
CRYAB	GGTTCTCTGCAACCTGGATGT	TGAAACCATGTTCATCCTGGCG	60°C
HSPD1	GTTACCCACAGTCTTCGCC	ATCACTGTTCTCCCTTGGC	60°C
UBE2I	AGACCACCCATTGGTTCGT	CTTCCTGGAATGGCGCACT	60°C
MDM2	CCTACTGATGGTGCTGAACCA	GCTTGGTCTAACCCAGGGTCT	60°C
FBXO32	CTGACCTGCCTTGTGCCTA	AATCGTTGCGGATCTGCCG	60°C
PINK1	GGGAGCCATGCCTATGAAA	CTCGGGCAGATGGTCTCTG	60°C
SQSTM1	CACCCCAATGTGATCTGCGA	TGTGCGAGAAGCCCTCAGA	60°C
CALCOCO2	GCCCAGCTGTCAACTCAAGA	CTTCTGGTCCTCCCTGTTCA	60°C

III.5. Protein expression analysis

III.5.1. Protein extraction

After culturing the iPSC-CM in 6-well plates, protein extraction could be performed. The culture medium was then removed and a PBS wash applied. After removal of the wash solution, 50µl/well of protein extraction solution was added. The protein extraction solution was composed of 1:100 Phosphatase Inhibitor Cocktail (100X) (78444, Thermo Scientific) and Cell Lysis Buffer (FNN0011, invitrogen). Cells were scraped from the well with a cell scraper, then the plate was left on ice for 30 min at 4°C. The 50µl of protein suspension was then collected and placed in a 1.5ml eppendorf before being centrifuged for 10min at 13,000g. The supernatant containing the protein lysate was recovered for subsequent steps (stored at -80°C). For protein concentration measurement, a BSA standard curve ranging from 0; 0.6; 1.2; 1.8; 2.4; 3 µg/µl was made by diluting BSA in Distilled water. Mixes were then made up of 1µl sample and 19µl BCA mix (1:8 Copper(II) sulfate solution (C2284, Sigma) in Bicinchoninic Acid solution (B9643, Sigma)). The solution was incubated for 30 min at 37°C. Protein concentration quantification was performed with the Nanophotometer (Implen), starting with the BSA sample to make the standard curve.

III.5.2. Western blot

40 µg soluble protein sample were diluted in sample 4X Bolt™ LDS Sample Buffer (B0007, Thermo Fisher) and 1:100 β-Mercaptoethanol (M6250, Sigma). The sample were reduce and denature by boiling at 95-100°C for 5 minutes. Proteins migrated into Blot 4-12 % Bis-Tris Plus gels (NW04120BOX, Invitrogen) in 1X SDS Running Buffer (B0002,

Thermo Scientific) at 90V and transferred on iBlot Transfer Stack, PVDF, regular size (IB401001, Invitrogen) with an iBlot 2 Gel Transfer Device (Invitrogen). After, membranes were incubated in iBind Flex Western Device (Invitrogen) with blocking solution from iBind Flex Solution Kit (SLF2020, Invitrogen), with primary antibodies 1:500 LC3A/B (D3U4C) XP® Rabbit mAb (12741; Cell Signaling) or 1:500 Anti-p62/SQSTM1 Rabbit (P0067, Merck) or 1:500 Anti-GAPDH rabbit (IMG-5143A, Novus biological) and with secondary antibodies 1:2000 Peroxidase AffiniPure F(ab')₂ Fragment Donkey Anti-Rabbit IgG (H+L) (711036152, Jackson Immuno Research Labs) or 1:2000 Peroxidase AffiniPure F(ab')₂ Fragment Rabbit Anti-Mouse IgG (H+L) (315036045, Jackson Immuno Research Labs) overnight at 4°C or for 2h30 at room temperature. Immunoreactivity was revealed by using SuperSignal West Dura Extended Duration Substrate (34076, Thermo Fisher Scientific) according to the manufacturer's instruction. Images were acquired on a iBright CL1500 System (Invitrogen).

III.6. Image analysis and Data mining

The goal of the image analysis was to generate, from a digital images, a measurements that describe the state of single cell. All the following step were performed with an in-house developed software for image and data processing (Phenolink - <https://github.com/Ksilink/PhenoLink>). After the image acquisition by the microscope, the images were segmented in order to identify each cell individually. A reference channel was used to identify Nuclei positions (mainly the one stained with Hoechst). This image was segmented and a nuclei label was set for each Nuclei. The Nuclei determination was based on intensity levels and shape features combined in decision tree to generate labels. Using this Nuclei labels, segmentation was occurred further to the other channels in order to generate Cell and Cytoplasm masks, from each of the mask the algorithm could then extract a set of measures. These measures were usually referred to as features. The measures could either be extracted on true cell masks when the cells/cytoplasm segmentation was applicable, otherwise a more simple approach using region of interest around the nuclei was used. These regions were usually referred to as Crops or ROI, and serves as masks. The features extraction could be applied to any crop size, the size used was 256x216 pixel areas, which was 10% of the initial image sizes in each axis.

Hand crafted features were mathematically defined measures extracting information that could explain the underlying characteristics of the studied object. The hand crafted

features extracted by the PhenoLink plugin can be found in the Table 3. Most of the analysis and graphical presentation was achieved using python coding via the Jupyter Notebook python interface. The panda and numpy libraries were used for their mathematical tools for data processing, and the plotly.express library was used for data visualization and graphing. Most of data were represented as boxplots, the notches of the box represent the 95% confidence interval of the median obtained by bootstrapping with parameter value 1,000. Each data point represents the mean of a single well of a 384-well plate comprised of nine images.

Thanks to this tool, it was also possible to use the features extracted from the images to create cell profiles. These cell profiles could then be used as input for the modeling of a classification tool for different cell profiles based on the ML technique LDA. LDA enables the generation of a classification model that maximizes the separation between classes while minimizing the variance within each class. By using part of the data for a training phase, the classification model can be tested. Performance is measured using the F1-score metric.

Table 3 : Handcraft features

Hand craft Feature	Feature Meaning
(Background Foreground)_(Mean Std)_{Channel Name}	Computes the signal intensities average and standard deviation in the background (below threshold) and foreground (above threshold) in the overall image
Blob_Count_(Accepted/Rejected)_{Channel Name Computed}_(Neg){Channel Name 1}_(Neg){Channel Name 2}_(Mean Std)	Average and standard deviation of the Counts the number of isolated area in the channel "Channel Name Computed" inside each crops. Computation is performed depending on the "signal positivity" with each subsequent channel {Channel Name 1} {Channel Name 2} (for 3 channel images, more combinations are created depending on the number of subsequent channels)
Blobs_Surfs_(Accepted Rejected)_{Channel Name Computed}_(Neg){Channel Name 1}_(Neg){Channel Name 2}_(Mean Std)	Average and standard deviation of the above thresholds surface for {Computed Channel Name} as ratio of pixels occupancy per crops window. Computation is performed depending on the "signal positivity" with each subsequent channel {Channel Name 1} {Channel Name 2} (for 3 channel images, more combinations are created depending on the number of subsequent channels)
Closeness_indicator	Confluence measures taking into accounts holes and nuclei distances.
Intensities_{Channel Name Computed}_(Neg){Channel Name1}_(Neg){Channel Name 2}_(Mean Std)	Signal measures of intensities (average and standard deviation) within crops. Computation is performed depending on the "signal positivity" with each subsequent channel {Channel Name 1} {Channel Name 2} (for 3 channel images, more combinations are created depending on the number of subsequent channels)
IsolatedAreas_{Channel Name}	Computes the number of isolated areas of pixels above the threshold for each {Channel Name}
Nuclei	Overall Number of Nuclei in the image
Nuclei_Circularity_(Accepted Rejected)_(Neg){Channel Name1}_(Neg){Channel Name 2}_(Mean Std)	Circularity measure between 0 & 1 see the picture for visual interpretation (left 0, right 1). Computation is performed depending on the "signal positivity" with each subsequent channel {Channel Name 1} {Channel Name 2} (for 3 channel images, more combinations are created depending on the number of subsequent channels)

Nuclei_Convexity_(Accepted Rejected)_(Neg){Channel Name1}_(Neg){Channel Name 2}_(Mean Std)	Convexity measure between 0 & 1 see the picture for visual interpretation (left 0, right 1).Computation is performed depending on the "signal positivity" with each subsequent channel {Channel Name 1} {Channel Name 2} (for 3 channel images, more combinations are created depending on the number of subsequent channels)
Nuclei_Counts_(Accepted Rejected)_(Neg){Channel Name1}_(Neg){Channel Name 2}_(Mean Std)	Count of the nuclei wrt to the non "nuclei" channel responses. Computation is performed depending on the "signal positivity" with each subsequent channel {Channel Name 1} {Channel Name 2} (for 3 channel images, more combinations are created depending on the number of subsequent channels)
Nuclei_Inertia_(Accepted Rejected)_(Neg){Channel Name1}_(Neg){Channel Name 2}_(Mean Std)	Inertia measure between 0 & 1 see the picture for visual interpretation (left 0, right 1).Computation is performed depending on the "signal positivity" with each subsequent channel {Channel Name 1} {Channel Name 2} (for 3 channel images, more combinations are created depending on the number of subsequent channels)
Nuclei_dists_(mean std)	Distances between nucleis (Mean + std) in μm
Nucs_(Axis0 Axis1)_(Mean Std)	Average and std deviation of each accepted nuclei main axis after an ellipsoidal fitting.
Overlapping_{Channel Name}_ {Channel Names}_(Mean Std)	Statistics of (above treshold) pixels that overlaps between the mentionned channel names
Peaks_Dists_(Accepted Rejected)_{Channel Computed}_(Neg){Channel Name 1}_(Neg){Channel Name 2}_(Mean Std)	Pattern recognition methods, extracting the peak distance at which the pattern is the most frequently found in the channel (Channel Computed) (in μm)
Peaks_Strength_(Accepted Rejected)_{Channel Computed}_(Neg){Channel Name 1}_(Neg){Channel Name 2}_(Mean Std)	Pattern recognition methods, extracting the height of the histogram at which the pattern is the most frequently found in the channel (Channel Computed) (in μm) (same histogram as for the Peaks Distance)
PerObjectArea_{Channel Name}_(Mean Std)	Statics on the Surface (number of pixel "above threshold") for a Channel in isolated areas
SurfaceRatio_{Channel Name}	Surface of the above threhsold pixel of each channels divided by the number of processed pixels
Surface_(Accepted Rejected)_{Channel Computed}_(Neg){Channel Name 1}_(Neg){Channel Name2}_(Mean Std)	Statistics of crops size normalized surface of above threshold intensities of {Channel Computed} with respect to each other channel signal positivity/negativity response/

Texture Haralick Features	Feature Meaning
Haralick_Texture_0	Angular Second Moment, mean of angular second moment for all angles shows homogenity in image, high values shows less homogenity and few dominant gray-tone transitions
Haralick_Texture_1	Angular Second Moment, max - min angular second moment between all angels
Haralick_Texture_2	Contrast, mean of contrast in all angels
Haralick_Texture_3	Contrast, max - min Contrast between all angels
Haralick_Texture_4	Correlation, mean, gray-tone linear-dependencies, the higher correlation means changes in gray value have linear dependencies
Haralick_Texture_5	Correlation, max-min
Haralick_Texture_6	Difference Variance , mean, the more difference variance, shows more random changes in gray-tone level in image
Haralick_Texture_7	Difference Variance , max-min
Haralick_Texture_8	Difference Entropy, mean the less difference entropy, shows more random changes in gray-tone level in image
Haralick_Texture_9	Difference Entropy, max-min
Haralick_Texture_10	Entropy, mean the less entropy, shows more random textures in image
Haralick_Texture_11	Entropy, max-min
Haralick_Texture_12	Correlation, mean similar to correlation but non-linear relations
Haralick_Texture_13	Correlation, max-min

Haralick_Texture_14	Inverse difference moment, mean high values shows that gray-tone transitions are small
Haralick_Texture_15	Inverse difference moment, max-min
Haralick_Texture_16	Max correlation coeff, mean
Haralick_Texture_17	Max correlation coeff, max-min
Haralick_Texture_18	Correlation, mean similar to correlation but non-linear relations
Haralick_Texture_19	Correlation, max-min
Haralick_Texture_20	Sum average, mean
Haralick_Texture_21	Sum average, max-min
Haralick_Texture_22	(Sum Entropy, mean, the less Sum entropy, shows more random changes in gray-tone level in image)
Haralick_Texture_23	Sum Entropy, max-min
Haralick_Texture_24	Sum Variance, mean, the more difference variance, shows more random changes in gray-tone level in image
Haralick_Texture_25	Sum Variance, max-min
Haralick_Texture_26	Variance the more variance, shows more random changes in gray-tone level in image

Texture Otsu Features	Feature Meaning
Otsu_feature_0	area histogram bin 1, histogram of areas of components, first 10 shows the histogram values if we calculate the area of all the component in image and make a histogram of areas with 10 bins (more big components, more values in higher bins)
Otsu_feature_1	area histogram bin 2, histogram of areas of components
Otsu_feature_2	area histogram bin 3, histogram of areas of components
Otsu_feature_3	area histogram bin 4, histogram of areas of components
Otsu_feature_4	area histogram bin 5, histogram of areas of components
Otsu_feature_5	area histogram bin 6, histogram of areas of components
Otsu_feature_6	area histogram bin 7, histogram of areas of components
Otsu_feature_7	area histogram bin 8, histogram of areas of components
Otsu_feature_8	area histogram bin 9, histogram of areas of components
Otsu_feature_9	area histogram bin 10, histogram of areas of components
Otsu_feature_10	max area, histogram of areas of components maximum area from all the components exist in image (each crop)
Otsu_feature_11	mean area, histogram of areas of components mean area of all the components exist in image (each crop)
Otsu_feature_12	median area, histogram of areas of components
Otsu_feature_13	min area, histogram of areas of components
Otsu_feature_14	Var area, histogram of areas of components variance of all sizes of components
Otsu_feature_15	Centroid_x, histogram of areas of components x centroid of all components
Otsu_feature_16	Centroid_Y, histogram of areas of components y centroid of all components
Otsu_feature_17	feature count, histogram of areas of components number of components
Otsu_feature_18	dist histogram bin 1, histogram distances from center. first 10 shows the histogram values if we calculate the distance of each component from center make a histogram of distances with 10 bins (more scattered components have more values in higher bins)
Otsu_feature_19	dist histogram bin 2, histogram distances from center
Otsu_feature_20	dist histogram bin 3, histogram distances from center
Otsu_feature_21	dist histogram bin 4, histogram distances from center
Otsu_feature_22	dist histogram bin 5, histogram distances from center
Otsu_feature_23	dist histogram bin 6, histogram distances from center
Otsu_feature_24	dist histogram bin 7, histogram distances from center
Otsu_feature_25	dist histogram bin 8, histogram distances from center)
Otsu_feature_26	dist histogram bin 9, histogram distances from center)
Otsu_feature_27	dist histogram bin 10, histogram distances from center maximum distance of one component from center
Otsu_feature_28	max dist, histogram distances from center maximum of same thing
Otsu_feature_29	mean dist, histogram distances from center mean of same thing
Otsu_feature_30	median dist, histogram distances from center median of same thing
Otsu_feature_31	min dist, histogram distances from center min of same thing
Otsu_feature_32	var dist, histogram distances from center var of same thing
Otsu_feature_33	Euler dist, histogram distances from center total number of components - total number of holes in components

III.7. Statistical analysis

Most of the data were presented as mean \pm standard error of the mean. Normality was verified using the test of Shapiro-Wilk and, when necessary, non-parametric tests were used for data not displaying a normal distribution. The Welch t-test was applied when the normalization were validated. For some experiment ANOVA Test were performed. Statistical significance is presented in the figures as * $p < 0.05$, ** $p < 0.01$, *** $p < 0.001$, **** $p < 0.0001$, and not significant (ns = $p > 0.05$). * p -value < 0.03 ** p -value < 0.01 . *** p -value < 0.001 . p -value < 0.0001 . The Z score are also represented on some figures.

III.8. Tool compounds treatment

iPSC-CM were treated with various molecules previously diluted in Dimethyl sulfoxide DMSO (D2650, Sigma). The cells were seeded manually in 384-well plates at D0, and at D1 the culture medium was renewed with T3 Dex medium. At D4, cells are treated using the V-Prep device (Agilent), it's a liquid handling system that automates liquid transfer for screening. This device ensures that cells are treated identically. At D7, either the treatment is renewed identically to continue the treatment over a longer period, or the culture medium is renewed identically for a so-called "recovery" phase. At D10, the culture is stopped to proceed with the immunocytostaining step. Here, the information on compounds preparation:

- DMSO 100% was a clean ampoule from D2650-5x5mL (Sigma-Aldrich/Merck).
- Flecainide acetate: (MW = 474.39 g.mol-1, powder stored at -20°C) 1.8 mg were resuspended in 379.5 μ L of DMSO 100% to yield a 10mM solution. Ref : HY-17429, MedChemExpress (via Clinisciences).
- Ranolazine dihydrochloride: (MW = 500.46 g.mol-1, powder stored at +4°C) 6 mg were resuspended in 1200 μ L of DMSO 100% to yield a 10mM solution. Ref : HY-17401, MedChemExpress (via Clinisciences).
- Verapamil hydrochloride: (MW = 491.06 g.mol-1, powder stored at +4°C) 4.1 mg were resuspended in μ L of 835 μ L DMSO 100% to yield a 10mM solution. Ref : HY-A0064 MedChemExpress (via Clinisciences).
- MG-132: (MW = 475.62 g.mol-1, powder stored at -20°C) 0.5 mg were resuspended in 105.0 μ L of DMSO 100% to yield a 10mM solution. Ref : HY-13259 MedChemExpress (via Clinisciences).

- Baflomycin A1: (MW = 622.83 g.mol-1, powder stored at -20°C) 0.5 mg whole tube resuspended in 80.3 μ L of DMSO 100% to yield a 10mM solution. Ref : HY-100558 MedChemExpress (via Clinisciences).
- Rapamycin: (MW = 914.17 g.mol-1, powder stored at -20°C) 3.5 mg were resuspended in 382.9 μ L of DMSO 100% to yield a 10mM solution. Ref : HY-10219 MedChemExpress (via Clinisciences).
- Tubastatine A: (MW = 335.40 g.mol-1, powder stored at -20°C) 4.8 mg were resuspended in 1430 μ L of DMSO 100% to yield a 10mM solution. Ref : HY-13271A MedChemExpress (via Clinisciences).
- SB203580: (MW = 413.90 g.mol-1, powder stored at -20°C) 3 mg were resuspended in 725 μ L of DMSO 100% to yield a 10mM solution. Ref : HY-10256A, MedChemExpress (via Clinisciences).
- GS6976: (MW = 377.42 g.mol-1, powder stored at -20°C) 5 mg whole tube resuspended in 1024 μ L of DMSO 100% to yield a 10mM solution. Ref : S71119, SelleckChem.
- Danicamtiv: (MW = 435.42 g.mol-1, powder stored at -20°C), 5 mg were resuspended in 1153.6 μ L of DMSO 100% to yield a 10 mM solution. Ref : HY-109128 Lot #78715 Vendor : MedChemExpress (via Clinisciences)
- Omecamtiv mecarbil: (MW = 401.43 g.mol-1, powder stored at -20°C) 5.0 mg were resuspended in 1245.5 μ L of DMSO 100% to yield a 10 mM solution. Ref : HY-14233 Lot #05330 Vendor : MedChemExpress (via Clinisciences)
- Bortezomib: (MW = 384.24 g.mol-1, powder stored at +4°C) 1.4 mg were resuspended in 364.3 μ L of DMSO 100% to yield a 10mM solution. Ref : HY-10227 Lot #45613 Vendor : MedChemExpress (via Clinisciences)
- Istaroxime hydrochloride: (MW = 396.95 g.mol-1, powder stored at -20°C) 5.0 mg were resuspended in 1259.6 μ L of DMSO 100% to yield a 10mM solution. Ref : HY-15718A Vendor : MedChemExpress (via Clinisciences)

IV. RESULTS

IV.1. Functional impairment associated with dilated cardiomyopathy due to a Desmin mutation (DES^{E439K})

The study of dilated cardiomyopathy (DCM) associated with myofibrillar myopathy (MFM) due to a mutation in *DES* gene encoding desmin protein can be driven using either *in vivo* or *in vitro* models (Brodehl et al., 2018). In this study, a special focused on human *in vitro* models was done. These models have the advantage of being patient-specific and reproducing the disease phenotypes present in patients (Tse et al., 2013). The observations made in such models enable physiopathological mechanisms to be correlated more closely to the development of the disease in the patient. Recent developments in the field of cardiomyocytes derived from human induced pluripotent stem cells (iPSC-CM) two dimensional models (2D) and the development of three dimensional models (3D complex structures combining, for examples, different cell types) open up exciting research possibilities (Veldhuizen et al., 2019). In a first approach, the engineered human myocardium (EHM), a 3D cardiac microtissue, was used. This model is crucial for studying the morphological and functional disturbances at the origin of cardiac damage in patients with DCM associated with MFM due to a DES^{E439K} mutation.

IV.1.1. Functional contraction in EHM 3D model

To assess the function of cardiac tissue, we have generated contracting rings of cardiac tissue (myTissue, Myriamed®) and examine the contractile function of these EHM. These tissues were described as being able to contract spontaneously and uniformly after 3 days of culture (Tiburcy et al., 2020). To develop these EHM, cardiomyocytes derived from induced pluripotent stem cells (iPSC-CM) were placed together with collagen matrix in special plates with two pillars in each well to ensure the generation of a ring-shaped microtissue. During contraction of these EHM, the deflection pole induced by EHM contraction in isometric conditions was measured. Thus, the contraction force generated by the EHM could be deduced (Figure 24A). Different EHM were generated from the following iPSC-CM:

- Control 1
- Patient 1 DES^{E439K}

- Patient 2 DES^{E439K}

Video analysis of EHM contractions revealed various metrics describing different aspects of EHM contraction, such as the spontaneous beating frequency, beating rhythm, force of contraction (FOC), resting tension, contraction time T1 and relaxation time T2 (Tiburcy et al., 2017) (Figure 24B). Several of these metrics showed a difference between the control 1 EHM and the DES^{E439K} patient EHM (Patient 1 DES^{E439K} and Patient 2 DES^{E439K}). In particular, the FOC was lower in the DES^{E439K} patient EHM than in the control EHM (Figure 24B). Resting tension (RT) is a parameter that refers to the initial muscle tension of the EHM at rest. Thus, the RT of DES^{E439K} patient EHM is significantly lower than the RT of control EHM. This may be due to myofibril disorganization caused by the DES^{E439K} mutation. Indeed, it has already been shown that resting tension can be associated with the degree of organization of myofibril (Thornell et al., 1976). Concerning the FOC, it was also measured by varying the calcium concentration in the medium ((Figure 24C). It was found that the contraction force of control EHM was consistently higher than in DES^{E439K} patient EHM, particularly in the Patient 2 DES^{E439K} (Figure 24C). On this last analysis, the two DES^{E439K} patient clones did not respond in the same way. Patient 2 DES^{E439K} FOC at different calcium concentrations was lower than FOC of Patient 1 DES^{E439K} . This discordance between the different DES^{E439K} EHM patient clones can be explained by various hypotheses, such as heterogeneity between iPSC cardiomyocyte differentiation batches or during EHM generation. These results highlight one of the limitations of the model, and underline the importance of quality control. Interestingly, despite this slight heterogeneity between DES^{E439K} patient EHM, the differences with control EHM are broadly the same for both DES^{E439K} patient EHM clones.

To conclude, these results show that the contractile function of the various EHM is deficient in DES^{E439K} patient EHM compared with control EHM. This confirms that the EHM do indeed reproduce the phenotype observed in DCM patients carrying a DES^{E439K} mutation (Brodehl et al., 2013).

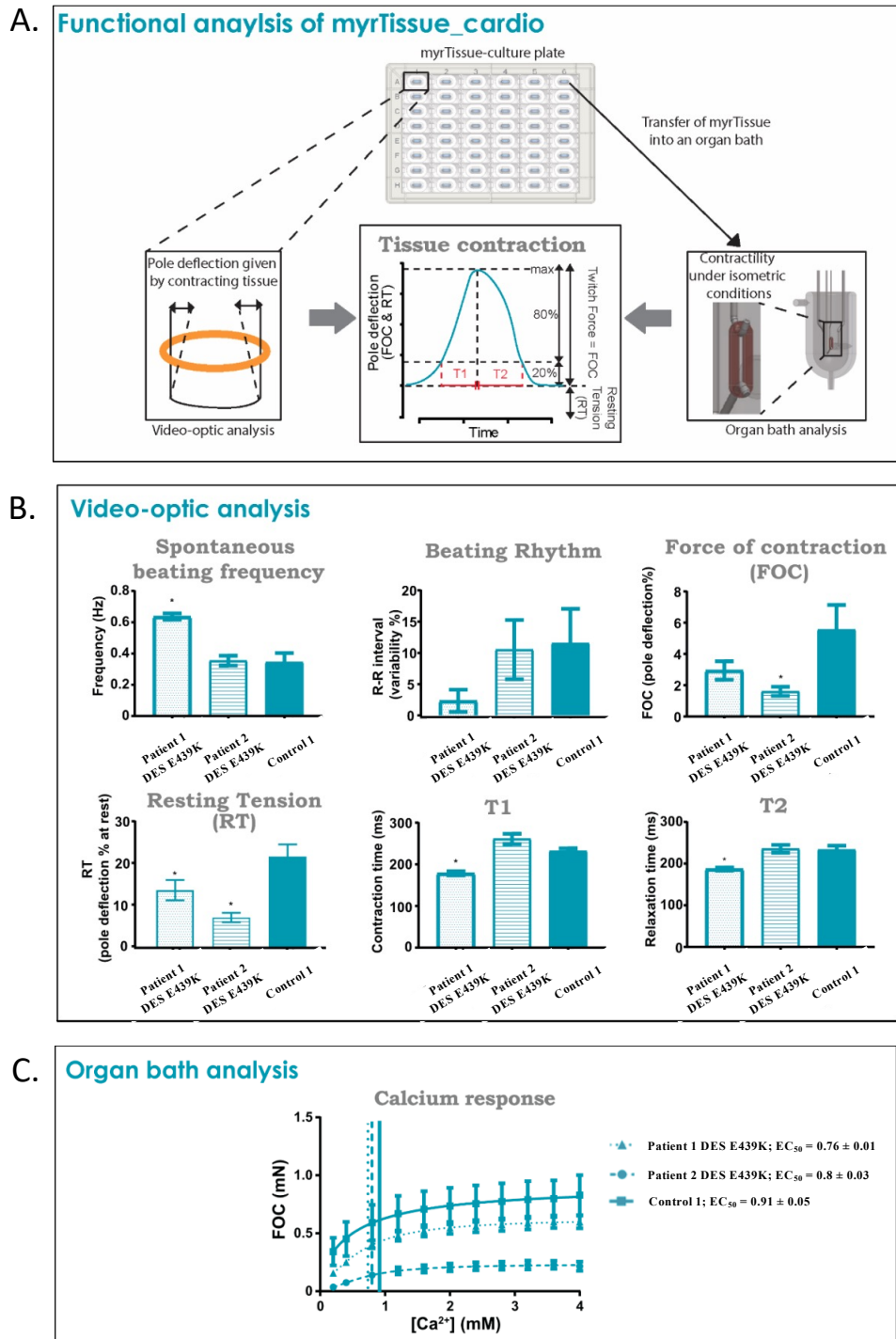


Figure 24 : Functional activities of EHM control (Control 1) and Patients DES^{E439K} (Patient 1 DES^{E439K}; Patient 2 DES^{E439K}). A. Functional analysis of EHM workflow. B. different parameters for measuring EHM contraction using video analysis C. Force of contraction (FOC) recorded under increasing calcium concentrations. n= 8-10 EHM per group

Following the demonstration of impaired contractile function in a context of dilated cardiomyopathy associated with desmin mutation (DES^{E439K}), it is crucial to explore the mechanisms explaining these perturbations. Many phenotypic observations of

cardiomyopathies can be associated to the disturbances of mitochondrial respiration, a key aspect of cellular physiology that influences energy production and metabolic regulation. Moreover, many studies have shown that disruption of mitochondrial function is a key phenotype of dilated cardiomyopathy associated with desminopathy (Alam et al., 2018; Milner et al., 2000; Tsikitis et al., 2018; Wiersma et al., 2019).

IV.1.2. Functional mitochondrial respiration in iPSC-CM

In order to measure the impact of the *DES*^{E439K} mutation on mitochondrial function, analyses of the mitochondrial respiratory activity of iPSC-CM were investigated. Analyses were performed using a mitochondrial stress assay using a seahorse on different iPSC-CM : Control, patient *DES*^{E439K} and isogenic *DES*^{E439K}. Real-time assessment of oxygen consumption rate (OCR) at baseline and after addition of inhibitors targeting specific respiratory complexes was performed (Figure 25A). From curves it is possible to calculate basal respiration, ATP-linked respiration, maximal respiration and reserve capacity (Figure 25B-F).

First, basal respiration is calculated from the difference in OCR in the initial state and following complete blockade of the respiratory chain by addition of rotenone and antimycin A. A decrease in basal respiration was detected in iPSC-CM carrying the *DES*^{E439K} mutation compared with control iPSC-CM (Figure 25B).

Then, the addition of oligomycin, an ATP synthase inhibitor, enables measurement of ATP-related respiration, meaning oxygen consumption specifically used for ATP biosynthesis. This parameter is lower in iPSC-CM carrying the *DES*^{E439K} mutation (Figure 25C), suggesting a weaker involvement of mitochondria in ATP generation in the presence of the mutation.

Carbonyl-4 (trifluoromethoxy) phenylhydrazone cyanide (FCCP) is an uncoupling agent that induces proton gradient collapse and disrupts mitochondrial membrane potential. The addition of FCCP results in an uninhibited flow of electrons through the electron transport chain, making it possible to measure the maximum rate of oxygen consumption. Maximum respiration is lower in iPSC-CM carrying the *DES*^{E439K} mutation, indicating lower total mitochondrial activity (Figure 25D). Reserve capacity, defined as the difference in OCR between basal and maximal respiration, is also lower in iPSC-CM carrying the *DES*^{E439K} mutation (Figure 25E).

Finally, to assess the role of glycolysis in iPSC-CM energy/metabolite production, the initial OCR was normalized to the initial extracellular acidification rate (ECAR). The ratio between OCR and ECAR, which indicates the cellular preference for oxidative phosphorylation over glycolysis, was calculated for the different groups. This ratio is lower in iPSC-CM carrying the *DES*^{E439K} mutation (Figure 25F). Overall, compared with control iPSC-CM, both types of *DES*^{E439K} mutant CMs show a decrease in mitochondrial respiration compensated by higher glycolytic activity. In addition, electron microscopy analysis also revealed a strong cytoplasmic accumulation of lipid droplets in *DES*^{E439K} iPSC-CM and Isogenic *DES*^{E439K} iPSC-CM compared with control iPSC-CM (Figure 25G-H). This observation was confirmed by cytometric quantification of intracellular lipids using BODIPY, a fluorescent hydrophobic dye for lipids (Figure 25H). Taken together, these results indicate that the metabolic activity of iPSC-CM is modified in the context of *DES*^{E439K} mutation.

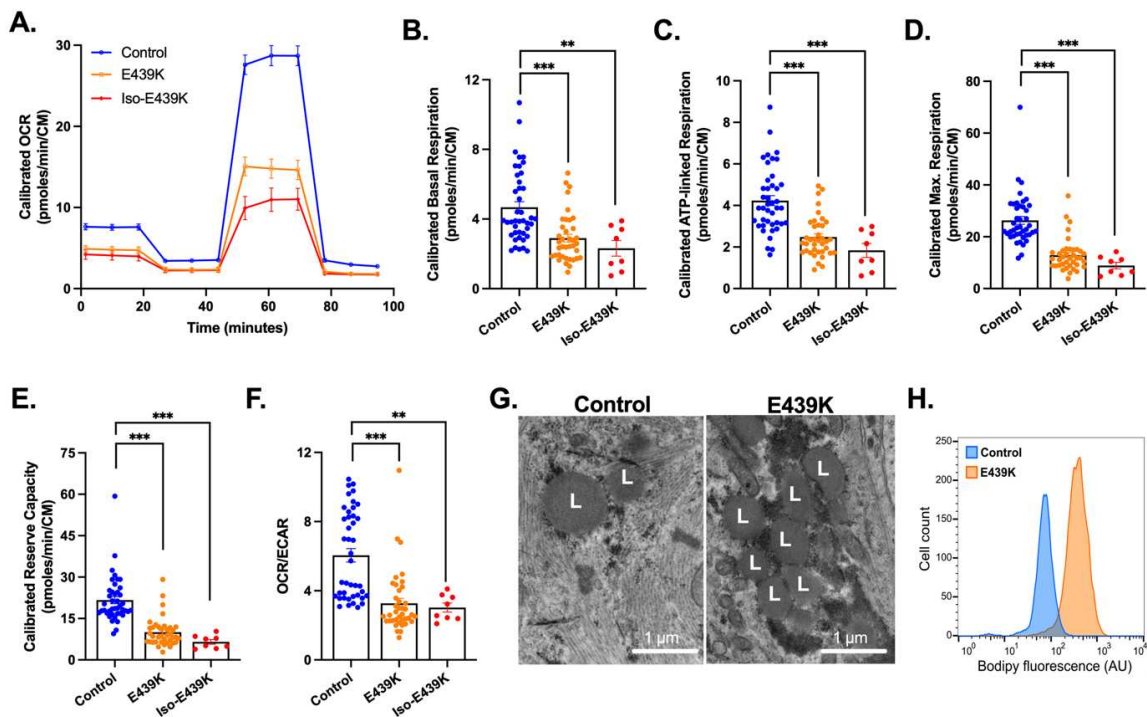


*Figure 25: Decreased mitochondrial respiration and altered metabolic activity in iPSC-CM with *DES* E439K mutation. (A) Representative mitochondrial oxygen consumption rate (OCR) profiles in Control-CMs, E439K-CMs and Iso-E439K-CMs. OCR profiles are expressed as pmol O₂/min normalized to the number of cardiomyocytes and calibrated to the lowest value of the plate after addition of rotenone and antimycin A. (B) Quantification of basal respiration, (C) ATP-linked respiration, (D) maximal respiration and (E) reserve capacity of cardiomyocytes. (F) Ratio of OCR to ECAR in iPSC-derived cardiomyocytes. Values are expressed as mean ± SEM. *, p < 0.05, **, p < 0.01, ***, p < 0.001. from (Hovhannisyan et al., 2023)*

In addition to mitochondrial perturbations, *DES*^{E439K} mutation has been described to induce a conformational defect in the desmin protein (Brodehl et al., 2018; Hovhannisyan et al., 2023). Thus, it may be relevant to investigate the state of cellular proteostasis and quality control systems in the context of *DES*^{E439K} mutation.

IV.1.3. Desmin aggregation and autophagic flux in iPSC-CM

Desmin aggregation

Many studies have shown that in a context of DCM associated with a *DES* mutation, a double event may occur (Clemen et al., 2013; Tsikitis et al., 2018). Firstly, loss of the three-dimensional network provided by desmin, and secondly, aggregation of the desmin protein. Regarding the specific localization of the mutation in the *DES* gene, it has been observed that different mutations can have different consequences on the formation of protein aggregates (Brodehl et al., 2022). Some mutations may further promote the formation of inclusions, while others may lead to specific structural alterations in desmin (Brodehl et al., 2018). Very few studies have been conducted on the *DES*^{E439K} mutation, however, it has already been shown that this mutation induces accumulation and patchy aggregation of desmin within the cytoplasm of iPSC-CM (Hovhannisyan et al., 2023). In order to visualize this phenomenon a study on iPSC-CM (Control, Isogenic *DES*^{E439K} and Patient *DES*^{E439K}) was performed. iPSC-CM were cultured 14 days after thawing before immunostaining with a desmin marker (Figure 26). Immunostaining showed that control iPSC-CM displayed a striated organization of desmin. While iPSC-CM carrying the *DES*^{E439K} mutation (Isogenic *DES*^{E439K} or Patient *DES*^{E439K}) did not show this organization, desmin was more likely to be aggregated in the form of dots or threads.

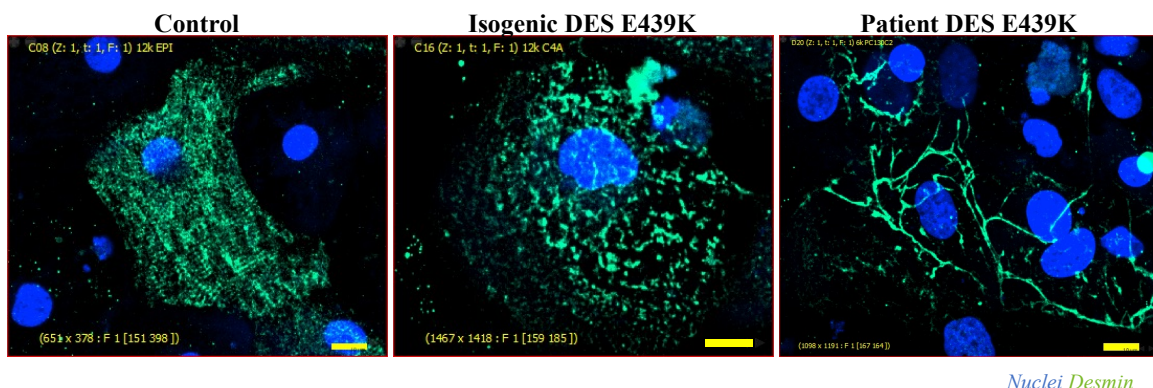


Figure 26 : Immunocytostaining with Desmin staining of iPSC-CM (Control, Isogenic *DES*^{E439K} and Patient *DES*^{E439K}). Scale bar = 10µm

We can suppose that the appearance of protein aggregates in the cell certainly induces a modification of the proteostasis. In desminopathy, protein aggregates can accumulate and be toxic to the cell (S. Singh et al., 2020). To maintain proteostasis in cell and ensure degradation of these aggregates, protein quality control (PQC) systems are activated (Henning & Brundel, 2017b). The role of these PQC systems is to ensure cell proteostasis, in particular by eliminating malformed or aggregated proteins present in the cell. These systems include chaperone proteins, which help to form the correct protein conformation, the ubiquitin proteasome system (UPS), which initially degrades malformed proteins, and the autophagic system, which degrades aggregated proteins and dysfunctional organelles (Henning & Brundel, 2017a). The presence of desmin aggregates and defective mitochondria suggests that the autophagic system could be strongly challenged (Hofmann et al., 2019). Moreover, some studies showed that desmin mutation can have an impact on autophagic flux (Sukhareva et al., 2023).

Autophagic flux in the iPSC-CM

Studies have shown that autophagy plays a major role in the response to cardiac stress (Maejima, 2020). Given the presence of protein aggregates and mitochondrial defects, it was of interest to study autophagic activity. Under basal conditions, autophagic function remains at a low level, helping to maintain cellular homeostasis. Autophagy can be rapidly activated under conditions of cellular stress, such as limited nutrient supply, deregulation of intracellular organelle homeostasis (e.g. accumulation of defective mitochondria) or accumulation of protein aggregates (Bhuiyan et al., 2013)

LC3b is a protein involved in the formation of the autophagosome around compounds to be degraded. LC3b exists in a cytosolic form (LC3b-I), where it is inactive, and in a phagophore-associated form, where it has undergone lipidation with a phosphatidylethanolamine residue (LC3b-II) (Yoshii & Mizushima, 2017). The study of autophagic flux in the different iPSC-CM was conducted using chloroquine (chlq), a molecule that blocks the activity of lysosomal hydrolases. This blockade leads to an accumulation of autophagic vacuoles, as well as of LC3b-II. Analysis of relative LC3b-II expression in not treated (NT) and chlq-treated conditions enables autophagic flux to be estimated. Thus, autophagic fluxes has been assessed in the Isogenic *DES*^{E439K} and Patient *DES*^{E439K} iPSC-CM carrying the *DES*^{E439K} mutation encoding desmin, compared with the Isogenic control iPSC-CM (Mizushima & Murphy, 2020) (Figure 27A).

It was observed that relative LC3b-II expression showed a significant increase, between NT and chlq-treated conditions, in iPSC-CM carrying the *DES*^{E439K} mutation compared with the isogenic control (Figure 27B). These results may indicate that autophagic flux is higher in iPSC-CM carrying the mutation than in the isogenic control iPSC-CM.

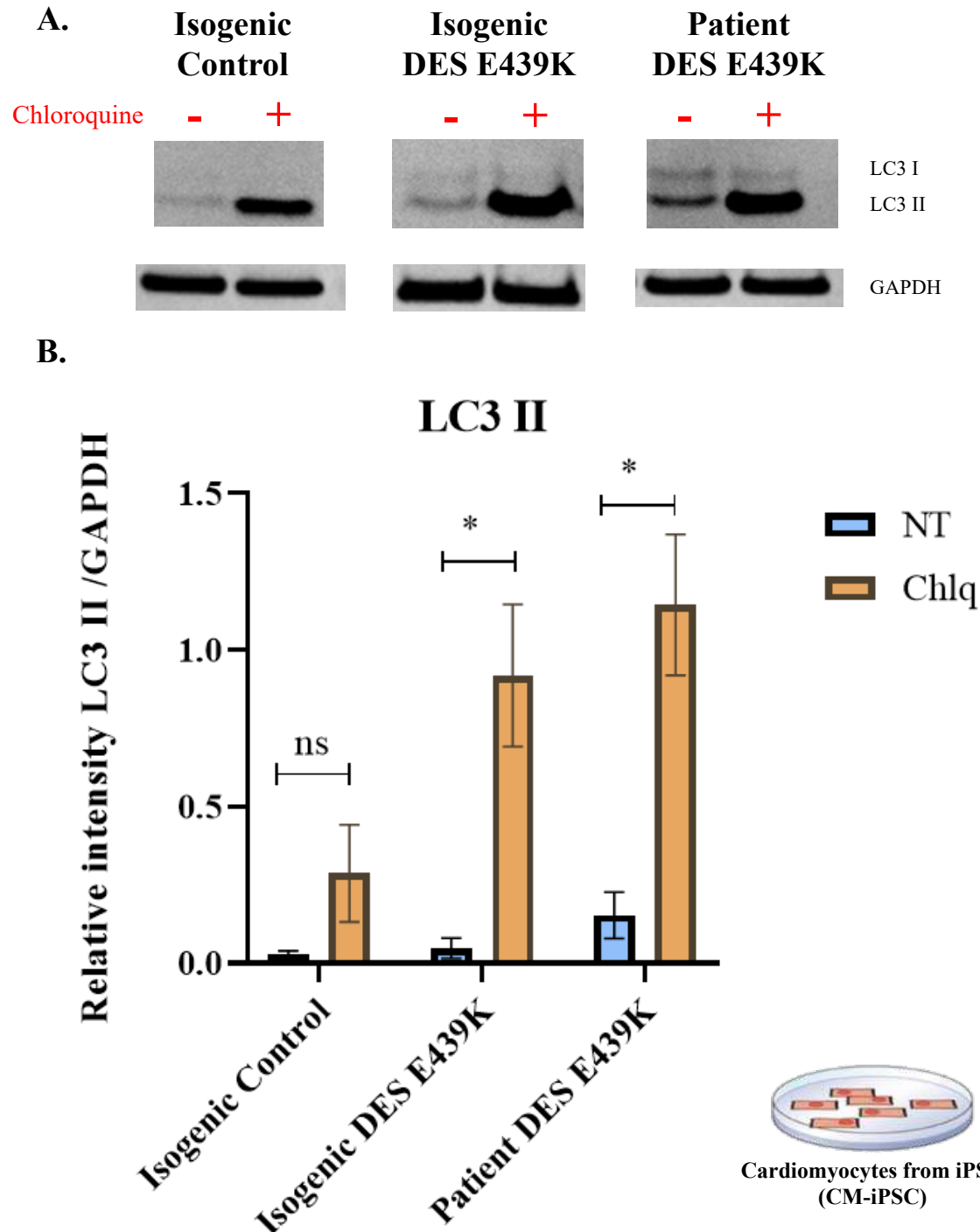


Figure 27 : Western blot of iPSC-CM (Isogenic control; Isogenic *DES*^{E439K}; Patient *DES*^{E439K}) in different condition +/- Chloroquine and staining of LC3 I and LC3 II (Autophagic flux marker) A.

*LC3-I and LC3-II protein levels were analyzed by performing Western blotting analysis, glyceraldehyde 3-phosphate dehydrogenase (GAPDH) was used as an internal control. B. Quantitative analysis of the results of Western blotting analysis, LC3-II levels normalized using the GAPDH levels. A two-tailed t-test was performed. Values are expressed as mean ± SEM. ns not significant. * p-value < 0,05*

Following the exploration of functional perturbations associated with DCM in the context of *DES*^{E439K} mutation, the integration of transcriptomic data may provide a deeper understanding of the underlying mechanisms of gene regulation, and reveal important signaling pathways involved in disease progression.

IV.2. Transcriptomic study on EHM models

The following work was conducted on the *in vitro* 3D EHM model. Transcriptomic analyses on iPSC-CM were also performed by the laboratory but are presented in a published study (Hovhannisyan et al., 2023), to be found in the appendix chapter VIII.

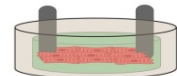
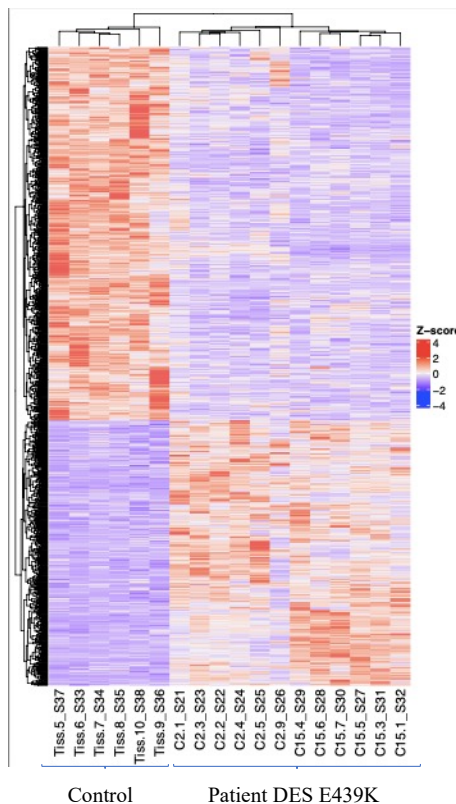
IV.2.1. Transcriptomic exploration using RNAseq

Transcriptome studies of EHM were implemented with the goal of identifying a transcriptomic phenotype that could explain the contractility defects previously observed. Analysis was performed on 3 groups of 6 EHM/group (replicates) : Control 1(Tiss) Patient 1 *DES*^{E439K} (C2) and Patient 2 *DES*^{E439K} (C15). First, we determine the gene expression levels. This included an analysis of differentially expressed genes (DEGs), the purpose of it being to identify genes whose expression varied significantly between the EHM control group and the EHM Patient *DES*^{E439K} groups. This analysis allowed the visualization of the different transcriptomic profiles of our groups and the identification of molecular signatures for EHM Patient *DES*^{E439K}. The transcriptomes of the different groups are presented in HeatMap form (Figure 28A). It was interesting to note that the transcriptomic signatures of the Patient *DES*^{E439K} EHM were different from the transcriptomic signature of the control EHM (Figure 28A).

Then, genes identified as differentially expressed were interpreted from a biological perspective. This analysis was based on Gene Ontology (GO) (Supek et al., 2011). GO is a standardized hierarchical classification of biological terms, which can be used to categorize genes according to their biological functions. In this way, it is possible to determine whether biological pathways are enriched in a given sample, in this case the *DES*^{E439K} patient EHM, compared with a reference sample, the control EHM (Figure 28B). Indeed, GO analysis demonstrated that genes of gene sets of multiple pathways involved in cardiac contraction

and cardiac conduction were selectively downregulated in Patient *DES*^{E439K} EHM. This may explain the deficiencies in force of contraction. Moreover, the GO analysis showed that a pathway involved in cellular response to oxidative stress were upregulated which can be associated with mitochondrial defect (Ramaccini et al., 2021). It was the same for several pathways involved in response to unfolded protein were upregulated. This may be associated with proteostasis disruption (Henning & Brundel, 2017a). Finally, there were also an upregulation in muscle developmental pathways which can be associated to a defect in the maturation of cardiac structures: it has already been shown that desmin plays a role in the development of cardiac muscle, and mutations can disrupt this process (Capetanaki et al., 2015).

A.



Engineered Human Myocardium (EHM)

B.

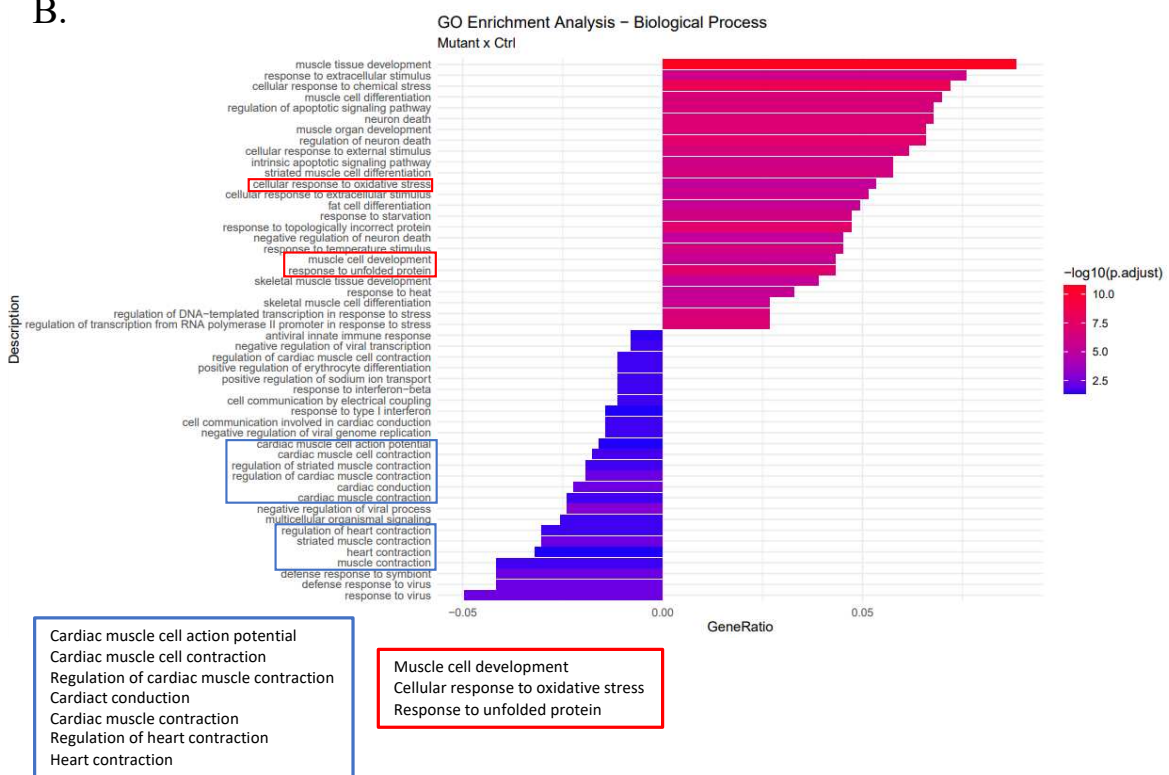


Figure 28 : Transcriptomics phenotypes of EHM control and patients DES^{E439K}. A. Heatmap of EHM transcripts based on DEG analysis. B. GO enrichment analysis summarized and visualized as a scatter plot using Revigo. Summarized exclusive set of GO terms related to biological process Up-regulate or Down-regulate in EHM Patient DES^{E439K} in comparison with EHM control

Based on GO biological process enrichment analyses and gene expression data collected during RNA-seq, the biological processes are represented by heatmaps of the gene expression of their component genes. In this way, it is possible to visualize the transcriptomic profile of the different EHM groups for each biological process (Cardiac contractility, Oxidative stress response, Chaperon heat shock protein, UPS and autophagy) (Figure 29). Firstly, this analysis confirms the observations previously made: a molecular signature of the genome is indeed present in the *DES*^{E439K} patient EHM compared with control EHM for genes involved in regulating cardiac contractility and oxidative stress response (Figure 29A-B). Secondly, with regard to proteostasis disruption, this study allowed a more detailed analysis of the different quality control systems (Figure 29C-E). Indeed, a transcriptomic signature was found, with up-regulation in *DES*^{E439K} EHM patients of genes involved in quality control systems involving firstly chaperone proteins, then the UPS and finally the autophagic system. Taken together, these results suggest that *DES*^{E439K} EHM display a transcriptomic signature of disruption of PQC systems.

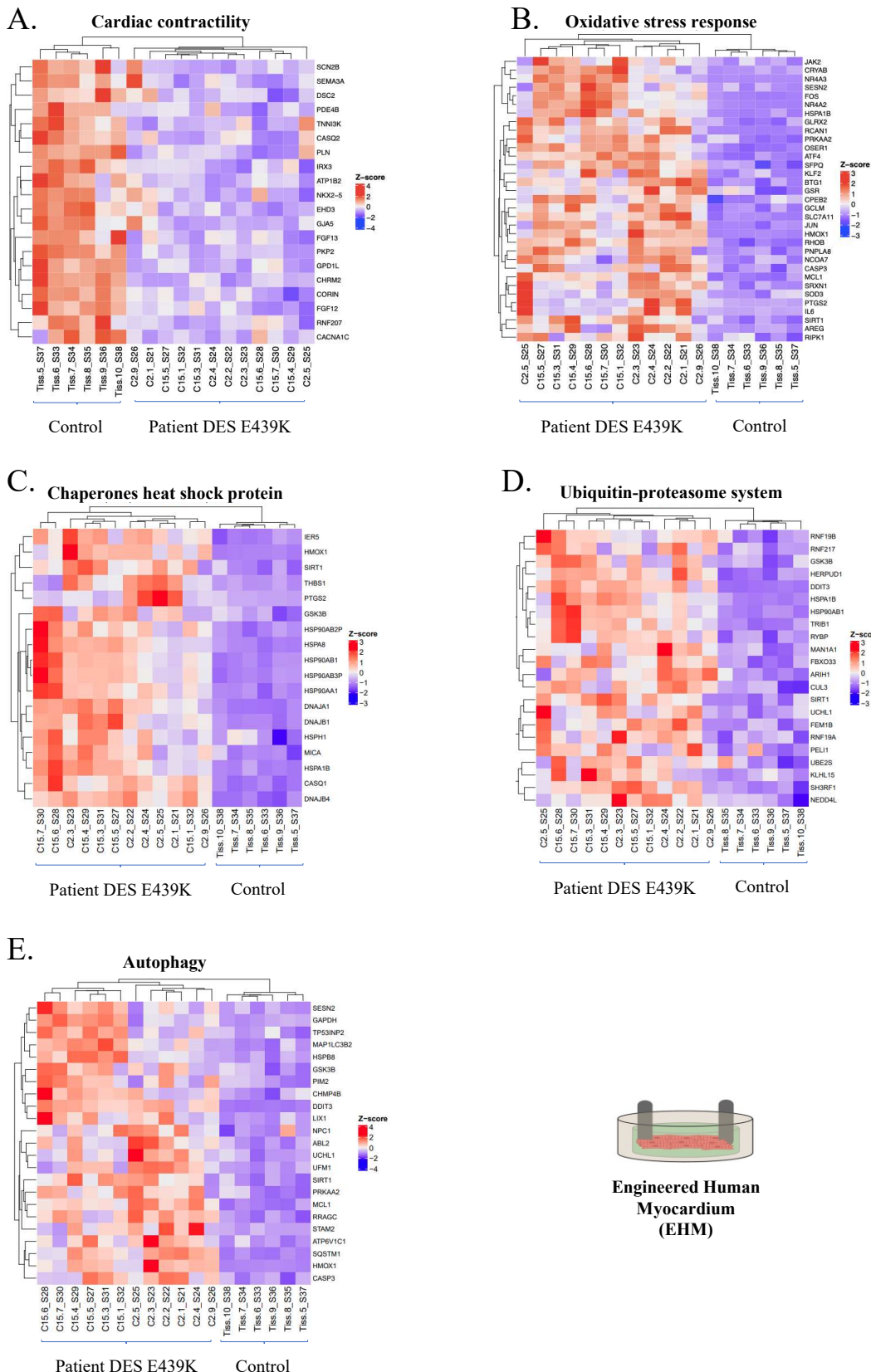


Figure 29 : Heatmap showing expression patterns of selected genes related to key biological process, giving specific transcriptomic profiles of EHM control and Patient DES^{E439K}. A-E Cardiac contractility, Oxidative stress response, Chaperones heat shock proteins, Ubiquitin proteasome system and autophagy.

While RNA-Seq analysis provides a global, high-throughput view of gene expression, RT-qPCR offers a more targeted and precise approach to specifically confirm and quantify the expression of genes of interest. Contractile disruption and oxidative stress linked to a mitochondrial defect are often reported in the literature concerning desmin mutation-associated dilated (Goldfarb & Dalakas, 2011; Milner et al., 2000; Ramaccini et al., 2021; Ramspacher et al., 2015), however proteostasis and cardiac immaturity aspect were less explored. Thus to further characterize these processes, and to confirm the observations on PQC processes and cardiac immaturity, RT-qPCR-based transcriptomic studies were conducted on specific genes.

IV.2.2. Transcriptomic validation RT-qPCR

Thus, the transcriptomes of EHM control 1, Patient 1 *DES*^{E439K}, Patient 2 *DES*^{E439K} were studied at the genetic level of the different quality control systems by RT-qPCR (Figure 30).

Chaperone protein system

The genes encoding chaperone proteins are the first to be affected when misfolded proteins appear (Figure 30A). CRYAB is a gene encoding α-B-Crystallin, a chaperone protein interacting with desmin (Sharma et al., 2017). No significant differences in CRYAB expression were observed between the different EHM. BAG3 encodes a co-chaperone protein of HSP70 and HSC70 which is prominently expressed in cardiac and skeletal muscle tissues (Sarparanta et al., 2020). Again, no significant differences were measured in BAG3 expression in the different EHM. HSPD1 encodes a chaperone protein involved in mitochondrial protein import and macromolecular assembly (Sarparanta et al., 2020). HSPD1 is significantly more expressed in *DES*^{E439K} patient EHM than in the control EHM. This last results strengthen the previous observations demonstrating mitochondrial defects. Thus, slight differences were noted in the gene expression of various chaperone proteins, but this PQC mechanism does not appear to be strongly solicited in the *DES*^{E439K} mutated EHM model.

Ubiquitin proteasome system

Then, genes encoding proteins involved in the UPS were investigated (Figure 30B). UBE2I encodes a protein member of the E2 ubiquitin conjugating enzyme family (Baumgarten et al., 2013). MDM2 is the main E3 ubiquitin ligase protein of p53 in mitotic cells, regulating cell growth, DNA repair, oxidative stress and apoptosis (Hauck et al.,

2017). FBXO32 is a muscle-specific ubiquitin-E3 ligase protein, this protein are localizes at the sarcomere and plays a role in muscle atrophy, cardiac hypertrophy, and atrophy development (Ghasemi et al., 2022). UBE2I expression in Control 1 EHM is either slightly higher than that in Patient 2 *DES*^{E439K} EHM or identical to the expression of this gene in the Patient 1 *DES*^{E439K} EHM. Gene expression of MDM2 and FBXO32 was up-regulated in EHM Patient *DES*^{E439K} compared with Control 1 EHM. These results suggest that the *DES*^{E439K} mutation induces a particular solicitation of the E3 ubiquitin ligase system which is specifically responsible for transferring ubiquitin to the target protein. Indeed, Mdm2 play a role in cardiac growth control, oxidative stress and mitochondrial disruption response through the regulation of p53, the Pgc-1 family of transcriptional coactivators and the pivotal antioxidant Pink1(Hauck et al., 2017).

Autophagic system

Finally, the study of genes marking the autophagic system focused on the following markers (Figure 30C) : CALCOCO2 (calcium-binding and coiled-coil domain-containing 2) a gene encoding a protein involved in most stages of autophagy, regulating the maturation process of autophagosomes and described as down-regulated in the context of cardiac dysfunction (Gil-Cayuela et al., 2019). PINK1 encodes a protein that coordinates autophagic quality control mechanisms in dysfunctional mitochondria, as part of the mitophagy process (Ding & Yin, 2012), PINK1 has been described as playing an important role in the regulation of mitochondrial quality and the development of cardiomyocyte maturity (H. Liu et al., 2023). SQSTM1/p62 codes for an autophagy receptor protein required for selective macroautophagy (aggrephagy) (van der Klooster et al., 2021). Thus, down-regulation of CALCOCO2 expression, up-regulation of PINK1 and SQSTM1/p62 were indeed observed in EHM Patient *DES*^{E439K} compared to EHM Control 1. These results indicate that various autophagy agents are significantly solicited in a context of DCM due to a Desmin mutation.

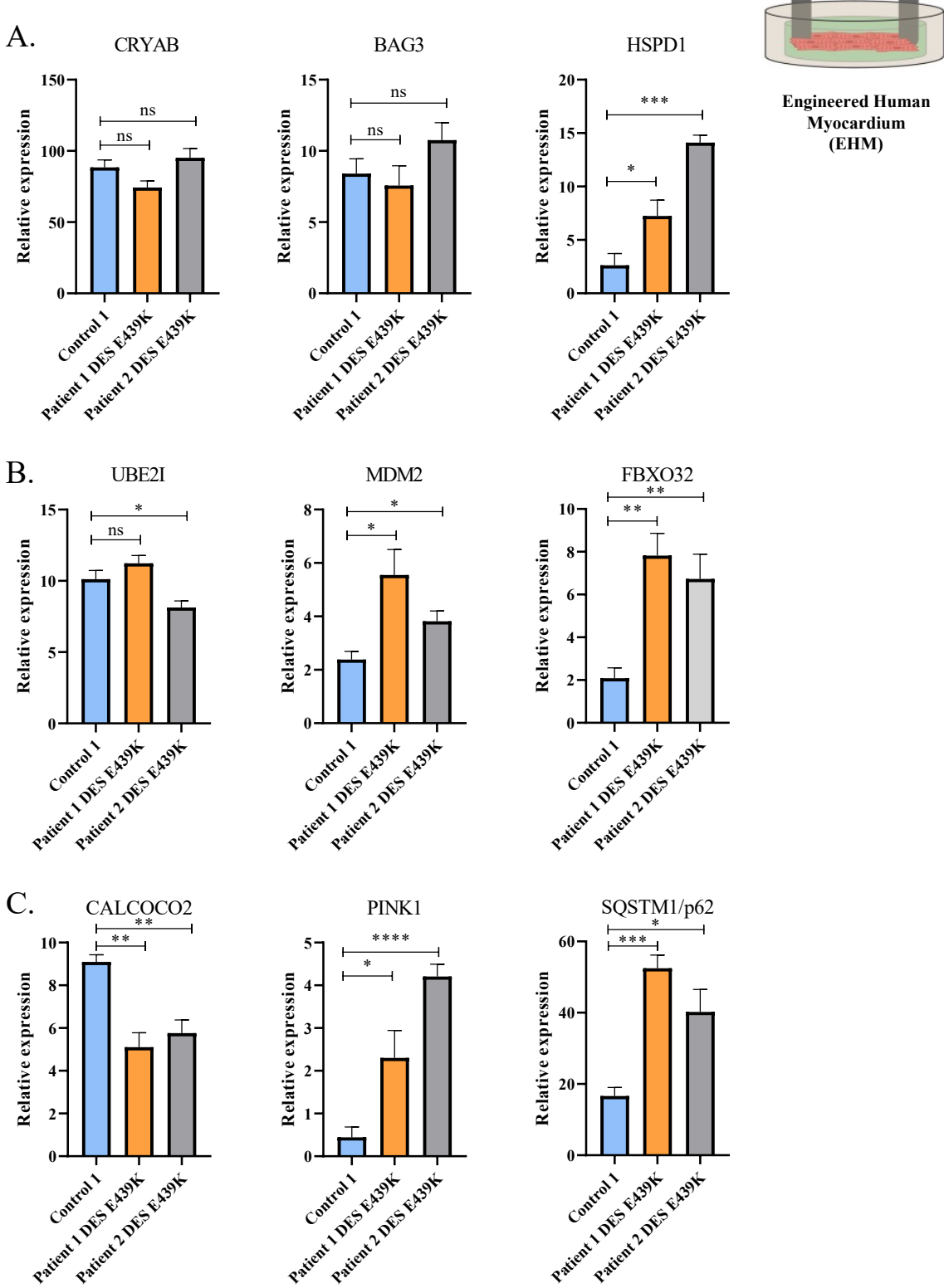


Figure 30 : Relative expression of Protein quality control (PQC) system genes measured by RT-qPCR in EHM (Control 1; Patient 1 DES^{E439K}; Patient 2 DES^{E439K}). A. Relative expression of genes coding for chaperones heat shock proteins (CRYAB; BAG3; HSPD1). B. Relative expression of genes coding for Ubiquitin proteasome proteins (UBE2I; MDM2; FBXO32). C. Relative expression of genes coding for Autophagic protein (CALCOCO2; PINK1; SQSTM1/p62). A two-tailed t-test

*was performed. Values are expressed as mean ± SEM from n=4 EHM per group. ns not significant.
* p-value<0.05 ** p-value<0.005. *** p-value<0.0005. **** p-value<0.00005.*

These results clearly show that all three PQC appear to be involved in this context of DCM associated with the *DES*^{E439K} mutation. Interestingly, several of the genes involved in these different systems are implicated in signaling involving mitochondrial defects, HSPD1 for chaperones system, MDM2 for UPS and PINK1 for autophagy. These data suggest that these quality control systems are not only solicited by the presence of protein aggregates, but also by the presence of mitochondrial dysfunction (Ghosh et al., 2020).

Cardiac maturation

Studies have shown that disruption of desmin and mitochondria can induce heart maturity defects (Capetanaki et al., 2015; H. Liu et al., 2023). Thus, three genes associated with cardiac maturation were also studied (Figure 31). MYH6, a gene encoding a myosin isoform, is mainly expressed in immature native cardiomyocytes (Machiraju & Greenway, 2019). In contrast, MYH7 is a gene that codes for an isoform of myosin protein and is expressed in mature, adult cardiomyocytes (Machiraju & Greenway, 2019). Interestingly, MYH6 expression is significantly higher in the EHM of *DES*^{E439K} patients than in control EHM. MYH7 expression was significantly higher in control EHM than in patient 1 *DES*^{E439K} EHM. Next, the expression of PLN encoding the phospholamban protein that is expressed in mature cardiomyocytes was also interrogated. PLN expression was significantly higher in control 1 EHM than in patient 1 *DES*^{E439K} and patient 2 *DES*^{E439K} EHM (Figure 31). These results suggest that cardiomyocytes in *DES*^{E439K} EHM were less mature than those in control EHM. Given that the production of the different cardiomyocytes was strictly identical, it can be assumed that the *DES*^{E439K} mutation is responsible for this defect in cardiac maturity. In fact, it can be a pathological phenotype. Indeed, it has been shown that a DCM context there is a re-expression of the foetal gene program (Mehdiabadi et al., 2022).

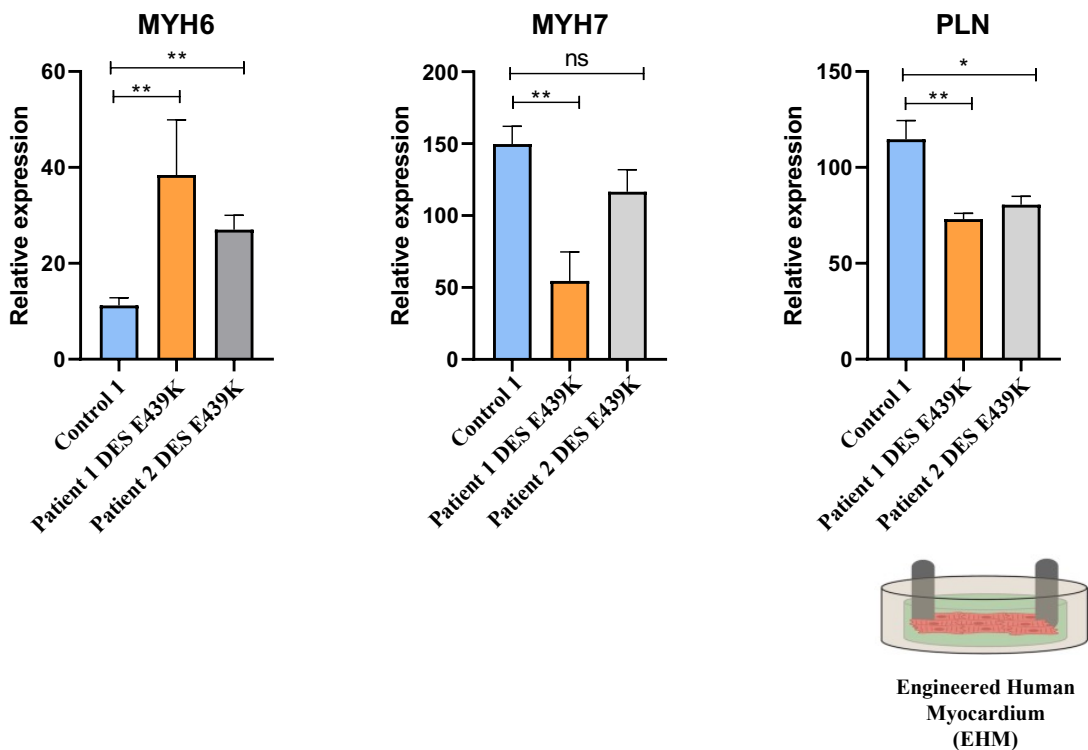


Figure 31 : Relative expression of cardiac maturation genes measured by RT-qPCR in EHM (Control 1; Patient 1 DES^{E439K}; Patient 2 DES^{E439K}). A two-tailed t-test was performed. ns not significant. * p-value<0.05 ** p-value<0.005.

In conclusion, it has been shown based on *in vitro* DCM models that the DES^{E439K} mutation encoding the desmin protein is responsible for a defect in cardiac contraction, mitochondrial respiration alteration associated with oxidative stress, desmin aggregation linked with PQC response and cardiac immaturity. Firstly, these disturbances are already reported in the literature related to desminopathy associated with DCM, indicating that these models seem relevant for modelling this disease (Brodehl et al., 2018; Capetanaki et al., 2015; Clemen et al., 2013; S. Singh et al., 2020). Secondly, it seems also relevant to use this knowledge of pathophysiological mechanisms to further investigate and better describe the establishment of the pathology, as well as to identify therapeutic approaches. More and more studies are in the field of drug discovery for the research of new therapeutic leads, are turning, in particular, to the high content imaging phenotypic screening assay (Pegoraro & Misteli, 2017). These methods can be used to describe disease phenotypes based on cell profiling using immunostaining and confocal microscope image acquisition. In addition, the use of annotated compounds for screening enables the identification of therapeutic pathways (Brodin et al., 2015). Knowledge of the compounds mechanisms of action can be

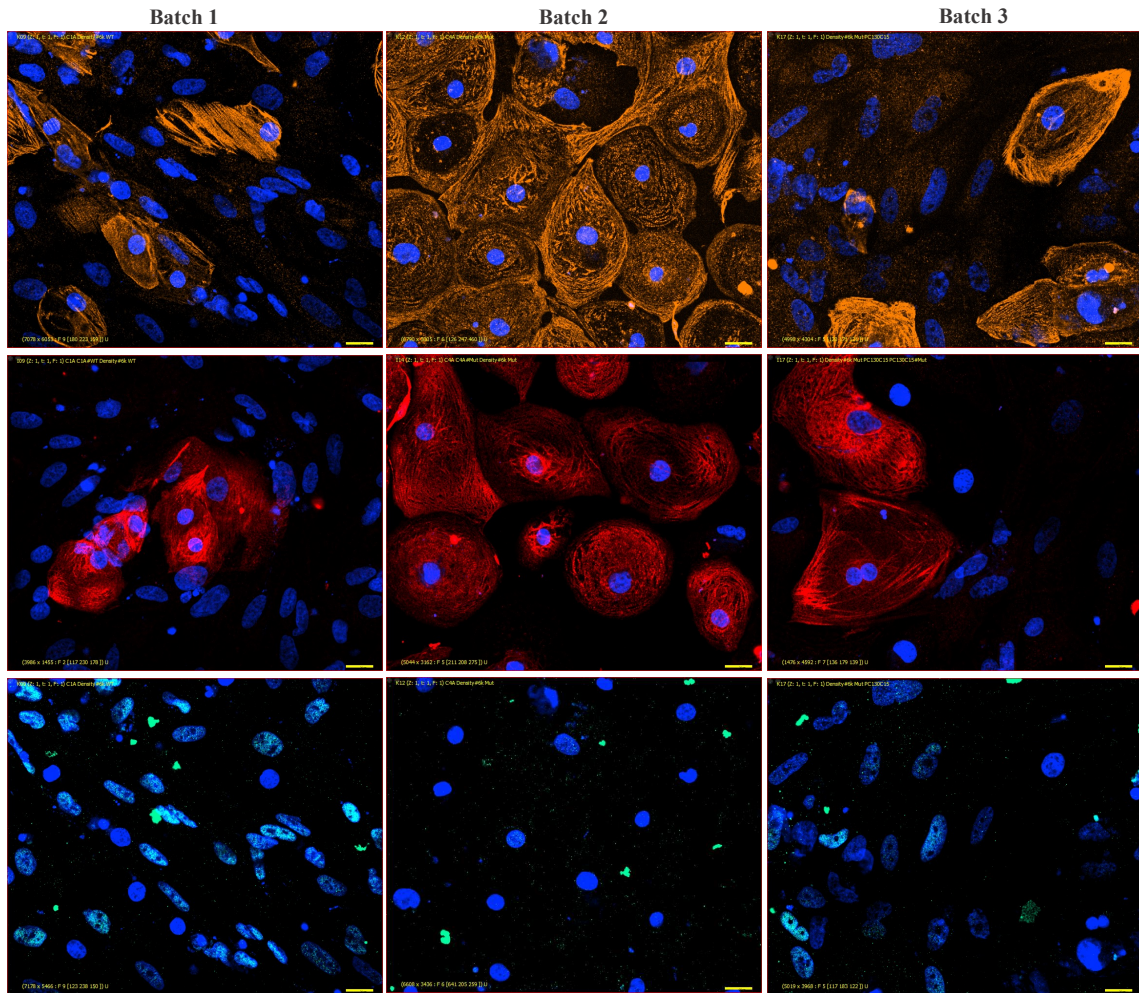
used to deduce the specific signaling pathways involved in phenotype establishment (Reisen et al., 2015).

IV.3. Optimization of iPSC-CM modeling dilated cardiomyopathy caused by *DES*^{E439K} mutations for High content imaging

IV.3.1. Developing cell imaging tools on 384 well plate

Development of a quality control process

Prior to setting up a high content imaging assay, as previously shown, iPSC were differentiated into iPSC-CM using different protocols. Although perfectly handled by the laboratory, iPSC-CM production is not exempt from inter-batch variability which can be attributed, non-exhaustively, to differences in terms of purity, state of maturation or proportion of iPSC-CM sub-types. It is important to limit this variability as much as possible to ensure the quality of future research. Thus, a quality control process for iPSC-CM batches has been set up. After the differentiation process described previously (III.1.2), iPSC-CM were thawed in 384-well plates and cultured for 3 to 6 days. It is generally the time necessary to allow sufficient time for the cells to recover from the thawing phase, as this is determined by the reappearance of cell contraction. It is also important to ensure that cardiomyocyte purity in culture, is not affected by the 384-well plate culture, which is essential for high content imaging. This is why quality control must be carried out in this type of culture plate. Following culture, the cells were fixed and immunocytostained (Figure 32). Staining for cardiac troponin T (cTnT), a sarcomeric protein specifically expressed in cardiomyocytes, was used to identify cardiomyocyte purity in a batch (Figure 32). Subsequently, markers to identify the proportions of different subtypes were selected. MYL2 is a contractile protein specifically expressed in ventricular cardiomyocyte and was selected to detect this subtype of cardiomyocytes. NR2F2, also known as COUP-TFII, is a transcription factor whose expression induces differentiation into atrial cardiomyocytes during development (Jiuru Li et al., 2022).



cTnT (iPSC-CM purity)

MYL2 (Ventricular iPSC-CM)

NR2F2 (Atrial iPSC-CM)

Figure 32 :Immunocytostaining of iPSC-CM batches with specific iPSC-CM marker (cTnT; MYL2; NR2F2). Scale bar = 10μm

Firstly, the identification of nuclei is based on the intensity and shape characteristics of the hoechst (DNA staining) signal (Figure 33). The signal thresholding parameters for distinguishing the signal of interest from the background have been determined manually. An example of three iPSC-CM batches in which plating efficiency has been determined is given on (Figure 33A). The images are binarized according to previously determined thresholds. To simplify analysis of the various images, segmentation of the single cells was carried out using the cropping method, where the region of interest (ROI) representing a cell is assumed to lie within a 256x216 pixel rectangle centered on its nucleus. In this way, each pink square represents a ROI that will enable us to perform single-cell analyses later in the procedure. The plating efficiency was determined by the ratio between the number

of nuclei counted in a well and the number of cells initially seeded during thawing (Figure 33B). Plating efficiency varied from batch to batch, with batches showing plating efficiency above 30% being accepted. Plating efficiency is not an eliminatory criteria for batch validation; this information enables better control of culture densities during experiments.

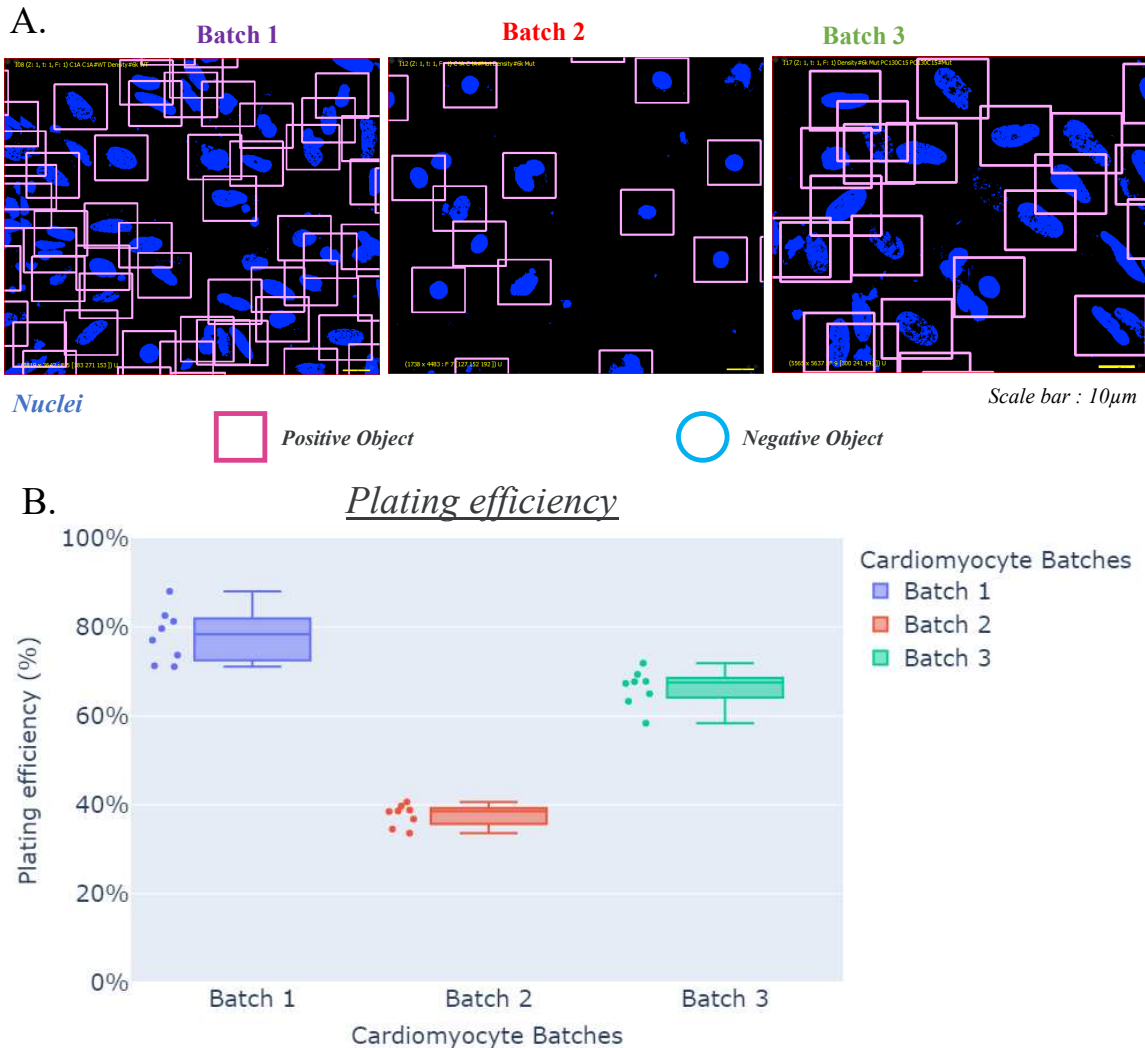


Figure 33 : Analysis of plating efficiency from different iPSC-CM batches. A. Immunocytostaing of cells nuclei based on hoechst staining. Pink square = positif object. Blue circle = negative object. Scale bar = 10 μ m. B. Quantification of plating efficiency depending of iPSC-CM batches. Values are expressed as mean \pm standard deviation of n= 8 technical replicates

In order to identify the iPSC-CM purity of a given batch, an analysis based on cTnT staining was conducted (Figure 34). The percentage of ROI surface area showing cTnT signal was calculated and a threshold was set. Cells above the threshold were considered to be iPSC-CM (visualized with the pink squares) (Figure 34A). Here, Batch 2 presented an acceptable purity of around 80%, while batches 1 and 3 presented iPSC-CM purities of less than 20% and were therefore invalidated (Figure 34B).

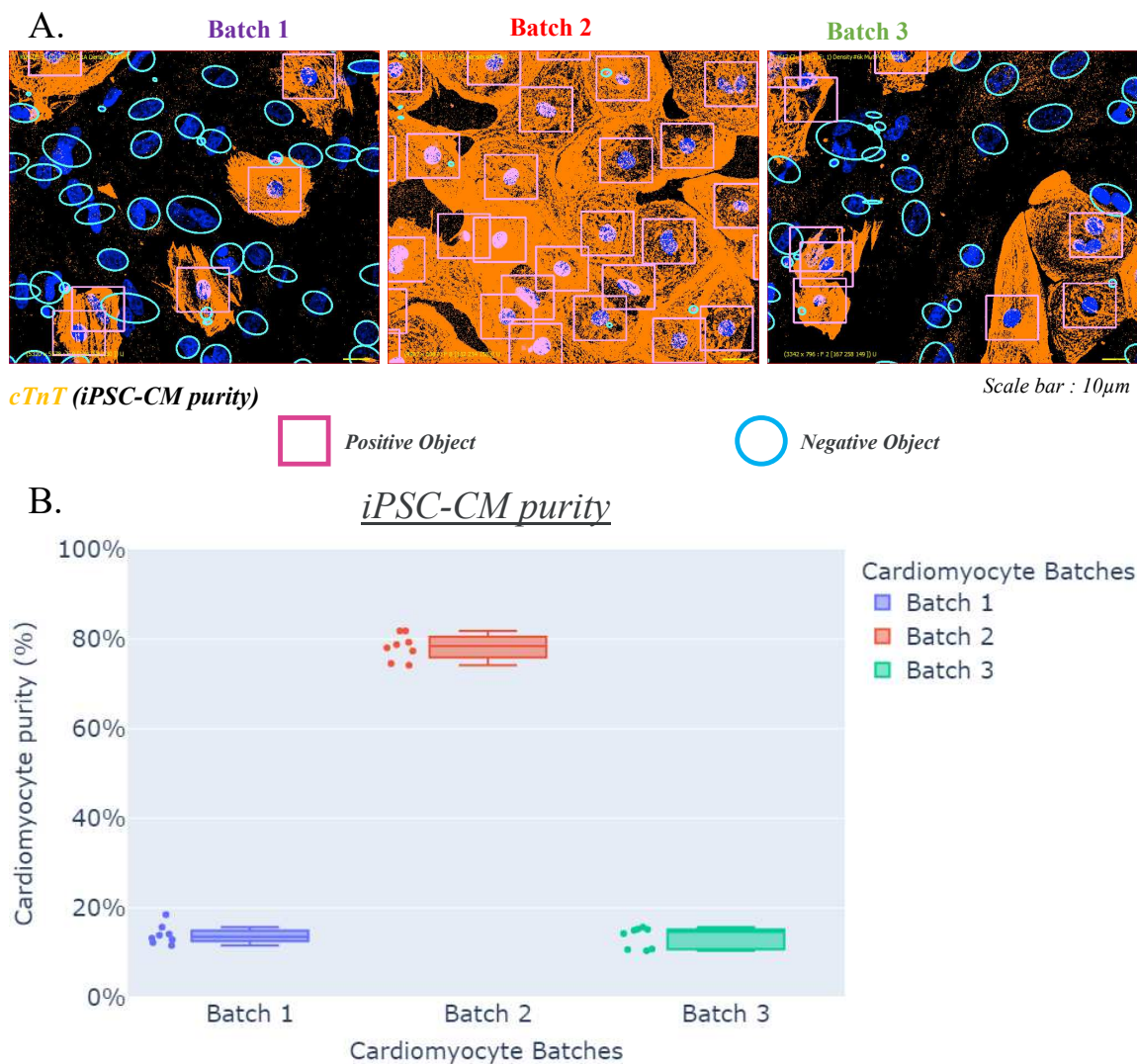


Figure 34 : Analysis of iPSC-CM purity from different iPSC-CM batches. A. Immunocytostaining of iPSC-CM based on cTnT staining. Pink square = positif object. Blue circle = negative object. Scale bar 10μm. B. Quantification of iPSC-CM purity depending of iPSC-CM batches. Values are expressed as mean ± standard deviation of n= 8 technical replicates

Quality control was pursued with a study of iPSC-CM subpopulations. Indeed, there are different types of cardiac muscle cells, notably ventricular and atrial iPSC-CM. Because DCM affects primarily the ventricles, the study was designed to study mainly ventricular iPSC-CM. Thus, the markers MYL2 for ventricular and NR2F2 for atrial iPSC-CM were used to characterize the subpopulations (Figure 35;Figure 36). Here, 3 different iPSC-CM batches were investigated on the basis of microscope images. Using the same analysis procedure as before, the nuclei were first identified in order to determine the ROIs and perform an analysis at single cell level. Thus, after defining the thresholds of the signals of interest above which a cell was considered positive for a given marker (MYL2 or NR2F2), it was possible to identify positive (pink square) or negative (blue circle) cells for a given

marker (Figure 35A;Figure 36A). By normalizing the number of cells positive for a marker (MYL2 or NR2F2) by the total number of cells identified in a batch, the percentages of ventricular cells (positive staining MYL2) per batch (Figure 35B) and the percentage of atrial cells (positive staining NR2F2) per batch (Figure 36B) were determined. The percentage of MYL2-positive iPSC-CM was less than 20% for batches 1 and 3, and only 30% for batch 2 (Figure 35A). The low rate of ventricular marker-positive iPSC-CM may also be due to the immaturity of the iPSC-CM, which express progressively the MYL2 marker during the differentiation of iPSC-CM (Bizy et al., 2013).

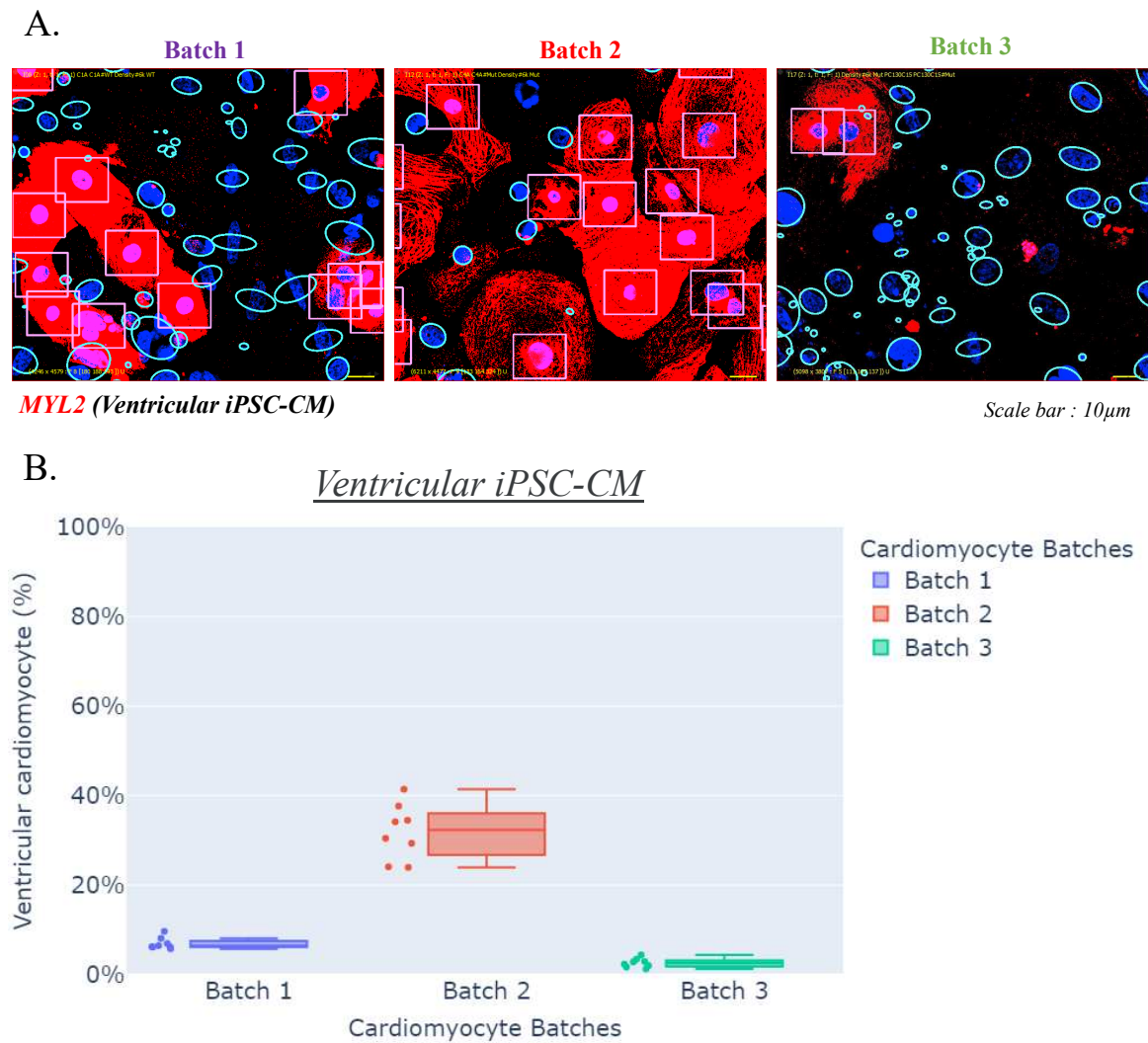


Figure 35 : Analysis of ventricular iPSC-CM proportion from different batches staining. A. Immunocytostaining of ventricular iPSC-CM based on MYL2 staining. Pink square = positif object. Blue circle = negative object. Scale bar 10 μ m. B. Quantification of ventricular iPSC-CM proportion depending of iPSC-CM batches. Values are expressed as mean \pm standard deviation of n= 8 technical replicates

Secondly, the rate of iPSC-CM positive for atrial staining was 80% in batch 1 and 40% in batch 3 (Figure 36B). As these batches have a fairly low iPSC-CM purity (Figure

34), it is surprising to find such high rates for atrial staining. Indeed, it was expected that the NR2F2 marker would be specific to atrial-iPSC-CM, but these results seem to indicate that other non-iPSC-CM cells, which are not positive for cTnT staining, may express NR2F2. Thus, NR2F2 staining does not appear to be specific to atrial cells alone. Moreover, some cells were negative for the two markers MYL2 and NRF2F2 but positive for cTnT. These cells were probably cardiac progenitors too immature to express the specific marker of a ventricular or atrial iPSC-CM.

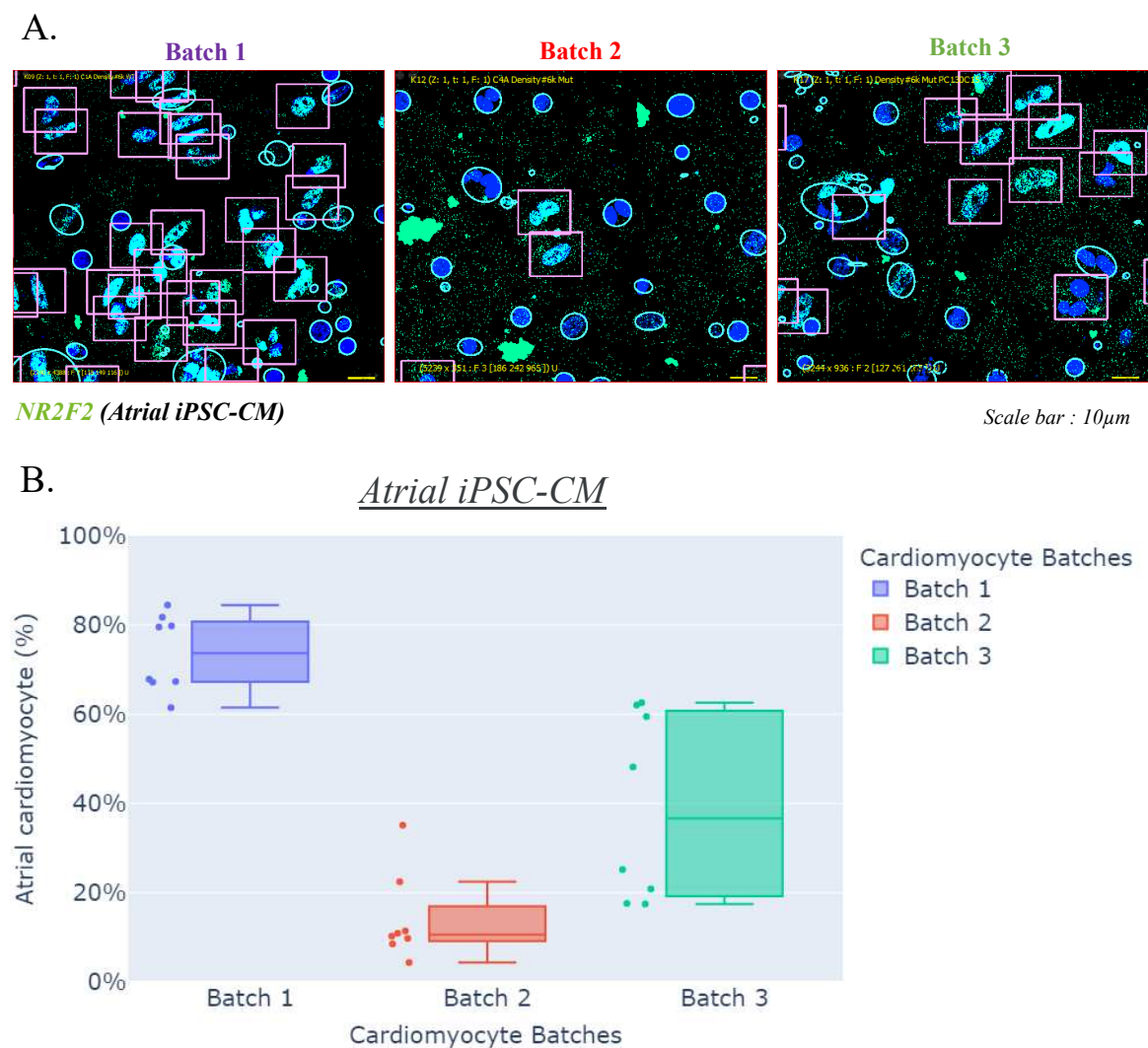


Figure 36 : Analysis of atrial iPSC-CM proportion from different batches. A. Immunocytostaining of atrial iPSC-CM based on NR2F2 staining. Pink square = positif object. Blue circle = negative object. Scale bar 10 μ m. B. Quantification of ventricular iPSC-CM proportion depending of iPSC-CM batches. Values are expressed as mean \pm standard deviation of n= 8 technical replicates

IV.3.2. Optimization Cell culture condition on 384 well plate format

Despite the fidelity of the iPSC-CM cell model to the *in vivo* cardiomyocytes present in the organism, it has been shown that these iPSC-CM present neonatal

cardiomyocyte characteristics (Vučković et al., 2022). Particularly in terms of desmin expression, which is expressed very early in development, and increases progressively over time (Tsikitis et al., 2018). Thus, to optimize the pathology modeling, iPSC-CM need to be as close as possible to adult cardiomyocytes. Two strategies for optimizing iPSC-CM cell culture were considered to induce cell maturation and, in particular, increased desmin expression. The two parameters tested were the composition of the culture medium and the duration of culture.

Phenotypic differences depending on culture medium

The aim was therefore to induce cardiac maturation in order to optimize the structural phenotype of iPSC-CM, notably at the level of desmin expression. The use of biochemical factor treatments is a strategy that has been highlighted in a number of studies (Machiraju & Greenway, 2019). Two treatments have been selected for this study based on literature (Birket et al., 2015) and previous work from the laboratory (Hovhannisyan et al., 2023). The "T3+Dex" culture medium, containing Thyroid and glucocorticoid hormones in RPMI+B27 was shown to be critical for cardiac maturation (Ming Li et al., 2014),(Rog-Zielinska et al., 2015). Indeed, many studies have shown that the combination of the thyroid hormone triiodothyronine (T3) and the glucocorticoid dexamethasone (Dex) enables the maturation of iPSC-CM, and in particular of structures that are important for the function of these cells and the development of T-tubules (Parikh et al., 2017) or structures involved in electrophysiological function (L. Wang et al., 2021). Finally, another method to strongly induce iPSC-CM maturation consists to provide oxidative substrates adapted to the metabolic needs of the iPSC-CM (X. Yang et al., 2019). During the first moment after birth, cardiomyocyte progenitors switch from glycolytic to oxidative metabolism to support the energy demands of functional aspect (Gaspar et al., 2014). This last medium was named "Maturation medium" and was composed with AlbuMAX that retained the rich composition of RPMI/B27 and was adapted to physiological needs of iPSC-CM. This medium was also formulated with a higher Ca^{2+} concentration for iPSC-CM contractility, a lower glucose concentration to promote fatty acid oxidation and supplementation with creatine, L-carnitine, and taurine to support iPSC-CM energetics in comparison with the classical medium for iPSC-CM (Feyen et al., 2020). As control condition, the classical cell culture medium composed of RPMI+B27 used for iPSC-CM (Laco et al., 2020) was used and named "Classic medium". This study was performed on 3 iPSC-CM (Isogenic Control, Isogenic *DES* ^{E439K}, Patient *DES* ^{E439K}). After thawing, the different culture media were

applied to the cells for 20 days, with renewal every two days. Then, the cells were fixed for immunocytostaining with desmin staining (Figure 37).

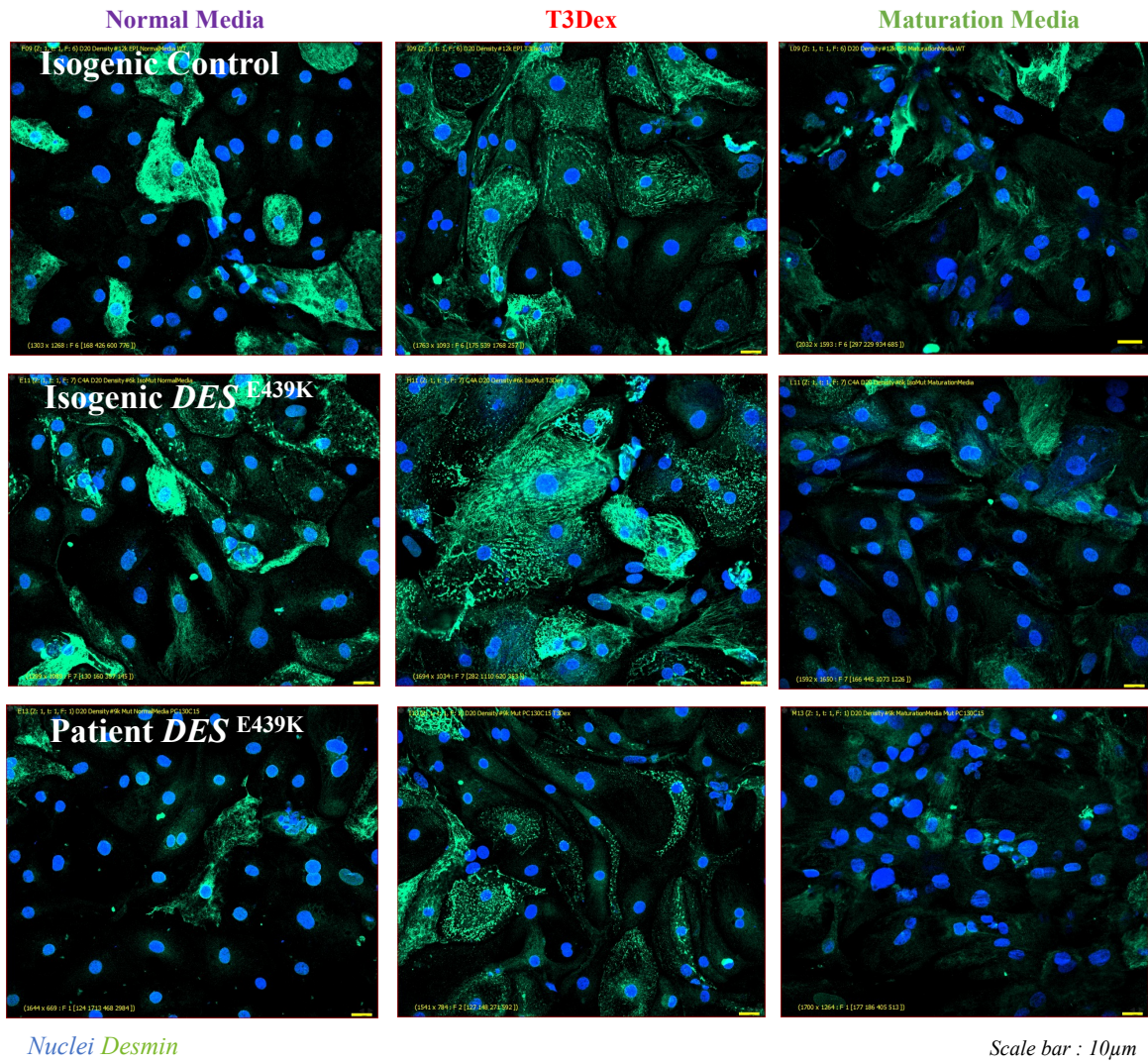
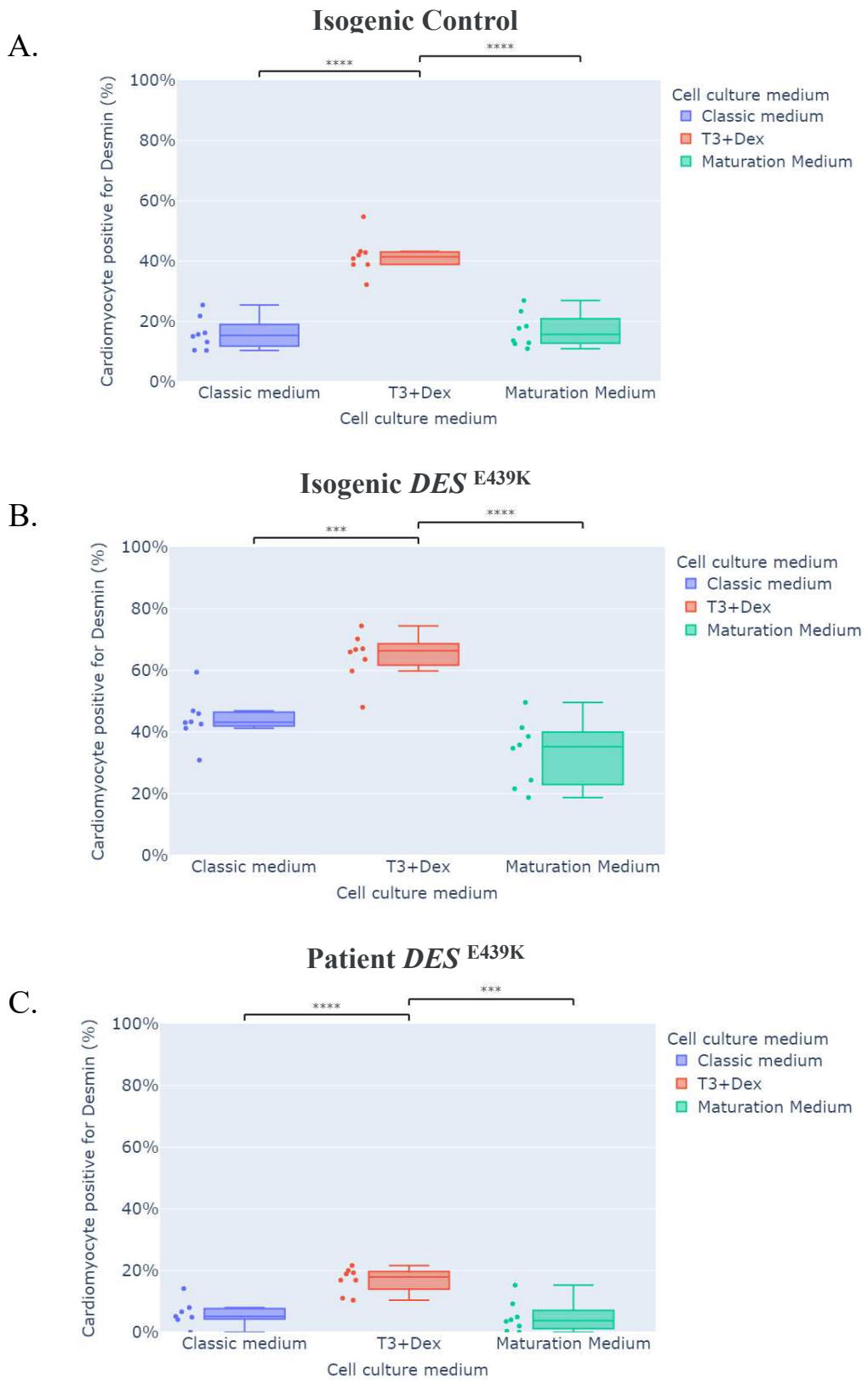


Figure 37 : Immunocytostaining with desmin staining on different iPSC-CM (Isogenic Control; Isogenic DES ^{E439K}; Patient DES ^{E439K}) cultures in different culture medium (Normal Media; T3Dex; Maturation Media). Scale bar = 10μm.

The desmin phenotype was chosen because the mutation studied is located on the gene coding (*DES*) for this protein. It was therefore important to have acceptable desmin expression for the subsequent studies. The efficacy of the treatment was assessed by the proportion of desmin-positive iPSC-CM in the different iPSC-CM (Figure 38). In all the different cell culture groups, desmin appeared to be increased more in the "T3 Dex" condition (Figure 38 A; B; C). As a result, this condition was selected for subsequent work.



*Figure 38 : Identification of the percentage of Desmin staining-positive in different iPSC-CM (A- Isogenic Control; B-Isogenic DES E439K; C-Patient DES E439K) depending on the culture medium (Normal Media; T3Dex; Maturation Media). Values are expressed as mean ± standard deviation of n= 8 technical replicates. A two-tailed t-test was performed. ns not significant. * p-value<0.05 ** p-value<0.005. *** p-value<0.0005. **** p-value<0.00005*

Phenotypic differences depending on cell culture time

Culture time is also an important factor in ensuring iPSC-CM maturity. Indeed, iPSC-CM derived from iPSCs after 20 days of differentiation display characteristics of progenitor iPSC-CM (Denning et al., 2016). The expression of desmin protein is relatively low in these cells, and vimentin protein is found instead, which mainly plays the role of cytoskeletal proteins in the early stages (Tsikitis et al., 2018). It is only after some time that desmin expression increases and this protein progressively assumes its role as an intermediate filament. Because the patient developed DCM due to a mutation in *DES*. It was interesting to study desmin expression at different times in our iPSC-CM culture (Figure 39). Two conditions were implemented: 10 days (D10) or 20 days (D20) of culture after thawing. Again three iPSC-CM were used (Figure 39A; B; C): Isogenic Control, Isogenic *DES*^{E439K}, and Patient 2 *DES*^{E439K}. These iPSC-CM were cultured in T3+DEX culture medium, which was renewed every two days. After the culture, the cells were fixed for immunocytostaining with desmin staining (Figure 39).

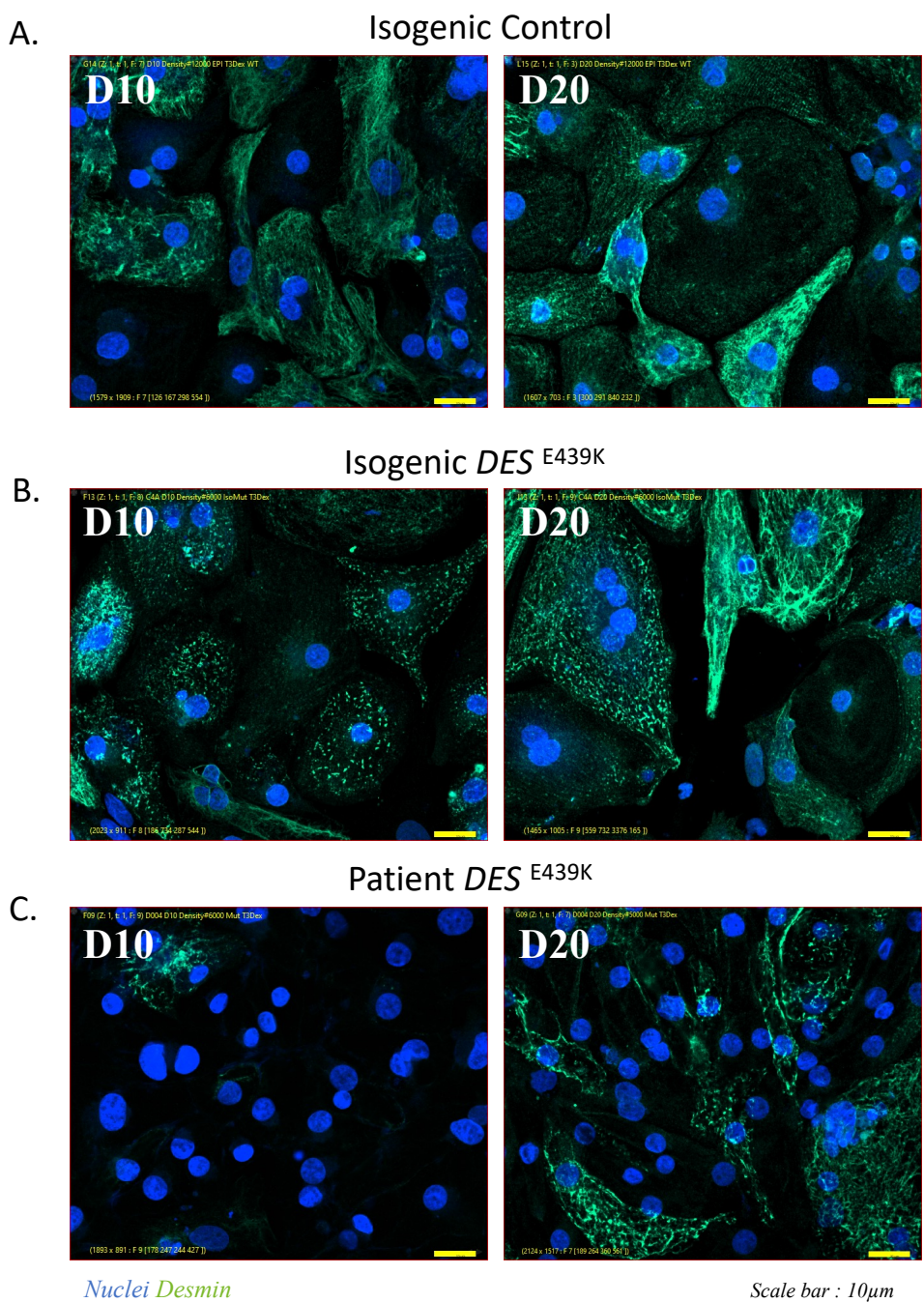


Figure 39 : Immunocytostaining with desmin staining of iPSC-CM culture D10 or D20 in different (A-Isogenic Control; B-Isogenic *DES*^{E439K}; C-Patient *DES*^{E439K}). Scale bar=10µm

The percentage of desmin-positive iPSC-CM was significantly higher at D20 than at D10 in all cell lines. Yet, the difference in desmin staining between D10 and D20 varied from line to line, with a more pronounced difference in patient 2 *DES*^{E439K} (Figure 40). Interestingly, the isogenic *DES*^{E439K} line shows a proportion of desmin-positive iPSC-CM of already 50% at D10.

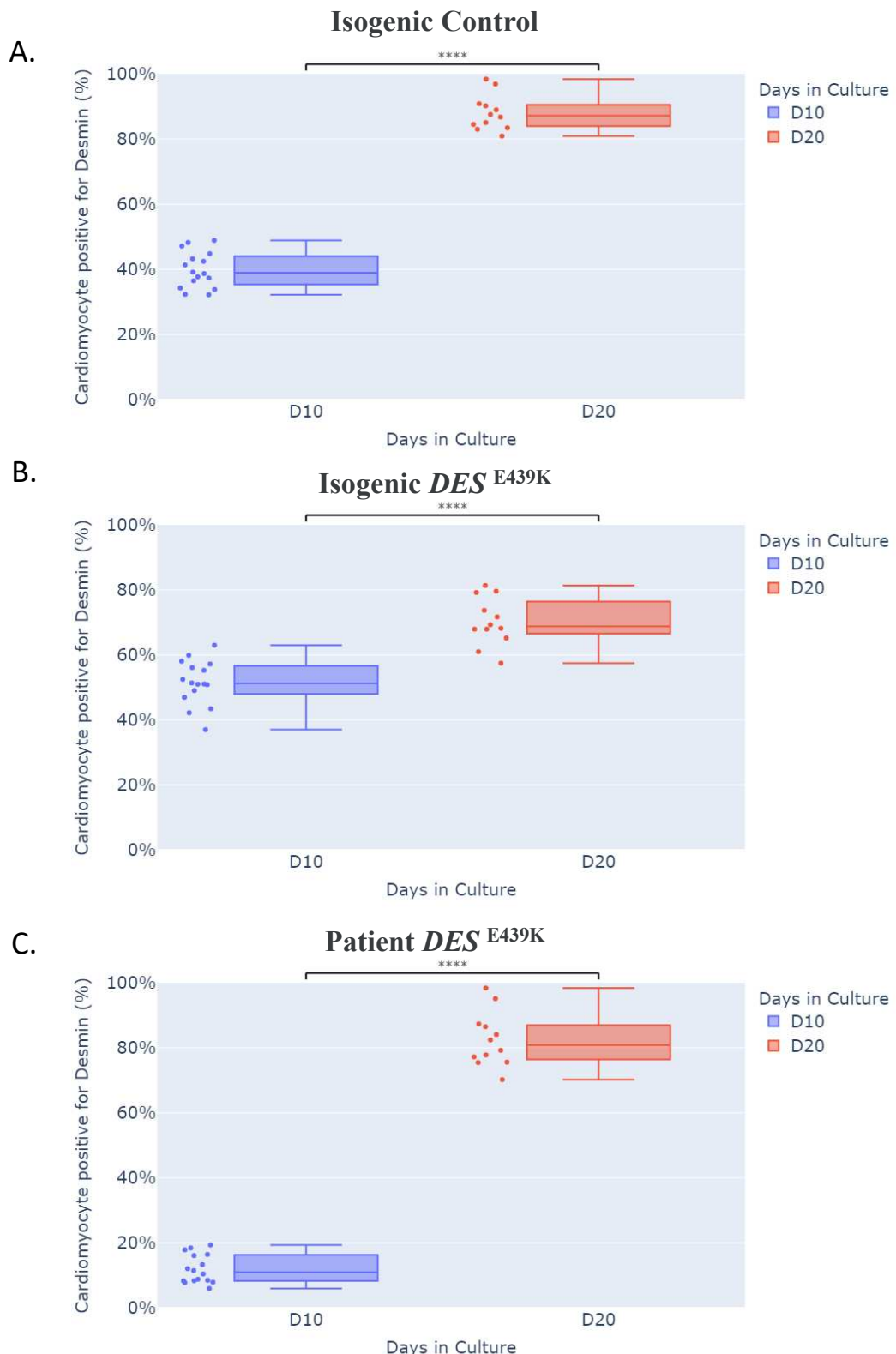


Figure 40 : Identification of the percentage of Desmin staining-positive iPSC-CM depending on the culture duration by days (D10; D20) in different cell lines (A-Isogenic Control; B-Isogenic DES ^{E439K}; C-Patient DES ^{E439K}). Values are expressed as mean ± standard deviation of n= 6 technical replicates from two experiments. A two-tailed t-test was performed. ns not significant. * p-value<0.05 ** p-value<0.005. *** p-value<0.0005. **** p-value<0.0005

IV.4. Implementation of a high-content imaging assay for screening

IV.4.1. Read out identification

As previously described, DCM associated with a desmin mutation (DES^{E439K} mutation) is characterized at the cellular level by a loss of the three-dimensional desmin network associated with protein aggregation. This disruption leads to sarcomeric disorganization and mitochondrial alteration (Hovhannisyan et al., 2023). Following the optimization of the iPSC-CM model, it was interesting to identify and study the disruptions associated with DCM in this model. Using immunocytostaining and confocal microscope image acquisition, it was possible to perform quantitative and qualitative analyses of the cellular structures of interest (Desmin, Sarcomere, Mitochondria). This allowed the morphological phenotype of iPSC-CM to be identified. The following study compared the morphological phenotypes of different groups of iPSC-CM:

- The "Control" group derived from healthy patients with no DCM
- The "Isogenic DES^{E439K} " group derived from control iPSC lines gene-edited (CRISPR-CAS9) for integration of the DES^{E439K} mutation into the cell genome
- The "Patient DES^{E439K} " group derived from patients with DCM due to the DES^{E439K} mutation

The goal of this work was to ensure that the iPSC-CM model was able to reproduce the morphological phenotypes associated with DCM due to a desmin mutation. In addition, the results of this study were also a first step in setting up a high-content imaging assay. This first step is known as "read-out identification", and consists in identifying the phenotypes that will subsequently be used to perform the assay. In fact, a high content imaging assay will enable to characterize, quantify the phenotypic properties, and to identify compounds capable of correcting pathological phenotypes.

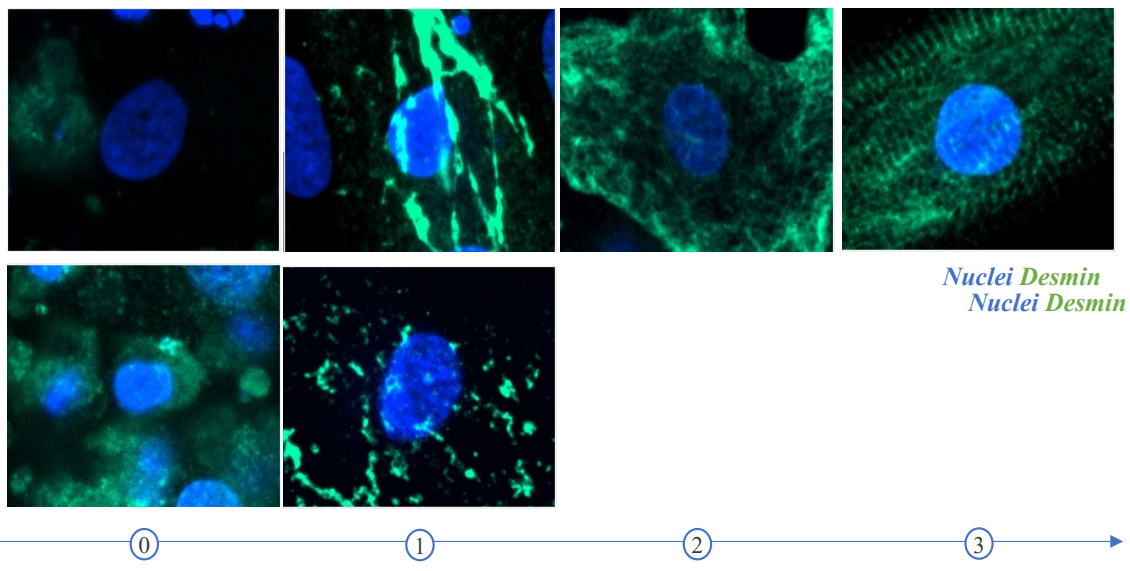
Desmin Annotated score

Firstly, a large number of desmin mutations are described as inducing a change in protein conformation that can lead to the rupture of the desmin network and/or to aggregates formation. To study this phenotype, three iPSC-CM groups (Control 2, Isogenic DES^{E439K} , Patient 1 DES^{E439K}) were cultured for 14 days in T3 Dex culture medium. After immunocytostaining and confocal image acquisition, the analysis strategy was based on manual annotation of each cell of a iPSC-CM group, indicating a score based on the

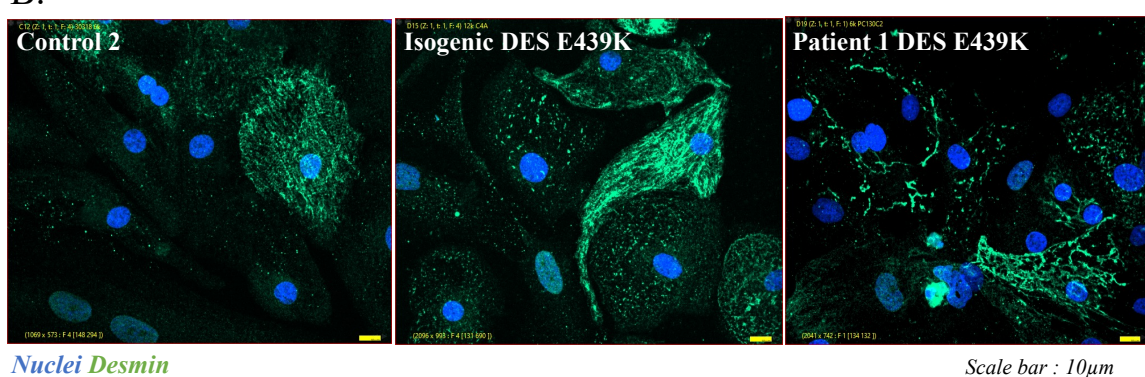
appearance and organization of the desmin staining (Figure 41A). Thus, when, in a single cell image, the desmin signal was predominantly in areas where the intensity appeared to be higher due to dense accumulation of desmin, probably indicating desmin aggregation, the single cell image was annotated as belonging to class 1. Class 1 was associated with single cells containing desmin aggregates. In some single cell images, the desmin signal appears diffused inside the cell, without forming clear patterns or organized structures. Fluorescence is homogeneously distributed in the image, with no indication of the formation of striated structures or distinct aggregates. This type of single cell was annotated class 2, these cells probably corresponded to cells in which desmin organization was less mature, in their early stages of three-dimensional network formation. Finally, some images of single cells showing a desmin signal were characterized by the presence of striated areas where a periodically higher signal intensity was observed, highlighting the concentration of desmin in specific regions. These cells were annotated class 3, the presence of striation testifying to the presence of organized structure which may be associated with the integrity of the desmin network and may be an indicator of cell maturity. Some single cell image were annotated score 0 and corresponded to cells with image artifact or a too weak signal, these iPSC-CM were not considered for the final analysis.

These different annotations were performed on immunocytostaining images of the following iPSC-CM: Control 2 (n=30); Isogenic *DES*^{E439K} (n=53); Patient 1 *DES*^{E439K} (n=35) (Figure 41B). Finally, the distribution of the different classes in each of the iPSC-CM was identified by indicating the frequency of annotation of each class in % within a given iPSC-CM (Figure 41D). Thus, it was observable that the control iPSC-CM has a class distribution tending towards classes 2 and 3 testifying to diffuse or striated desmin organization. On the contrary, for the iPSC-CM Isogenic *DES*^{E439K} and Patient 1 *DES*^{E439K}, their class distribution tended towards scores 1 and 2, reflecting aggregated or diffuse desmin organization. These data allow to deduce that iPSC-CM carrying a *DES*^{E439K} mutation (Isogenic or Patient) have desmin organization that tends towards aggregation. In contrast, the desmin organization of control iPSC-CM tends towards striation. It is also interesting to note the high proportion of iPSC-CM from the three iPSC-CM types in the class 2. Thus result may be explained by the intermediate level of maturity of this cell model where some iPSC-CM were in the early stages of three-dimensional network formation or before desmin aggregate accumulation.

A.



B.



C.

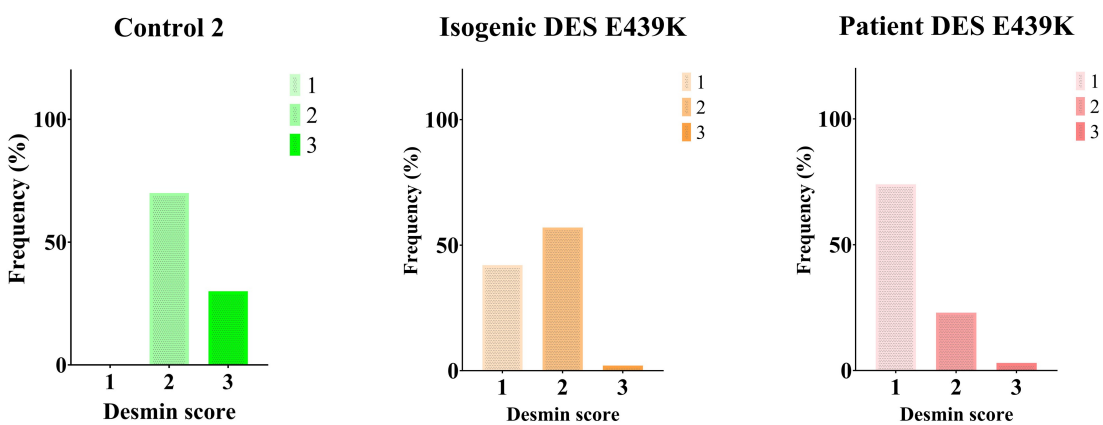
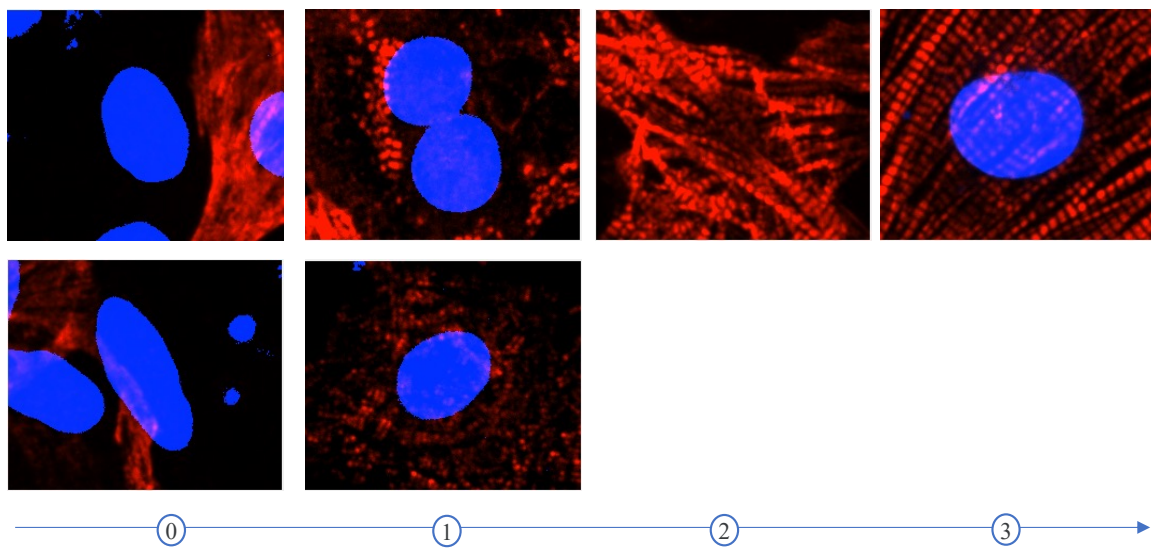


Figure 41 : Manual annotation of iPSC-CM according to desmin organization. A. Classification score of the iPSC-CM with 3 classes based on desmin organization from iPSC-CM stained with desmin. B. Immunocytostaining with desmin of iPSC-CM (Control 2; Isogenic DES^{E439K}; Patient DES^{E439K}). Scale bar=10μm. C. Frequency of distribution of the 3 classes in each iPSC-CM (Control 2; Isogenic DES^{E439K}; Patient DES^{E439K})

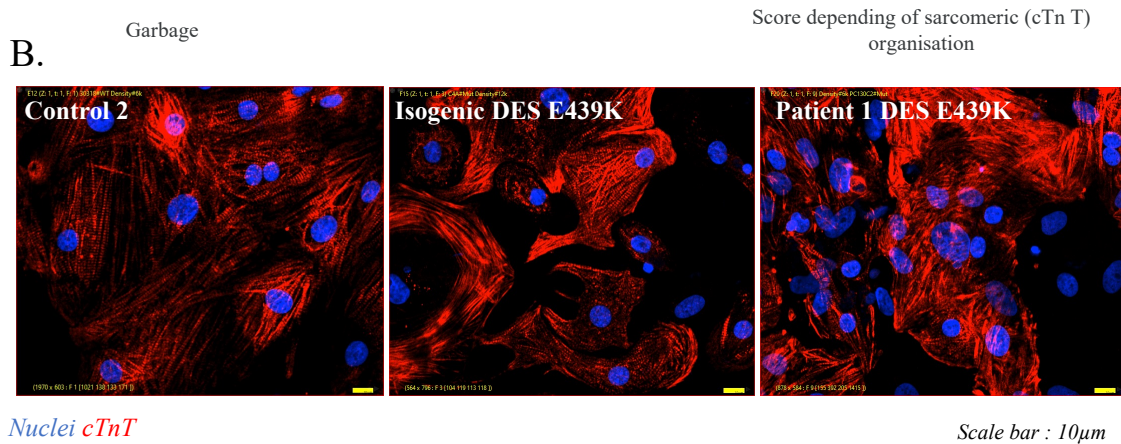
Cardiac troponin T annotated score

Secondly, it is interesting to study the sarcomeric phenotype that is described to be strongly impacted in a context of DCM (McNally EM, 2017). To this aim, the manual annotation strategy of iPSC-CM from different cell lines cultured for 14 days in T3 Dex medium was also used, relying on immunocytostaining of sarcomeric-type protein cTnT cardiac isoform. The annotation consisted in indicating a class 1 score when cTnT presented a disorganized, poorly striated appearance (Figure 42A). A class 2 score corresponded to iPSC-CM with striated sarcomeric fibers but not necessarily well aligned with each other. Score 3 reflected cells with striated and aligned sacromeric fibers. Finally, score 0 corresponded to images showing an artifact or with a cTnT signal too low to be interpreted. The annotations were performed on immunocytostaining images of the following iPSC-CM: Control 2; Isogenic *DES*^{E439K}; Patient 1 *DES*^{E439K}) (Figure 42B). Finally, by looking at the frequency of annotation of each class in % within a given iPSC-CM, it is possible to deduce the distribution trends of the different classes in each iPSC-CM (Figure 42C). The iPSC-CM Control 2 showed a distribution with a frequency spike in class 2, while the iPSC-CM carrying the *DES*^{E439K} mutation showed distributions with a frequency spike in class 1 (Figure 42D). This indicates that iPSC-CM Control will be more likely to develop striated sarcomeres than iPSC-CM carrying *DES*^{E439K}, which will develop less striated sarcomeres. It is interesting to note the low frequencies of distribution of class 3 (iPSC-CM displaying both striated and well-aligned sarcomeric fiber organization) in the different iPSC-CM groups. This phenomenon reflects the limitations of the cell model in terms of iPSC-CM maturity.

A.



B.



C.

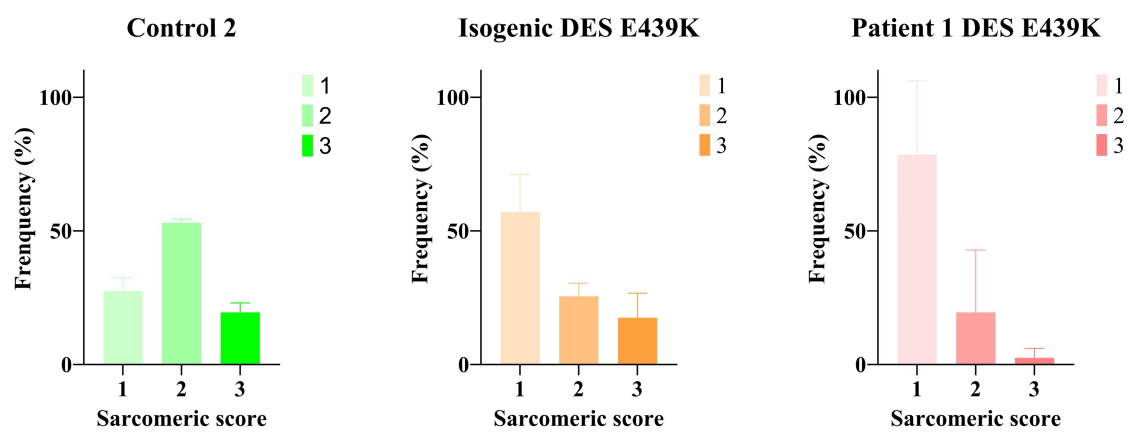
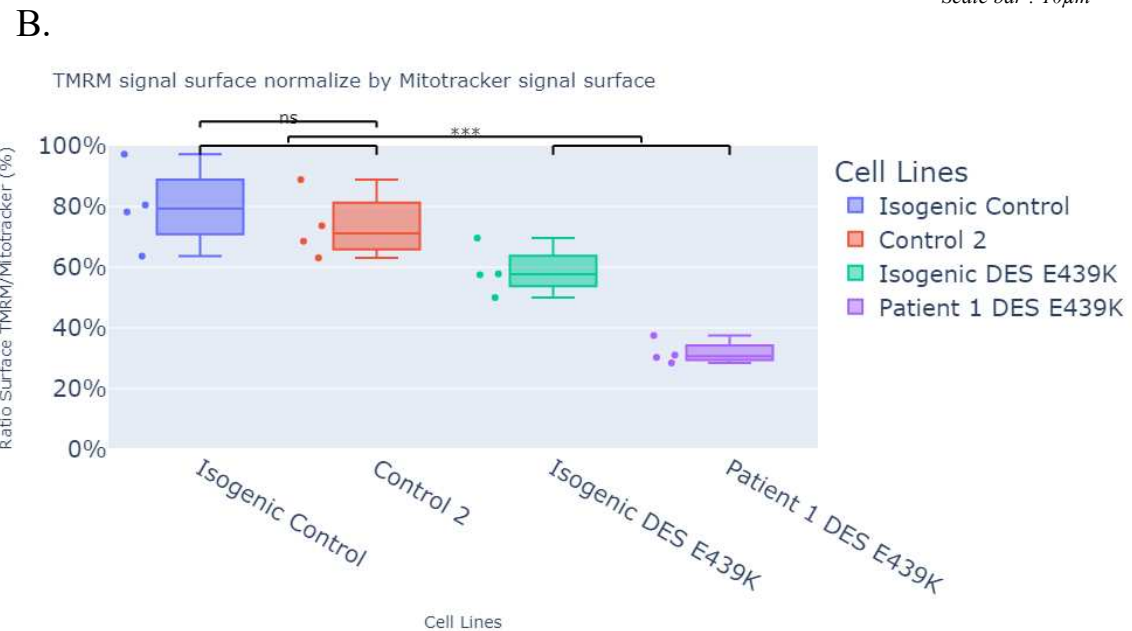
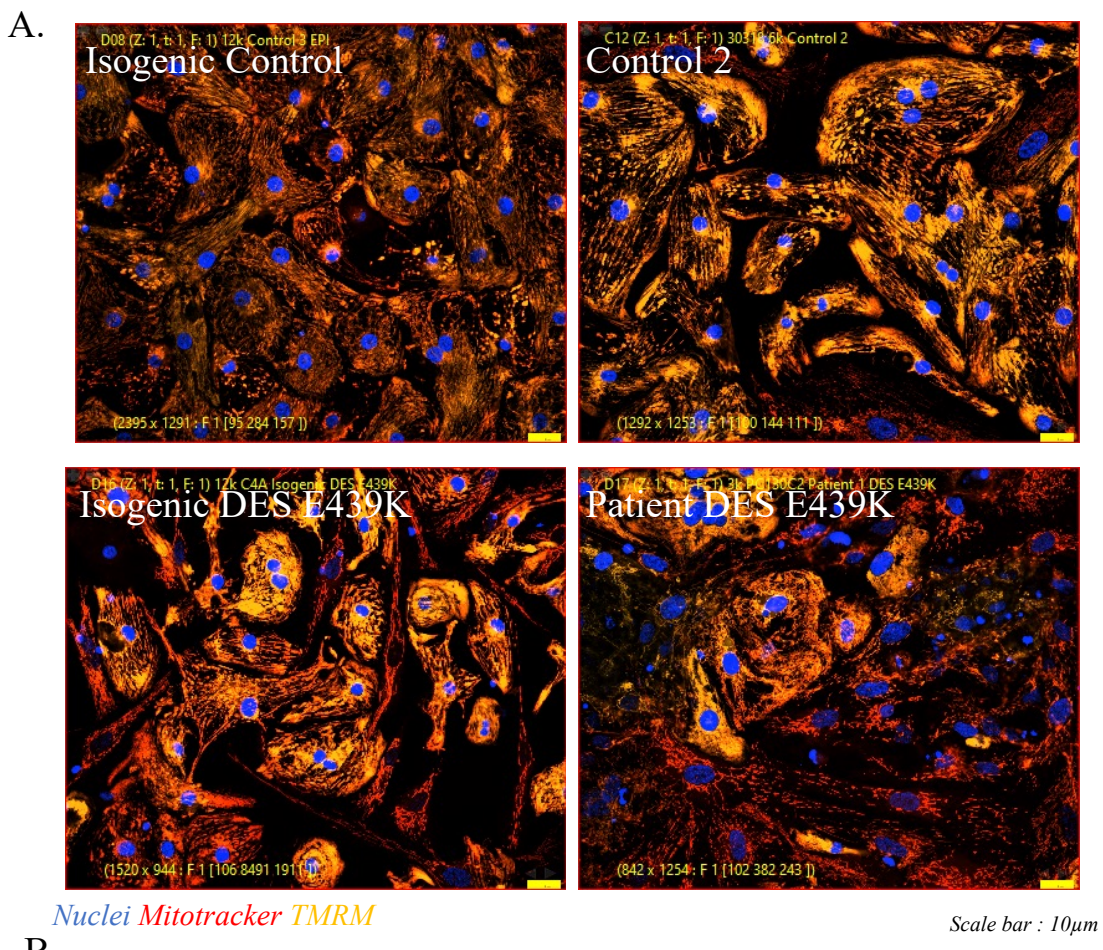


Figure 42 : Manual annotation of iPSC-CM according to sarcomere organization. A. Classification score of the iPSC-CM with 3 classes based on sarcomere organization from iPSC-CM stained with cTnT staining. B. Immunocytostaining of iPSC-CM (Control 2; Isogenic DES ^{E439K}; Patient DES ^{E439K}) with cTnT marker. Scale bar=10μm. C. Frequency of distribution of the 3 classes in each iPSC-CM (Control 2; Isogenic DES ^{E439K}; Patient 1 DES ^{E439K}). Values are expressed as mean ± standard deviation of n= 2 technical replicates

Mitochondria Assay (Ratio TMRM/Mitotracker)

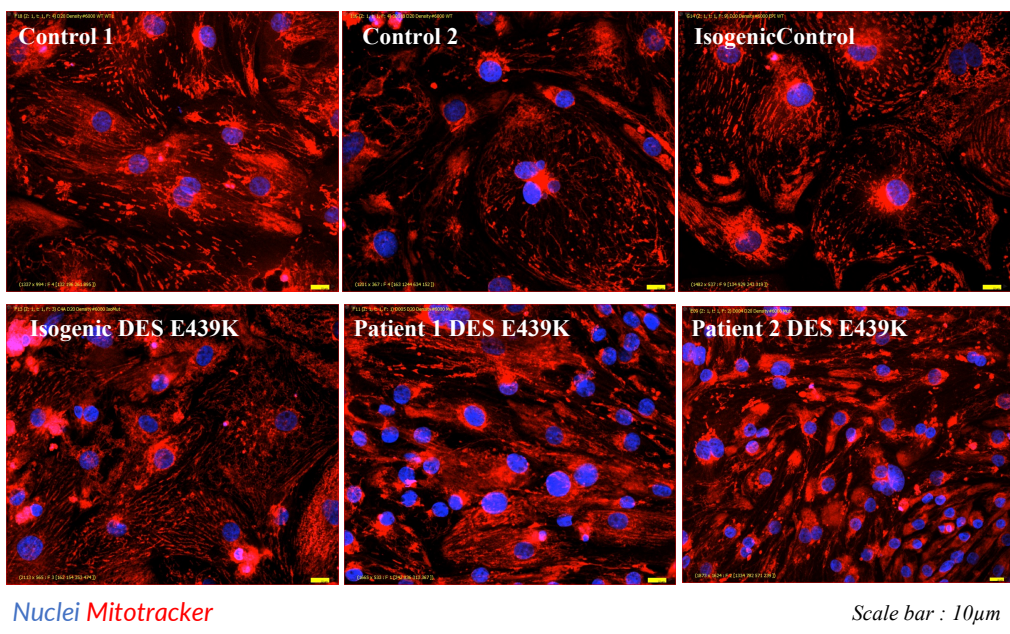
Finally, it has been demonstrated that the function of mitochondria is strongly affected in the context of DCM due to a mutation in the *DES* gene encoding desmin (Hovhannisyan et al., 2023). We could infer that the activity of mitochondria may also be affected and can be used as a marker of the disease in iPSC-CM. To verify this hypothesis, different iPSC-CM (Isogenic Control; Control 2; Isogenic *DES*^{E439K}; Patient 1 *DES*^{E439K}) were cultured for 14 days in T3 Dex culture medium (Figure 43). Cells were stained with TMRM, a mitochondrial marker that stains mitochondrial membrane potential when fairly high (Figure 43A). Thus, it is described that only active mitochondria are stained with this marker. iPSC-CM are also stained with Mitotracker, a mitochondrial marker that is less sensitive to mitochondrial membrane potential and will stain all the mitochondria present in the culture (Figure 43A). Analysis of the TMRM staining surface normalized by the Mitotracker staining surface enables us to deduce the percentage of active mitochondria in given iPSC-CM group (Figure 43B). The percentage of active mitochondria was found to be higher in control iPSC-CM (Isogenic Control and Control 2) than in iPSC-CM carrying the *DES*^{E439K} mutation (Isogenic *DES*^{E439K} and Patient *DES*^{E439K}). These data confirm that the *DES*^{E439K} mutation induced disruption of mitochondrial activity. Interestingly, the Isogenic *DES*^{E439K} iPSC-CM appears to have a higher percentage of active mitochondria than the Patient 1 *DES*^{E439K} iPSC-CM.



*Figure 43 :Mitochondria assay A. live staining of iPSC-CM (Isogenic Control; Control 2; Isogenic DES E439K; Patient 1 DES E439K) with TMRM and Mitotracker. Scale bar=10 μ m. B. Ratio Surface TMRM signal normalize by Mitotracker signal in different iPSC-CM groups. Values are expressed as mean \pm standard deviation of n= 4 technical replicates. A two-tailed t-test was performed. ns not significant. * p-value<0.05 ** p-value<0.005. *** p-value<0.0005*

To better characterize this initial observation on the mitochondrial phenotype, an experiment based on the culture of 6 iPSC-CM (Control 1; Control 2; Isogenic Control; Isogenic DES DES^{E439K} ; Patient 1 DES^{E439K} ; Patient 2 DES^{E439K}) cultured for 20 days in T3 Dex medium was conducted. Live staining of the different iPSC-CM was performed using Mitotracker (Figure 44A). After cell segmentation and based on variations in Mitotracker signal intensity, it was possible to count the number of mitochondria per cell in a given iPSC-CM (Figure 44B). The results showed that the number of mitochondria per iPSC-CM was significantly higher in control iPSC-CM (Control 1; Control 2; Isogenic Control) than in iPSC-CM carrying the DES^{E439K} mutation (Isogenic DES^{E439K} ; Patient 1 DES^{E439K} ; Patient 2 DES^{E439K}). These data suggest that the mitochondria content is affected due to the DES^{E439K} mutation that may be correlated to a possible disruption of the mitochondrial network. Once again, the Isogenic DES^{E439K} iPSC-CM appears to present an intermediate phenotype.

A.



B.

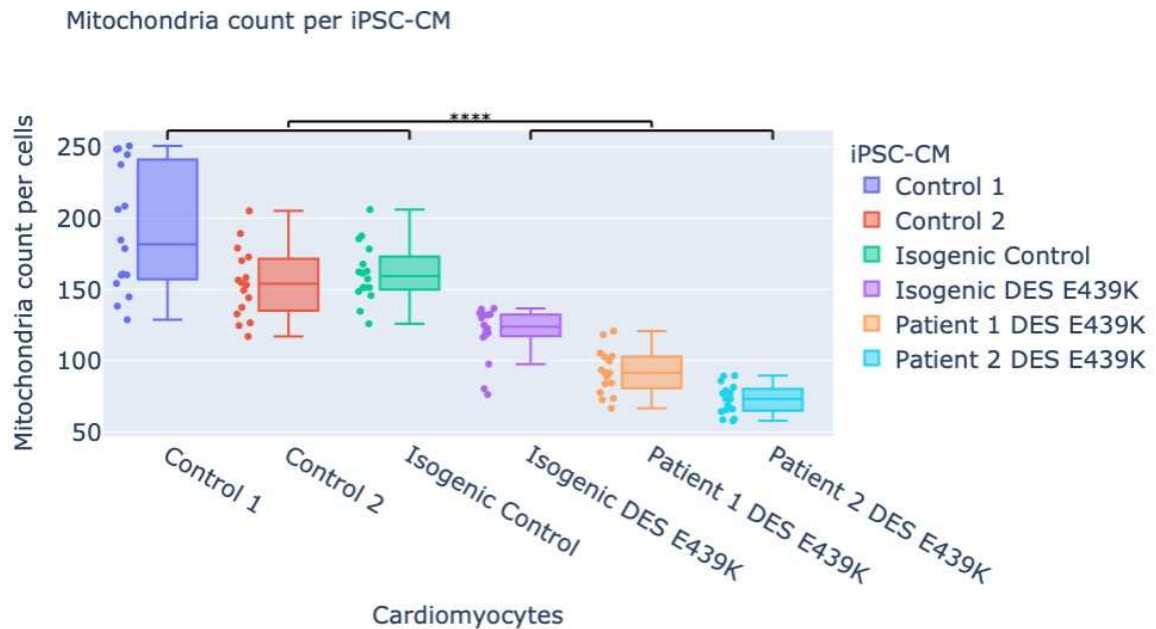


*Figure 44 : Analysis of mitochondria count per cells A. Live staining of iPSC-CM (Control 1; Control 2; Isogenic Control; Isogenic DES^{E439K}; Patient 1 DES^{E439K}; Patient 2 DES^{E439K}) with Mitotracker. B. Mitochondria count per cell for each iPSC-CM (Control 1; Control 2; Isogenic Control; Isogenic DES^{E439K}; Patient 1 DES^{E439K}; Patient 2 DES^{E439K}). Values are expressed as mean ± standard deviation of n= 16 technical replicates. A two-tailed t-test was performed. ns not significant. * p-value<0.05 ** p-value<0.005. *** p-value<0.0005. **** p-value<0.0005.*

In conclusion, several phenotypes were highlighted in the *in vitro* 2D iPSC-CM model of DCM associated with the DES^{E439K} mutation. Firstly, disorganization of the desmin network and the propensity to form desmin aggregates. Secondly, the sarcomeric disorganization visualized with the staining of the cardiac isoform of the sarcomeric protein

cTnT. Finally, the mitochondrial dysfunction on both the activity and the number of mitochondria was demonstrated.

These observations suggest that it would be possible to perform a phenotypic screening based on the subcellular organization of iPSC-CM carrying the *DES* ^{E439K} mutation in comparison with control iPSC-CM. Previous results had been generated manually or using single-parameter image analysis. As a first step, therefore, it was necessary to develop an automated image analysis model compatible with high-content imaging.

IV.4.2. Cell profiling classification model

Setting up a high content imaging requires the prior development of an automated image analysis model (Brodin et al., 2015). High content imaging relies on the acquisition of a large number of images using automated confocal microscopy. As phenotypic signatures can be very slight, the use of machine learning can be an interesting tool for measuring significant differences according to cell state in an automated way (Scheeder et al., 2018). Thus, based on the immunocytostaining of iPSC-CM with the staining of desmin, cTnT and Mitotracker a machine learning automated single-cell image analysis workflow was setting up. The objective was to develop a model capable of finely distinguishing control iPSC-CM and iPSC-CM carrying the *DES* ^{E439K} mutation.

Workflow

The first step is to segment the images to identify ROI corresponding to a single cell. The software uses the intensity levels and shape of the Hoechst nuclear staining to identify and label the nuclei present in the image. Then, the others staining, will be analyzed in the area surrounding the nucleus (ROI of 256x216 pixels that is subsequently called a crop). Within each crop it is possible to extract image characteristics associated with a value for each marker. These characteristics are called features, and allow us to quantify different aspects of the staining signal, such as intensity, shape or texture. This step is called feature extraction (Caicedo et al., 2017),(McQuin et al., 2018) and is performed using the phenolink software (developed by Ksilink) that can extract around 50 features per staining. By calculating the average of each feature for a given cell population and combining the different feature averages, the cellular profile of a iPSC-CM can be generated. In this way, the cellular profiles of control and mutant iPSC-CM groups were generated.

In order to generate a classification model with two classes: Control iPSC-CM cellular profile and *DES*^{E439K} iPSC-CM cellular profile, machine learning technology, and more specifically the Linear Discriminant Analysis (LDA) method, was implemented. LDA is a supervised machine learning technique used in classification and dimensionality reduction. The main objective of LDA is to determine a linear combination of features that maximizes the separation between different classes (inter-class variability) of data while minimizing the intra-class variability (Choubey et al., 2020). The advantage of a linear approach is the explicability of the feature combinations. This method is particularly useful for classifying data into pre-established groups (labels). The first phase, known as training set, involves the presentation to the algorithm of different cellular profiles labelled "control cellular profile" or "*DES*^{E439K} cellular profile", enabling the conceptualization of a two-class prediction model (control versus *DES*^{E439K}). This is followed by a "testing set" phase, in which known but unlabeled cellular profiles are presented to the models, with the aim of assessing their predictive power by looking at the results of its classification predictions, i.e. the percentages of true positives and false negatives (Gerbin et al., 2021a). The development of this classification tool was carried out on different iPSC-CM (Figure 45). Control iPSC-CM carrying no genetic mutation known to induce DCM (Control 1; Control 2; Isogenic control) and *DES*^{E439K} iPSC-CM carrying the *DES*^{E439K} mutation known to induce DCM (Isogenic *DES*^{E439K}; Patient 1 *DES*^{E439K}; Patient 2 *DES*^{E439K}) (Wahbi et al., 2012b) were used. Cells were grown for 20 days in T3 Dex culture medium (Figure 45).

Workflow

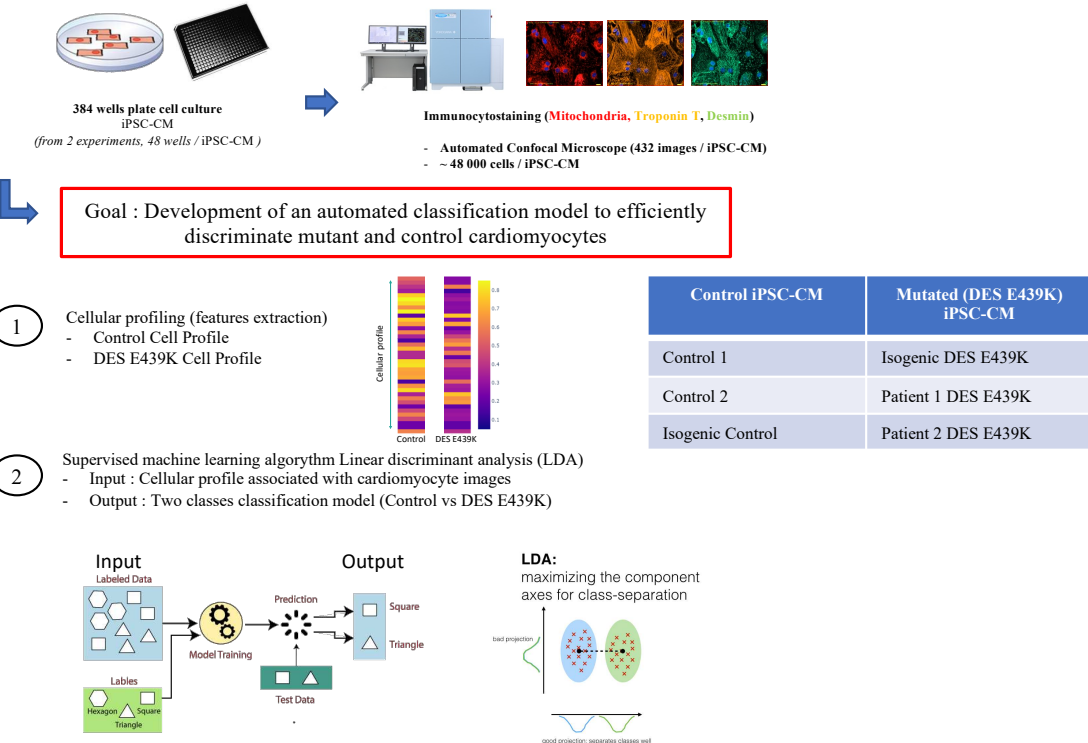


Figure 45 : Workflow and implementation of a two classes LDA machine learning-based classification model for iPSC-CM cellular profiles Control and DES E439K

Feature extraction and selection

After immunocytostaining of iPSC-CM with the three staining (Desmin, cTnT and Mitotracker) and image acquisition using an automated microscope, the feature extraction and selection process was performed (Figure 46A). Imaging features such as intensity, surface area, signal texture, etc. were associated with a given staining, allowing features to be extracted from individual staining or from all staining combined. This enabled the generation of specific staining cellular profiles or cellular profiles from the combination of staining. Thus, for each staining, 56 features were extracted at single cell level. For each of these features, an ANOVA test was performed between the control group and the mutated line group. When the P-value obtained was less than 0.03, the feature was selected and considered statistically significant (Figure 46B). Next, to remove the features that are correlated and give no additional information a statistical test of Pearson's correlation coefficient was applied to refine the selection of features to those that were not correlated (Figure 46C). In fact, some features may give exactly the same information and therefore prove uninformative for cellular profile description.

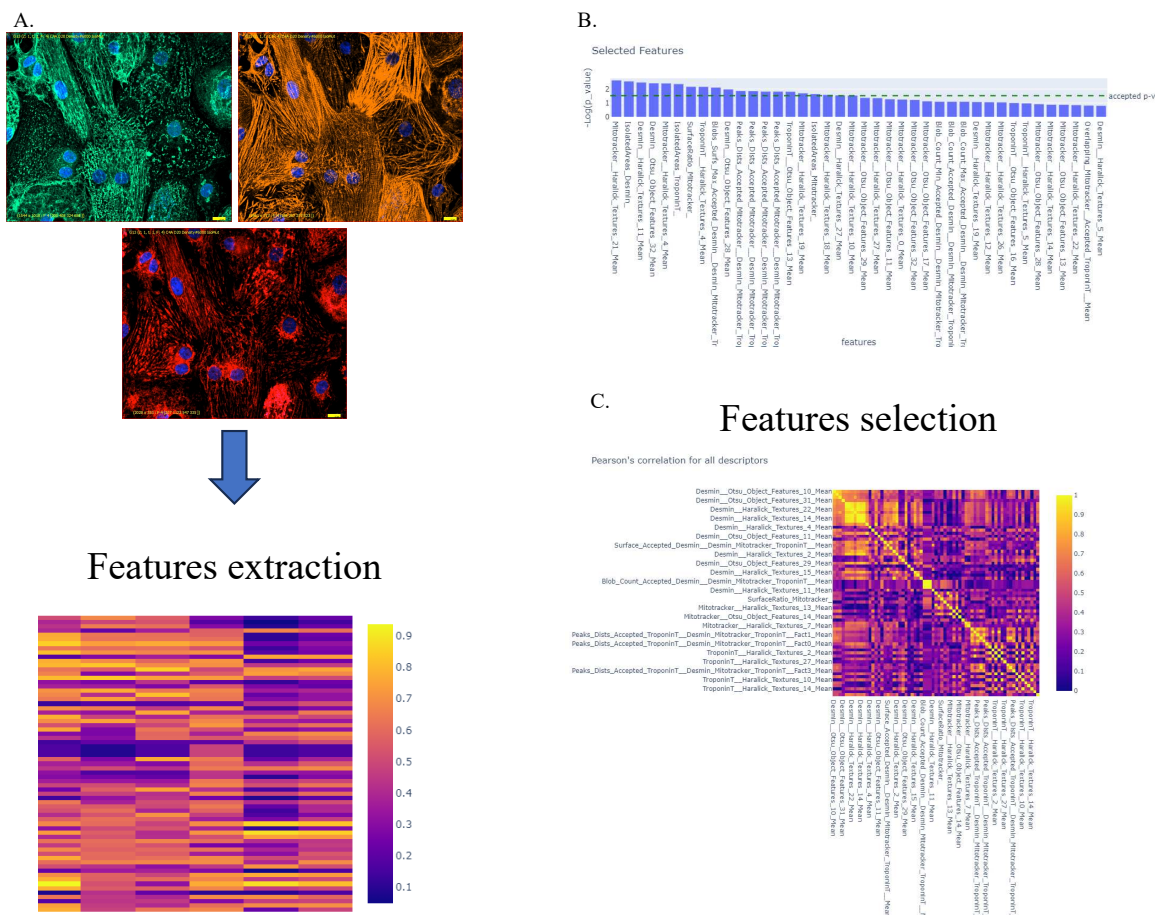
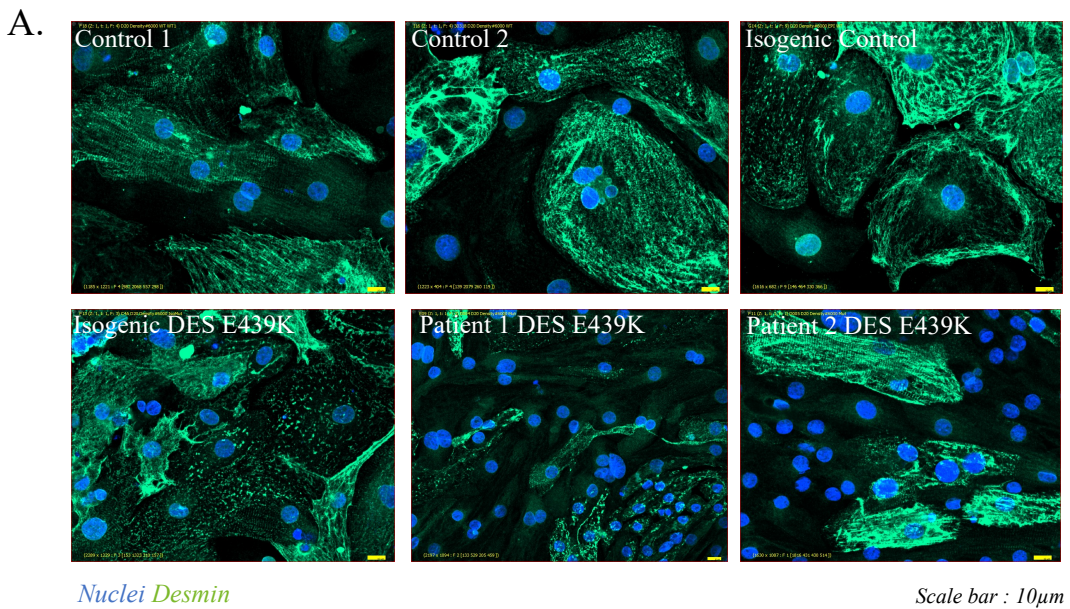


Figure 46 : Features extraction and selection. A Features extraction from stained single cell images. Scale bar=10 μ m. B. Selection of the relevant features based on ANOVA Test F-value (P-value < 0.03). C. Exclusion of the correlated descriptors feature based on Pearsons correlation

Desmin cellular profile

First, the cellular profile associated only with the desmin organization was studied (Figure 47;Figure 48). From images acquired after immunocytostaining of the different iPSC-CM with desmin staining (Figure 47A), the feature extraction and selection was done. 23 features were selected for describing the desmin-like cellular profile, it represented 41% of all initial features extracted. On the basis of this selection, the desmin-like cellular profile for each cell line was determined and represented by a heat map (Figure 47B).



B.

From 56 Features
→23 Features were selected (41%)

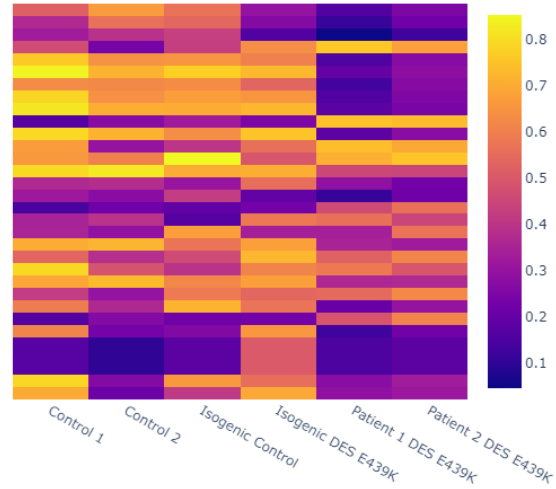
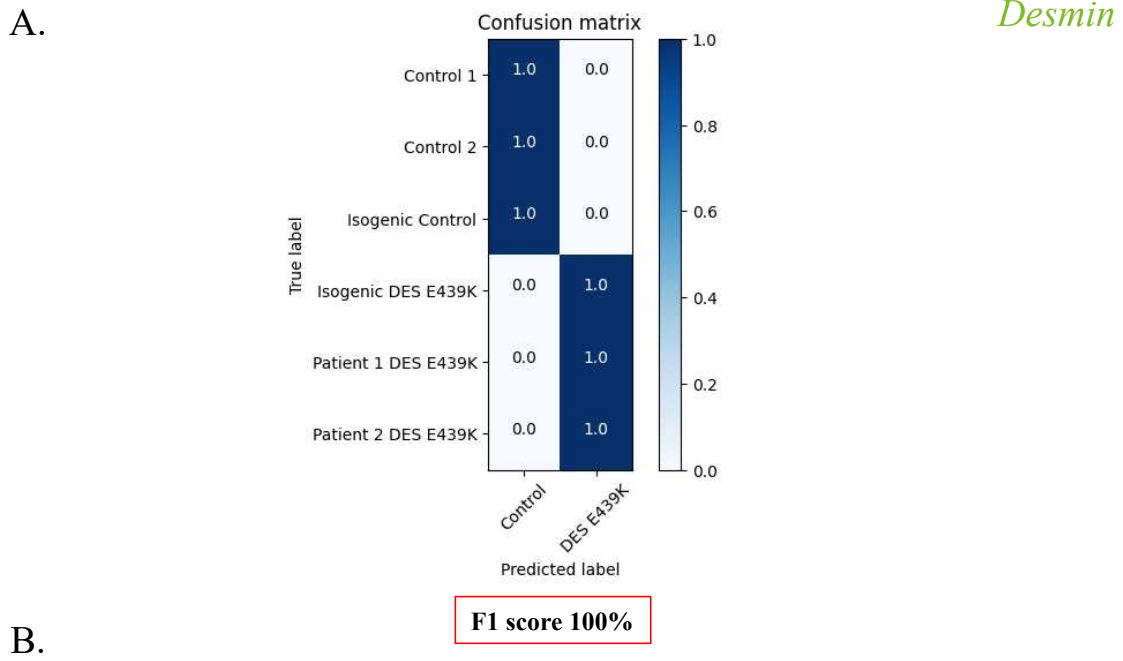


Figure 47: Cellular profiling of different cell lines based on Desmin phenotype A. Immunocytostaining of iPSC-CM (Control 1; Control 2; Isogenic Control; Isogenic DES^{E439K}; Patient 1 DES^{E439K}; Patient 2 DES^{E439K}) with Desmin staining. Scale bar=10 μ m. B. HeatMap of all the selected desmin features used for the cellular profiling of each iPSC-CM.

From the desmin cellular profiles of the different iPSC-CM, an automated classification models has been implemented to discriminate control and *DES*^{E439K} cellular profiles. The training set was based on 70% of the data, while the test set was based on the remaining 30% (Gerbin et al. 2021b). From the testing set result, prediction scores of the algorithm were determined and presented in a confusion matrix (Figure 48A). The rows correspond to the iPSC-CM cellular profiles and the columns to the two classes (Control profile and *DES*^{E439K} profile) in which the model indicates the prediction score for the classification of a cellular profile in a given class. Indeed, this confusion matrix of prediction scores showed that the classification model presents an excellent F1 score of

100% (which is a machine learning evaluation metric that measures the model's accuracy). This result testifying the strong desmin phenotype signature between Control and DES^{E439K} iPSC-CM as the model is able to correctly classify (discriminate) both type of cellular profile based on desmin signal. This testing set result of the automated classification model based on desmin signal is also shown with a 2D space LDA projection of the different iPSC-CM cellular profiles (Figure 48B). The green area corresponded to the control class, and the red area corresponded to the DES^{E439K} class. Each point represented the a cellular profile from one well of iPSC-CM.



B.

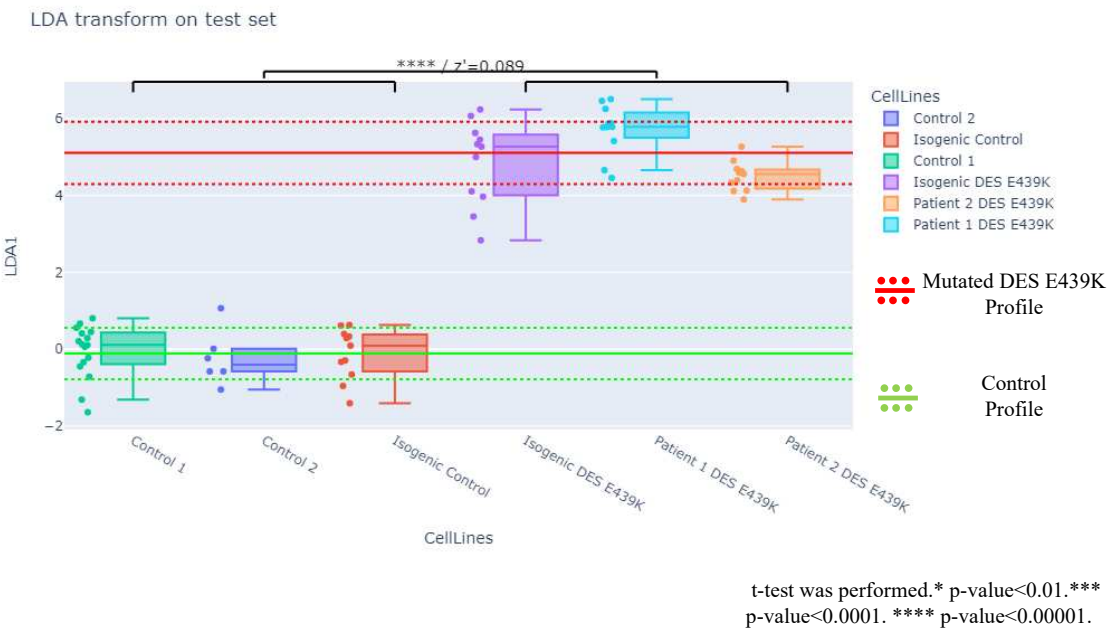


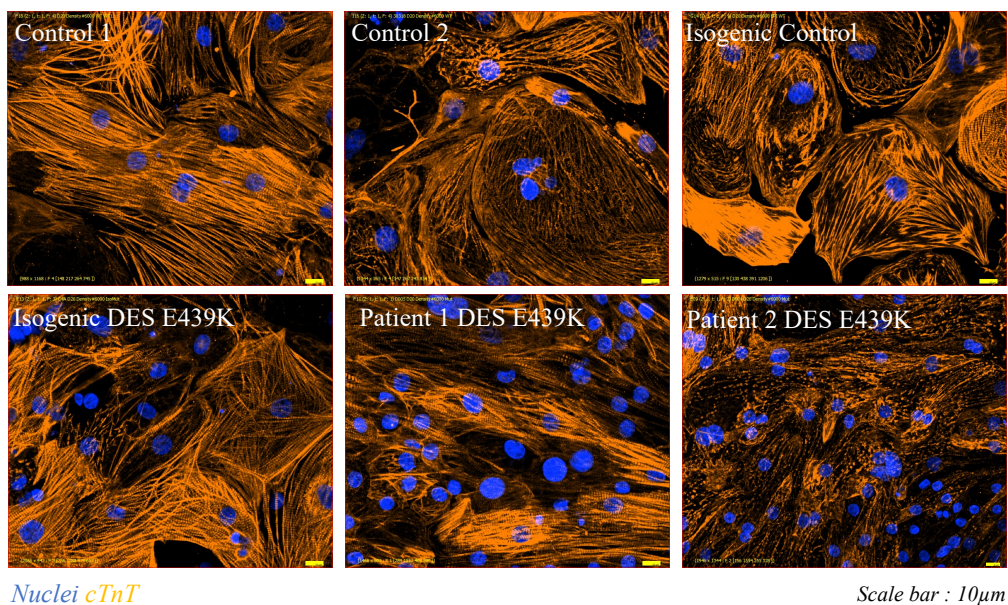
*Figure 48 : Performance of a 2 class (Control profile vs DES^{E439K} profile) classification model based on desmin phenotype. A. Confusion matrix of predicted label specifying the performance of the classification model. B. 2D space LDA projection of the different iPSC-CM desmin cellular profiles. Red area represent mutated DES^{E439K} profile and green area represent control profile. A two-tailed t-test was performed. ns not significant. * p-value<0.05 ** p-value<0.005. *** p-value<0.0005. **** p-value<0.0005. and Z score*

Indeed the cellular profiles from iPSC-CM controls were correctly projected in the control profile class and the cellular profiles from iPSC-CM DES^{E439K} were projected in the DES^{E439K} profile class area. Moreover, based on this classification model the two groups of iPSC-CM cellular profiles were significantly separated.

Cardiac troponin T cellular profile

Next, the cellular profile associated only with the cTnT phenotype was investigated (Figure 49; Figure 50). From the images acquired after cTnT immunocytostaining of the different iPSC-CM (Figure 49A), and based on the procedure of features extraction and selection, 16 features (32% from all the initial features) were used for the cTnT iPSC-CM cellular profile generation. Thus, the cTnT cellular profile of each iPSC-CM was determined and represented by a heat map (Figure 49B).

A.



Nuclei cTnT

Scale bar : 10 μ m

B.

From 50 Features
→16 Features were
selected (32%)

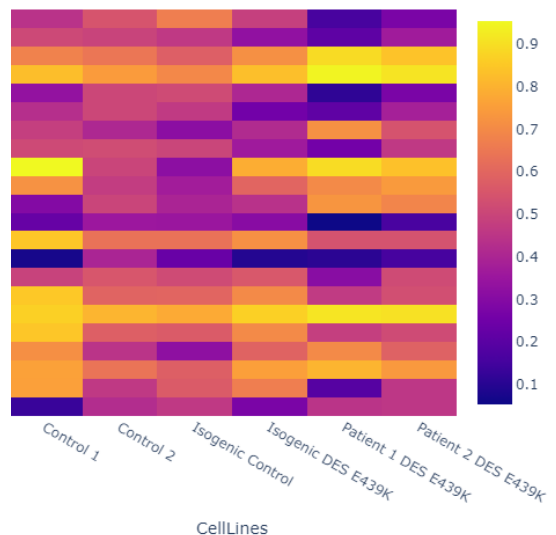


Figure 49 : Cellular profiling of different cell lines based on cTnT phenotype. A. Immunocytostaining of iPSC-CM (Control 1; Control 2; Isogenic Control; Isogenic DES^{E439K}; Patient 1 DES^{E439K}; Patient 2 DES^{E439K}) with cTnT staining. Scale bar=10 μ m. B. HeatMap of all the selected cTnT features used for the cellular profiling of each iPSC-CM

As previously for desmin, the cTnT cellular profiles of the different iPSC-CM were partially used to generated an automated classification model specific with two classes Control profile and *DES*^{E439K} profile. Again, the training set was based on 70% of the data, while the testing set was based on the remaining 30%. The result of the testing set of this automated classification model cTnT specific is presented with a confusion matrix of the predicted scores for this classification model (Figure 50A). It showed that for some iPSC-CM, the prediction score wasn't the score expected. In fact, the F1 score of the classification model cTnT specific was only 81%. These results could also be visualized with an LDA projection in 2D space, where the green area corresponded to the control profile class and the red area represented the *DES*^{E439K} profile class (Figure 50B). These results may suggest that the cTnT phenotype alone is not yet strong enough to clearly differentiate between control and *DES*^{E439K} cellular profiles. This may be due to the maturity of the iPSC-CM model not yet being sufficient to clearly visualize the sarcomeric pathological phenotype.

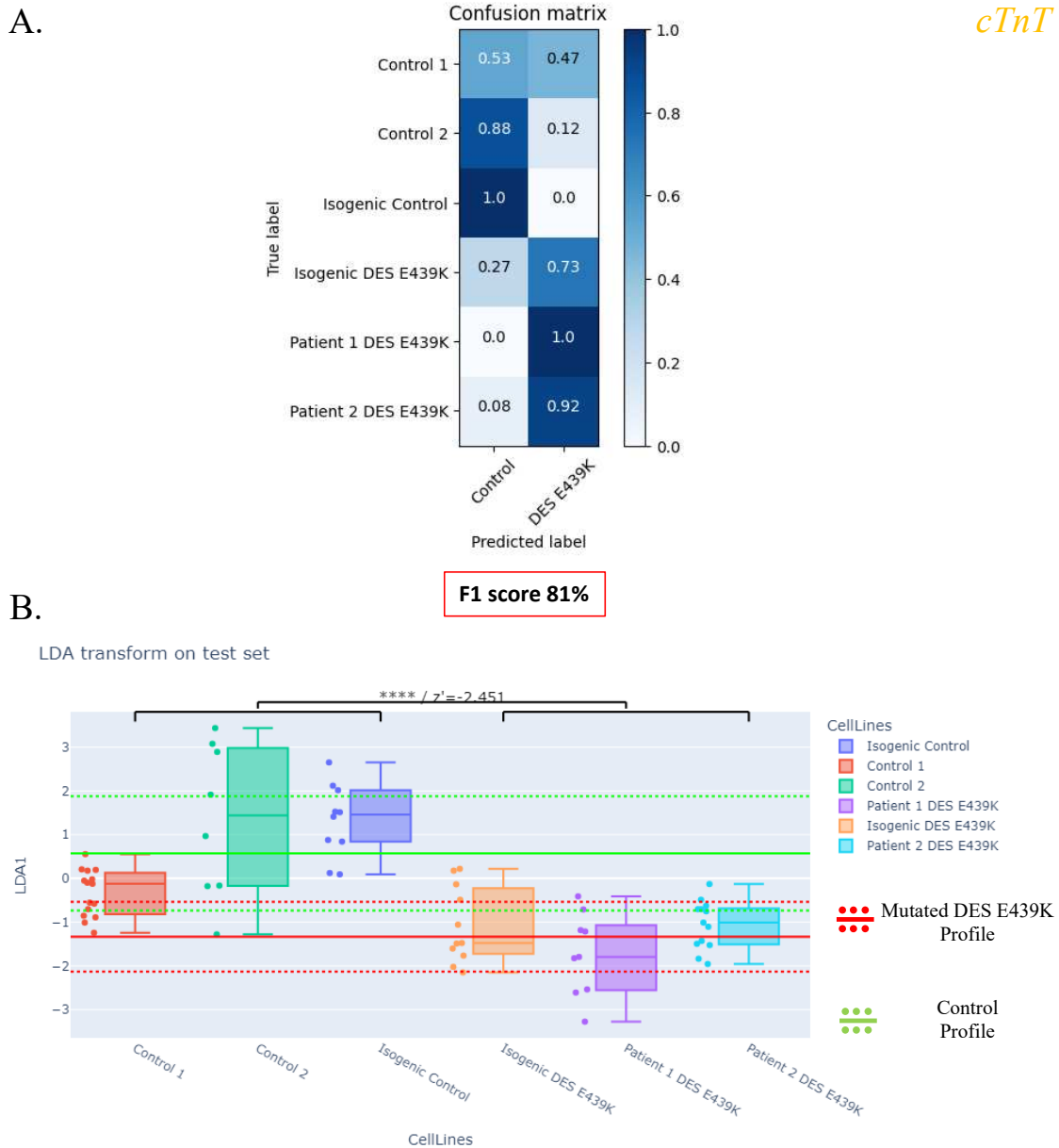


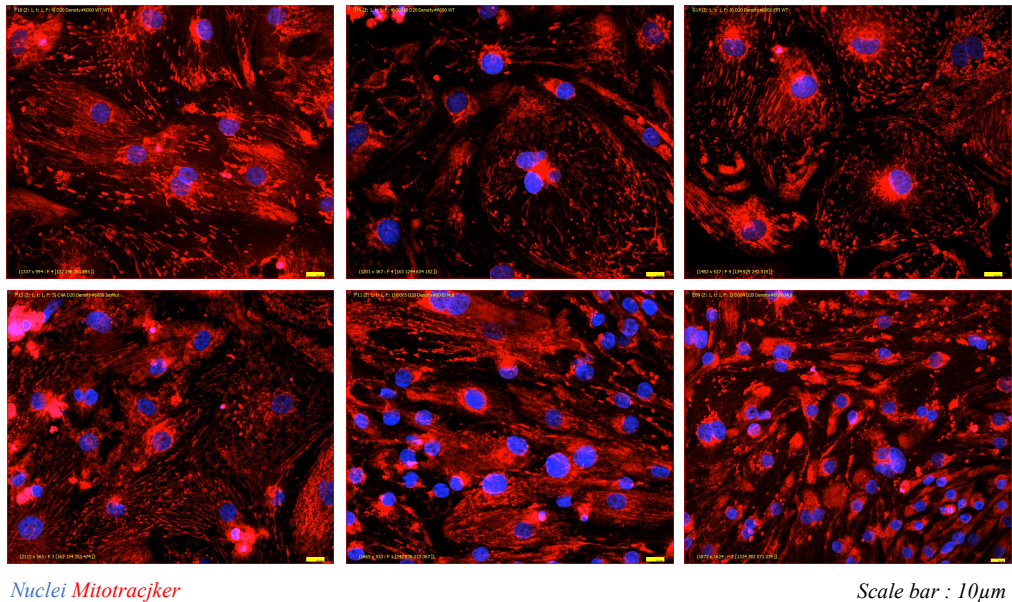
Figure 50 : Performance of a 2 class (Control profile vs DES ^{E439K} profile) classification model based on *cTnT* phenotype. A. Confusion matrix of predicted label specifying the performance of the classification model. B. 2D space LDA projection of the different iPSC-CM *cTnT* cellular profiles. Red area represent mutated DES ^{E439K} profile and green area represent control profile. A two-tailed t-test was performed. ns not significant. * p-value<0.05 ** p-value<0.005. *** p-value<0.0005. **** p-value<0.0005. and Z score

Mitochondria cellular profile

To continue, the cellular profile associated uniquely with the mitochondria phenotype was studied (Figure 51; Figure 52). From images acquired after live staining of the different iPSC-CM with Mitotracker, features were extracted and selected (Figure 51A). Here, 10 features were selected, 19% from all the initial features. Based on the selection of

the mitochondria features, cellular profiles for each iPSC-CM was determined and represented with a HeatMap (Figure 51B).

A.



Nuclei *Mitotracker*

Scale bar : 10 μ m

B.

From 51 Features
→10 Features were
selected (19%)

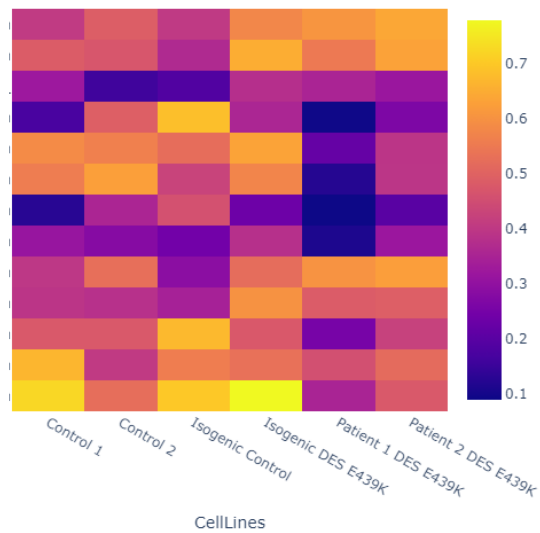


Figure 51 : Cellular profiling of different cell lines based on mitochondria phenotype A. live staining of iPSC-CM (Control 1; Control 2; Isogenic Control; Isogenic DES^{E439K}; Patient 1 DES E439K; Patient 2 DES E439K) with mitotracker staining. Scale bar=10 μ m. B. HeatMap of all the selected mitochondria features used for the cellular profiling of each iPSC-CM.

From a part of the mitochondrial cellular profiles of the different iPSC-CM, again, an automated classification models specific to mitochondria phenotype with two classes control profile and DES^{E439K} profile was implemented. The training set was based on 70% of the data, while the testing set was based on the remaining 30%. The results of the testing set were showed with a confusion matrix of predicted score of each iPSC-CM cellular profile in each classes (Figure 52A). These results showed that some predicted score wasn't

expected, for example, the control 2 cellular profile should not have been 38% predicted as a profile belonging to the DES^{E439K} class. Indeed, the F1 score of the classification model mitochondria specific was only 85%. These results could also be visualized with an LDA projection in 2D space, where the green area corresponded to the control profile class and the red area represented the DES^{E439K} profile class (Figure 52B). It highlighted that the classification model mitochondria specific is able to separate the two classes into two distinct zones.

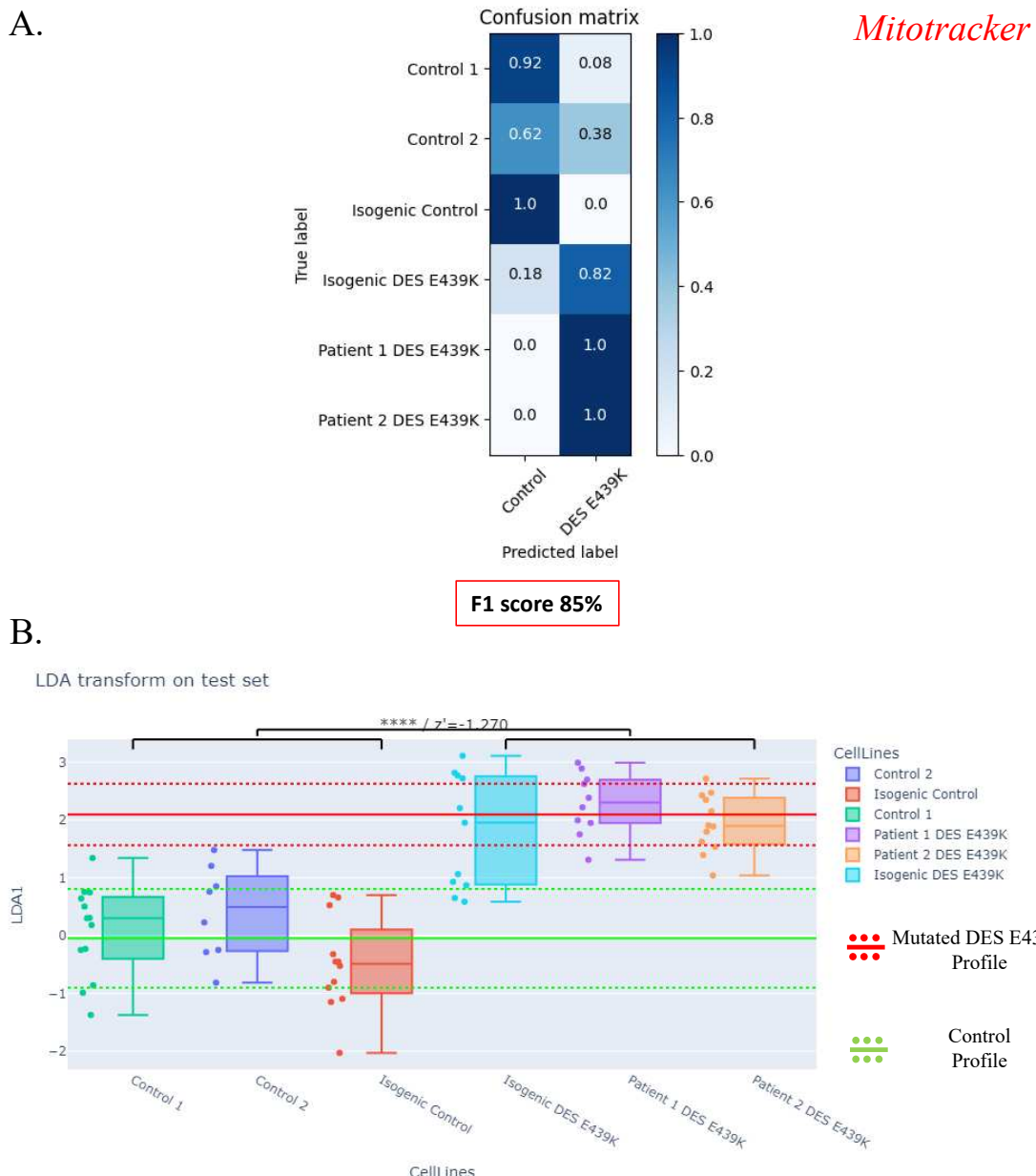


Figure 52 : Performance of a 2 class (Control profile vs DES^{E439K} profile) classification model based on mitochondria phenotype. A. Confusion matrix of predicted label specifying the performance of the classification model. B. 2D space LDA projection of the different iPSC-CM mitochondria cellular profiles. Red area represent mutated DES^{E439K} profile and green area

represent control profile. A two-tailed t-test was performed. ns not significant. * p-value<0.05 ** p-value<0.005. *** p-value<0.0005. **** p-value<0.0005. and Z score

These data suggest that the mitochondria phenotype may be sufficient to distinguish control iPSC-CM from mutant *DES*^{E439K} iPSC-CM. However, the classification model is not robust enough to confidently separate control cellular profiles from mutant *DES*^{E439K} cellular profiles.

From all the observations made previously, it can be deduced that the desmin phenotype is the most marked in distinguishing a control cellular profile from a *DES*^{E439K} cellular profile which is not surprising considering that the mutation affects desmin. The respective F1 scores of the classification models specific to the desmin, cTnT and mitochondria phenotypes were 100%, 81% and 85%. These results support the hypothesis that in the iPSC-CM model and culture conditions used for this experiment, the desmin phenotype was most affected by the *DES*^{E439K} mutation, followed by the mitochondrial phenotype and finally the sarcomeric phenotype (cTnT). These two last phenotypes, despite an non-sufficient robustness to be considered alone to discriminate Control versus mutant iPSC-CM, were demonstrated to be affected in these mutant iPSC-CM confirming our previous observation. In the setting of DCM due to *DES* mutation, it has been shown that desmin mutation initially induces loss of the desmin network and protein aggregation, followed rapidly by mitochondrial dysfunction, before being accompanied by sarcomeric disorganization (Capetanaki et al., 2015). The maturity of iPSC-CM was probably at a point where the desmin phenotype was already well established, the mitochondrial phenotype was in progress and the sarcomeric phenotype in its early stages.

Although the classification model specific to the desmin phenotype could be sufficient for further study and the implementation of a high content imaging screening assay. It is worth considering the establishment of a classification model based on all phenotypes (desmin , cTnT , mitochondria), as the aim of the assay is to identify pathophysiological mechanisms and compounds influencing the overall pathological phenotype.

Combined cellular profile

Thus, as before, the same exercise was performed based on combination of the three phenotypes: Desmin, cTnT and Mitochondria (Figure 53; Figure 54). Confocal microscope images were acquired following immunocytostaining of the three structures in each iPSC-CM (Control 1; Control 2; Isogenic Control; Isogenic *DES*^{E439K}; Patient 1 *DES*^{E439K};

Patient 2 *DES*^{E439K}) (Figure 53A). 49 features (31% from all features extracted) were selected for the following step.

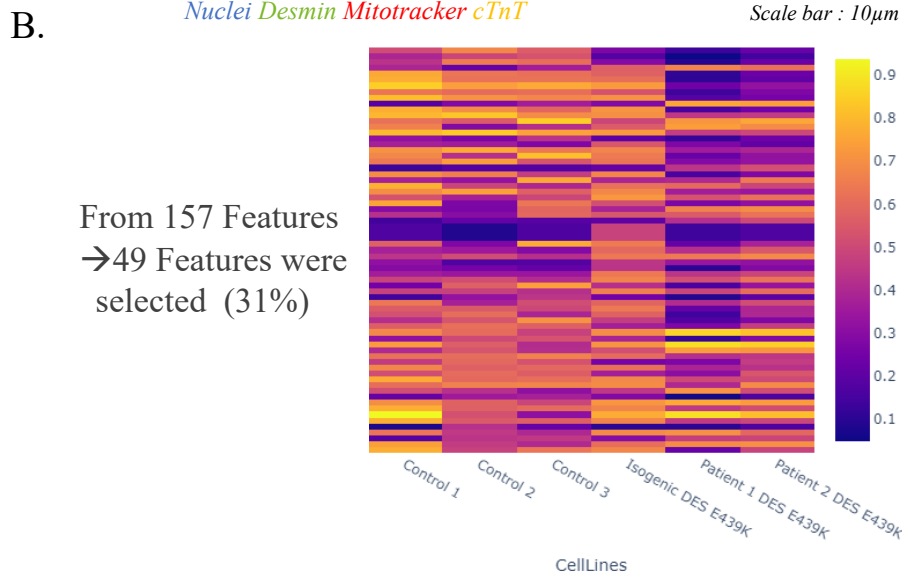
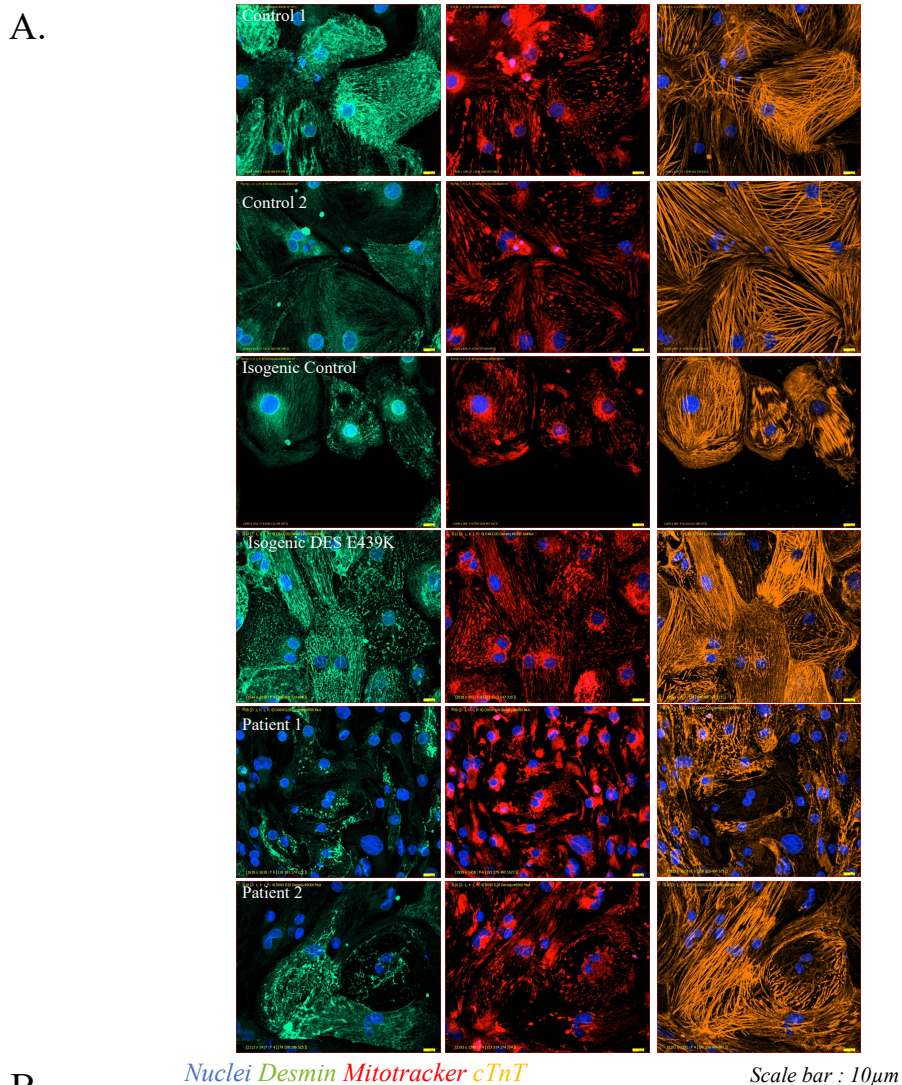
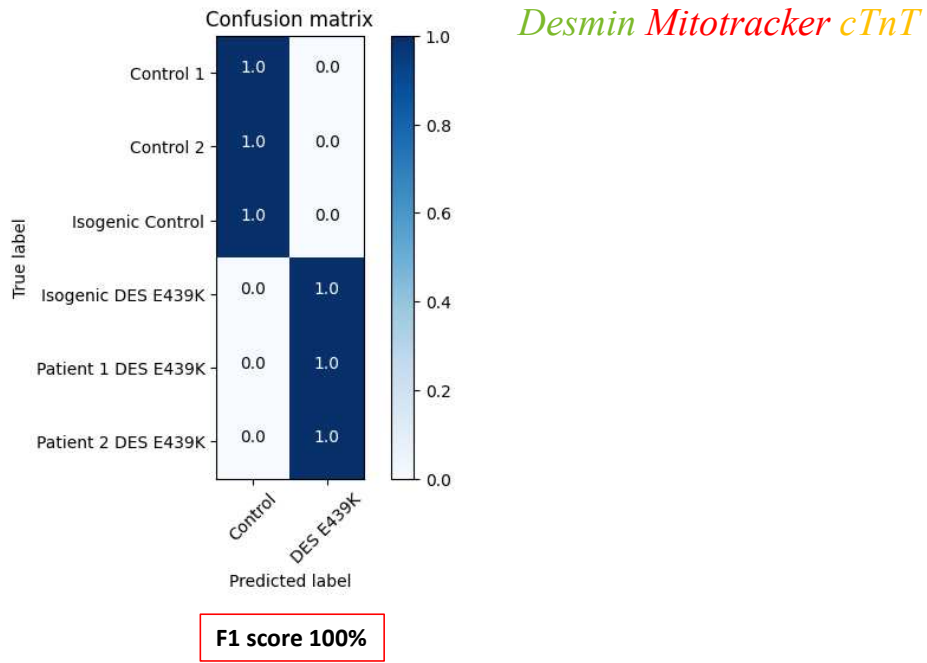


Figure 53 : Cellular profiling of different cell lines based on combined phenotype A. Immunocytostaining of iPSC-CM (Control 1; Control 2; Isogenic Control; Isogenic DES^{E439K}; Patient 1 DES^{E439K}; Patient 2 DES^{E439K}) with Desmin, cTnT staining and Mitotracker live staining. B. HeatMap of all the selected combined features used for the cellular profiling of each iPSC-CM.

From these features, the cellular profiles of each iPSC-CM were determined and plotted in a heat map (Figure 53B). These cellular profiles were then used to set up an automated classification model based on the three phenotypes and with two classes : Control profile and *DES*^{E439K} profile. Once again, 70% of the data were used for the training set and 30% for the testing set. The results of this testing set phase was visualized with a confusion matrix of the different iPSC-CM cellular profile and their prediction score in each classes: control profile class or *DES*^{E439K} profile class (Figure 54A). The F1 score of the classification model based on all phenotype were at 100%, meaning that this model is accurate. This result were confirmed with the 2D space LDA projection visualization of this classification model where the two area represented each classes (green area for control profile class and red area for *DES*^{E439K} profile class) were clearly separated (Figure 53B). The different iPSC-CM cellular profile of each groups were projected as expected. These data validate the classification model based on the three phenotypes Desmin, cTnT and mitochondria.

A.



B.

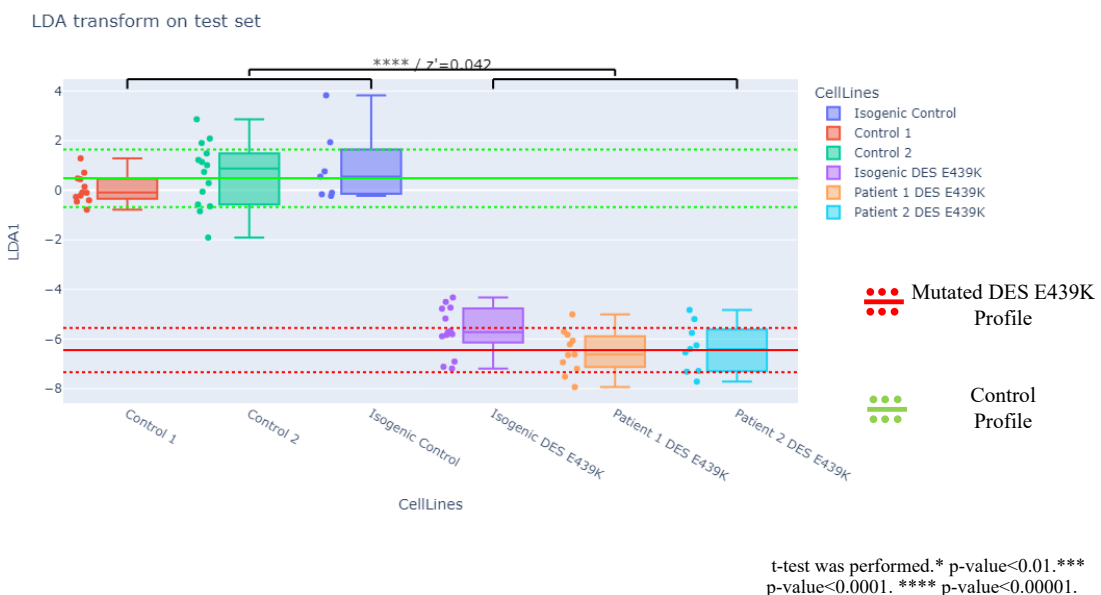


*Figure 54 : Performance of a 2 class (Control profile vs DES ^{E439K} profile) classification model based on combined phenotype. A. Confusion matrix of predicted label specifying the performance of the classification model. B. 2D space LDA projection of the different iPSC-CM combined cellular profile. Red area represent mutated DES ^{E439K} profile and green area represent control profile. A two-tailed t-test was performed. ns not significant. * p-value<0.05 ** p-value<0.005. *** p-value<0.0005. **** p-value<0.00005. and Z score*

In conclusion, this work has enabled the development and implement of an automated classification model based on machine learning, allowing the discrimination finely and automatically of control and *DES* ^{E439K} iPSC-CM. The automated nature of this tool will enable a large number of analyses to be perfomed in a short period of time. Moreover, the sensitivity of this classification model will enable the identification of significant variations

in phenotypes as function of different compounds treatment. This model is therefore perfectly suited to the implementation and execution of high content imaging screening.

IV.4.3. Tool compounds identification

Before considering high content imaging screening, it is necessary to ensure that the phenotype of iPSC-CM is likely to be affected after treatment with compounds, and that the analytical image analysis model chosen for read-out identification is capable of measuring these phenotypic variations (Blanchet et al., 2015). In addition, based on their mechanism of action (MOA) the identification of compounds that can be used as positive controls in the screening assay can already provide information on the establishment of the disease phenotype. All the compounds tested have a well-known MOA. Compounds that induce a phenotypic variation and interact with a particular physiological mechanism will provide interesting leads to better characterize the development of the pathology. The following work consisted in treating isogenic *DES*^{E439K} iPSC-CM with compounds. Then, to evaluate the cellular profile of these iPSC-CM treated with each compound and to use a classification model control profile class versus *DES*^{E439K} profile class. Finally, the compounds that induced the cellular profile of the treated iPSC-CM to be projected not in the *DES*^{E439K} profile class but in the control profile class were selected. These compounds are referred to as Hit (Figure 55). The purpose of this chapter is to highlight the methodology used to address the various challenges.

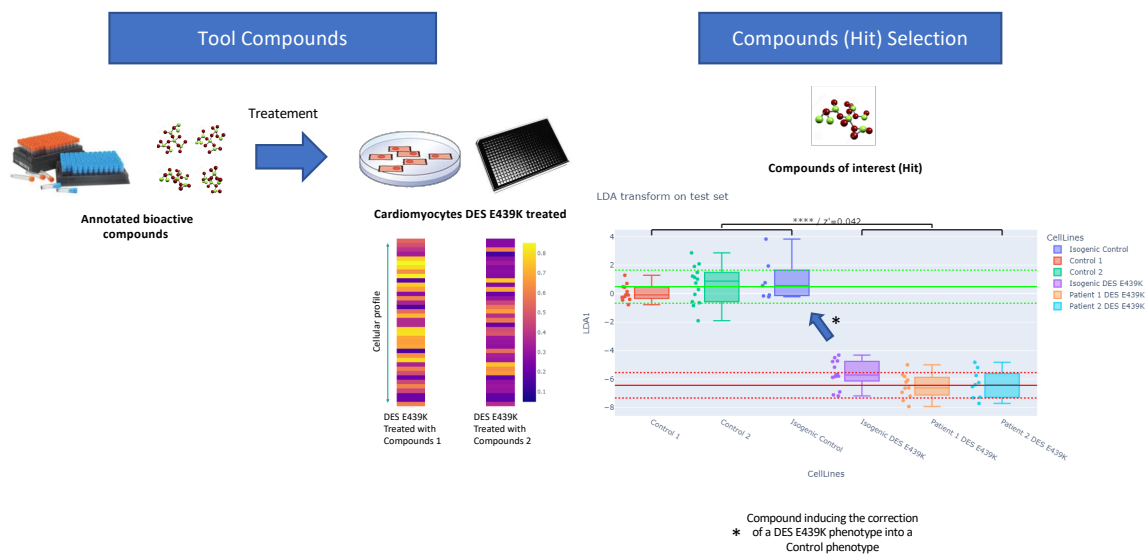


Figure 55 : Tool compounds workflow

Firstly, the treatment conditions for iPSC-CM were assessed. iPSC-CM were cultured for 10 days in T3DEX culture medium after thawing. Compound treatments were

started on day 4 of culture for 6 days. Four well per treatment and concentration were implemented. However, two of these wells were only one-time compound addition on day 4 of culture, while for the other two wells, there was a two-time repletion of compound treatment on days 4 of culture and 6 of culture. Although it would be more relevant to compare the results of each approach and because the different effects induced on the cells seemed identical, it was decided to consider only the overall treatment period. Indeed, the four wells were considered as replicates for the following results, it enabled analyses to be based on a larger sample size per condition.

A panel of molecules has been selected and tested for the identification of positive or negative controls, confirming that iPSC-CM can respond to treatment and that the image analysis tools can quantify these variations. A first group of molecules are described in the literature as promoting cardiac contraction function by various mechanisms, electrophysiological or regulating the activity of the actomyosin complex Table 4: Danicamтив, Omecamтив mecarbil, Istaroxime hydrochloride, Flecainide acetate, Ranolazine dihydrochloride, Verapamil hydrochloride, GO6976 and (Echt & Ruskin, 2020; Lehman et al., 2022; Rahate et al., 2020; Sossalla et al., 2010; Van Den Hoogenhof et al., 2018) combination1 (GO6976+SB203580). This group of compound is mostly expected to have an effect on sarcomeric phenotype. The second group of molecules involved those described as playing a role in unfolded protein response mechanisms Table 5: Tubastatin A, SB203580, Rapamycin. This group of compound is mostly expected to have an effect on desmin and mitochondrial phenotype The third and final group of molecules corresponded to those described as capable of inducing deleterious effects on iPSC-CM and often used as negative controls Table 6: MG-132, Bortezomib, Bafilomycin, Doxorubicin, combination2 (MG-132+Bafilomycin). This group of compound is expected to have no rescue effect, these compounds are expected to aggravate the phenotype. Isogenic *DES*^{E439K} iPSC-CM were treated with these compounds at different concentration: 0,0111μM; 0,0308 μM; 0,1 μM; 0,308 μM; 1 μM; 3,08 μM; 10 μM.

Table 4 : Promote cardiac contraction function

Compounds	Mechanism of action	Reference
Danicamтив	Cardiac myosin activator, which acts by increasing the affinity of myosin for ATP	(Lehman et al., 2022)
Omeacamiv mecarbil	Cardiac myosin activator by binding to the head of myosin	(Lehman et al., 2022)
Istaroxime hydrochloride	Activator of the sarcoplasmic reticulum Ca^{2+} ATPase isoform 2a (SERCA2a) and Na^+/K^+ ATPase inhibitor	(Rahate et al., 2020)
Flecainide acetate	Class Ic antiarrhythmic that inhibits sodium channels	(Echt & Ruskin, 2020)
Ranolazine dihydrochloride	Antianginal agent Sodium channel inhibitor, inhibits late over peak I_{Na}	(Sossalla et al., 2010)
Verapamil hydrochloride	Calcium channel inhibitor, specifically L-type calcium channels	(Lai et al., 2021)
GO 6976	Selective inhibitor of PKC kinase α and β isoforms	(Perea-Gil et al., 2022)
Combination 1 (GO 6976+SB 203580)	Small molecule kinase inhibitors	(Perea-Gil et al., 2022)

Table 5 : Play a role in unfolded protein response

Compounds	Mechanism of action	Reference
SB 203580	Small molecule kinase inhibitors, autophagy activator	(Cuenda et al., 1995)
Tubastatin A	HDAC6 histone deacetylase inhibitor	(Jin Yang et al., 2022)
Rapamycin	Rapamycin target inhibitor (mTOR)	(Jiang et al., 2020)

Table 6 : Induce Deleterious effects on iPSC-CM

Compounds	Mechanism of action	Reference
Doxorubicin	Anti-cancer agent of the anthracycline class interacts with DNA, causing DNA breaks and inhibiting RNA synthesis, leading to cell death	(Hasinoff et al., 2017)
Bortezomib	Proteasome inhibitor, specifically blocking the 26S protein	(Di Lernia et al., 2020)
Bafilomycin	Inhibitor of vacuole proton ATPase (V-ATPase), interfering with the acidification process in lysosomes	(Shaikh et al., 2019)
MG-132	Proteasome inhibitor, specifically blocking the 26S	(Yuedong Ma et al., 2011)
Combination 2 (MG-132+Bafilomycin)	Autophagy and proteasome inhibition	(Korolchuk et al., 2009)

After culture and treatment with compounds, Isogenic *DES*^{E439K} iPSC-CM were immunocytostained for desmin, cTnT and mitochondrial staining (live staining Mitotracker). Images were acquired using an automated confocal microscope, and analysis was based on the Cellular profiling supervised LDA machine learning classification model previously described (Cell profiling classification model).

2 classes (Isogenic Control vs Isogenic *DES*^{E439K})

First, a classification model presenting two classes: Isogenic Control and Isogenic *DES*^{E439K} was used. The cellular profiles used to generate the two classes were generated from images of untreated iPSC-CM isogenic control or isogenic *DES*^{E439K} culture 10 days in T3DEX (Figure 56A). The cellular profiles associated with the treatment of a given compound were projected onto this classification model, presented in the form of a 2D space LDA projection (Figure 56B). The red area corresponded to the space of cellular profiles classified as Isogenic *DES*^{E439K} and the green area corresponded to the space of cellular profiles classified as Isogenic Control. Each point represented a cellular profile generated from images of iPSC-CM isogenic *DES*^{E439K} treated with a compound at a given concentration (Figure 56B). The arrows show cellular profiles that were projected in the Isogenic control type cellular profile area. The images associated with the cellular profiles

indicated by the arrows showed that the iPSC-CM treated presented a damaged iPSC-CM appearance characteristic of toxicity (Figure 56B). Therefore, a two-class classification model (Isogenic Control and Isogenic *DES*^{E439K}) did not seem to be ideal for interpreting the treatment effects of compounds. Indeed, some compounds cellular profiles are mistakenly judged by the model to be Isogenic control cellular profiles, whereas they do not have the appearance of Isogenic control iPSC-CM. To avoid this type of error, it may be useful to add a third class of cellular profile into the classification model: Toxic cellular profile.

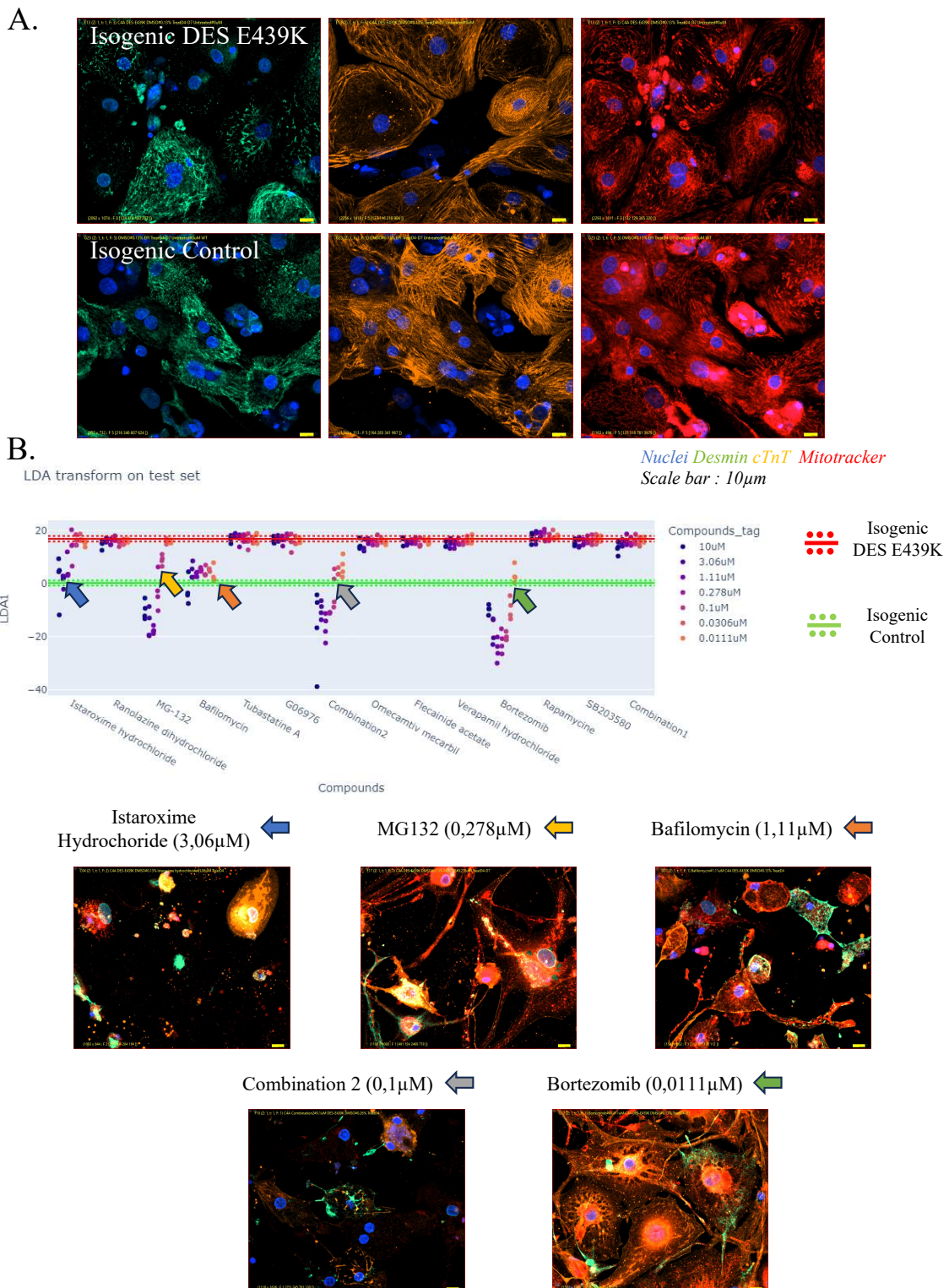


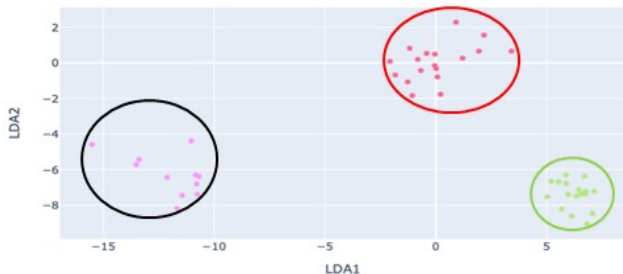
Figure 56 : Two classes supervised LDA machine learning classification model of Isogenic Control and DES^{E439K} iPSC-CM and projection of different treated Isogenic DES^{E439K} cellular profile. A. Immunocytostaining of iPSC-CM (Isogenic Control; Isogenic DES^{E439K}) with Desmin, Mitotracker and cTnT. Scale bar=10μm. B. LDA projection of the different Treated Isogenic DES^{E439K} cellular profile based on the three phenotype. Red area represent mutated DES^{E439K} profile and green area represent control profile. The arrows indicate Treated Isogenic DES^{E439K} cellular profiles associated with a iPSC-CM treated image.

3 classes (Isogenic Control, Isogenic *DES*^{E439K} and Toxic cellular profile)

A 3-class classification model was then implemented. This model consisted of typical cellular profile classes: Isogenic Control, Isogenic *DES*^{E439K} and Toxic cellular profile (Figure 57). Once again, the Isogenic Control and Isogenic *DES*^{E439K} classes were set up on the basis of cellular profiles generated from images of untreated Isogenic Control and Isogenic *DES*^{E439K} iPSC-CM. Concerning the toxic profile class, different strategies could be considered. Firstly, the class of toxic profiles could be based on the cell profile obtained from iPSC-CM treated with doxorubicin (Figure 57A). Secondly, the class of toxic profiles could also be based on cell profiles from iPSC-CM treated with doxorubicin or bortezomib (Figure 57B). Finally, the class of toxic profiles could be based on cell profiles from iPSC-CM treated with doxorubicin, bortezomib or baflomycin (Figure 57C). These compounds already been described as inducing a cardiotoxic profile (Grafton et al., 2021). Three different classification models were generated respectively based on the three type of toxic profile class. For each Classification model a training phase on 70% of these different cellular profile groups followed by a testing phase with the remaining 30% was conducted. The 2D space LDA projection of the different cellular profile types onto the testing phase shows that the three classification model were capable of separating the three cellular profile types: Isogenic Control, Isogenic *DES*^{E439K}, Toxic profile (Figure 57).

A.

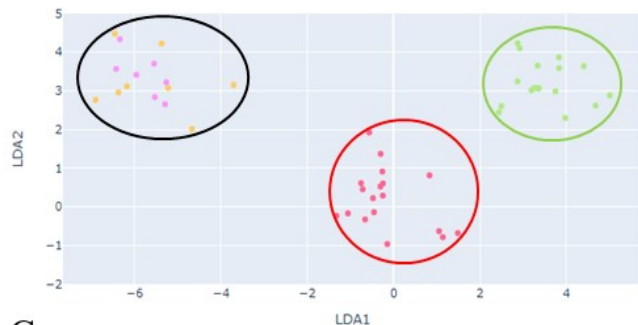
LDA transform on test set



Training with Toxic profile based on :
➤ Doxorubicin

B.

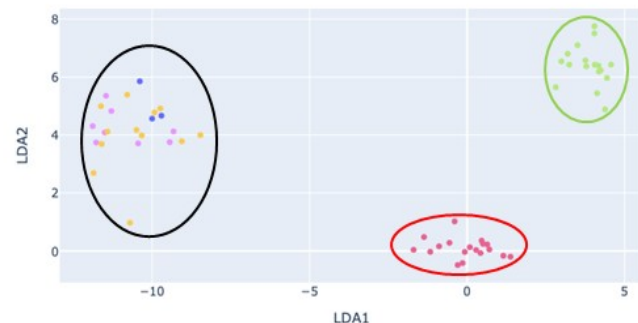
LDA transform on test set



Training with Toxic profile based on :
➤ Doxorubicin
➤ Bortezomib

C.

LDA transform on test set



Training with Toxic profile based on :
➤ Doxorubicin
➤ Bortezomib
➤ Bafilomycin

Toxic Profile

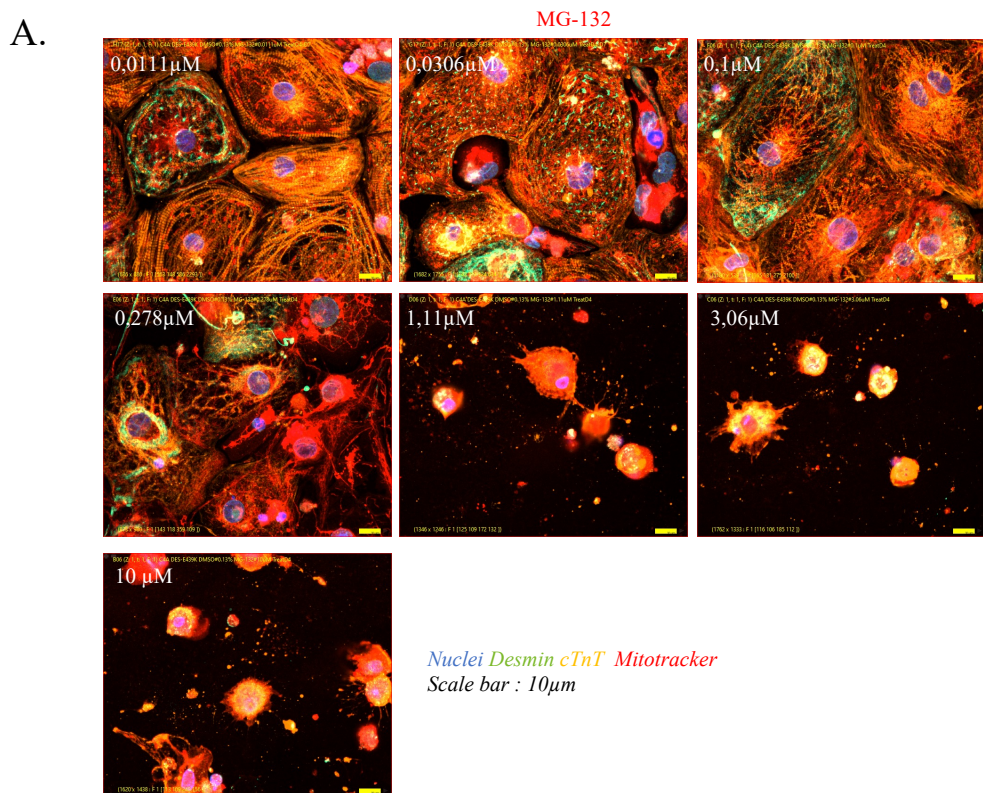
Isogenic Control

Isogenic DES E439K

Figure 57 : 2D space projection of a three classes supervised LDA machine learning classification model of Isogenic Control, Isogenic DES ^{E439K} and Toxic cellular profile. A. Toxic profile was based Doxorubicin treated isogenic DES ^{E439K} cellular profile B. Doxorubicin or Bortezomib treated isogenic DES ^{E439K} cellular profiles. C. Doxorubicin, Bortezomib or Bafilomycin treated isogenic DES ^{E439K} cellular profiles.

In order to identify which of the previously described processes will be used to characterize the toxic profile class, an experiment based on the cellular profile classification of iPSC-CM isogenic DES ^{E439K} treated with MG-132 at different concentrations was

realized (Figure 58). It was shown that MG-132, a proteasome inhibiting compound, could have beneficial effects at low concentrations but proved toxic when the concentration was too high (Surova et al., 2009). Immunocytostaining of iPSC-CM Isogenic *DES*^{E439K} treated with different concentrations of MG-132 showed that, at the highest concentrations, there appeared to be a toxicity phenomenon with significant cell death (Figure 58). It was therefore interesting to study the predictive scores of MG-132 cell profiles in the three classification models, which differed only in the toxic profile class. In the first classification model, where the toxic profile class training set was based only on Doxorubicin cell profiles, the MG-132 0.1 μ M cellular profile was not at all predicted as belonging to the toxic profile class. Whereas in the other two classification models, where the toxic profile class was based on the cell profiles Doxorubicin and Bortezomib or Doxorubicin, Bortezomib and Bafilomycin, the cell profile MG-132 0.1 μ M was 25% predicted as a toxic profile (Figure 58B). These results showed that the last two classification models were more sensitive than the first. The addition of the Bafilomycin cellular profile to generate the toxic profile class did not appear to increase the sensitivity of the model. Thus, the classification model where the toxic profile class is based on the Doxorubicin and Bortezomib cellular profiles was selected. Indeed, it is preferable to save the Bafilomycin cellular profiles for later and consider it as a test where it will be expected that these cellular profiles will be predicted as toxic. This will enhance confidence in the classification model.



B.

3 classes Classification based on the 3 phenotypes: Desmin cTnT Mitochondria

➤ Classification of Isogenic DES E439K MG-132 treated cellular profile

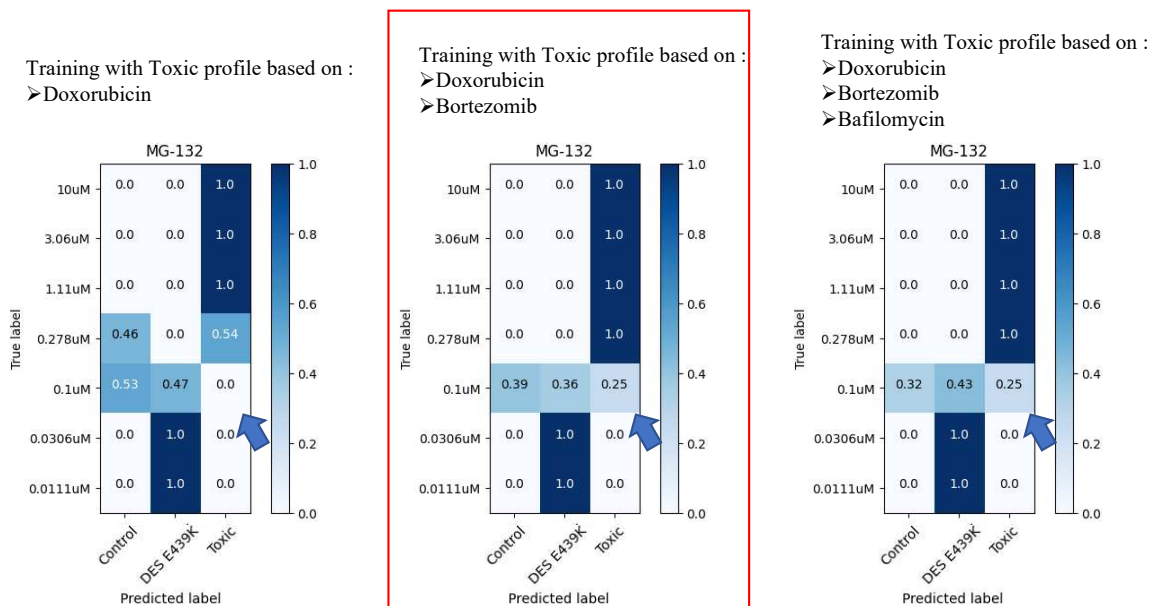


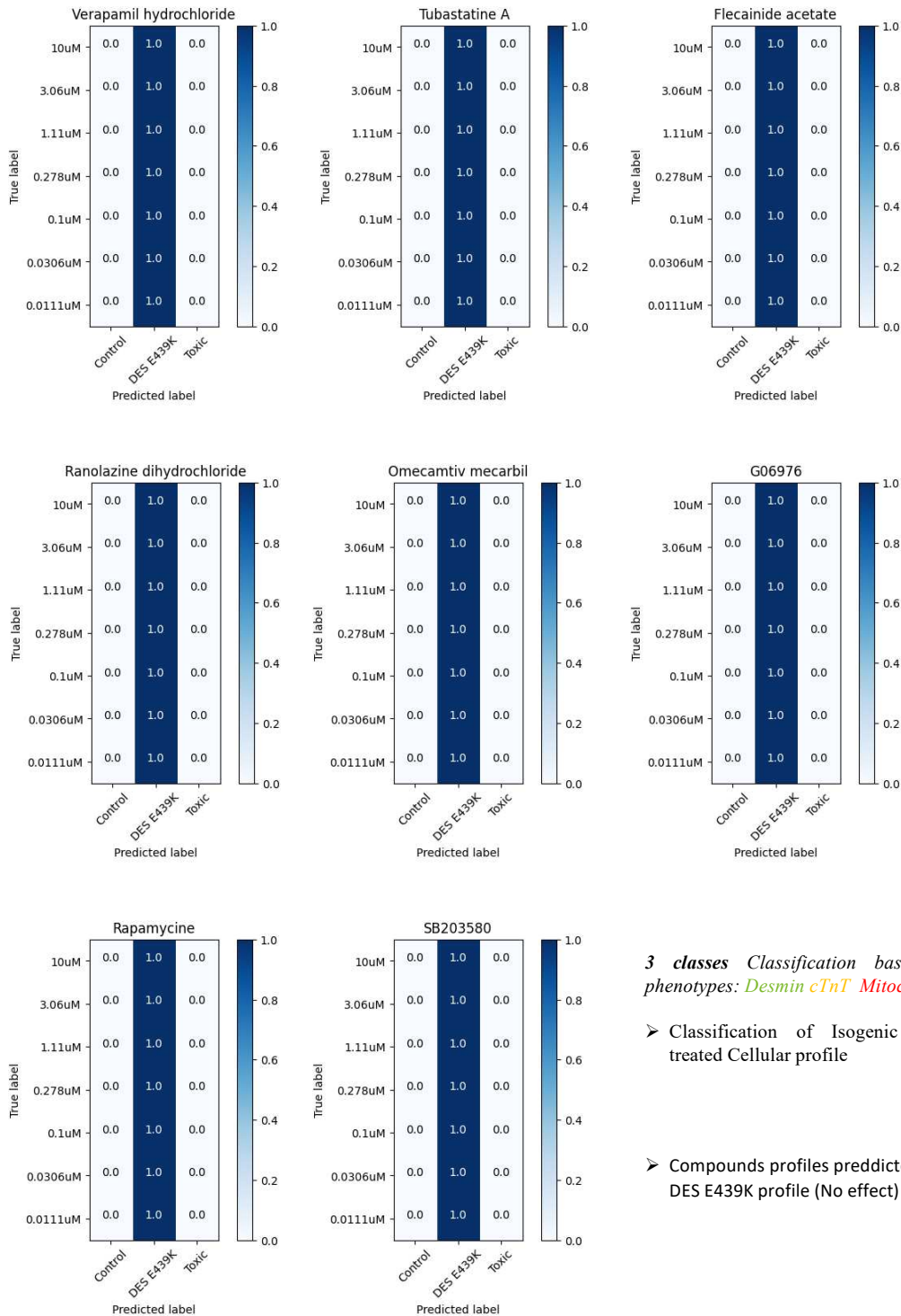
Figure 58 : MG-132 cellular profiles prediction score in different classification models. A. Immunocytostaining of iPSC-CM Isogenic DES E439K treated at different concentration. Scale bar=10 μ m. B. Confusion matrix of the different classification models and prediction score of MG-132 cellular profiles. These classification models are distinguished on the basis of toxic class, either

according of the cellular profile of doxorubicin alone or Doxorubicin and Bortezomib or Doxorubicin, Bortezomib and Bafilomycin

Next, the cellular profiles of compounds at different concentrations were presented to the classification model, which indicated the percentage of prediction to a given class (Isogenic Control, Isogenic *DES* ^{E439K}, Toxic profile). Cellular profiles predicted as the Isogenic *DES* ^{E439K} class could thus be interpreted as compounds not inducing any effect on iPSC-CM (Figure 59). The cellular profiles predicted as the toxic class could be interpreted as compounds inducing a toxic effect on the cells (Figure 60). Finally, the cellular profiles predicted as the control isogenic class could be interpreted as compounds inducing a rescue of the pathological phenotype towards the control phenotype (Figure 61).

Compounds cellular profile predicted as Isogenic *DES* ^{E439K} class (No effect)

Firstly, 8 compounds were predicted as Isogenic *DES* ^{E439K} by the classification model (Figure 59). These compounds did not appear to induce any significant effect on the overall phenotype of Isogenic *DES* ^{E439K} iPSC-CM based on Desmin, cTnT and mitochondria staining. Despite the increased concentration of these compounds, no significant variation was identified in the cellular profile of iPSC-CM treated with these compounds.



3 classes Classification based on the 3 phenotypes: *Desmin* *cTnT* *Mitochondria*

➤ Classification of Isogenic DES E439K treated Cellular profile

➤ Compounds profiles predicted as DES E439K profile (No effect)

Figure 59 : Confusion matrix of predicted classification of different compounds treated Isogenic DES E439K cellular profile in the three classes (Isogenic Control, DES E439K and Toxic cellular profile). Here the compounds that don't seem to have any effect.

Compounds cellular profile predicted as Toxic profile class (Toxic effect)

Then, 2 compounds induced cellular profiles that were mostly predicted as toxic profiles (Figure 60). These include bafilomycin and combination 2 (a combination of bafilomycin and MG-132). It was interesting to note that for the both compounds, the first

concentration 0,0111 μ M cellular profiles were not 100% predicted as toxic. This suggests that the effect was not yet strong enough to clearly distinguish the toxic phenotype on iPSC-CM. A percentage of cellular profiles are even predicted as Isogenic control. This reflects one of the limitations of the classification model, which showed the difficulties of differentiating the control phenotype from a phenotype tending towards the toxic phenotype at low concentration.

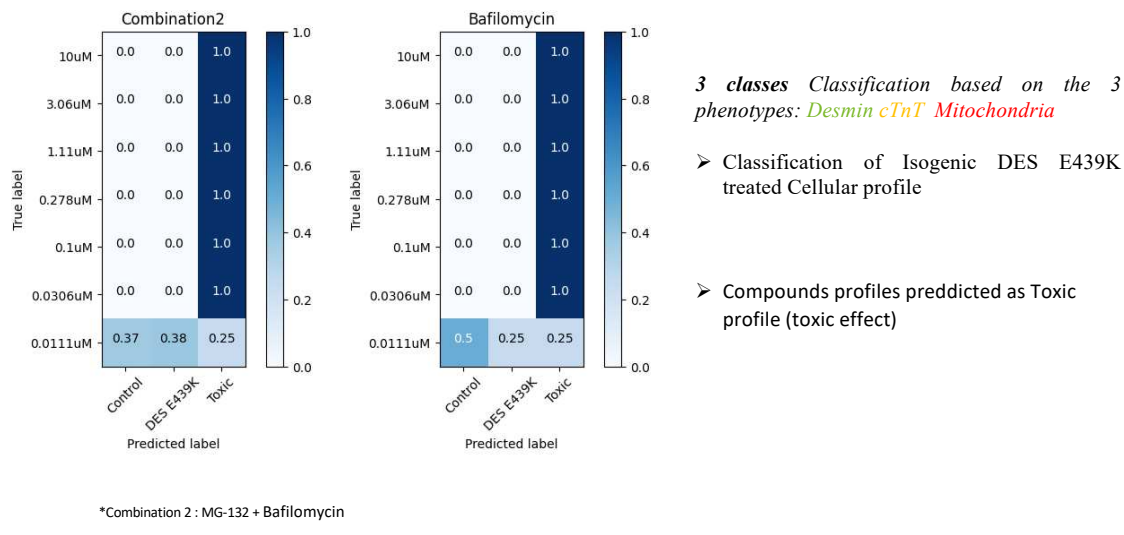


Figure 60 : Confusion matrix of predicted classification of different compounds treated Isogenic DES E^{439K} cellular profile in the three classes (Isogenic Control, DES E^{439K} and Toxic cellular profile). Here the compounds that seem to have toxic effect.

Compounds cellular profile predicted as Isogenic control class (Rescue effect)

Finally, two compounds induced cell profiles partly predicted in the class Isogenic control profile (Figure 61). First, Istaroxime hydrochloride is an inhibitor of Na⁺/K⁺-ATPase and an activator of sarcoplasmic/endoplasmic reticulum calcium ATPase 2 (SERCA 2) (Rahate et al., 2020). In the first concentrations (from 0.0111 μ M to 0.1 μ M) the induced cellular profiles were predicted as Isogenic DES E^{439K} , no rescue was observed. At the 0.278 μ M concentration, 25% of induced cellular profiles were predicted as Isogenic Control, suggesting phenotypic rescue. At higher concentrations (from 1.11 μ M to 10 μ M), cellular profiles were predicted as toxic profiles, showing that istaroxime hydrochloride could be toxic at higher concentrations (Figure 61). It would be interesting to confirm these results with a complementary experiment, testing concentrations around 0.278 μ M and highlighting a dose-response effect. Then, Combination 1 referred to concomitant treatment with compounds GO 6976 and SB 203580, which are kinase inhibitors described to rescue DCM phenotype by the activation of the transcription factor ATF4 (Perea-Gil et al., 2022). In the first concentration from 0,0111 μ M to 3,06 μ M the induced cellular profiles were

predicted as Isogenic DES^{E439K} , no rescue was observed. At 10 μ M the induce cellular profile were predicted at 39% as Isogenic control, suggesting a rescue (Figure 61). Thus, It would be also interesting to further testing concentrations around 10 μ M in order to highlight a dose-response effect.

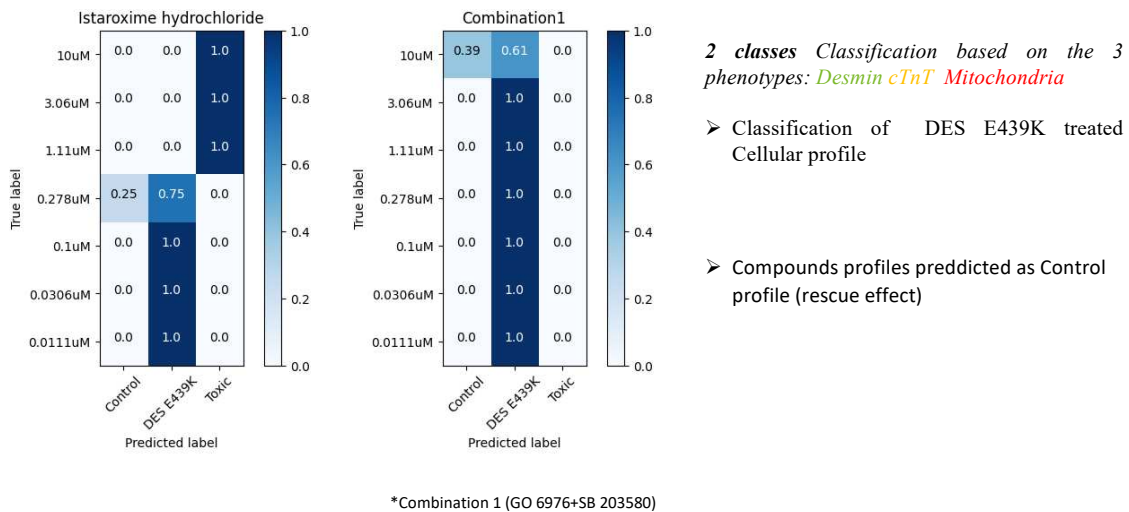


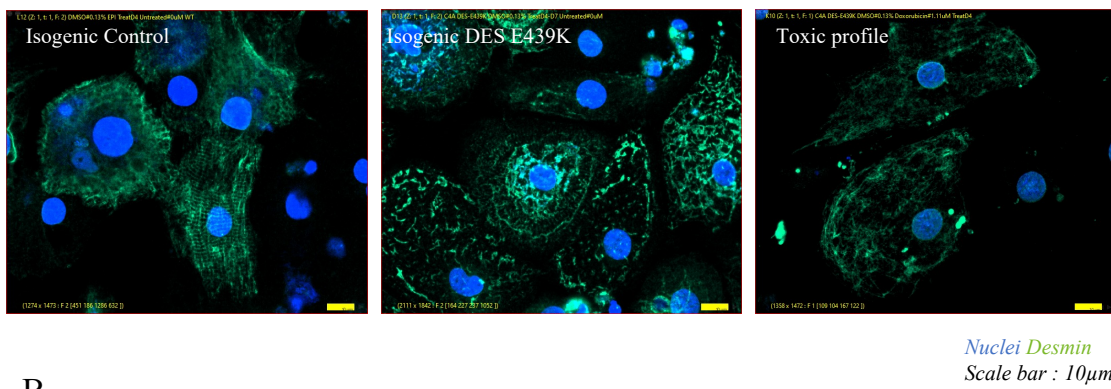
Figure 61 : Confusion matrix of predicted classification of different compounds treated Isogenic DES^{E439K} cellular profile in the three classes (Isogenic Control, DES^{E439K} and Toxic cellular profile). Here the compounds that seem to have a rescue effect.

Following this initial analysis, it was decided to study the specific effects of the compounds by focusing on a single phenotype each time (Desmin, cTnT or mitochondria). In fact, certain compounds previously classified as having no effect when all three phenotypes are studied at the same time, may induce effects on one phenotype in particular. This strategy enables better characterization of the compounds effects on iPSC-CM Isogenic DES^{E439K} .

3 classes from DESMIN Cellular profile

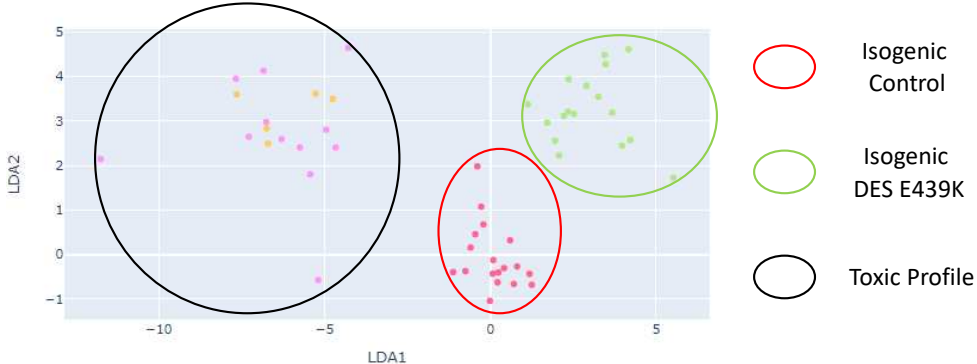
The desmin phenotype was the first to be studied. As a reminder, this phenotype had been shown to be the most evident in DES^{E439K} iPSC-CM compared to Control iPSC-CM (IV.4). A 3-class classification model was generated from different types of cellular profiles induced from Desmin immunocytostaining of iPSC-CM Isogenic control, Isogenic DES^{E439K} untreated and treated with toxic compounds (Doxorubicin and Bortezomib). (Figure 62A). The classification model enabled the separation of three groups of cellular profiles: Isogenic control, isogenic DES^{E439K} and Toxic cellular profile (Figure 62B).

A.



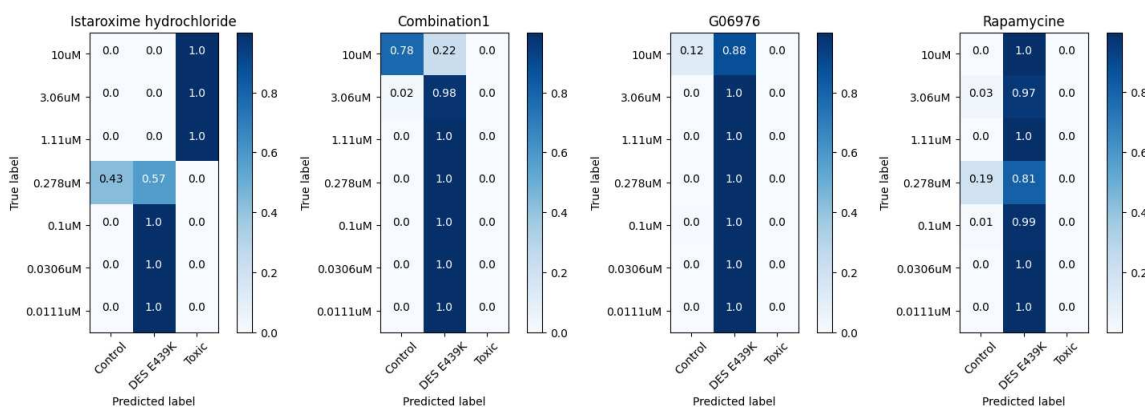
B.

3 classes Classification based on 1 phenotype: Desmin



C.

➤ Compounds profiles predicted as Control profile (rescue effect) for the desmin phenotype



*Combination 1 (GO 6976+SB 203580)

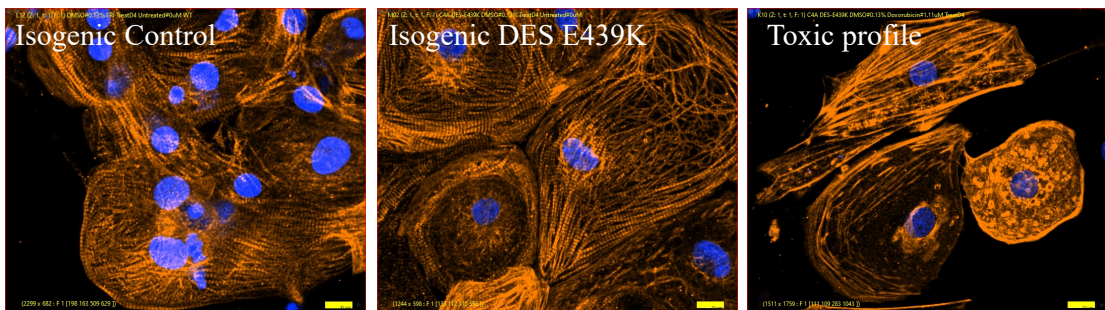
Figure 62: Three classes (Isogenic Control, Isogenic DES E439K and Toxic cellular profile) supervised LDA machine learning classification model only based on Desmin staining. A. Immunostaining of iPSC-CM (Isogenic Control, Isogenic DES E439K and Isogenic DES E439K treated with toxic compounds). Scale bar=10μm. B. 2D space LDA projection of the three groups of Isogenic Control, DES E439K and Toxic (Doxorubicin or Bortezomib) cellular profile based on Desmin phenotype. C. Predicted classification confusion matrix of compounds treated Isogenic DES E439K cellular profile which look to have an effect on Desmin phenotype.

Then, the different cellular profiles associated with Isogenic *DES*^{E439K} treated with the compounds were projected in this Desmin classification model. By focusing only on compounds that appear to have a rescue effect on iPSC-CM Isogenic *DES*^{E439K}, 4 compounds were identified as inducing an effect on the Desmin phenotype (Figure 62C). Firstly, istaroxime hydrochloride at 0.278µM induced a desmin cellular profile 43% predicted as Isogenic Control and combination 1 at 10µM induced a desmin cellular profile 78% predicted as Isogenic Control. Then, the protein kinase C inhibitor GO 6976 at 10µM induced a desmin cellular profile 12% predicted as Isogenic Control. The Rapamycin (0.278µM) an inhibitor of mTOR/p70S6K pathway and autophagic flux stimulator (X. Ma et al., 2019), induced a desmin cellular profile 19% predicted as Isogenic Control.

3 classes from cTnT Cellular profile

The same strategy as previously was implemented for the cTnT phenotype. First, cellular profiles were generated from images of Isogenic control, Isogenic *DES*^{E439K} and Isogenic *DES*^{E439K} toxic cellular profile (Doxorubicin or Bortezomib treated) iPSC-CM were cTnT stained (Figure 63A). Setting up the classification model based on these three cellular profiles showed that the cTnT Isogenic control and Isogenic *DES*^{E439K} cellular profiles were very close. (Figure 63B). This observation implies that the cTnT cellular profiles Isogenic control and Isogenic *DES*^{E439K} were kind of similar and that the distinction between the two can be quite delicate.

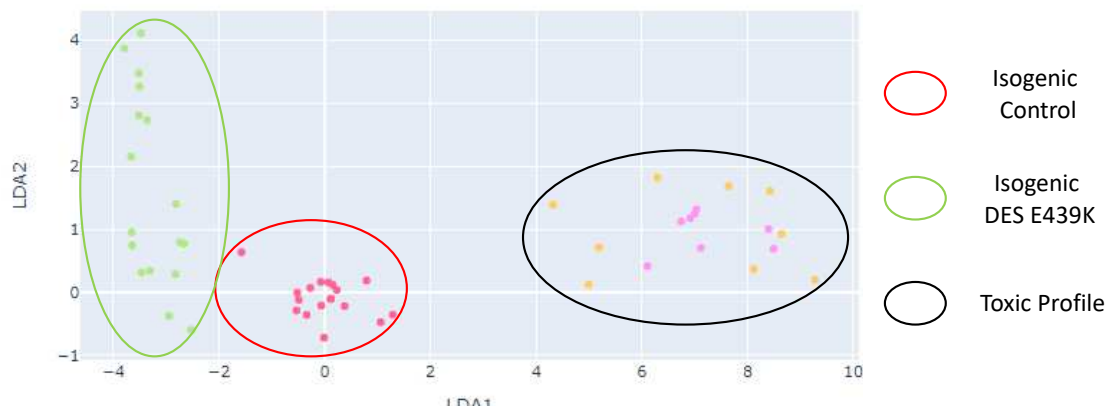
A.



B.

3 classes Classification based on 1 phenotype: cTnT

Nuclei cTnT
Scale bar : 10 μ m



C.

➤ Compounds profiles predicted as Control profile (rescue effect) for the cTnT phenotype

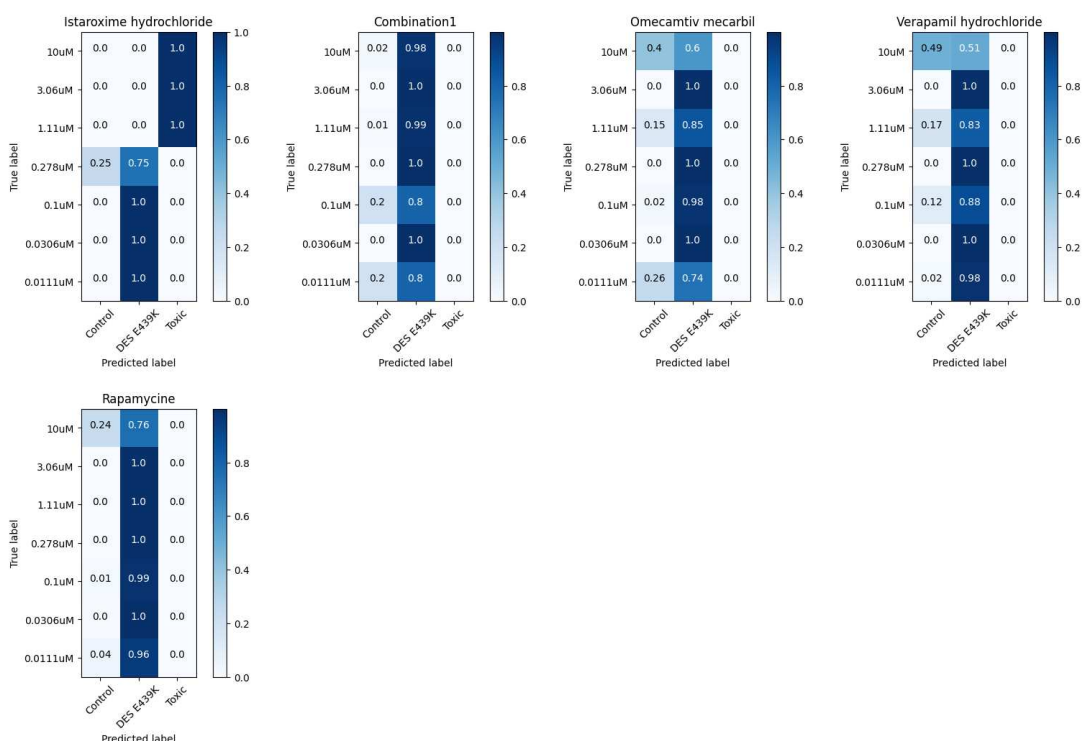


Figure 63 : Three classes (Isogenic Control, Isogenic DES ^{E439K} and Toxic cellular profile) supervised LDA machine learning classification model only based on cTnT staining. A. Immunocytochemistry of iPSC-CM (Isogenic Control, Isogenic DES ^{E439K} and Isogenic DES E439K treated with toxic compounds). Scale bar=10 μ m. B. 2D space LDA projection of the three groups

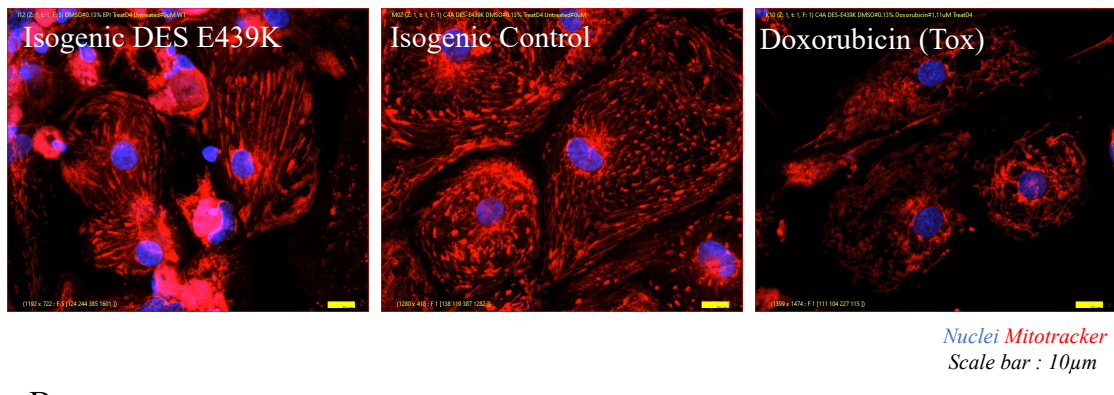
of Isogenic Control, DES^{E439K} and Toxic (Doxorubicin or Bortezomib) cellular profile based on Desmin phenotype. C. Predicted classification confusion matrix of compounds treated Isogenic DES^{E439K} cellular profile which look to have an effect on cTnT phenotype.

The different cTnT cellular profiles associated with Isogenic DES^{E439K} iPSC-CM treated with the compounds were projected in this cTnT classification model. Only cellular profiles associated with compounds appearing to induce a rescue effect on iPSC-CM were selected. Thus, 5 compounds were identified as inducing a rescue effect on the cTnT (Figure 63C). Istaroxime hydrochloride and combination 1 induce cellular profiles partially predicted as isogenic control at distinct concentrations. Omecamtiv mecarbil, a myosin activator known to induce contractility by promoting and stabilizing a state of actin-bound force (Lehman et al., 2022), also seems to induce rescue at different concentrations to the point of omecamtiv mecarbil 10µM inducing a percentage prediction of the cTnT cellular profile to 47% as Isogenic (Figure 63C). Verapamil hydrochloride is an L-type calcium channel blocker, which can reduce intracellular calcium overload, particularly in the sarcoplasmic reticulum (Van Den Hoogenhof et al., 2018). This compound is also seems to induce a rescue effect at different concentration, to induce a percentage prediction of the cTnT cellular profile verapamil hydrochloride 10µM at 50% as Isogenic control (Figure 63C). Finally, Rapamycin seems to also induce a cTnT cellular profile predicted at 24% as Isogenic control for 10µM concentration (Figure 63C).

3 classes from MITOCHONDRIA Cellular profile

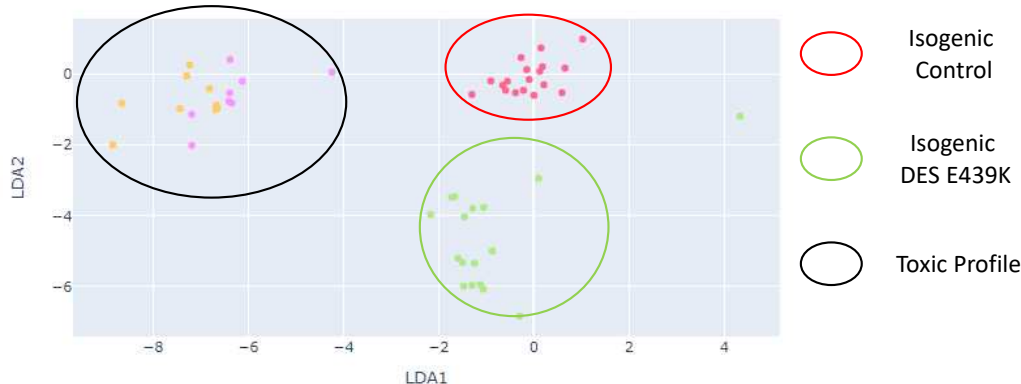
Finally, the effects on mitochondrial phenotype were investigated. As before, cellular profiles were generated from images of Isogenic control, Isogenic DES^{E439K} and Isogenic DES^{E439K} toxic cellular profile (Doxorubicin or Bortezomib treated) iPSC-CM in which mitochondria were stained (Figure 64A). The projection of the different groups of typical cellular profiles after the generation of the mitochondria classification model showed that the three types of cellular profiles were distinguishable in three different projection spaces (Figure 64B).

A.



B.

3 classes Classification based on 1 phenotype: Mitochondria



C.

➤ Compounds profiles predicted as Control profile (rescue effect) for the Mitochondria phenotype

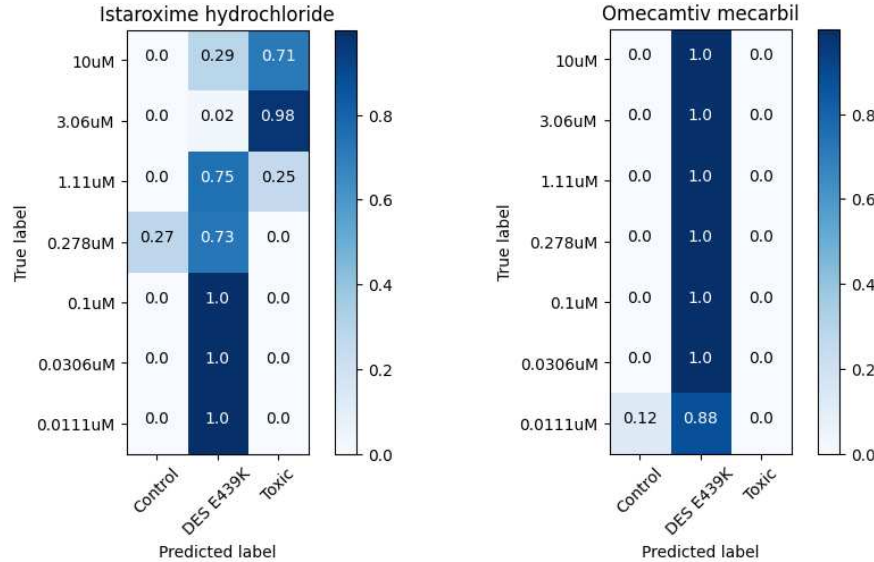


Figure 64 : Three classes (Isogenic Control, Isogenic DES ^{E439K} and Toxic cellular profile) supervised LDA machine learning classification model only based on mitochondria staining. A. Immunoctostaining of iPSC-CM (Isogenic Control, Isogenic DES ^{E439K} and Isogenic DES treated with toxic compounds). Scale bar=10 μ m. B. 2D space LDA projection of the three groups

of Isogenic Control, DES^{E439K} and Toxic (Doxorubicin or Bortezomib) cellular profile based on mitochondria phenotype. C. Predicted classification confusion matrix of compounds treated Isogenic DES^{E439K} cellular profile which look to have an effect on mitochondria phenotype.

Concerning the effects observed on mitochondrial cellular profiles due to compound treatment, 2 compounds were identified as inducing a rescue effect on mitochondrial phenotype (Figure 64C). Istaroxime hydrochloride induce mitochondrial cellular profiles partially predicted as isogenic control for the concentration 0,278µM, for the higher concentration the mitochondrial cellular profiles were predicted as toxic profile. Omecamtiv mecarbil is then found and also seems to induce a slight rescue at 0.0111µM (Figure 64C). Interestingly, combination 1 treatment had no measurable effect on mitochondrial phenotype alone.

In addition, this work has shown that effects on different phenotypes can be quantified both by relying on all three phenotypes at the same time, or on a single one at a time. This opens up a wide range of possibilities for interpreting and characterizing iPSC-CM treatments. It would be interesting to increase the number of replicates and images acquired for this type of experiment, in order to improve the precision and robustness of the test. From a biological point of view, It may be interesting to study the mechanisms of action of compounds that have been selected as rescue-inducing. This information could then be used to deduce the pathophysiological mechanisms involved in establishing phenotypes.

Mitochondria assay, identification of Positive and Negative Control

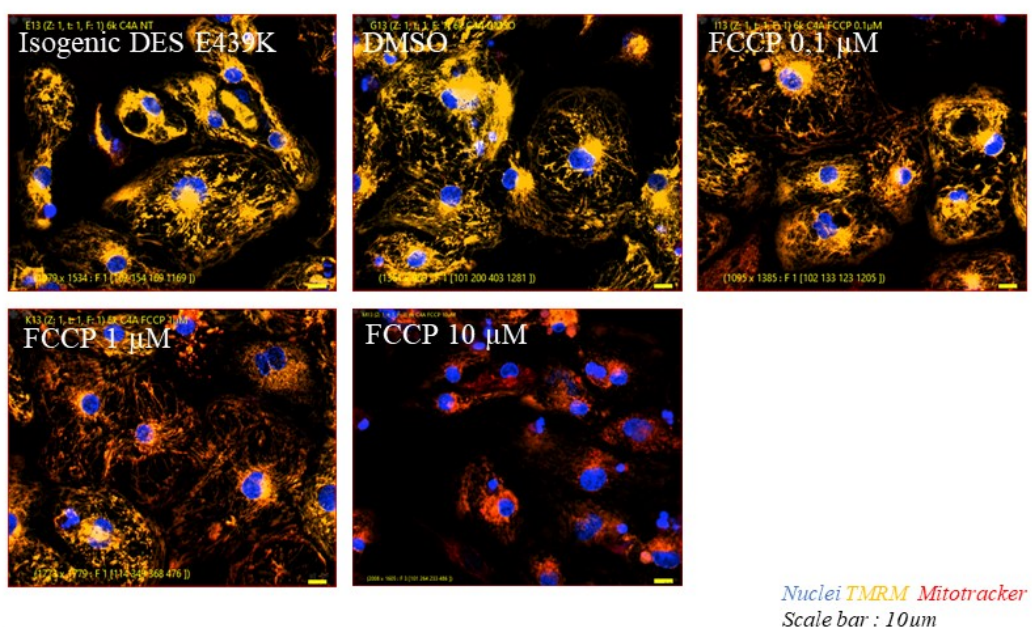
In parallel with previous work demonstrating that it is possible to induce effects on iPSC-CM by treatment with compounds and to measure them using the image analysis tool for classifying cellular profiles, a study was conducted to demonstrate that it is possible to quantify the effects of compound treatments on mitochondrial activity. This study follows on from the assay previously described (Figure 43).

Negative Control (FCCP)

First, Isogenic DES^{E439K} iPSC-CM were cultured for 6 days in T3DEX culture medium before being treated 15min with FCCP mitochondrial membrane uncoupling agent (Mostafavi et al., 2021) and to be live-stained with TMRM (Active mitochondria marker) and Mitotracker (Total mitochondria marker) (Figure 65A). The ratio of the TMRM staining area to the Mitotracker staining area was calculated as function of the treatment conditions (Figure 65B). Different treatment conditions were tested. The “not treated” (NT)

condition corresponds to the first negative control, where iPSC-CM were not treated. The DMSO condition refers to the second negative control, where iPSC-CM were treated with the same concentration of DMSO as in the FCCP 10 μ M condition. Indeed, the last three conditions correspond to conditions where iPSC-CM were treated with 3 concentrations of FCCP (0.1 μ M; 1 μ M and 10 μ M) (Figure 65B). No significant differences was observed between NT and DMSO conditions, indicating that DMSO had no effect on iPSC-CM. Then, under the conditions of treatment of iPSC-CM with the different concentrations of FCCP, a significant decrease in the TMRM/Mitotracker surface ratio can be observed under FCCP 1 μ M and 10 μ M conditions. This decrease seems to follow a dose-response dynamic.

A.



Nuclei TMRM Mitotracker
Scale bar : 10 μ m

B.

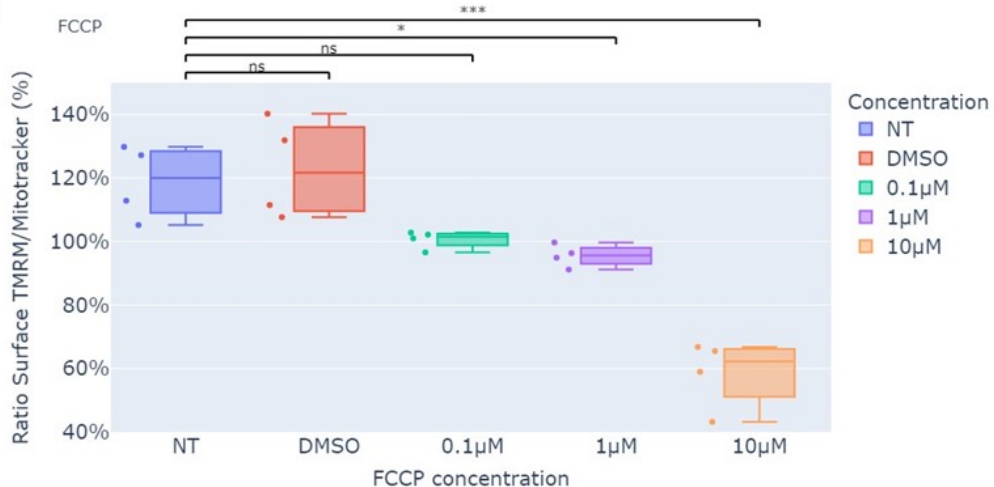
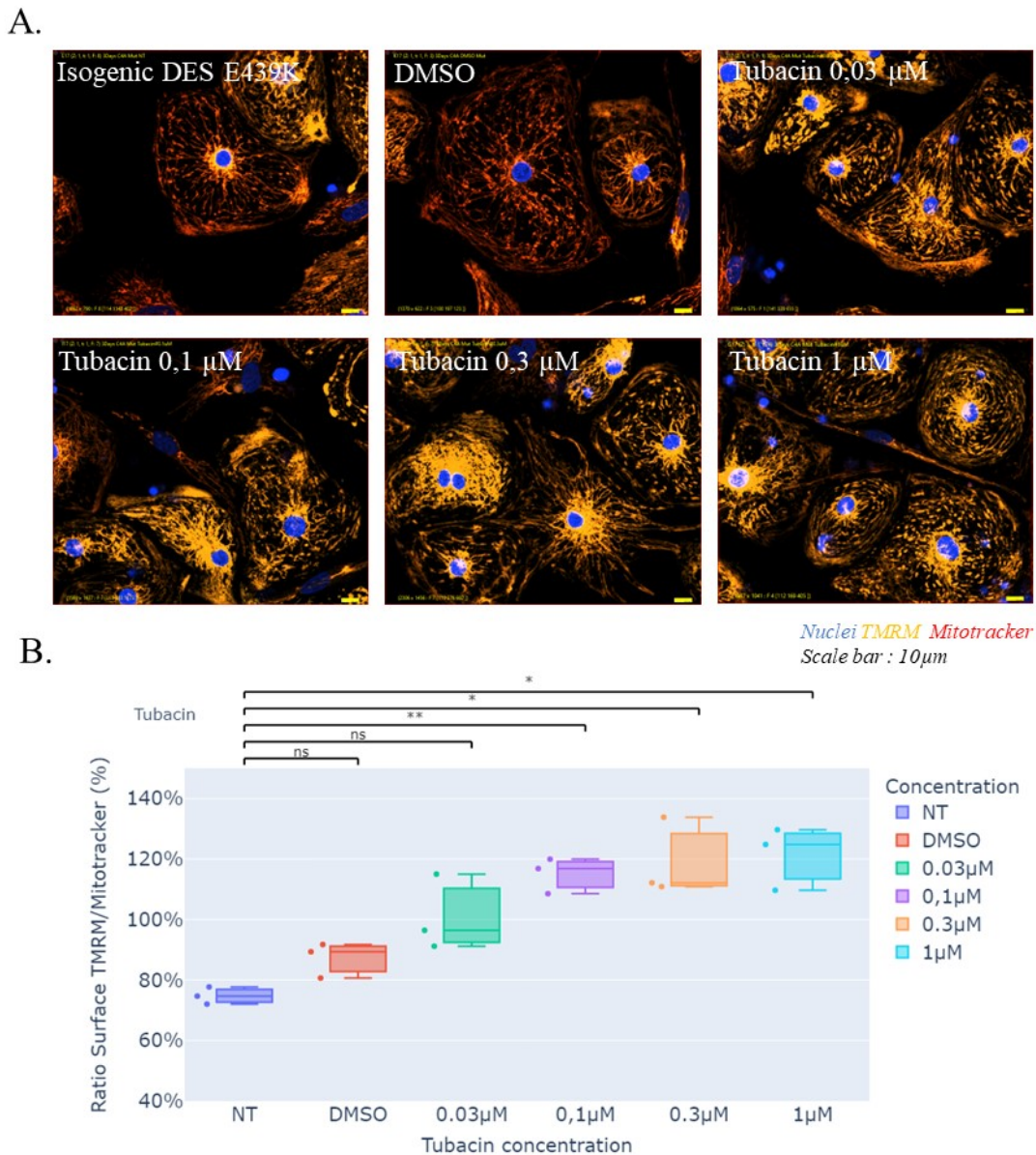


Figure 65 : A. Live staining TMRM/Mitotracker of Isogenic DES E^{439K} iPSC-CM treated with FCCP at different concentration. Scale bar=10 μ m. B. Ratio Surface TMRM signal normalize by Mitotracker signal of Isogenic DES E^{439K} iPSC-CM depending of the FCCP concentration. Values

*are expressed as mean ± standard deviation of n= 4 technical replicates. A two-tailed t-test was performed. ns not significant. * p-value<0.05 ** p-value<0.005. *** p-value<0.0005. **** p-value<0.0005.*

Positive Control (Tubacin)

Isogenic *DES* E439K iPSC-CM were cultured for 7 days in T3DEX culture medium before treatment for 3 days with Tubacin an HDAC6 inhibitor (D. Zhang et al., 2016). HDAC6 has been described to have a regulator role in mitochondrial dynamics (English & Barton, 2021). On the last day of treatment, iPSC-CM were live-stained with TMRM (Active mitochondria) and Mitotracker (Total mitochondria) (Figure 66A). The ratio of the TMRM staining area to the Mitotracker staining area as function of the treatment conditions was calculated (Figure 66B). Once again, different treatment conditions were tested. The NT condition corresponded to the first negative control, where iPSC-CM were not treated. The DMSO condition referred to the second negative control, where iPSC-CM were treated with the same concentration of DMSO found in the 1μM Tubacin condition. Indeed, the last four conditions corresponded to conditions where iPSC-CM were treated with 4 concentrations of Tubacin (0.03; 0.1μM; 0.3μM and 1μM) (Figure 66B). As previously, no significant difference was measured between NT and DMSO conditions. Treatment of iPSC-CM with different concentrations of Tubacin induced a significant increase in the TMRM/Mitotracker surface ratio in the 0.1μM, 0.3μM and 1μM Tubacin conditions. This increase seems to follow a dose-response dynamic.

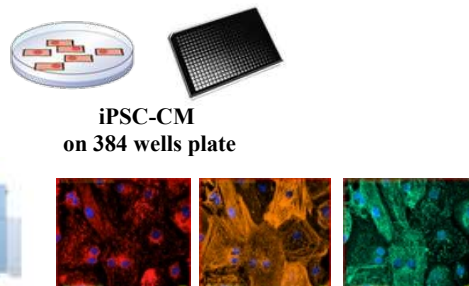


*Figure 66 : A. Live staining TMRM/Mitotracker of Isogenic DES ^{E439K} iPSC-CM treated with Tubacin at different concentration B. Ratio Surface TMRM signal normalize by Mitotracker signal of Isogenic DES ^{E439K} iPSC-CM depending of the Tubacin concentration. Values are expressed as mean \pm standard deviation of n= 3 technical replicates. A two-tailed t-test was performed. ns not significant. * p-value<0.05 ** p-value<0.005. *** p-value<0.0005. **** p-value<0.0005.*

These results showed that it was possible to induce effects on mitochondrial activity in iPSC-CM. These effects can be quantified by analysis of the TMRM/Mitotracker surface ratio. Because of its live staining approach, this mitochondrial assay is difficult to perform on a large scale in a high-content assay testing thousands of molecules. However, it can be considered as a secondary assay after an initial identification of compounds inducing an effect on iPSC-CM (Hit), the mitochondrial assay can be used to refine the Hit selection.

iPSC-CM culture optimisation

DES^{E439K}



Immunocytostaining (Mitochondria, Troponin T, Desmin)

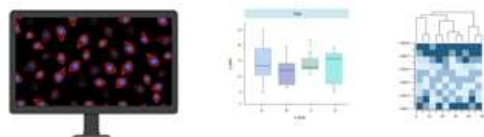
- ✓ Cellular batches quality control
- ✓ Optimisation cell culture for desmin expression ↑

Physiopathologic mechanism



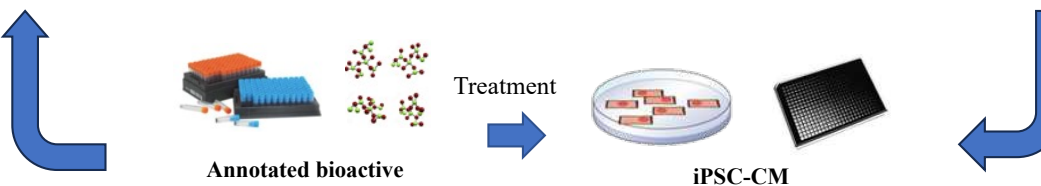
- ✓ EHM contractility ↓
- ✓ iPSC-CM mitochondrial respiration ↓
- ✓ iPSC-CM Desmin aggregation ↑
- ✓ iPSC-CM Autophagic flux ↑
- ✓ EHM PQC response transcriptomic signature ↑

Phenotype quantification



- ✓ Manual annotation Desmin → Mislocalisation ↑
- ✓ Manual annotation TroponinT → Disorganisation ↑
- ✓ Ratio TMRM/Mitotracker ↓
- ✓ Automated classification models → Strong F1 score ↑

Small screening



- ✓ Toxic profile class implementation
- ✓ Rescue effect
 - Istaroxime hydrochloride
 - GO 6976 and SB 203580 combination
 - Tubacin

- Characterisation of physiopathologic mechanism
 ➤ Identification of new therapeutic approaches

↓ Decrease ↑ Increase

Figure 67 : Results overview

V. DISCUSSION

V.1. Disease modeling: a perspective on opportunities and limitations

Throughout my thesis, I utilized various human-induced pluripotent stem cell (iPSC) lines. These encompassed healthy iPSC lines, iPSC lines derived from patients (obtained by isolating peripheral mononuclear blood cells from one *DES*^{E439K} patient and subsequently reprogramming them into iPSC lines), and genetically modified iPSC lines where a *DES*^{E439K} mutation was introduced. The advantage of patient-derived *in vitro* models lies, firstly, in their direct derivation from the patient. This implies that the whole genetic “environment” that could be relevant to the severity of the symptoms is still under investigation. Furthermore, this lets researchers reproduce pathological cellular or tissue phenotypes based on the same perturbations as in the patient. On the other hand, we employed isogenic iPSC lines with and without *DES*^{E439K} mutation, which enabled us to precisely examine the impact of *DES*^{E439K} mutation on the development of relevant *in vitro* disease phenotypes. Both approaches are ideal for studying pathophysiological mechanisms, understanding cellular responses to perturbation or evaluating potential treatments (Nicholson et al., 2022). In cardiac pathology studies, these models are particularly interesting due to the difficulties inherent in isolating adult human cardiomyocytes from patients. The *in vitro* human models used here are based on induced pluripotent stem cells that were differentiated into cardiomyocytes (iPSC-CM). The production of these cells was possible due to an efficient cardiac differentiation protocol that was optimized in our labs. Several types of protocol exist, and will vary according to the research objectives, depending on the precision of the targeted cardiac subtypes, for example ventricular vs atrial cardiomyocytes. In all cases, one of the limitation in this field is the lack of generating fully mature iPSC-CM (Denning et al., 2016).

V.1.1. Immaturity of iPSC-CM

Most cardiac differentiation protocols yield iPSC-CM that share characteristics with isolated fetal immature cardiomyocytes (Feyen et al., 2020). In this project, it was shown that iPSC-CM had low levels of lineage-specific labeling in the ventricular (MYL2) and atrial (NR2F2) cardiac (Jiuru Li et al., 2022). This may be associated with the immaturity of iPSC-CM still at a progenitor stage not expressing lineage-specific markers (Bizy et al.,

2013). Regarding atrial cell staining, it would be interesting to find a more specific stain than NR2F2 (COUP-TFII). Indeed, some cells were negative to cardiac cTnT isoform staining and positive to NR2F2 staining. It has been shown that NR2F2 play a multifunctional role in the development and regulation of various physiological processes in tissues such as cardiovascular, reproductive system, endocrine organs and adipose tissue (Polvani et al., 2020). Thus, it would be interesting to find another marker more specific to atrial cardiac lineages. A study highlighted the involvement of Human Atrial Natriuretic Peptide (hANP) in the relationship between stretch and arrhythmogenesis in the human atrium. In fact, hANP is synthesized and stored as a pro-hormone in granules localized in human atrial cardiomyocytes (Lonardo et al., 2004). In the future, the identification of atrial cardiac lineages could be based on hANP staining.

Immunocytochemistry for desmin revealed that a certain proportion of iPSC-CM lacked desmin expression. Indeed, expression of desmin has been shown to be progressively increase during the development and maturation of iPSC-CM in prenatal rat heart (Ya et al., 1997). Given the pivotal role of desmin in cardiomyocyte function and its close association with structural and functional maturity (Tsikitis et al., 2018), inducing iPSC-CM maturation was a crucial aspect of this project to more accurately generate adult iPSC-CM. Two strategies for promoting iPSC-CM maturation were explored. The first strategy, based on extended culture time, demonstrated a positive correlation between duration and desmin expression, indicating that longer culture periods led to greater desmin expression. Additionally, a chemical approach involving treatment with glucocorticoid hormones, dexamethasone, and triiodothyronine, also exhibited an increase in desmin expression. These findings underscored the feasibility of inducing iPSC-CM maturation to enhance the model. Another study on iPSC-CM maturation also shown that glucocorticoid hormones dexamethasone and triiodothyronine treatment could be an effective approach to rapidly enhance electrophysiological maturation of iPSC-CM (L. Wang et al., 2021).

Interestingly, desmin levels varied among different iPSC-CM groups (Control; Isogenic *DES*^{E439K}; Patient *DES*^{E439K}), despite identical differentiation and culture conditions. This discrepancy suggests that factors specific to the genetic background of each cell line may influence desmin expression during development. Studies on desmin expression in muscle tissue have shown that the desmin gene is controlled by a combination of different transcriptional regulatory regions in muscle tissues (Paulin & Li, 2004). Moreover, this team show that the transcriptional regulator MyoD, MEF2, and Mt site, function

synergistically to produce maximum expression of the desmin gene in myotubes (Gao et al., 1998). It would therefore be interesting to explore the mechanisms of transcriptomic regulation of the *DES* gene in the different lines. Metabolic stimulation was also tested by inducing a shift from glycolytic to fatty acid-based oxidative metabolism. Although described by other studies as a successful strategy (Feyen et al., 2020; X. Yang et al., 2019), this maturation method did not improve desmin expression levels. This result should be relativized or confirmed with a complementary quantitative experiment such as a western blot quantifying desmin expression according to iPSC-CM metabolic conditions. Future exploration of additional characteristics, such as sarcomeric organization at the morphological level or calcium flux measurement at the functional level, could provide further insights into cardiac maturity.

The maturity of iPSC-CM holds significant relevance in pathological modeling. Notably, the expression of specific pathological phenotypes has been observed to correlate with the maturation level of iPSC-CM (Vučković et al., 2022). The results of annotation analyses of iPSC-CM at single-cell level in the different groups (Control, Isogenic *DES*^{E439K} and Patient *DES*^{E439K}) showed for the desmin phenotype, a high proportion of iPSC-CM displaying a diffuse desmin signal, testifying to an organization that is neither striated, as found in healthy adult iPSC-CM, or aggregated, as can be found in iPSC-CM carrying *DES*^{E439K}. Indeed, iPSC-CM are probably at an early stage of cardiac development where desmin are not yet fully organised. This early stage of maturity can explain the annotation analysis based on cTnT phenotype, where in all three groups a low frequency of iPSC-CM displaying striated sarcomeric fiber was observed. Thus, the cTnT phenotype made it difficult to robustly discriminate control iPSC-CM from those carrying the *DES*^{E439K} mutation. Indeed, the results of the automated classification model based on cTnT phenotype confirmed that sarcomeric organization was the least prominent pathological phenotype in comparison with desmin and mitochondrial phenotypes. An increase in iPSC-CM maturity would probably lead to better visibility of pathological phenotypes.

Work not presented in this thesis exploring other iPSC-CM maturation strategies has been realized. Indeed, the cultured of iPSC-CM on an innovative soft well plate containing micropatterned vitronectin-coated hydrogels was investigated (Figure 72). The use of a soft stiffness (11kPa) and micropatterned (Width 28μm) plate seems interesting to improve the distribution of iPSC-CM sarcomeric organization state towards a majority of well-organized iPSC-CM (Figure 73;Figure 74). Thus, Optimization of the culture medium,

rigidity and anisotropy were then investigated as important parameters for *in vitro* iPSC-CM development (Rodriguez et al., 2019).

V.1.2. Isogenic pairs CRISPR/Cas9 and Monogenic disease

In vitro modeling usually focuses on a specific genetic mutation, assuming that this mutation is the main cause of the pathology. However, in some cases, diseases may result from a complex interaction between several genetic and environmental factors. Even if a genetic mutation is identified as responsible for a disease, other genetic variations in the individual's genetic background may influence the clinical presentation and severity of the disease and may then play a significant role (Panda et al., 2023). To assess the specific severity of the *DES*^{E439K} mutation, the *in vitro* modeling was based on CRISPR/Cas9 genetic engineering. This genome-editing method enabled the introduction of the *DES*^{E439K} mutation into a control line, thus producing an isogenic pair with the same genetic background and distinct only at the level of the *DES* mutation. The phenotypic differences identified between iPSC-CM isogenic *DES*^{E439K} and isogenic control could be directly attributed to the presence of the *DES*^{E439K} mutation.

Since dilated cardiomyopathy associated with the *DES*^{E439K} mutation is a monogenic disease (Wahbi et al., 2012b), it was expected that isogenic *DES*^{E439K} iPSC-CM would display similar phenotypes as patient *DES*^{E439K} iPSC-CM. Our results presented in the thesis showed the phenotypic isogenic *DES*^{E439K} iPSC-CM appeared to be affected a bit less severely, than the patient *DES*^{E439K} iPSC-CM. For example, the analyses of desmin and cTnT morphological phenotypes reveal that isogenic iPSC-CM appeared to have an intermediate profile between control iPSC-CM and patient *DES*^{E439K}. Finally, mitochondrial monoparametric analyses also showed more severe decreases in mitochondrial activity and mitochondrial number in patient *DES*^{E439K} iPSC-CM than in isogenic *DES*^{E439K} iPSC-CM. These results clearly demonstrate that *DES*^{E439K} mutation induce specifically several perturbations in iPSC-CM. But it also highlights that genetic background may contribute to the phenotype observed. In general, the severity of the perturbations seems to be higher in iPSC-CM derived from patient cells. To take into account this limitation and ensure that the phenotypes observed are mainly due to the *DES*^{E439K} mutation, it would be interesting to edit the genome of the patient *DES*^{E439K} line to correct the mutation. In this way, a new isogenic pair would be generated comprising the patient *DES*^{E439K} line and a corrected *DES* line which could then be combined with a

control line (Figure 68). Moreover, the generation of iPSCs from other patients affected by dilated cardiomyopathy associated with myofibrillar myopathy due to DES^{E439K} would also be a considerable contribution. The specificity of CRISPR/Cas9 still needs improvement. A major concern with the application of this system is off-target mutagenesis (Yuanwu Ma, Zhang, et al., 2014). Many studies have reported off-target events and an increasing attention has been given to improving the specificity of this approach (S. W. Cho et al., 2013; Yuanwu Ma, Shen, et al., 2014).

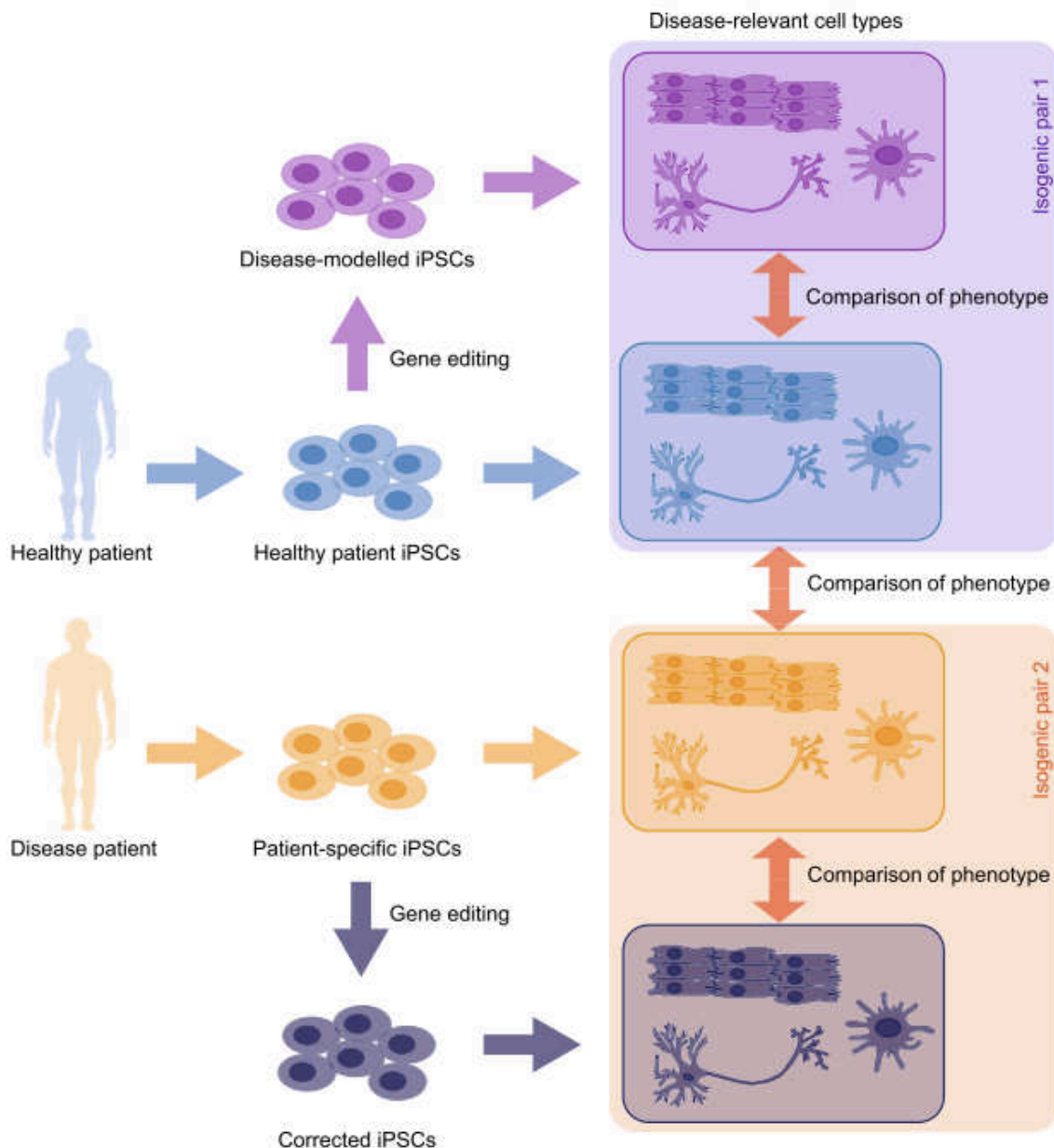


Figure 68 : Strategies for genome editing in iPSC disease modelling from (Bassett, 2017a)

V.1.3. Engineered human myocardium limited for high-throughput phenotypic studies

To overcome the limitations of the *in vitro* 2D model, more complex structures were considered for the studies led during the PhD. Thus, the engineered human myocardium (EHM) has been used. Composed of iPSC-CM, primary fibroblast and collagen fiber, the EHM allows more faithful reproduction of the structure and function of human cardiac muscle. Control EHM and EHM derived from *DES*^{E439K} patients were generated for this work and revealed a defect in the contractile functionality of *DES*^{E439K} patient EHM. This functional phenotype is a key phenotype of the pathology and is obviously found in patients carrying the *DES*^{E439K} mutation.

V.2. Characterization of phenotypes associated with *DES*^{E439K} mutation

The purpose of this research was to set up a model allowing the high throughput evaluation of cellular phenotype of dilated cardiomyopathy associated with myofibrillar myopathy due to a *DES*^{E439K} mutation. It was already known that most of the desminopathies induce a loss of the desmin network, which may be associated with desmin aggregation, mitochondrial network alteration and myofibril disorganization associated with a contractility defect (Tsikitis et al., 2018).

V.2.1. *DES*^{E439K} induced Desmin aggregation, Mitochondria alteration and Sarcomere defect

Firstly, this project shows the emergence of a desmin phenotype characterized by the loss of desmin network and by what seem to be aggregation structures. This information is interesting because *DES* mutations affecting the C-terminal tail of the protein are associated with loss of the desmin network, but not necessarily with aggregation (Brodehl et al., 2018). This phenomenon of desmin aggregation due to the *DES*^{E439K} mutation has also been highlighted in work conducted in the laboratory and published (Hovhannisyan et al., 2023).

Secondly, the mitochondrial phenotype was also highlighted. Staining of active mitochondria with high mitochondrial membrane potential showed that the *DES*^{E439K} mutation appeared to induce a decrease in the proportion of active mitochondria. Moreover, the total number of mitochondria also appeared to be lower in iPSC-CM carrying the *DES*^{E439K} mutation. These results point to a disruption of the mitochondrial network, which may

be associated with an imbalance in mitochondrial homeostasis. The idea that a desminopathy environment could be associated with disruption of mitochondrial fission/fusion equilibrium has been indicated in several studies (Alam et al., 2018). These disturbances in the mitochondrial network are likely to induce the functional disruption of mitochondrial respiration highlighted in this project. This is probably at the origin of the oxidative stress present in this *DES*^{E439K} mutation context, as shown by the RNAseq result indicating up-regulation of the oxidative stress response pathway.

Finally, this work also clearly confirms the appearance of a sarcomeric phenotype associated with the *DES*^{E439K} mutation, as shown by the result of annotation of iPSC-CM based on the cardiac cTnT signal. iPSC-CM carrying the *DES*^{E439K} mutation appear to display disorganized sarcomeric structure. Indeed, desmin confer mechanical stability to the sarcomere by forming transverse connections between adjacent myofibrils and provided the three dimensional organization of the sarcomere (Marzuca-Nassr et al., 2018). As suggested by studies on a *DES*^{-/-} mice model (Z. Li et al., 1997) and *DES*^{-/-} zebrafish model (Mei Li et al., 2013), loss of desmin can leads to disorganization and eventually disintegration of the Z-discs. Thus, the *DES*^{E439K} mutation could induce a loss of desmin function leading to sarcomere disorganization. Then, it is possible to associate the sarcomeric phenotype with the appearance of a contractile function defect in *DES*^{E439K} EHM. However, this contractile defect may also be due to other causes, such as a reduction in the energy resources available to the cell as a result of other disturbances associated with the *DES*^{E439K} mutation (S. Singh et al., 2020).

V.2.2. Proteostasis response to aggregate protein and dysfunctional mitochondrial stress

RNAseq analysis of EHM revealed up-regulation of unfolded protein and oxidative stress response mechanisms. We can drive the hypothesis that the formation of desmin aggregates together with mitochondrial dysfunction may be correlated to these mechanisms. Indeed, studies have shown that in a context of proteostasis and mitochondrial stress, protein and organelle quality control mechanisms can be requested to ensure cellular homeostasis (Brundel, 2020; Ghosh et al., 2020; Henning & Brundel, 2017a). Further analysis of the transcriptome from *DES*^{E439K} EHM showed up-regulation of genes involved in the chaperone, UPS and autophagic protein systems. This strongly suggests that the PQC machinery is activated in the context of *DES*^{E439K} mutation. There is an up-regulation

expression of the following proteins: The mitochondrial protein-specific chaperone protein HSPD1(Melber & Haynes, 2018), which plays a role in oxidative stress response and mitochondrial protein quality regulation; the protein Mdm2, which also plays a role in oxidative stress and mitochondrial disruption response through the regulation of p53 (Hauck et al., 2017); the mitochondrial Pink1 kinase involved in mitophagy regulation (Ramaccini et al., 2021). These events suggest that mitochondrial stress plays an important role in the activation of PQC systems (Figure 69), which is not only due to the presence of desmin aggregates. Indeed, there is different mitochondrial stress response pathway. First, the degradation of damaged mitochondria is mediated by mitophagy. The kinase PINK1 is stabilized specifically on damaged mitochondria, where it recruits the ubiquitin ligase Parkin, which ubiquitinates multiple mitochondrial outer membrane proteins. Ubiquitinated mitochondria are then engulfed by autophagosomes and trafficked to lysosomes where they are degraded (Ashrafi & Schwarz, 2013). Then, the kinase GCN2, which is activated during mitochondrial dysfunction, mediates translation attenuation by phosphorylating the translation initiation factor eIF2 α , which serves to reduce the influx of proteins into mitochondria (Harding et al., 2003). Accumulation of mislocalized mitochondrial proteins in the cytosol stimulates proteasome activity to limit the accumulation of the toxic proteins in a pathway dubbed unfolded protein response activated by mistargeted proteins (Wrobel et al., 2015). Finally, the mitochondrial unfolded protein response (UPRmt) is regulated by the competing organelle targeting sequences in the transcription factor ATFS-1. If ATFS-1 is imported into the mitochondrial matrix via the UPRmt, the transcription factor is degraded. However, if ATFS-1 cannot be imported due to mitochondrial dysfunction, it is trafficked to the nucleus, via the NLS, to activate transcription of protein involves in UPRmt (Pellegrino et al., 2014).

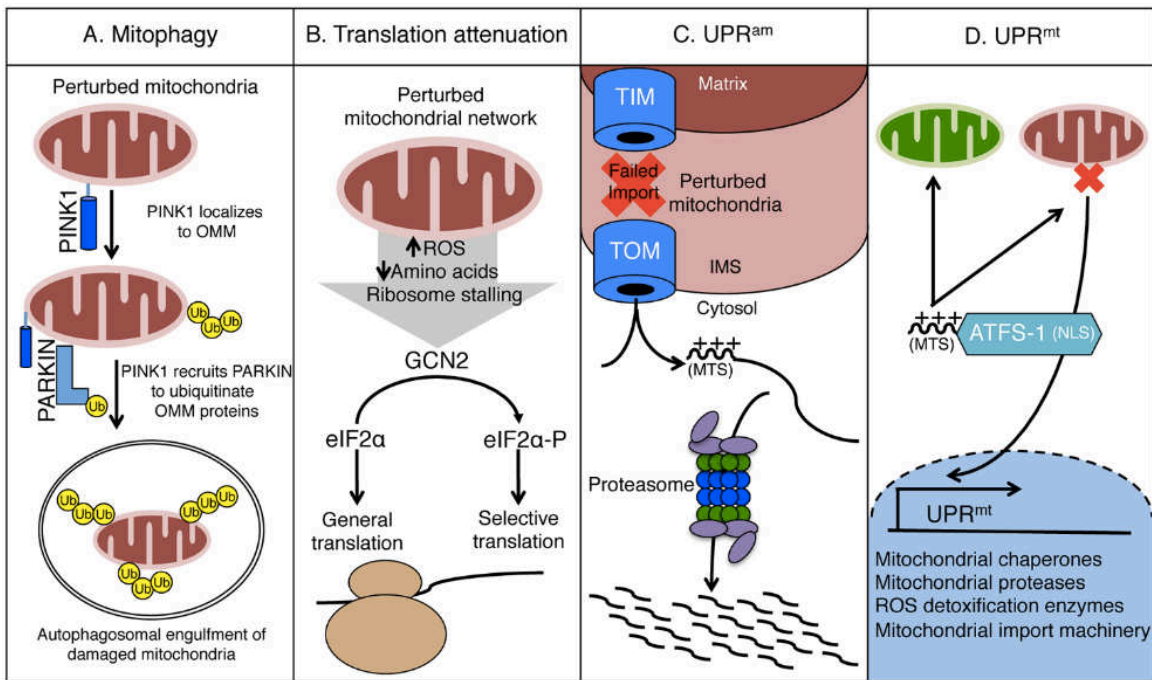


Figure 69 : Mitochondrial stress response pathway from (Melber & Haynes, 2018)

Secondly, analysis of autophagic flux clearly showed an increase of the process in iPSC-CM *DES* E439K compared with iPSC-CM controls. This is an interesting finding, as the autophagic system is a process for degrading aggregated proteins and defective organelles, it is essential for ensuring both protein and mitochondrial homeostasis (Sciarretta et al., 2018). Moreover, an analysis on the protein expression of p62/SQSTM1, a cargo protein involved in the autophagic process (Yoshii & Mizushima, 2017) seemed to indicate, in patient *DES* E439K iPSC-CM, a form of autophagic flux blockade (data not shown in the thesis due to the lack of statistical test, Figure 75). It is possible that overactivation of this system induces saturation of the process (Ghosh et al., 2020). It would be interesting to carry out further studies to identify the state of the different phases of autophagy. Moreover, it might be useful to study in detail the potential saturation of autophagic systems. In particular, investigation of macroautophagy (degradation of aggregates) and mitophagy (degradation of mitochondria) would allow us to estimate their respective states and provide information on the mechanisms involved in this disruption. Although closely related and interconnected, it has been shown that these two systems can be regulated differently in post-myocardial infarction (Sciarretta et al., 2018). In the context of post-myocardial infarction, macroautophagy has been described as inhibited via activation of the pro-apoptotic kinase Mst1 (Maejima et al., 2013). Whereas mitophagy was activated via overexpression of the ubiquitin ligase Parkin (Kubli et al., 2013).

The study of proteostasis-related mechanisms involved in the establishment or maintenance of pathological cell phenotypes was conducted with the aim of identifying therapeutic targets for DCM associated with desminopathy. Indeed, this work could be used to implement a tool compound assay targeting compounds with mechanisms of action interacting with PQC systems. The objective would be to restoring morphological and functional defects involving desmin, mitochondria and sarcomeres. Thus, a study showed that treatment of C2C12 myoblastic cells expressing mutant *DES* with PPP242, an inducer of autophagy, resulted in a decrease of desmin aggregation (Cabet et al., 2015). Another study reported that treatment of *CryAB*^{R120G} mice with Oxypurinol, a xanthine oxidase inhibitor that reduces ROS production and oxidative stress, induced an improvement in mitochondrial function (Maloyan et al., 2009).

We highlight that some annotated compounds look to induce rescue of the pathological phenotype in *DES*^{E439K} isogenic iPSC-CM. First, Istaroxime hydrochloride is a steroidal drug unrelated to cardiac glycosides that improves cellular calcium cycling by dual action. Firstly, SERCA 2a stimulation which cause rapid Ca²⁺ sequestration in sarcoplasmic reticulum during diastole (lusitropism) without enhancing spontaneous Ca²⁺ efflux from the sarcoplasmic reticulum. Secondly, Na⁺-K⁺ ATPase inhibition which induce cytosolic calcium accumulation during systole (inotropism) (Micheletti et al., 2007). A study indicated that preventing serine 663 phosphorylation of SERCA2, significantly increases SERCA2 activity, contributing to the protection and recovery of ischemic heart (Gonnot et al., 2023). Then, the combination of GO 6976 an inhibitor of protein kinase C (Martiny-Baron et al., 1993) and SB 203580 an inhibitor of a Map kinase (Cuenda et al., 1995) were described to rescue dilated cardiomyopathy phenotype (Perea-Gil et al., 2022). The rescue occurs by the activating of transcription factor 4 (ATF4) and its downstream effector genes (Perea-Gil et al., 2022). During endoplasmic reticulum (ER) stress response, the PERK-eIF2α-ATF4 signaling pathway is activated (Doyle et al., 2011). ATF4 is activated by the phosphorylation of the eukaryotic initiation factor 2α (eIF2α). ATF4 up-regulates the pro-apoptotic factor C/EBPα-homologous CHOP which subsequently regulates the balance between proapoptotic and antiapoptotic B-cell lymphoma (BCL)-2 family proteins (Ghemrawi et al., 2018). ATF4 and CHOP will also initiate the UPRmt which active the mitophagy (Jin Li et al., 2019).

Indeed, these results encouraged further investigation of the ER stress process. By re-analysing the transcriptomic signatures of EHM *DES*^{E439K}, it was possible to identify an up-regulation of genes involved in ER stress response mechanisms (Figure 70).

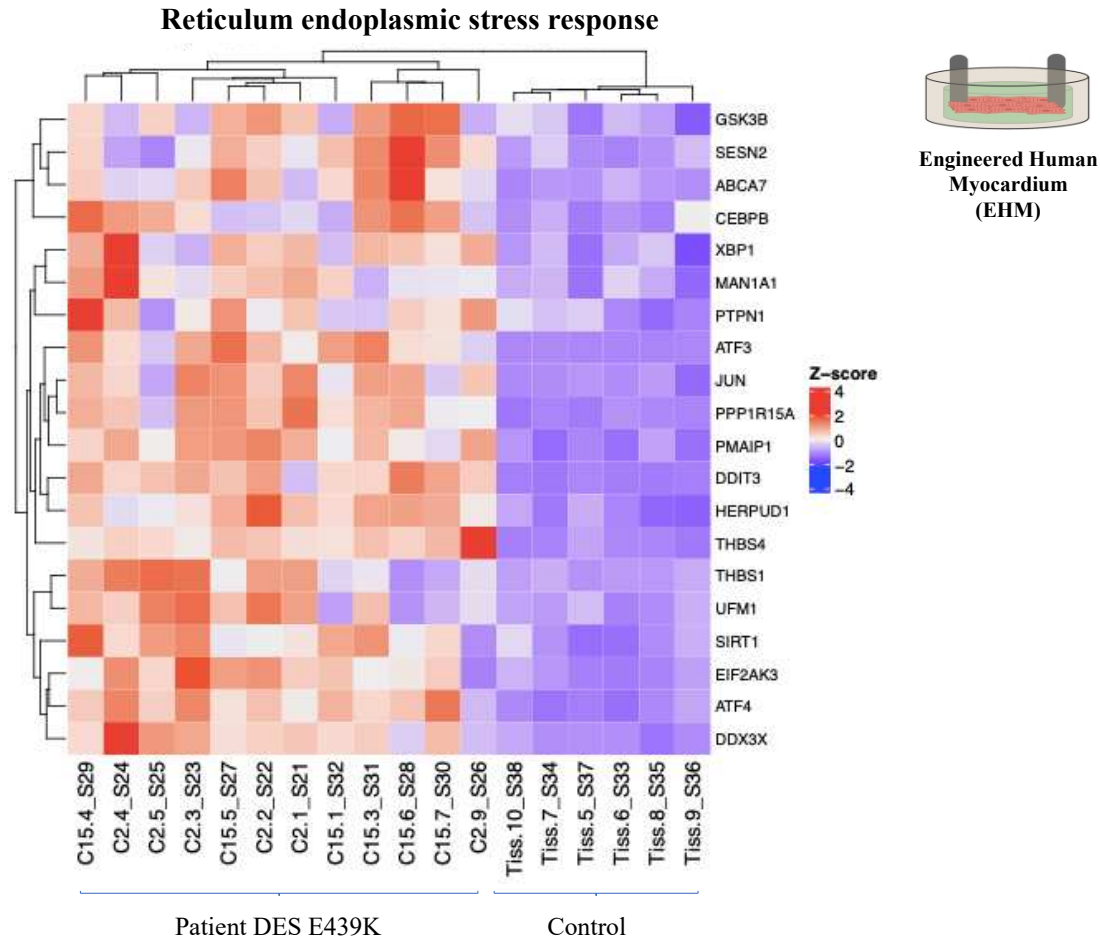


Figure 70 : Heatmap showing expression patterns of selected genes related to ER stress response process, giving specific transcriptomic profiles of EHM Patient *DES*^{E439K} and control

The ER stress response is a complex cellular mechanism which is activated in response to disturbances in the homeostatic equilibrium of the ER (Figure 71). The ER stress response aims to restore protein homeostasis by regulating protein synthesis, promoting correct protein folding, or inducing degradation of misfolded proteins. The ER stress response could be a key element to explore, particularly if protein aggregates or mitochondrial dysfunction can influence this response. Indeed modulation of the ER stress response could potentially offer therapeutic strategies to mitigate the effects of the *DES*^{E439K} mutation. It would be interesting to study this pathway in greater depth in the future, in order to better characterize the mechanisms underlying the establishment and maintenance of pathology. Modulation of the ER stress response could potentially offer

therapeutic strategies to mitigate the effects of the *DES*^{E439K} mutation (Pietrafesa et al., 2023).

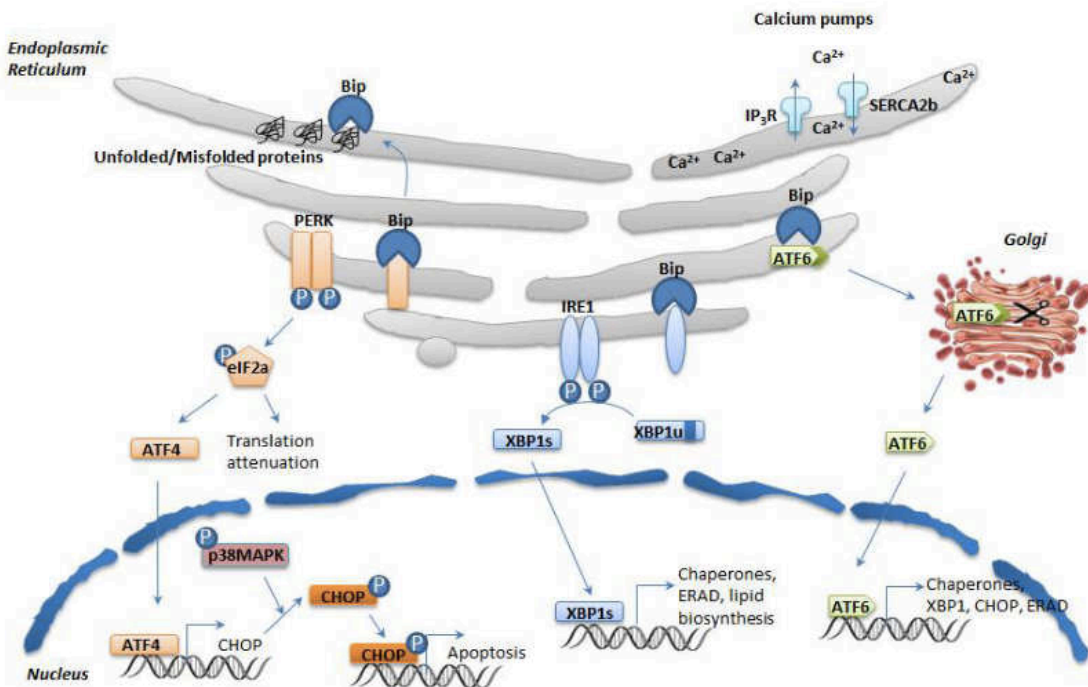


Figure 71 : Endoplasmic reticulum stress and Unfolded protein response from (Jin Li et al., 2019)

Furthermore, treatment of *DES*^{E439K} isogenic iPSC-CM with the HDAC6 inhibitor tubucin induced an increase in the ratio of active mitochondria. Targeting the restoration of mitochondrial activity and function is a very interesting therapeutic approach. It has been shown that the transfer of exogenous functional mitochondria restores the metabolism and contractile function in *DES*^{E439K} iPSC-CM (Hovhannisyan et al., 2023). Moreover, SAHA an HDACs inhibitor has been described as an inducer of autophagy and mitochondrial biogenesis to maintain mitochondrial homeostasis during cardiac ischemia/reperfusion injury (Jing Yang et al., 2019). Moreover, it was determined that HDAC6 is a key regulator in multiple mechanisms of mitochondrial dynamics and may contribute to mitochondrial dysregulation in peripheral neuropathy (English & Barton, 2021). Indeed, HDAC6 is a cytoplasmic Class II histone deacetylase, known to target and enzymatically remove acetyl groups from post-translationally modified non-histone proteins, such as microtubules, and significantly alter target protein function (Hubbert et al., 2002). HDACs have recently been recognized as key modulators in controlling cardiac proteostasis by changing acetylation status of various proteins (McLendon et al., 2014). Inhibition of HDAC6 had already been shown to be cardioprotective at the sarcomere level in a BAG3 mouse model of dilated

cardiomyopathy (Jin Yang et al., 2022). Nevertheless, Tubastatin A, another HDAC6 inhibitor, was tested in our compound assays on isogenic *DES*^{E439K} iPSC-CM and cell profile classification analyses showed no effect on desmin, cTnT and mitochondrial phenotypes. In fact, a large number of HDAC6 inhibitors differ in selectivity and activity, based on their different zinc binding groups (X. X. Wang et al., 2018). In conclusion, HDAC6 inhibition seems to be a really interesting way of restoring mitochondrial function, and an interesting therapeutic approach for dilated cardiomyopathy.

V.2.3. *DES*^{E394K} impairs cardiac development

Transcriptomic analysis of the patient *DES*^{E439K} EHM showed a signature of cardiac immaturity not found in the control EHM. Since the generation of EHM from the different groups was executed under the same conditions, it can be deduced that the *DES*^{E439K} mutation is responsible for the cardiac immaturity. Indeed, a variety of cardiac pathophysiologic conditions induce the postnatal heart returns to the “fetal” gene program. These adaptive mechanisms are also a feature of the failing heart muscle, where at a certain point this fetal-like reprogramming no longer suffices to support cardiac structure and function (Taegtmeyer et al., 2010). Moreover, the desmin protein is known to play a role in cardiac development (Höllrigl et al., 2007).

V.3. High-content imaging and screening strategies

The final challenge of this project was to set up a high-content imaging assay based on image-based profiling. These approaches are a real challenge, enabling more in-depth studies to characterize pathophysiological mechanisms and identify new therapeutic approaches.

V.3.1. Phenotypic characterization using HCI and image-based profiling

Firstly, high content imaging and image-based profiling provide a standardized and automated approach for studying the morphological phenotypes of iPSC-CM. Once the parameters have been established, a large quantity of images can be acquired and analyzed automatically, saving significant time compared with traditional methods. The automation of these approaches reduces operator bias, thus improving the reproducibility of experiments. Image-based profiling focuses on the phenotypic characterization of cells using quantitative descriptors extracted from images. It enables the identification of unique cellular signatures associated with specific conditions, facilitating the classification and

understanding of cellular phenotypes (Chandrasekaran et al., 2020). In this project, the goal was to identify phenotypic signatures allowing to discriminate the cellular profiles of iPSC-CM carrying a *DES*^{E439K} mutation from the cellular profiles of iPSC-CM controls.

The acquisition of high-resolution images from single cells offered the possibility of performing detailed analysis of cellular characteristics, allowing rare events to be identified or to quantify the severity of different phenotypes. In order to perform a single-cell analysis, the cells were segmented using the cropping method, which consisted after segmentation of the nuclei, in cropping around a nucleus and considering a crop to be equivalent to one cell (Heo et al., 2017). This technique allows simple segmentation of cells and avoids the need for membrane staining to identify cell borders. However, this segmentation does not allow access to information such as cell shape and size. In addition, cell overlap at high densities means that cropping may not provide correct separation between adjacent cells.

In this project, the performance results (F1 score) for different classification models (Control cellular profile versus *DES*^{E439K} cellular profile) specific to a given phenotype (Desmin, cTnT or Mitochondria) enabled the hierarchization of phenotypes according to their severity to be presumed. Thus, the classification model specific to the desmin phenotype presented an F1 score of 100%. The mitochondrial phenotype classification model had an F1 score of 85%. Finally, the cTnT phenotype classification model had an F1 score of 81%. These results indicate that the phenotypic signature permitting the distinction between control and *DES*^{E439K} cellular profiles is most pronounced in the desmin phenotype, then mitochondrial and finally cTnT. According to studies on the establishment of these pathology, desminopathy is characterized by the appearance of the desmin phenotype followed by the mitochondrial phenotype before the sarcomeric phenotype (Alam et al., 2020). Multiparametric analysis enables the simultaneous measurement of several parameters, in this case several phenotypes (desmin, cTnT or mitochondria). It was thus possible to generate a classification model based on all three phenotypes simultaneously, with an F1 score of 100%. Indeed, this was expected after the F1 score of 100% obtained only with the desmin phenotype. Moreover, the Z scores of the two models (Desmin and combined) are kind of identical. Thus, the combination of the three phenotypes does not seem to improve the separability of the two iPSC-CM groups, reflecting the strong phenotypic signature of desmin in this model. It would be interesting to study other types of combination, such as mitochondria and cTnT, and then evaluate classification performance.

A machine learning algorithm (LDA) is used to implement classification models that aim to separate control and *DES*^{E439K} cell profiles based on morphological phenotypes. This type of algorithm maximizes dataset separation, so in this study the objective was to separate the set of control cell profiles with the set of *DES*^{E439K} cell profiles, while minimizing the variance within each dataset. Moreover, it would be possible to improve the performance of classification models by relying on another, more powerful type of algorithm: deep learning (Angermueller et al., 2016). Deep learning excels at handling complex data, so if the control and pathological phenotypes are too close and difficult to distinguish, this method may be more appropriate. Indeed, deep learning models can learn complex, non-linear representations of data, making them suitable for more challenging tasks. However, they can be less interpretable due to their complexity. This is why the LDA method has been prioritized in this project, as the interpretability of the features used for profiling remains important for a better understanding of the phenotypes studied.

V.3.2. Screening and tool compounds

High-content imaging can be used to screen compounds. Depending on the compounds involved, these assays can have different objectives. Firstly, they can be used to identify new drug candidates by evaluating the effects of a variety of compounds on cells. Secondly, certain assays can lead to the clustering of compounds according to the phenotypic effect that the treatment will induce, thus it is possible to deduce the mode of action of unknown compounds from the fact that they are clustered based on the effect they induce with compounds whose mechanism of action is known. Finally, compounds can be used as experimental tools to explore biological mechanisms. These are often specifically designed to target a particular pathway or protein. The use of such compounds makes it possible to specifically investigate a biological process (Pegoraro & Misteli, 2017). This last aspect was particularly interesting for this thesis project. Indeed, this type of assay was selected to better characterize the establishment or maintenance of *DES*^{E439K} cellular phenotype based on desmin, cTnT and mitochondria.

The assay used in this project was therefore based on a classification model distinguishing isogenic control cellular profiles from isogenic *DES*^{E439K} cellular profiles. Initial results from the compound assay showed that some cellular profiles were incorrectly classified by the model as control, whereas the iPSC-CM images associated with these cellular profiles showed cellular toxicity characteristics. Thus, the classification models

were optimized to add a third class: the toxic cell profiles. Indeed, in most screening assays, a negative control inducing a cell toxicity phenotype is often used (Grafton et al., 2021; Perea-Gil et al., 2022).

The treatment modalities during screening must be established. First of all, the concentration of the compounds may be important: a too high a concentration may induce non-specific or toxic effects, while a too low concentration may have no detectable effect. With these constraints in mind, it was decided to use a range of concentrations from nM to μ M in this study. This allowed us to identify dose-response effects to determine the effective concentration range without causing toxicity. The results showed very little dose response for a rescue effect, but were more clearly identified for a toxic effect. It would be interesting to refine the panel of concentrations tested around those that seemed interesting for inducing a rescue effect.

Next, treatment duration and time were selected according to the modalities commonly used in this type of screening assay based on iPSC-CM (Grafton et al., 2021; Perea-Gil et al., 2022). Here, cell culture lasted ten days after thawing, with treatments starting on day 4 of culture. Two approaches were performed: first only one-time compound addition on day 4 of culture. Secondly, two-time repletion of compound treatment, first one on days 4 of culture and second one on day 6 of culture. Initially, the effects induced on cells by these two approaches were to be compared. Unfortunately, the sample sizes were too small for statistical tests. However, the effects induced on the cells by the treatments seemed similar in both approaches. Thus, they were considered as replicates for subsequent analyses. This appears to be a limitation of this experiment, which should be repeated to validate the results. In future, it would be preferable to use a single treatment duration. This duration could be selected by identifying the temporal dynamics of cellular responses to treatment, or the half-life of the proteins studied in the phenotypes of interest, such as desmin, cTnT or mitochondria. For example, in a study of C2C12 murine myoblasts transiently transfected with an expression vector encoding a GFP-tagged D399Y mutant desmin, the kinetics of mutant desmin aggregation were assessed, showing that aggregates were produced during the early latent period, 20 hours after transfection. In addition, a late stationary phase was identified 48 hours after transfection (Cabet et al., 2015). The same study showed that compound treatment for 16h, immediately after transfection, could lead to a decrease in aggregation.

Finally, the identification of compounds inducing a rescue effect was not the same according to the phenotype on which the classification model was based. Thus, Omecamtiv Mercabil seemed to have a small positive effect on cTnT and mitochondria phenotypes but no effect on desmin. Indeed, Omecamtiv Mercabil is a myosin activator, it could be interesting to investigate the interaction of myosin with cTnT and mitochondria. A study show that Omecamtiv Mercabil increase the Ca^{2+} sensitivity in myofilaments by favorising the connection between myosin and actin filament (Utter et al., 2015). This type of interpretation can help to determine new concepts to describe the pathophysiological mechanisms involved in the development of a specific phenotype.

To conclude, a more pragmatic approach could involve sequential screening, initially focusing on a simple phenotype, such as desmin. Then, with the selected compounds, another screening could be conducted based on the mitochondrial phenotype, and so forth. Each screening assay would be optimized in terms of culture time and treatment conditions according to the phenotype under investigation. After the selection of compounds (hits) inducing a rescue effect, a validation step could be undertaken using more complex functional assays, on the same model or on a 3D model such as EHM (Lampart et al., 2023). Hit could even be tested on another model of desminopathy associated with a distinct *DES* mutation. High-throughput screening assays open up a vast array of possibilities, often constrained by financial and time limitations.

VI. CONCLUSION AND PERSPECTIVE

Myofibrillar myopathies linked to desmin, also known as desminopathies, are rare genetic diseases caused by mutations in the *DES* gene primarily characterized by the progressive appearance of muscle weakness. In many cases, these pathologies are also associated with dilated cardiomyopathy, leading to heart failure, which is a major cause of death in these patients. Indeed, in addition to the disorders of cardiac contractility common to all dilated cardiomyopathies, those induced by a *DES* gene mutation are characterized by the presence of protein aggregates, mitochondrial dysfunction and myofibril disorganization. To date, no effective treatment, pharmacological or surgical approach, can reverse this progressive and disabling heart disease.

The purpose of this PhD was first to characterize the functional and morphological phenotypes of the pathology. Then to better shed light on pathophysiological mechanisms involved in the establishment and maintenance of the disease in order to open the way toward new therapeutic approaches. In this context, the precise aim was to focus on the state of proteostasis and protein quality control systems (PQC) in this pathological context.

First, functional defects were observed such as decrease in cardiac contractility in EHM and mitochondrial respiration in iPSC-CM carrying the mutation. Associated to these perturbations, we then highlighted strong morphological phenotypes characterized by desmin aggregation and disorganization of sarcomeric structures. In this context, we demonstrated that protein quality control systems were activated, probably in response to functional and morphological perturbations. The autophagic system, responsible for degrading abnormal protein aggregates but also dysfunctional organelles such as mitochondria, seemed particularly involved. Secondly, a multiparametric approach using high content imaging (HCI) was developed. HCI consists in simultaneously detecting and correlating a broad range of features extracted from immunocytostained cell images, based on machine learning (algorithms artificial intelligence). This method allows us to characterize pathological phenotypes more finely and to set up treatment assays with annotated compounds. The identification of compounds inducing phenotype rescue enabled the deduction of mechanisms involved in the establishment or maintenance of pathological phenotypes, based on the mechanisms of action of compounds already known.

In conclusion, we have demonstrated that protein quality control, mitochondrial and endoplasmic reticulum stress response mechanisms seem to play a role in the establishment or maintenance of the disease. Thus, they represent an interesting therapeutic target for patients with dilated cardiomyopathy associated with myofibrillar myopathy due to a *DES* mutation. Moreover, this thesis project highlights the complementarity of different strategies for identifying new therapeutic targets. Indeed, the identification and characterization of pathophysiological mechanisms responsible for the emergence and maintenance of functional and morphological phenotypes can be achieved in different ways. Firstly, through transcriptomic, biochemical and proteomic studies, where the objective is to target, at the molecular level, the perturbations responsible for the establishment of phenotypes. Secondly, by pathological phenotypic studies, where the objective is to identify disruptive agents (biological compounds, RNAi, etc.) which may rescue cells into a wild-type phenotype. Knowing the mechanisms of action of these disruptive agents, and comparing them with the molecular disruptions previously identified, these approaches could lead to the deduction of the pathophysiological mechanism cascade involved in the disease.

Finally, it would be interesting to study more precisely the mechanisms of protein and mitochondrial stress responses in relation with endoplasmic reticulum stress response systems in the context of *DES* ^{E439K} mutation. Moreover, it would be relevant to extend these studies to other *DES* mutations and other gene mutations known to induce dilated cardiomyopathy. The implementation of the HCI model could lead to a high-content screening assay of a large number of pharmacological molecules, which could open the way to the discovery of new therapeutic molecules for the treatment of dilated cardiomyopathy.

VII. BIBLIOGRAPHIE

- Agnetti, G., Herrmann, H., & Cohen, S. (2022). New roles for desmin in the maintenance of muscle homeostasis. In *FEBS Journal* (Vol. 289, Issue 10, pp. 2755–2770). John Wiley and Sons Inc. <https://doi.org/10.1111/febs.15864>
- Alam, S., Abdullah, C. S., Aishwarya, R., Miriyala, S., Panchatcharam, M., Peretik, J. M., Wayne Orr, A., James, J., Robbins, J., & Bhuiyan, M. S. (2018). Aberrant mitochondrial fission is maladaptive in desmin mutation-Induced cardiac proteotoxicity. *Journal of the American Heart Association*, 7(14). <https://doi.org/10.1161/JAHA.118.009289>
- Alam, S., Abdullah, C. S., Aishwarya, R., Morshed, M., Nitu, S. S., Miriyala, S., Panchatcharam, M., Kevil, C. G., Orr, A. W., & Bhuiyan, M. S. (2020). Dysfunctional mitochondrial dynamic and oxidative phosphorylation precedes cardiac dysfunction in R120G- α crystallin-induced desmin-related cardiomyopathy. *Journal of the American Heart Association*, 9(23), 1–18. <https://doi.org/10.1161/JAHA.120.017195>
- Angermueller, C., Pärnamaa, T., Parts, L., & Stegle, O. (2016). Deep learning for computational biology. *Molecular Systems Biology*, 12(7), 878. <https://doi.org/10.15252/msb.20156651>
- Arrigo, A. P., Simon, S., Gibert, B., Kretz-Remy, C., Nivon, M., Czekalla, A., Guillet, D., Moulin, M., Diaz-Latoud, C., & Vicart, P. (2007). Hsp27 (HspB1) and α B-crystallin (HspB5) as therapeutic targets. *FEBS Letters*, 581(19), 3665–3674. <https://doi.org/10.1016/j.febslet.2007.04.033>
- Ashrafi, G., & Schwarz, T. L. (2013). The pathways of mitophagy for quality control and clearance of mitochondria. *Cell Death and Differentiation*, 20(1), 31–42. <https://doi.org/10.1038/cdd.2012.81>
- Bär, H., Strelkov, S. V., Sjöberg, G., Aebi, U., & Herrmann, H. (2004). The biology of desmin filaments: How do mutations affect their structure, assembly, and organisation? *Journal of Structural Biology*, 148(2), 137–152. <https://doi.org/10.1016/j.jsb.2004.04.003>
- Bassett, A. R. (2017a). Editing the genome of hiPSC with CRISPR/Cas9: disease models. *Mammalian Genome*, 28(7–8), 348–364. <https://doi.org/10.1007/s00335-017-9684-9>
- Bassett, A. R. (2017b). Editing the genome of hiPSC with CRISPR/Cas9: disease models. *Mammalian Genome*, 28(7–8), 348–364. <https://doi.org/10.1007/s00335-017-9684-9>
- Batonnet-Pichon, S., Behin, A., Cabet, E., Delort, F., Vicart, P., & Lilienbaum, A. (2017). Myofibrillar Myopathies: New Perspectives from Animal Models to Potential Therapeutic Approaches. *Journal of Neuromuscular Diseases*, 4(1), 1–15. <https://doi.org/10.3233/JND-160203>
- Baumgarten, A., Bang, C., Tscherner, A., Engelmann, A., Adams, V., Von Haehling, S., Doehner, W., Pregla, R., Anker, M. S., Blecharz, K., Meyer, R., Hetzer, R., Anker, S. D., Thum, T., & Springer, J. (2013). TWIST1 regulates the activity of ubiquitin proteasome system via the miR-199/214 cluster in human end-stage dilated cardiomyopathy. *International Journal of Cardiology*, 168(2), 1447–1452. <https://doi.org/10.1016/j.ijcard.2012.12.094>
- Béhin, A., Salort-Campana, E., Wahbi, K., Richard, P., Carlier, R. Y., Carlier, P., Laforêt, P., Stojkovic, T., Maisonobe, T., Verschueren, A., Franques, J., Attarian, S., Maues De Paula, A., Figarella-Branger, D., Bécane, H. M., Nelson, I., Duboc, D., Bonne, G., Vicart, P., ... Eymard, B. (2015). Myofibrillar myopathies: State of the art, present and future challenges. *Revue Neurologique*, 171(10), 715–729. <https://doi.org/10.1016/j.neurol.2015.06.002>
- Bermúdez-Chacón, R. ;, Gonnet, G. H. ;, & Smith, K. (2015). Automatic problem-specific hyperparameter optimization and model selection for supervised machine learning: Technical Report Technical Report. ETH-Zürich. <https://doi.org/10.3929/ethz-a-010558061>

- Bhuiyan, S., Pattison, J. S., Osinska, H., James, J., Gulick, J., McLendon, P. M., Hill, J. A., Sadoshima, J., & Robbins, J. (2013). Enhanced autophagy ameliorates cardiac proteinopathy. *Journal of Clinical Investigation*, 123(12), 5284–5297. <https://doi.org/10.1172/JCI70877>
- Bickle, M. (2010). The beautiful cell: High-content screening in drug discovery. *Analytical and Bioanalytical Chemistry*, 398(1), 219–226. <https://doi.org/10.1007/s00216-010-3788-3>
- Birket, M. J., Ribeiro, M. C., Kosmidis, G., Ward, D., Leitoguinho, A. R., van de Pol, V., Dambrot, C., Devalla, H. D., Davis, R. P., Mastroberardino, P. G., Atsma, D. E., Passier, R., & Mummery, C. L. (2015). Contractile Defect Caused by Mutation in MYBPC3 Revealed under Conditions Optimized for Human PSC-Cardiomyocyte Function. *Cell Reports*, 13(4), 733–745. <https://doi.org/10.1016/j.celrep.2015.09.025>
- Bizy, A., Guerrero-Serna, G., Hu, B., Ponce-Balbuena, D., Willis, B. C., Zarzoso, M., Ramirez, R. J., Sener, M. F., Mundada, L. V., Klos, M., Devaney, E. J., Vikstrom, K. L., Herron, T. J., & Jalife, J. (2013). Myosin light chain 2-based selection of human iPSC-derived early ventricular cardiac myocytes. *Stem Cell Research*, 11(3), 1335–1347. <https://doi.org/10.1016/j.scr.2013.09.003>
- Blanchet, L., Smeitink, J. A. M., Van Emst - De Vries, S. E., Vogels, C., Pellegrini, M., Jonckheere, A. I., Rodenburg, R. J. T., Buydens, L. M. C., Beyrath, J., Willems, P. H. G. M., & Koopman, W. J. H. (2015). Quantifying small molecule phenotypic effects using mitochondrial morpho-functional fingerprinting and machine learning. *Scientific Reports*, 5, 1–7. <https://doi.org/10.1038/srep08035>
- Bondué, A., Tännler, S., Chiapparo, G., Chabab, S., Ramialison, M., Paulissen, C., Beck, B., Harvey, R., & Blanpain, C. (2011). Defining the earliest step of cardiovascular progenitor specification during embryonic stem cell differentiation. *Journal of Cell Biology*, 192(5), 751–765. <https://doi.org/10.1083/jcb.201007063>
- Boogerd, C. J., Perini, I., Kyriakopoulou, E., Han, S. J., La, P., van der Swaan, B., Berkhouit, J. B., Versteeg, D., Monshouwer-Kloots, J., & van Rooij, E. (2023). Cardiomyocyte proliferation is suppressed by ARID1A-mediated YAP inhibition during cardiac maturation. *Nature Communications*, 14(1), 1–17. <https://doi.org/10.1038/s41467-023-40203-2>
- Bova, M. P., Yaron, O., Huang, Q., Ding, L., Haley, D. A., Stewart, P. L., & Horwitz, J. (1999). Mutation R120G in alphaB-crystallin, which is linked to a desmin-related myopathy, results in an irregular structure and defective chaperone-like function. *Proceedings of the National Academy of Sciences of the United States of America*, 96(11), 6137–6142. <https://doi.org/10.1073/pnas.96.11.6137>
- Bray, M.-A., Singh, S., Han, H., Davis, C. T., Borgeson, B., Hartland, C., Kost-Alimova, M., Gustafsdottir, S. M., Gibson, C. C., & Carpenter, A. E. (2016). Cell Painting, a high-content image-based assay for morphological profiling using multiplexed fluorescent dyes. *Nature Protocols*, 11(9), 1757–1774. <https://doi.org/10.1038/nprot.2016.105>
- Brieler, J. A. Y., Breeden, M. A., Tucker, J., & Louis, S. (2017). *Cardiomyopathy: An Overview*.
- Brodehl, A., Dieding, M., Cakar, H., Klauke, B., Walhorn, V., Gummert, J., Anselmetti, D., & Milting, H. (2013). Functional characterization of desmin mutant p.P419S. In *European Journal of Human Genetics* (Vol. 21, Issue 6, pp. 589–590). Nature Publishing Group. <https://doi.org/10.1038/ejhg.2012.212>
- Brodehl, A., Gaertner-Rommel, A., & Milting, H. (2018). Molecular insights into cardiomyopathies associated with desmin (DES) mutations. In *Biophysical Reviews* (Vol. 10, Issue 4, pp. 983–1006). Springer Verlag. <https://doi.org/10.1007/s12551-018-0429-0>
- Brodehl, A., Holler, S., Gummert, J., & Milting, H. (2022). The N-Terminal Part of the 1A Domain of Desmin Is a Hot Spot Region for Putative Pathogenic DES Mutations Affecting Filament Assembly. *Cells*, 11(23). <https://doi.org/10.3390/cells11233906>
- Brodin, P., Delnery, E., & Soleilhac, E. (2015). High content screening in chemical biology:

- Overview and main challenges. In *Medecine/Sciences* (Vol. 31, Issue 2, pp. 187–196). Editions EDK. <https://doi.org/10.1051/medsci/20153102016>
- Brundel, B. J. J. M. (2020). The Role of Proteostasis Derailment in Cardiac Diseases. In *Cells* (Vol. 9, Issue 10). NLM (Medline). <https://doi.org/10.3390/cells9102317>
- Buikema, J. W., Lee, S., Goodyer, W. R., Maas, R. G., Chirikian, O., Li, G., Miao, Y., Paige, S. L., Lee, D., Wu, H., Paik, D. T., Rhee, S., Tian, L., Galdos, F. X., Puluca, N., Beyersdorf, B., Hu, J., Beck, A., Venkamatran, S., ... Wu, S. M. (2020a). Wnt Activation and Reduced Cell-Cell Contact Synergistically Induce Massive Expansion of Functional Human iPSC-Derived Cardiomyocytes. *Cell Stem Cell*, 27(1), 50-63.e5. <https://doi.org/10.1016/j.stem.2020.06.001>
- Buikema, J. W., Lee, S., Goodyer, W. R., Maas, R. G., Chirikian, O., Li, G., Miao, Y., Paige, S. L., Lee, D., Wu, H., Paik, D. T., Rhee, S., Tian, L., Galdos, F. X., Puluca, N., Beyersdorf, B., Hu, J., Beck, A., Venkamatran, S., ... Wu, S. M. (2020b). Wnt Activation and Reduced Cell-Cell Contact Synergistically Induce Massive Expansion of Functional Human iPSC-Derived Cardiomyocytes. *Cell Stem Cell*, 27(1), 50-63.e5. <https://doi.org/10.1016/j.stem.2020.06.001>
- Bunnage, M. E., Chekler, E. L. P., & Jones, L. H. (2013). Target validation using chemical probes. *Nature Chemical Biology*, 9(4), 195–199. <https://doi.org/10.1038/nchembio.1197>
- Cabet, E., Batonnent-Pichon, S., Delort, F., Gausserès, B., Vicart, P., & Lilienbaum, A. (2015). Antioxidant treatment and induction of autophagy cooperate to reduce desmin aggregation in a cellular model of desminopathy. *PLoS ONE*, 10(9), 1–26. <https://doi.org/10.1371/journal.pone.0137009>
- Caicedo, J. C., Cooper, S., Heigwer, F., Warchal, S., Qiu, P., Molnar, C., Vasilevich, A. S., Barry, J. D., Bansal, H. S., Kraus, O., Wawer, M., Paavolainen, L., Herrmann, M. D., Rohban, M., Hung, J., Hennig, H., Concannon, J., Smith, I., Clemons, P. A., ... Carpenter, A. E. (2017). Data-analysis strategies for image-based cell profiling. *Nature Methods*, 14(9), 849–863. <https://doi.org/10.1038/nmeth.4397>
- Caicedo, J. C., Singh, S., & Carpenter, A. E. (2016). Applications in image-based profiling of perturbations. In *Current Opinion in Biotechnology* (Vol. 39, pp. 134–142). Elsevier Ltd. <https://doi.org/10.1016/j.copbio.2016.04.003>
- Cannone, E., Guglielmi, V., Marchetto, G., Tobia, C., Gnutti, B., Cisterna, B., Tonin, P., Barbon, A., Vattemi, G., & Schiavone, M. (2023). Human Mutated MYOT and CRYAB Genes Cause a Myopathic Phenotype in Zebrafish. *International Journal of Molecular Sciences*, 24(14). <https://doi.org/10.3390/ijms241411483>
- Capetanaki, Y., Bloch, R. J., Kouloumenta, A., Mavroidis, M., & Psarras, S. (2007). Muscle intermediate filaments and their links to membranes and membranous organelles. In *Experimental Cell Research* (Vol. 313, Issue 10, pp. 2063–2076). Academic Press Inc. <https://doi.org/10.1016/j.yexcr.2007.03.033>
- Capetanaki, Y., Milner, D. J., & Weitzer, G. (1997). Desmin in muscle formation and maintenance: Knockouts and consequences. *Cell Structure and Function*, 22(1), 103–116. <https://doi.org/10.1247/csf.22.103>
- Capetanaki, Y., Papathanasiou, S., Diokmetzidou, A., Vatsellas, G., & Tsikitis, M. (2015). Desmin related disease: A matter of cell survival failure. *Current Opinion in Cell Biology*, 32(Dcm), 113–120. <https://doi.org/10.1016/j.ceb.2015.01.004>
- Chan, G. K. Y., Richards, G. R., Peters, M., & Simpson, P. B. (2005). High content kinetic assays of neuronal signaling implemented on BD pathway HT. *Assay and Drug Development Technologies*, 3(6), 623–636. <https://doi.org/10.1089/adt.2005.3.623>
- Chandrasekaran, S. N., Ceulemans, H., Boyd, J. D., & Carpenter, A. E. (2020). Image-based profiling for drug discovery: due for a machine-learning upgrade? *Nature Reviews Drug Discovery*. <https://doi.org/10.1038/s41573-020-00117-w>

- Charrier, E. E., & Janmey, P. A. (2016). Mechanical Properties of Intermediate Filament Proteins. *Methods in Enzymology*, 568, 35–57. <https://doi.org/10.1016/bs.mie.2015.09.009>
- Chen, F., Chang, R., Trivedi, M., Capetanaki, Y., & Cryns, V. L. (2003). Caspase proteolysis of desmin produces a dominant-negative inhibitor of intermediate filaments and promotes apoptosis. *Journal of Biological Chemistry*, 278(9), 6848–6853. <https://doi.org/10.1074/jbc.M212021200>
- Cho, J., Lee, H., Rah, W., Chang, H. J., & Yoon, Y. S. (2022). From engineered heart tissue to cardiac organoid. *Theranostics*, 12(6), 2758–2772. <https://doi.org/10.7150/thno.67661>
- Cho, S. W., Kim, S., Kim, J. M., & Kim, J. S. (2013). Targeted genome engineering in human cells with the Cas9 RNA-guided endonuclease. *Nature Biotechnology*, 31(3), 230–232. <https://doi.org/10.1038/nbt.2507>
- Choubey, D. K., Kumar, M., Shukla, V., Tripathi, S., & Dhandhania, V. K. (2020). Comparative Analysis of Classification Methods with PCA and LDA for Diabetes. *Current Diabetes Reviews*, 16(8), 833–850. <https://doi.org/10.2174/1573399816666200123124008>
- Claeyssen, C., Bulangalire, N., Bastide, B., Agbulut, O., & Cieniewski-Bernard, C. (2023). Desmin and its molecular chaperone, the α B-crystallin: How post-translational modifications modulate their functions in heart and skeletal muscles? *Biochimie*, 216, 137–159. <https://doi.org/10.1016/j.biochi.2023.10.002>
- Clemen, C. S., Herrmann, H., Strelkov, S. V., & Schröder, R. (2013). Desminopathies: Pathology and mechanisms. In *Acta Neuropathologica* (Vol. 125, Issue 1, pp. 47–75). <https://doi.org/10.1007/s00401-012-1057-6>
- Clemen, C. S., Stöckigt, F., Strucksberg, K. H., Chevessier, F., Winter, L., Schütz, J., Bauer, R., Thorweihe, J. M., Wenzel, D., Schlötzer-Schrehardt, U., Rasche, V., Krsmanovic, P., Katus, H. A., Rottbauer, W., Just, S., Müller, O. J., Friedrich, O., Meyer, R., Herrmann, H., ... Schröder, R. (2015). The toxic effect of R350P mutant desmin in striated muscle of man and mouse. *Acta Neuropathologica*, 129(2), 297–315. <https://doi.org/10.1007/s00401-014-1363-2>
- Cohen, S., Zhai, B., Gygi, S. P., & Goldberg, A. L. (2012). Ubiquitylation by Trim32 causes coupled loss of desmin, Z-bands, and thin filaments in muscle atrophy. *Journal of Cell Biology*, 198(4), 575–589. <https://doi.org/10.1083/jcb.201110067>
- Conover, G. M., Henderson, S. N., & Gregorio, C. C. (2008). A Myopathy-linked Desmin Mutation Perturbs Striated Muscle Actin Filament Architecture. *Molecular Biology of the Cell*, 20(3), 834–845. <https://doi.org/10.1091/mbc.e08-07-0753>
- Cuenda, A., Rouse, J., Doza, Y. N., Meier, R., Cohen, P., Gallagher, T. F., Young, P. R., & Lee, J. C. (1995). SB 203580 is a specific inhibitor of a MAP kinase homologue which is stimulated by cellular stresses and interleukin-1. *FEBS Letters*, 364(2), 229–233. [https://doi.org/10.1016/0014-5793\(95\)00357-f](https://doi.org/10.1016/0014-5793(95)00357-f)
- Cyganek, L., Hasenfuss, G., Guan, K., Cyganek, L., Tiburcy, M., Sekeres, K., & Gerstenberg, K. (2018). Deep phenotyping of human induced pluripotent stem cell – derived atrial and ventricular cardiomyocytes Find the latest version : Deep phenotyping of human induced pluripotent stem cell – derived atrial and ventricular cardiomyocytes. *JCI Insight*, 3(12), e99941. [10.1172/jci.insight.99941](https://doi.org/10.1172/jci.insight.99941)
- D'Amico, A., Benedetti, S., Petrini, S., Sambuughin, N., Boldrini, R., Menditto, I., Ferrari, M., Verardo, M., Goldfarb, L., & Bertini, E. (2005). Major myofibrillar changes in early onset myopathy due to de novo heterozygous missense mutation in lamin A/C gene. *Neuromuscular Disorders*, 15(12), 847–850. <https://doi.org/10.1016/j.nmd.2005.09.007>
- Danuser, G. (2011). Computer vision in cell biology. *Cell*, 147(5), 973–978. <https://doi.org/10.1016/j.cell.2011.11.001>

- Denning, C., Borgdorff, V., Crutchley, J., Firth, K. S. A., George, V., Kalra, S., Kondrashov, A., Hoang, M. D., Mosqueira, D., Patel, A., Prodanov, L., Rajamohan, D., Skarnes, W. C., Smith, J. G. W., & Young, L. E. (2016). Cardiomyocytes from human pluripotent stem cells: From laboratory curiosity to industrial biomedical platform. *Biochimica et Biophysica Acta - Molecular Cell Research*, 1863(7), 1728–1748. <https://doi.org/10.1016/j.bbamcr.2015.10.014>
- Di Lernia, G., Leone, P., Solimando, A. G., Buonavoglia, A., Saltarella, I., Ria, R., Ditonno, P., Silvestris, N., Crudele, L., Vacca, A., & Racanelli, V. (2020). Bortezomib treatment modulates autophagy in multiple myeloma. *Journal of Clinical Medicine*, 9(2). <https://doi.org/10.3390/jcm9020552>
- Ding, W. X., & Yin, X. M. (2012). Mitophagy: Mechanisms, pathophysiological roles, and analysis. In *Biological Chemistry* (Vol. 393, Issue 7, pp. 547–564). <https://doi.org/10.1515/hsz-2012-0119>
- Diokmetzidou, A., Soumaka, E., Kloukina, I., Tsikitis, M., Makridakis, M., Varela, A., Davos, C. H., Georgopoulos, S., Anesti, V., Vlahou, A., & Capetanaki, Y. (2016). Desmin and α B-crystallin interplay in the maintenance of mitochondrial homeostasis and cardiomyocyte survival. *Journal of Cell Science*, 129(20), 3705 LP – 3720. <https://doi.org/10.1242/jcs.192203>
- Dorsch, L. M., Schuldt, M., Knežević, D., Wiersma, M., Kuster, D. W. D., van der Velden, J., & Brundel, B. J. J. M. (2019). Untying the knot: protein quality control in inherited cardiomyopathies. *Pflugers Archiv European Journal of Physiology*, 471(5), 795–806. <https://doi.org/10.1007/s00424-018-2194-0>
- Doyle, K. M., Kennedy, D., Gorman, A. M., Gupta, S., Healy, S. J. M., & Samali, A. (2011). Unfolded proteins and endoplasmic reticulum stress in neurodegenerative disorders. *Journal of Cellular and Molecular Medicine*, 15(10), 2025–2039. <https://doi.org/10.1111/j.1582-4934.2011.01374.x>
- Dunlop, R. A., Brunk, U. T., & Rodgers, K. J. (2009). Oxidized proteins: Mechanisms of removal and consequences of accumulation. *IUBMB Life*, 61(5), 522–527. <https://doi.org/10.1002/iub.189>
- Echt, D. S., & Ruskin, J. N. (2020). Use of Flecainide for the Treatment of Atrial Fibrillation. *American Journal of Cardiology*, 125(7), 1123–1133. <https://doi.org/10.1016/j.amjcard.2019.12.041>
- Eisner, V., Csordás, G., & Hajnóczky, G. (2013). Interactions between sarco-endoplasmic reticulum and mitochondria in cardiac and skeletal muscle-pivotal roles in Ca^{2+} and reactive oxygen species signaling. *Journal of Cell Science*, 126(14), 2965–2978. <https://doi.org/10.1242/jcs.093609>
- English, K., & Barton, M. C. (2021). HDAC6: A Key Link Between Mitochondria and Development of Peripheral Neuropathy. *Frontiers in Molecular Neuroscience*, 14(August), 1–11. <https://doi.org/10.3389/fnmol.2021.684714>
- Even, C., Abramovici, G., Delort, F., Rigato, A. F., Bailleux, V., de Sousa Moreira, A., Vicart, P., Rico, F., Batonnet-Pichon, S., & Briki, F. (2017). Mutation in the Core Structure of Desmin Intermediate Filaments Affects Myoblast Elasticity. *Biophysical Journal*, 113(3), 627–636. <https://doi.org/10.1016/j.bpj.2017.06.020>
- Ferreiro, A., Ceuterick-De Groote, C., Marks, J. J., Goemans, N., Schreiber, G., Hanefeld, F., Fardeau, M., Martin, J. J., Goebel, H. H., Richard, P., Guicheney, P., & Bönnemann, C. G. (2004). Desmin-Related Myopathy with Mallory Body-like Inclusions Is Caused by Mutations of the Selenoprotein N Gene. *Annals of Neurology*, 55(5), 676–686. <https://doi.org/10.1002/ana.20077>
- Ferrer, I., & Olivé, M. (2008). Molecular pathology of myofibrillar myopathies. *Expert Reviews in Molecular Medicine*, 10, e25. <https://doi.org/DOI: 10.1017/S1462399408000793>

- Feyen, D. A. M., McKeithan, W. L., Bruyneel, A. A. N., Spiering, S., Hörmann, L., Ulmer, B., Zhang, H., Briganti, F., Schweizer, M., Hegyi, B., Liao, Z., Pölönen, R. P., Ginsburg, K. S., Lam, C. K., Serrano, R., Wahlquist, C., Kreymerman, A., Vu, M., Amatya, P. L., ... Mercola, M. (2020). Metabolic Maturation Media Improve Physiological Function of Human iPSC-Derived Cardiomyocytes. *Cell Reports*, 32(3). <https://doi.org/10.1016/j.celrep.2020.107925>
- Fountoulakis, M., Soumaka, E., Rapti, K., Mavroidis, M., Tsangaris, G., Maris, A., Weisleder, N., & Capetanaki, Y. (2005). Alterations in the heart mitochondrial proteome in a desmin null heart failure model. *Journal of Molecular and Cellular Cardiology*, 38(3), 461–474. <https://doi.org/10.1016/j.yjmcc.2004.12.008>
- Ganguly, S., Mitra, A., & Sarkar, S. (2014). Role of α -Crystallin B in Regulation of Stress Induced Cardiomyocyte Apoptosis. In *Cardiovascular & Hematological Agents in Medicinal Chemistry* (Vol. 12, Issue 2, pp. 60–65). <https://doi.org/http://dx.doi.org/10.2174/1871525713666150123151731>
- Gao, J., Li, Z., & Paulin, D. (1998). A novel site, Mt, in the human desmin enhancer is necessary for maximal expression in skeletal muscle. *Journal of Biological Chemistry*, 273(11), 6402–6409. <https://doi.org/10.1074/jbc.273.11.6402>
- Gaspar, J. A., Doss, M. X., Hengstler, J. G., Cadenas, C., Hescheler, J., & Sachinidis, A. (2014). Unique metabolic features of stem cells, cardiomyocytes, and their progenitors. *Circulation Research*, 114(8), 1346–1360. <https://doi.org/10.1161/CIRCRESAHA.113.302021>
- Gavriliidis, C., Laredj, L., Solinhac, R., Messaddeq, N., Viaud, J., Laporte, J., Sumara, I., & Hnia, K. (2018). The MTM1-UBQLN2-HSP complex mediates degradation of misfolded intermediate filaments in skeletal muscle. *Nature Cell Biology*, 20(2), 198–210. <https://doi.org/10.1038/s41556-017-0024-9>
- Gerbin, K. A., Grancharova, T., Donovan-Maiye, R. M., Hendershott, M. C., Anderson, H. G., Brown, J. M., Chen, J., Dinh, S. Q., Gehring, J. L., Johnson, G. R., Lee, H., Nath, A., Nelson, A. M., Sluzewski, M. F., Viana, M. P., Yan, C., Zaunbrecher, R. J., Cordes Metzler, K. R., Gaudreault, N., ... Gunawardane, R. N. (2021a). Cell states beyond transcriptomics: Integrating structural organization and gene expression in hiPSC-derived cardiomyocytes. *Cell Systems*, 1–18. <https://doi.org/10.1016/j.cels.2021.05.001>
- Gerbin, K. A., Grancharova, T., Donovan-Maiye, R. M., Hendershott, M. C., Anderson, H. G., Brown, J. M., Chen, J., Dinh, S. Q., Gehring, J. L., Johnson, G. R., Lee, H. W., Nath, A., Nelson, A. M., Sluzewski, M. F., Viana, M. P., Yan, C., Zaunbrecher, R. J., Cordes Metzler, K. R., Gaudreault, N., ... Gunawardane, R. N. (2021b). Cell states beyond transcriptomics: Integrating structural organization and gene expression in hiPSC-derived cardiomyocytes. *Cell Systems*, 12(6), 670–687.e10. <https://doi.org/10.1016/j.cels.2021.05.001>
- Ghasemi, S., Mahdavi, M., Maleki, M., Salahshourifar, I., & Kalayinia, S. (2022). A novel likely pathogenic variant in the FBXO32 gene associated with dilated cardiomyopathy according to whole-exome sequencing. *BMC Medical Genomics*, 15(1), 1–8. <https://doi.org/10.1186/s12920-022-01388-5>
- Ghemrawi, R., Battaglia-Hsu, S. F., & Arnold, C. (2018). Endoplasmic reticulum stress in metabolic disorders. *Cells*, 7(6), 1–35. <https://doi.org/10.3390/cells7060063>
- Ghosh, R., Vinod, V., Symons, J. D., & Boudina, S. (2020). Protein and Mitochondria Quality Control Mechanisms and Cardiac Aging. In *Cells* (Vol. 9, Issue 4). NLM (Medline). <https://doi.org/10.3390/cells9040933>
- Gibson, C. C., Zhu, W., Davis, C. T., Bowman-Kirigin, J. A., Chan, A. C., Ling, J., Walker, A. E., Goitre, L., Delle Monache, S., Retta, S. F., Shiu, Y.-T. E., Grossmann, A. H., Thomas, K. R., Donato, A. J., Lesniewski, L. A., Whitehead, K. J., & Li, D. Y. (2015). Strategy for Identifying Repurposed Drugs for the Treatment of Cerebral Cavernous Malformation. *Circulation*, 131(3), 289–299. <https://doi.org/10.1161/CIRCULATIONAHA.114.010403>

- Gil-Cayuela, C., López, A., Martínez-Dolz, L., González-Juanatey, J. R., Lago, F., Roselló-Lletí, E., Rivera, M., & Portolés, M. (2019). The altered expression of autophagy-related genes participates in heart failure: NRBP2 and CALCOCO2 are associated with left ventricular dysfunction parameters in human dilated cardiomyopathy. *PLoS ONE*, 14(4), 1–15. <https://doi.org/10.1371/journal.pone.0215818>
- Goldfarb, L. G., & Dalakas, M. C. (2011). Tragedy in a heartbeat: Malfunctioning desmin causes skeletal and cardiac muscle disease. *Journal of Clinical Investigation*, 121(1), 455. <https://doi.org/10.1172/JCI45852>
- Goldfracht, I., Protze, S., Shiti, A., Setter, N., Gruber, A., Shaheen, N., Nartiss, Y., Keller, G., & Gepstein, L. (2020). Generating ring-shaped engineered heart tissues from ventricular and atrial human pluripotent stem cell-derived cardiomyocytes. *Nature Communications*, 11(1), 1–15. <https://doi.org/10.1038/s41467-019-13868-x>
- Gonnot, F., Boulogne, L., Brun, C., Dia, M., Gouriou, Y., Bidaux, G., Chouabe, C., Crola Da Silva, C., Ducreux, S., Pillot, B., Kaczmarczyk, A., Leon, C., Chanon, S., Perret, C., Sciandra, F., Dargar, T., Gache, V., Farhat, F., Sebbag, L., ... Gomez, L. (2023). SERCA2 phosphorylation at serine 663 is a key regulator of Ca²⁺ homeostasis in heart diseases. *Nature Communications*, 14(1). <https://doi.org/10.1038/s41467-023-39027-x>
- Grafton, F., Ho, J., Ranjbarvaziri, S., Farshidfar, F., Budan, A., Steltzer, S., Maddah, M., Loewke, K. E., Green, K., Patel, S., Hoey, T., & Mandegar, M. A. (2021). Deep learning detects cardiotoxicity in a high-content screen with induced pluripotent stem cell-derived cardiomyocytes. *ELife*, 10. <https://doi.org/10.7554/ELIFE.68714>
- Granger, B. L., & Lazarides, E. (1980). Synemin: a new high molecular weight protein associated with desmin and vimentin filaments in muscle. *Cell*, 22(3), 727–738. [https://doi.org/10.1016/0092-8674\(80\)90549-8](https://doi.org/10.1016/0092-8674(80)90549-8)
- Greener, J. G., Kandathil, S. M., Moffat, L., & Jones, D. T. (2022). A guide to machine learning for biologists. In *Nature Reviews Molecular Cell Biology* (Vol. 23, Issue 1, pp. 40–55). Nature Research. <https://doi.org/10.1038/s41580-021-00407-0>
- Haggarty, S. J., Mayer, T. U., Miyamoto, D. T., Fathi, R., King, R. W., Mitchison, T. J., & Schreiber, S. L. (2001). Erratum: Dissecting cellular processes using small molecules: Identification of colchicine-like, taxol-like and other small molecules that perturb mitosis (Chem. Biol. (2000) 7 (275–286)). *Chemistry and Biology*, 8(12), 1265. [https://doi.org/10.1016/S1074-5521\(01\)00083-7](https://doi.org/10.1016/S1074-5521(01)00083-7)
- Harding, H. P., Zhang, Y., Zeng, H., Novoa, I., Lu, P. D., Calfon, M., Sadri, N., Yun, C., Popko, B., Paules, R., Stojdl, D. F., Bell, J. C., Hettmann, T., Leiden, J. M., & Ron, D. (2003). An integrated stress response regulates amino acid metabolism and resistance to oxidative stress. *Molecular Cell*, 11(3), 619–633. [https://doi.org/10.1016/s1097-2765\(03\)00105-9](https://doi.org/10.1016/s1097-2765(03)00105-9)
- Hasinoff, B. B., Patel, D., & Wu, X. (2017). Molecular Mechanisms of the Cardiotoxicity of the Proteasomal-Targeted Drugs Bortezomib and Carfilzomib. *Cardiovascular Toxicology*, 17(3), 237–250. <https://doi.org/10.1007/s12012-016-9378-7>
- Hauck, L., Stanley-Hasnain, S., Fung, A., Grothe, D., Rao, V., Mak, T. W., & Billia, F. (2017). Cardiac-specific ablation of the E3 ubiquitin ligase Mdm2 leads to oxidative stress, broad mitochondrial deficiency and early death. In *PLoS ONE* (Vol. 12, Issue 12). <https://doi.org/10.1371/journal.pone.0189861>
- Hauser, M. A., Horrigan, S. K., Salmikangas, P., Torian, U. M., Viles, K. D., Dancel, R., Tim, R. W., Taivainen, A., Bartoloni, L., Gilchrist, J. M., Stajich, J. M., Gaskell, P. C., Gilbert, J. R., Vance, J. M., Pericak-Vance, M. A., Carpen, O., Westbrook, C. A., & Speer, M. C. (2000). Myotilin is mutated in limb girdle muscular dystrophy 1A. *Human Molecular Genetics*, 9(14), 2141–2147. <https://doi.org/10.1093/hmg/9.14.2141>
- Henderson, M., De Waele, L., Hudson, J., Eagle, M., Sewry, C., Marsh, J., Charlton, R., He, L.,

- Blakely, E. L., Horrocks, I., Stewart, W., Taylor, R. W., Longman, C., Bushby, K., & Barresi, R. (2013). Recessive desmin-null muscular dystrophy with central nuclei and mitochondrial abnormalities. *Acta Neuropathologica*, 125(6), 917–919. <https://doi.org/10.1007/s00401-013-1113-x>
- Henning, R. H., & Brundel, B. J. J. M. (2017a). Proteostasis in cardiac health and disease. *Nature Reviews Cardiology*, 14(11), 637–653. <https://doi.org/10.1038/nrcardio.2017.89>
- Henning, R. H., & Brundel, B. J. J. M. (2017b). Proteostasis in cardiac health and disease. In *Nature Reviews Cardiology* (Vol. 14, Issue 11, pp. 637–653). Nature Publishing Group. <https://doi.org/10.1038/nrcardio.2017.89>
- Heo, Y. J., Lee, D., Kang, J., Lee, K., & Chung, W. K. (2017). Real-time Image Processing for Microscopy-based Label-free Imaging Flow Cytometry in a Microfluidic Chip. *Scientific Reports*, 7(1), 1–9. <https://doi.org/10.1038/s41598-017-11534-0>
- Herman, D., Kańduła, M. M., Freitas, L. G. A., van Dongen, C., Le Van, T., Mesens, N., Jaensch, S., Gustin, E., Micholt, L., Lardeau, C. H., Varsakelis, C., Reumers, J., Zoffmann, S., Will, Y., Peeters, P. J., & Ceulemans, H. (2023). Leveraging Cell Painting Images to Expand the Applicability Domain and Actively Improve Deep Learning Quantitative Structure-Activity Relationship Models. *Chemical Research in Toxicology*, 36(7), 1028–1036. <https://doi.org/10.1021/acs.chemrestox.2c00404>
- Hernandez, D. A., Bennett, C. M., Dunina-Barkovskaya, L., Wedig, T., Capetanaki, Y., Herrmann, H., & Conover, G. M. (2016). Nebulette is a powerful cytolinker organizing desmin and actin in mouse hearts. *Molecular Biology of the Cell*, 27(24), 3869–3882. <https://doi.org/10.1091/mbc.E16-04-0237>
- Heymans, S., Lakdawala, N. K., Tschöpe, C., & Klingel, K. (2023). Dilated cardiomyopathy: causes, mechanisms, and current and future treatment approaches. *The Lancet*, 402(10406), 998–1011. [https://doi.org/10.1016/S0140-6736\(23\)01241-2](https://doi.org/10.1016/S0140-6736(23)01241-2)
- Hnia, K., Ramspacher, C., Vermot, J., & Laporte, J. (2015). Desmin in muscle and associated diseases: beyond the structural function. *Cell and Tissue Research*, 360(3), 591–608. <https://doi.org/10.1007/s00441-014-2016-4>
- Hofmann, C., Katus, H. A., & Doroudgar, S. (2019). Protein Misfolding in Cardiac Disease. *Circulation*, 139(18), 2085–2088. <https://doi.org/10.1161/CIRCULATIONAHA.118.037417>
- Hofner, M., Höllrigl, A., Puz, S., Stary, M., & Weitzer, G. (2007). Desmin stimulates differentiation of cardiomyocytes and up-regulation of brachyury and nkx2.5. *Differentiation*, 75(7), 605–615. <https://doi.org/10.1111/j.1432-0436.2007.00162.x>
- Höllrigl, A., Hofner, M., Stary, M., & Weitzer, G. (2007). Differentiation of cardiomyocytes requires functional serine residues within the amino-terminal domain of desmin. *Differentiation*, 75(7), 616–626. <https://doi.org/10.1111/j.1432-0436.2007.00163.x>
- Horvath, P., Aulner, N., Bickle, M., Davies, A. M., Nery, E. Del, Ebner, D., Montoya, M. C., Östling, P., Pietiäinen, V., Price, L. S., Shorte, S. L., Turcatti, G., Von Schantz, C., & Carragher, N. O. (2016). Screening out irrelevant cell-based models of disease. *Nature Reviews Drug Discovery*, 15(11), 751–769. <https://doi.org/10.1038/nrd.2016.175>
- Hovhannisyan, Y., Li, Z., Callon, D., Suspène, R., Batoumeni, V., Canette, A., Blanc, J., Hocini, H., Lefebvre, C., El-Jahrani, N., L'honoré, A., Kordeli, E., Fornes, P., Concorde, J.-P., Tachdjian, G., Rodriguez, A.-M., Vartanian, J.-P., Béhin, A., Wahbi, K., ... Agbulut, O. (2023). Critical contribution of mitochondria in the development of cardiomyopathy linked to desmin mutation. *BioRxiv*, 2023.09.14.557734. <https://doi.org/10.1101/2023.09.14.557734>
- Hubbert, C., Guardiola, A., Shao, R., Kawaguchi, Y., Ito, A., Nixon, A., Yoshida, M., Wang, X.-F., & Yao, T.-P. (2002). HDAC6 is a microtubule-associated deacetylase. *Nature*, 417(6887), 455–458. <https://doi.org/10.1038/417455a>

- Hudson, J., Titmarsh, D., Hidalgo, A., Wolvetang, E., & Cooper-White, J. (2012). Primitive cardiac cells from human embryonic stem cells. *Stem Cells and Development*, 21(9), 1513–1523. <https://doi.org/10.1089/scd.2011.0254>
- Hughes, J. P., Rees, S. S., Kalindjian, S. B., & Philpott, K. L. (2011). Principles of early drug discovery. *British Journal of Pharmacology*, 162(6), 1239–1249. <https://doi.org/10.1111/j.1476-5381.2010.01127.x>
- Hughes, R. E., Elliott, R. J. R., Dawson, J. C., & Carragher, N. O. (2021). High-content phenotypic and pathway profiling to advance drug discovery in diseases of unmet need. *Cell Chemical Biology*, 28(3), 338–355. <https://doi.org/10.1016/j.chembiol.2021.02.015>
- Japp, A. G., Gulati, A., Cook, S. A., Cowie, M. R., & Prasad, S. K. (2016). The Diagnosis and Evaluation of Dilated Cardiomyopathy. *Journal of the American College of Cardiology*, 67(25), 2996–3010. <https://doi.org/10.1016/j.jacc.2016.03.590>
- Jiang, M., Liu, T., Zhang, J., Gao, S., Tao, B., Cao, R., Qiu, Y., Liu, J., Li, Y., Wang, Y., & Cao, F. (2020). Rapamycin Promotes Cardiomyocyte Differentiation of Human Induced Pluripotent Stem Cells in a Stage-Dependent Manner. *Stem Cells and Development*, 29(18), 1229–1239. <https://doi.org/10.1089/scd.2020.0025>
- Karacosta, L. G. (2021). From imaging a single cell to implementing precision medicine: An exciting new era. *Emerging Topics in Life Sciences*, 5(6), 837–847. <https://doi.org/10.1042/ETLS20210219>
- Karbowski, M., Oshima, Y., & Verhoeven, N. (2022). Mitochondrial proteotoxicity: implications and ubiquitin-dependent quality control mechanisms. *Cellular and Molecular Life Sciences*, 79(11), 1–23. <https://doi.org/10.1007/s00018-022-04604-8>
- Kayman Kürekçi, G., Kural Mangit, E., Koyunlar, C., Unsal, S., Saglam, B., Ergin, B., Gizer, M., Uyanik, I., Boustanabadimaranal Düz, N., Korkusuz, P., Talim, B., Puralı, N., Hughes, S. M., & Dincer, P. R. (2021). Knockout of zebrafish desmin genes does not cause skeletal muscle degeneration but alters calcium flux. *Scientific Reports*, 11(1), 1–15. <https://doi.org/10.1038/s41598-021-86974-w>
- Khan, R. S., Pahl, E., Dellefave-Castillo, L., Rychlik, K., Ing, A., Yap, K. L., Brew, C., Johnston, J. R., McNally, E. M., & Webster, G. (2022). Genotype and Cardiac Outcomes in Pediatric Dilated Cardiomyopathy. *Journal of the American Heart Association*, 11(1). <https://doi.org/10.1161/JAHA.121.022854>
- Knezevic, T., Myers, V. D., Gordon, J., Tilley, D. G., Sharp, T. E., Wang, J. F., Khalili, K., Cheung, J. Y., & Feldman, A. M. (2015). BAG3: a new player in the heart failure paradigm. *Heart Failure Reviews*, 20(4), 423–434. <https://doi.org/10.1007/s10741-015-9487-6>
- Komuro, J., Tokuoka, Y., Seki, T., Kusumoto, D., Hashimoto, H., Katsuki, T., Nakamura, T., Akiba, Y., Kuoka, T., Kimura, M., Yamada, T., Fukuda, K., Funahashi, A., & Yuasa, S. (2022). Development of non-bias phenotypic drug screening for cardiomyocyte hypertrophy by image segmentation using deep learning. *Biochemical and Biophysical Research Communications*, 632, 181–188. <https://doi.org/10.1016/j.bbrc.2022.09.108>
- Korolchuk, V. I., Mansilla, A., Menzies, F. M., & Rubinsztein, D. C. (2009). Autophagy inhibition compromises degradation of ubiquitin-proteasome pathway substrates. *Molecular Cell*, 33(4), 517–527. <https://doi.org/10.1016/j.molcel.2009.01.021>
- Kouroupi, G., Antoniou, N., Prodromidou, K., Taoufik, E., & Matsas, R. (2020). Patient-derived induced pluripotent stem cell-based models in parkinson's disease for drug identification. *International Journal of Molecular Sciences*, 21(19), 1–26. <https://doi.org/10.3390/ijms21197113>
- Kubli, D. A., Zhang, X., Lee, Y., Hanna, R. A., Quinsay, M. N., Nguyen, C. K., Jimenez, R., Petrosyans, S., Murphy, A. N., & Gustafsson, Å. B. (2013). Parkin protein deficiency exacerbates cardiac injury and reduces survival following myocardial infarction. *Journal of*

Biological Chemistry, 288(2), 915–926. <https://doi.org/10.1074/jbc.M112.411363>

- Kuisk, I. R., Li, H., Tran, D., & Capetanaki, Y. (1996). A single MEF2 site governs desmin transcription in both heart and skeletal muscle during mouse embryogenesis. *Developmental Biology*, 174(1), 1–13. <https://doi.org/10.1006/dbio.1996.0046>
- Laco, F., Lam, A. T. L., Woo, T. L., Tong, G., Ho, V., Soong, P. L., Grishina, E., Lin, K. H., Reuveny, S., & Oh, S. K. W. (2020). Selection of human induced pluripotent stem cells lines optimization of cardiomyocytes differentiation in an integrated suspension microcarrier bioreactor. *Stem Cell Research and Therapy*, 11(1), 1–16. <https://doi.org/10.1186/s13287-020-01618-6>
- Lai, J. L., Lian, Y. E., Wu, J. Y., Wang, Y. D., & Bai, Y. N. (2021). Verapamil induces autophagy to improve liver regeneration in non-alcoholic fatty liver mice. *Adipocyte*, 10(1), 532–545. <https://doi.org/10.1080/21623945.2021.1983241>
- Lampart, F. L., Iber, D., & Doumpas, N. (2023). Organoids in high-throughput and high-content screenings. *Frontiers in Chemical Engineering*, 5(March), 1–11. <https://doi.org/10.3389/fceng.2023.1120348>
- Lehman, S. J., Crocini, C., & Leinwand, L. A. (2022). Targeting the sarcomere in inherited cardiomyopathies. *Nature Reviews Cardiology*, 19(6), 353–363. <https://doi.org/10.1038/s41569-022-00682-0>
- Li, H., Zheng, L., Mo, Y., Gong, Q., Jiang, A., & Zhao, J. (2016). Voltage-dependent anion channel 1(VDAC1) participates the apoptosis of the mitochondrial dysfunction in desminopathy. *PLoS ONE*, 11(12), 1–17. <https://doi.org/10.1371/journal.pone.0167908>
- Li, Jin, Zhang, D., Brundel, B. J. J. M., & Wiersma, M. (2019). Imbalance of ER and Mitochondria Interactions: Prelude to Cardiac Ageing and Disease? In *Cells* (Vol. 8, Issue 12). NLM (Medline). <https://doi.org/10.3390/cells8121617>
- Li, Jiuru, Wiesinger, A., Fokkert, L., Boukens, B. J., Verkerk, A. O., Christoffels, V. M., Boink, G. J. J., & Devalla, H. D. (2022). Molecular and electrophysiological evaluation of human cardiomyocyte subtypes to facilitate generation of composite cardiac models. *Journal of Tissue Engineering*, 13. <https://doi.org/10.1177/20417314221127908>
- Li, Mei, Andersson-Lendahl, M., Sejersen, T., & Arner, A. (2013). Knockdown of desmin in zebrafish larvae affects interfilament spacing and mechanical properties of skeletal muscle. *Journal of General Physiology*, 141(3), 335–345. <https://doi.org/10.1085/jgp.201210915>
- Li, Ming, Iismaa, S. E., Naqvi, N., Nicks, A., Husain, A., & Graham, R. M. (2014). Thyroid hormone action in postnatal heart development. *Stem Cell Research*, 13(3), 582–591. <https://doi.org/10.1016/j.scr.2014.07.001>
- Li, Z., Colucci-Guyon, E., Pinçon-Raymond, M., Mericskay, M., Pournin, S., Paulin, D., & Babinet, C. (1996). Cardiovascular lesions and skeletal myopathy in mice lacking desmin. *Developmental Biology*, 175(2), 362–366. <https://doi.org/10.1006/dbio.1996.0122>
- Li, Z., Mericskay, M., Agbulut, O., Butler-Browne, G., Carlsson, L., Thornell, L.-E., Babinet, C., & Paulin, D. (1997). Desmin Is Essential for the Tensile Strength and Integrity of Myofibrils but Not for Myogenic Commitment, Differentiation, and Fusion of Skeletal Muscle . *The Journal of Cell Biology*, 139(1), 129–144. <https://doi.org/10.1083/jcb.139.1.129>
- Lian, X., Zhang, J., Azarin, S. M., Zhu, K., Hazeltine, L. B., Bao, X., Hsiao, C., Kamp, T. J., & Palecek, S. P. (2013). Directed cardiomyocyte differentiation from human pluripotent stem cells by modulating Wnt/β-catenin signaling under fully defined conditions. *Nature Protocols*, 8(1), 162–175. <https://doi.org/10.1038/nprot.2012.150>
- Lin, S., Schorpp, K., Rothenaigner, I., & Hadian, K. (2020). Image-based high-content screening in drug discovery. *Drug Discovery Today*, 25(8), 1348–1361. <https://doi.org/10.1016/j.drudis.2020.06.001>

- Liu, G. S., Morales, A., Vafiadaki, E., Lam, C. K., Cai, W. F., Haghghi, K., Adly, G., Hershberger, R. E., & Kranias, E. G. (2015). A novel human R25C-phospholamban mutation is associated with super-inhibition of calcium cycling and ventricular arrhythmia. *Cardiovascular Research*, 107(1), 164–174. <https://doi.org/10.1093/cvr/cvv127>
- Liu, H., Wang, L., Xu, H., Tan, B., Yi, Q., Deng, H., Chen, Y., He, B., Tian, J., & Zhu, J. (2023). Quantitative proteomic and phosphoproteomic analysis reveal the relationship between mitochondrial dysfunction and cytoskeletal remodeling in hiPSC-CMs deficient in PINK1. *Journal of Translational Medicine*, 21(1), 1–20. <https://doi.org/10.1186/s12967-023-04467-y>
- Liu, J., Tang, M., Mestril, R., & Wang, X. (2006). Aberrant protein aggregation is essential for a mutant desmin to impair the proteolytic function of the ubiquitin-proteasome system in cardiomyocytes. *Journal of Molecular and Cellular Cardiology*, 40(4), 451–454. <https://doi.org/10.1016/j.jmcc.2005.12.011>
- Ljosa, V., & Carpenter, A. E. (2009). Introduction to the quantitative analysis of two-dimensional fluorescence microscopy images for cell-based screening. *PLoS Computational Biology*, 5(12), 1–10. <https://doi.org/10.1371/journal.pcbi.1000603>
- Lonardo, G., Cerbai, E., Casini, S., Giunti, G., Bonacchi, M., Battaglia, F., Fiorani, B., Stefano, P. L., Sani, G., & Mugelli, A. (2004). Atrial natriuretic peptide modulates the hyperpolarization-activated current (If) in human atrial myocytes. *Cardiovascular Research*, 63(3), 528–536. <https://doi.org/10.1016/j.cardiores.2004.03.004>
- Ma, X., Mani, K., Liu, H., Kovacs, A., Murphy, J. T., Foroughi, L., French, B. A., Weinheimer, C. J., Kraja, A., Benjamin, I. J., Hill, J. A., Javaheri, A., & Diwan, A. (2019). Transcription factor EB activation rescues advanced α B-crystallin mutation-induced cardiomyopathy by normalizing desmin localization. *Journal of the American Heart Association*, 8(4). <https://doi.org/10.1161/JAHA.118.010866>
- Ma, Yuanwu, Shen, B., Zhang, X., Lu, Y., Chen, W., Ma, J., Huang, X., & Zhang, L. (2014). Heritable multiplex genetic engineering in rats using CRISPR/Cas9. *PloS One*, 9(3), e89413. <https://doi.org/10.1371/journal.pone.0089413>
- Ma, Yuanwu, Zhang, L., & Huang, X. (2014). Genome modification by CRISPR/Cas9. *FEBS Journal*, 281(23), 5186–5193. <https://doi.org/10.1111/febs.13110>
- Ma, Yuedong, Chen, B., Liu, D., Yang, Y., Xiong, Z., Zeng, J., & Dong, Y. (2011). MG132 treatment attenuates cardiac remodeling and dysfunction following aortic banding in rats via the NF- κ B/TGF β 1 pathway. *Biochemical Pharmacology*, 81(10), 1228–1236. <https://doi.org/10.1016/j.bcp.2011.03.009>
- Machiraju, P., & Greenway, S. C. (2019). Current methods for the maturation of induced pluripotent stem cellderived cardiomyocytes. *World Journal of Stem Cells*, 11(1), 33–43. <https://doi.org/10.4252/wjsc.v11.i1.33>
- Maejima, Y. (2020). The critical roles of protein quality control systems in the pathogenesis of heart failure. *Journal of Cardiology*, 75(3), 219–227. <https://doi.org/10.1016/j.jcc.2019.09.019>
- Maejima, Y., Kyoi, S., Zhai, P., Liu, T., Li, H., Ivessa, A., Sciarretta, S., Del Re, D. P., Zablocki, D. K., Hsu, C.-P., Lim, D.-S., Isobe, M., & Sadoshima, J. (2013). Mst1 inhibits autophagy by promoting the interaction between Beclin1 and Bcl-2. *Nature Medicine*, 19(11), 1478–1488. <https://doi.org/10.1038/nm.3322>
- Malandraki-Miller, S., & Riley, P. R. (2021). Use of artificial intelligence to enhance phenotypic drug discovery. *Drug Discovery Today*, 26(4), 887–901. <https://doi.org/10.1016/j.drudis.2021.01.013>
- Maloyan, A., Gulick, J., Glabe, C. G., Kayed, R., & Robbins, J. (2007). Exercise reverses preamyloid oligomer and prolongs survival in α B-crystallin-based desmin-related cardiomyopathy. *Proceedings of the National Academy of Sciences of the United States of America*, 104(14), 5995–6000. <https://doi.org/10.1073/pnas.0609202104>

- Maloyan, A., Osinska, H., Lammerding, J., Lee, R. T., Cingolani, O. H., Kass, D. A., Lorenz, J. N., & Robbins, J. (2009). Biochemical and mechanical dysfunction in a mouse model of desmin-related myopathy. *Circulation Research*, 104(8), 1021–1028. <https://doi.org/10.1161/CIRCRESAHA.108.193516>
- Martiny-Baron, G., Kazanietz, M. G., Mischak, H., Blumberg, P. M., Kochs, G., Hug, H., Marmé, D., & Schächtele, C. (1993). Selective inhibition of protein kinase C isozymes by the indolocarbazole Gö 6976. *The Journal of Biological Chemistry*, 268(13), 9194–9197.
- Marzuca-Nassr, G. N., Vitzel, K. F., Mancilla-Solorza, E., & Márquez, J. L. (2018). Sarcomere structure: The importance of desmin protein in muscle atrophy. *International Journal of Morphology*, 36(2), 576–583. <https://doi.org/10.4067/S0717-95022018000200576>
- Masui, S., Nakatake, Y., Toyooka, Y., Shimosato, D., Yagi, R., Takahashi, K., Okochi, H., Okuda, A., Matoba, R., Sharov, A. A., Ko, M. S. H., & Niwa, H. (2007). Pluripotency governed by Sox2 via regulation of Oct3/4 expression in mouse embryonic stem cells. *Nature Cell Biology*, 9(6), 625–635. <https://doi.org/10.1038/ncb1589>
- Mazzarotto, F., Tayal, U., Buchan, R. J., Midwinter, W., Wilk, A., Whiffin, N., Govind, R., Mazaika, E., De Marvao, A., Dawes, T. J. W., Felkin, L. E., Ahmad, M., Theotokis, P. I., Edwards, E., Ing, A. Y., Thomson, K. L., Chan, L. L. H., Sim, D., Baksi, A. J., ... Walsh, R. (2020). Reevaluating the Genetic Contribution of Monogenic Dilated Cardiomyopathy. *Circulation*, 141(5), 387–398. <https://doi.org/10.1161/CIRCULATIONAHA.119.037661>
- McCormick, E. M., Kenyon, L., & Falk, M. J. (2015). Desmin common mutation is associated with multi-systemic disease manifestations and depletion of mitochondria and mitochondrial DNA. *Frontiers in Genetics*, 6(JUN), 1–5. <https://doi.org/10.3389/fgene.2015.00199>
- McLendon, P. M., Ferguson, B. S., Osinska, H., Shenuarin Bhuiyan, M., James, J., McKinsey, T. A., & Robbins, J. (2014). Tubulin hyperacetylation is adaptive in cardiac proteotoxicity by promoting autophagy. *Proceedings of the National Academy of Sciences of the United States of America*, 111(48), E5178–E5186. <https://doi.org/10.1073/pnas.1415589111>
- McNally EM, M. L. (2017). DCM: genetic determinants and mechanisms. *Circulation Research*, 121(7), 731–748. <https://doi.org/10.1161/CIRCRESAHA.116.309396.Dilated>
- McQuin, C., Goodman, A., Chernyshev, V., Kamentsky, L., Cimini, B. A., Karhohs, K. W., Doan, M., Ding, L., Rafelski, S. M., Thirstrup, D., Wiegraebe, W., Singh, S., Becker, T., Caicedo, J. C., & Carpenter, A. E. (2018). CellProfiler 3.0: Next-generation image processing for biology. *PLoS Biology*, 16(7). <https://doi.org/10.1371/journal.pbio.2005970>
- Mehdiabadi, N. R., Boon Sim, C., Phipson, B., Kalathur, R. K. R., Sun, Y., Vivien, C. J., ter Huurne, M., Piers, A. T., Hudson, J. E., Oshlack, A., Weintraub, R. G., Konstantinov, I. E., Palpant, N. J., Elliott, D. A., & Porrello, E. R. (2022). Defining the Fetal Gene Program at Single-Cell Resolution in Pediatric Dilated Cardiomyopathy. *Circulation*, 146(14), 1105–1108. <https://doi.org/10.1161/CIRCULATIONAHA.121.057763>
- Melber, A., & Haynes, C. M. (2018). UPR mt regulation and output: A stress response mediated by mitochondrial-nuclear communication. *Cell Research*, 28(3), 281–295. <https://doi.org/10.1038/cr.2018.16>
- Michael Hay, David W Thomas, John L Craighead, Celia Economides, & Jesse Rosenthal. (2014). Clinical development success rates for investigational drugs. *Nature Biotechnology*, 32(1), 40–51. <https://www.nature.com/articles/nbt.2786>
- Micheletti, R., Palazzo, F., Barassi, P., Giacalone, G., Ferrandi, M., Schiavone, A., Moro, B., Parodi, O., Ferrari, P., & Bianchi, G. (2007). Istaroxime, a stimulator of sarcoplasmic reticulum calcium adenosine triphosphatase isoform 2a activity, as a novel therapeutic approach to heart failure. *The American Journal of Cardiology*, 99(2A), 24A-32A. <https://doi.org/10.1016/j.amjcard.2006.09.003>
- Milner, D. J., Mavroidis, M., Weisleder, N., & Capetanaki, Y. (2000). Desmin cytoskeleton linked

- to muscle mitochondrial distribution and respiratory function. *Journal of Cell Biology*, 150(6), 1283–1297. <https://doi.org/10.1083/jcb.150.6.1283>
- Mizushima, N., & Murphy, L. O. (2020). Autophagy Assays for Biological Discovery and Therapeutic Development. In *Trends in Biochemical Sciences* (Vol. 45, Issue 12, pp. 1080–1093). Elsevier Ltd. <https://doi.org/10.1016/j.tibs.2020.07.006>
- Molkentin, J. D., Lin, Q., Duncan, S. A., & Olson, E. N. (1997). Requirement of the transcription factor GATA4 for heart tube formation and ventral morphogenesis. *Genes and Development*, 11(8), 1061–1072. <https://doi.org/10.1101/gad.11.8.1061>
- Mostafavi, S., Balafkan, N., Pettersen, I. K. N., Nido, G. S., Siller, R., Tzoulis, C., Sullivan, G. J., & Bindoff, L. A. (2021). Distinct Mitochondrial Remodeling During Mesoderm Differentiation in a Human-Based Stem Cell Model. *Frontiers in Cell and Developmental Biology*, 9. <https://doi.org/10.3389/fcell.2021.744777>
- Mummery, C. L., Zhang, J., Ng, E. S., Elliott, D. A., Elefanty, A. G., & Kamp, T. J. (2012). Differentiation of Human Embryonic Stem Cells and Induced Pluripotent Stem Cells to Cardiomyocytes. *Circulation Research*, 111(3), 344–358. <https://doi.org/10.1161/CIRCRESAHA.110.227512>
- Nakagawa, M., Takizawa, N., Narita, M., Ichisaka, T., & Yamanaka, S. (2010). Promotion of direct reprogramming by transformation-deficient Myc. *Proceedings of the National Academy of Sciences of the United States of America*, 107(32), 14152–14157. <https://doi.org/10.1073/pnas.1009374107>
- Nicholson, M. W., Ting, C. Y., Chan, D. Z. H., Cheng, Y. C., Lee, Y. C., Hsu, C. C., Huang, C. Y., & Hsieh, P. C. H. (2022). Utility of iPSC-Derived Cells for Disease Modeling, Drug Development, and Cell Therapy. *Cells*, 11(11). <https://doi.org/10.3390/cells11111853>
- Niwa, H., Ogawa, K., Shimosato, D., & Adachi, K. (2009). A parallel circuit of LIF signalling pathways maintains pluripotency of mouse ES cells. *Nature*, 460(7251), 118–122. <https://doi.org/10.1038/nature08113>
- Orvedahl, A., Sumpter, R., Xiao, G., Ng, A., Zou, Z., Tang, Y., Narimatsu, M., Gilpin, C., Sun, Q., Roth, M., Forst, C. V., Wrana, J. L., Zhang, Y. E., Luby-Phelps, K., Xavier, R. J., Xie, Y., & Levine, B. (2011). Image-based genome-wide siRNA screen identifies selective autophagy factors. *Nature*, 480(7375), 113–117. <https://doi.org/10.1038/nature10546>
- Panda, A., Suvakov, M., Mariani, J., Drucker, K. L., Park, Y., Jang, Y., Kollmeyer, T. M., Sarkar, G., Bae, T., Kim, J. J., Yoon, W. H., Jenkins, R. B., Vaccarino, F. M., & Abyzov, A. (2023). Clonally Selected Lines After CRISPR-Cas Editing Are Not Isogenic. *CRISPR Journal*, 6(2), 176–182. <https://doi.org/10.1089/crispr.2022.0050>
- Parikh, S. S., Blackwell, D. J., Gomez-Hurtado, N., Frisk, M., Wang, L., Kim, K., Dahl, C. P., Fiane, A., Tønnessen, T., Kryshtal, D. O., Louch, W. E., & Knollmann, B. C. (2017). Thyroid and Glucocorticoid Hormones Promote Functional T-Tubule Development in Human-Induced Pluripotent Stem Cell-Derived Cardiomyocytes. *Circulation Research*, 121(12), 1323–1330. <https://doi.org/10.1161/CIRCRESAHA.117.311920>
- Pattison, J. S., & Robbins, J. (2008). Protein misfolding and cardiac disease: Establishing cause and effect. *Autophagy*, 4(6), 821–823. <https://doi.org/10.4161/auto.6502>
- Paulin, D., & Li, Z. (2004). Desmin: A major intermediate filament protein essential for the structural integrity and function of muscle. *Experimental Cell Research*, 301(1), 1–7. <https://doi.org/10.1016/j.yexcr.2004.08.004>
- Pegoraro, G., & Misteli, T. (2017). High-Throughput Imaging for the Discovery of Cellular Mechanisms of Disease. *Trends in Genetics*, 33(9), 604–615. <https://doi.org/10.1016/j.tig.2017.06.005>
- Pellegrino, M. W., Nargund, A. M., Kirienko, N. V., Gillis, R., Fiorese, C. J., & Haynes, C. M.

- (2014). Mitochondrial UPR-regulated innate immunity provides resistance to pathogen infection. *Nature*, 516(7531), 414–417. <https://doi.org/10.1038/nature13818>
- Perea-Gil, I., Seeger, T., Bruyneel, A. A. N., Termglinchan, V., Monte, E., Lim, E. W., Vadgama, N., Furihata, T., Gavidia, A. A., Arthur Ataam, J., Bharucha, N., Martinez-Amador, N., Ameen, M., Nair, P., Serrano, R., Kaur, B., Feyen, D. A. M., Diecke, S., Snyder, M. P., ... Karakikes, I. (2022). Serine biosynthesis as a novel therapeutic target for dilated cardiomyopathy. *European Heart Journal*. <https://doi.org/10.1093/eurheartj/ehac305>
- Pietrafesa, G., De Zio, R., Scorza, S. I., Armentano, M. F., Pepe, M., Forleo, C., Procino, G., Gerbino, A., Svelto, M., & Carmosino, M. (2023). Targeting unfolded protein response reverts ER stress and ER Ca²⁺ homeostasis in cardiomyocytes expressing the pathogenic variant of Lamin A/C R321X. *Journal of Translational Medicine*, 21(1), 1–18. <https://doi.org/10.1186/s12967-023-04170-y>
- Polvani, S., Pepe, S., Milani, S., & Galli, A. (2020). COUP-TFII in Health and Disease. 1–30.
- Pu, W. T., Ishiwata, T., Juraszek, A. L., Ma, Q., & Izumo, S. (2004). GATA4 is a dosage-sensitive regulator of cardiac morphogenesis. *Developmental Biology*, 275(1), 235–244. <https://doi.org/10.1016/j.ydbio.2004.08.008>
- Punn, N. S., & Agarwal, S. (2021). Automated diagnosis of COVID-19 with limited posteroanterior chest X-ray images using fine-tuned deep neural networks. *Applied Intelligence*, 51(5), 2689–2702. <https://doi.org/10.1007/s10489-020-01900-3>
- Quinlan, R. A., Elliott, J. L., Der Perng, M., Prescott, A. R., Jansen, K. A., & Koenderink, G. H. (2013). The specificity of the interaction between α B-crystallin and desmin filaments and its impact on filament aggregation and cell viability. *Philosophical Transactions of the Royal Society B: Biological Sciences*, 368(1617), 1–15. <https://doi.org/10.1098/rstb.2012.0375>
- Rahate, K., Bhatt, L. K., & Prabhavalkar, K. S. (2020). SERCA stimulation: A potential approach in therapeutics. *Chemical Biology and Drug Design*, 95(1), 5–15. <https://doi.org/10.1111/cbdd.13620>
- Rainer, P. P., Dong, P., Sorge, M., Fert-Bober, J., Holewinski, R. J., Wang, Y., Foss, C. A., An, S. S., Baracca, A., Solaini, G., Glabe, C. G., Pomper, M. G., Van Eyk, J. E., Tomaselli, G. F., Paolocci, N., & Agnetti, G. (2018). Desmin Phosphorylation Triggers Preamyloid Oligomers Formation and Myocyte Dysfunction in Acquired Heart Failure. *Circulation Research*, 122(10), e75–e83. <https://doi.org/10.1161/CIRCRESAHA.117.312082>
- Rakovic, A., Ziegler, J., Mårtensson, C. U., Prasuhn, J., Shurkewitsch, K., König, P., Paulson, H. L., & Klein, C. (2019). PINK1-dependent mitophagy is driven by the UPS and can occur independently of LC3 conversion. *Cell Death and Differentiation*, 26(8), 1428–1441. <https://doi.org/10.1038/s41418-018-0219-z>
- Ramaccini, D., Montoya-Uribe, V., Aan, F. J., Modesti, L., Potes, Y., Wieckowski, M. R., Krga, I., Glibetić, M., Pinton, P., Giorgi, C., & Matter, M. L. (2021). Mitochondrial Function and Dysfunction in Dilated Cardiomyopathy. In *Frontiers in Cell and Developmental Biology* (Vol. 8). Frontiers Media S.A. <https://doi.org/10.3389/fcell.2020.624216>
- Ramspacher, C., Steed, E., Boselli, F., Ferreira, R., Faggianelli, N., Roth, S., Spiegelhalter, C., Messaddeq, N., Trinh, L., Liebling, M., Chacko, N., Tessadori, F., Bakkers, J., Laporte, J., Hnia, K., & Vermot, J. (2015). Developmental Alterations in Heart Biomechanics and Skeletal Muscle Function in Desmin Mutants Suggest an Early Pathological Root for Desminopathies. *Cell Reports*, 11(10), 1564–1576. <https://doi.org/10.1016/j.celrep.2015.05.010>
- Reisen, F., Sauty De Chalon, A., Pfeifer, M., Zhang, X., Gabriel, D., & Selzer, P. (2015). Linking Phenotypes and Modes of Action Through High-Content Screen Fingerprints. *Assay and Drug Development Technologies*, 13(7), 415–427. <https://doi.org/10.1089/adt.2015.656>
- Rihel, J., Prober, D. A., Arvanites, A., Lam, K., Zimmerman, S., Jang, S., Haggarty, S. J., Kokel, D., Rubin, L. L., Peterson, R. T., & Schier, A. F. (2010). Zebrafish behavioral profiling links

- drugs to biological targets and rest/wake regulation. *Science (New York, N.Y.)*, 327(5963), 348–351. <https://doi.org/10.1126/science.1183090>
- Rodriguez, M. L., Beussman, K. M., Chun, K. S., Walzer, M. S., Yang, X., Murry, C. E., & Sniadecki, N. J. (2019). Substrate Stiffness, Cell Anisotropy, and Cell-Cell Contact Contribute to Enhanced Structural and Calcium Handling Properties of Human Embryonic Stem Cell-Derived Cardiomyocytes. *ACS Biomaterials Science and Engineering*, 5(8), 3876–3888. <https://doi.org/10.1021/acsbiomaterials.8b01256>
- Rog-Zielinska, E. A., Craig, M. A., Manning, J. R., Richardson, R. V., Gowans, G. J., Dunbar, D. R., Gharbi, K., Kenyon, C. J., Holmes, M. C., Hardie, D. G., Smith, G. L., & Chapman, K. E. (2015). Glucocorticoids promote structural and functional maturation of foetal cardiomyocytes: A role for PGC-1α. *Cell Death and Differentiation*, 22(7), 1106–1116. <https://doi.org/10.1038/cdd.2014.181>
- Rohban, M. H., Singh, S., Wu, X., Berthet, J. B., Bray, M. A., Shrestha, Y., Varelas, X., Boehm, J. S., & Carpenter, A. E. (2017). Systematic morphological profiling of human gene and allele function via cell painting. *eLife*, 6, 1–23. <https://doi.org/10.7554/eLife.24060>
- Roukos, V., & Misteli, T. (2014). Deep Imaging: The next frontier in microscopy. *Histochemistry and Cell Biology*, 142(2), 125–131. <https://doi.org/10.1007/s00418-014-1239-5>
- Sanbe, A., Daicho, T., Mizutani, R., Endo, T., Miyauchi, N., Yamauchi, J., Tanonaka, K., Glabe, C., & Tanoue, A. (2009). Protective effect of geranylgeranylacetone via enhancement of HSPB8 induction in desmin-related cardiomyopathy. *PLoS ONE*, 4(4). <https://doi.org/10.1371/journal.pone.0005351>
- Sanbe, A., Marunouchi, T., Yamauchi, J., Tanonaka, K., Nishigori, H., & Tanoue, A. (2011). Cardioprotective effect of nicorandil, a mitochondrial atp-sensitive potassium channel opener, prolongs survival in HSPB5 R120G transgenic mice. *PLoS ONE*, 6(4). <https://doi.org/10.1371/journal.pone.0018922>
- Sanbe, A., Osinska, H., Saffitz, J. E., Glabe, C. G., Kayed, R., Maloyan, A., & Robbins, J. (2004). Desmin-related cardiomyopathy in transgenic mice: A cardiac amyloidosis. *Proceedings of the National Academy of Sciences of the United States of America*, 101(27), 10132–10136. <https://doi.org/10.1073/pnas.0401900101>
- Sarparanta, J., Jonson, P. H., Kawan, S., & Udd, B. (2020). Neuromuscular diseases due to chaperone mutations: A review and some new results. *International Journal of Molecular Sciences*, 21(4). <https://doi.org/10.3390/ijms21041409>
- Schaaf, S., Shibamiya, A., Mewe, M., Eder, A., Stöhr, A., Hirt, M. N., Rau, T., Zimmermann, W. H., Conradi, L., Eschenhagen, T., & Hansen, A. (2011). Human engineered heart tissue as a versatile tool in basic research and preclinical toxicology. *PLoS ONE*, 6(10). <https://doi.org/10.1371/journal.pone.0026397>
- Scheeder, C., Heigwer, F., & Boutros, M. (2018). Machine learning and image-based profiling in drug discovery. *Current Opinion in Systems Biology*, 10, 43–52. <https://doi.org/10.1016/j.coisb.2018.05.004>
- Schröder, R., & Schoser, B. (2009). Myofibrillar myopathies: A clinical and myopathological guide: Mini-symposium: Protein aggregate myopathies. *Brain Pathology*, 19(3), 483–492. <https://doi.org/10.1111/j.1750-3639.2009.00289.x>
- Schultheiss, H. P., Fairweather, D. L., Caforio, A. L. P., Escher, F., Hershberger, R. E., Lipshultz, S. E., Liu, P. P., Matsumori, A., Mazzanti, A., McMurray, J., & Priori, S. G. (2019). Dilated cardiomyopathy. *Nature Reviews Disease Primers*, 5(1). <https://doi.org/10.1038/s41572-019-0084-1>
- Sciarretta, S., Maejima, Y., Zablocki, D., & Sadoshima, J. (2018). The Role of Autophagy in the Heart. *The Annual Review of Physiology Is Online At*, 80, 1–26. <https://doi.org/10.1146/annurev-physiol-021317>

- Selcen, D. (2011). Myofibrillar myopathies. *Neuromuscular Disorders*, 21(3), 161–171. <https://doi.org/10.1016/j.nmd.2010.12.007>
- Sen-Chowdhry, S., Syrris, P., Prasad, S. K., Hughes, S. E., Merrifield, R., Ward, D., Pennell, D. J., & McKenna, W. J. (2008). Left-Dominant Arrhythmogenic Cardiomyopathy. An Under-Recognized Clinical Entity. *Journal of the American College of Cardiology*, 52(25), 2175–2187. <https://doi.org/10.1016/j.jacc.2008.09.019>
- Sequeira, V., Nijenkamp, L. L. A. M., Regan, J. A., & Van Der Velden, J. (2014). The physiological role of cardiac cytoskeleton and its alterations in heart failure. *Biochimica et Biophysica Acta - Biomembranes*, 1838(2), 700–722. <https://doi.org/10.1016/j.bbamem.2013.07.011>
- Shaikh, S., Nandy, S. K., Cantí, C., & Lavandero, S. (2019). Bafilomycin-A1 and ML9 Exert Different Lysosomal Actions to Induce Cell Death. *Current Molecular Pharmacology*, 12(4), 261–271. <https://doi.org/10.2174/1874467212666190308131250>
- Shalem, O., Sanjana, N. E., Hartenian, E., Shi, X., Scott, D. A., Mikkelsen, T., Heckl, D., Ebert, B. L., Root, D. E., Doench, J. G., & Zhang, F. (2014). Genome-scale CRISPR-Cas9 knockout screening in human cells. *Science (New York, N.Y.)*, 343(6166), 84–87. <https://doi.org/10.1126/science.1247005>
- Sharma, S., Conover, G. M., Elliott, J. L., Der Perng, M., Herrmann, H., & Quinlan, R. A. (2017). α B-crystallin is a sensor for assembly intermediates and for the subunit topology of desmin intermediate filaments. *Cell Stress and Chaperones*, 22(4), 613–626. <https://doi.org/10.1007/s12192-017-0788-7>
- Singh, S., Kadioglu, H., Patel, K., Carrier, L., & Agnelli, G. (2020). Is Desmin Propensity to Aggregate Part of its Protective Function? *Cells*, 9(2), 491. <https://doi.org/10.3390/cells9020491>
- Singh, S. R., & Robbins, J. (2018). Desmin and cardiac disease: An unfolding story. In *Circulation Research* (Vol. 122, Issue 10, pp. 1324–1326). Lippincott Williams and Wilkins. <https://doi.org/10.1161/CIRCRESAHA.118.312965>
- Smolina, N., Khudiakov, A., Knyazeva, A., Zlotina, A., Sukhareva, K., Kondratov, K., Gogvadze, V., Zhivotovsky, B., Sejersen, T., & Kostareva, A. (2020). Desmin mutations result in mitochondrial dysfunction regardless of their aggregation properties. *Biochimica et Biophysica Acta - Molecular Basis of Disease*, 1866(6), 165745. <https://doi.org/10.1016/j.bbadic.2020.165745>
- Sommer, C., & Gerlich, D. W. (2013). Machine learning in cell biology-teaching computers to recognize phenotypes. *Journal of Cell Science*, 126(24), 5529–5539. <https://doi.org/10.1242/jcs.123604>
- Sossalla, S., Kallmeyer, B., Wagner, S., Mazur, M., Maurer, U., Toischer, K., Schmitto, J. D., Seipelt, R., Schöndube, F. A., Hasenfuss, G., Belardinelli, L., & Maier, L. S. (2010). Altered Na⁺ Currents in Atrial Fibrillation. Effects of Ranolazine on Arrhythmias and Contractility in Human Atrial Myocardium. *Journal of the American College of Cardiology*, 55(21), 2330–2342. <https://doi.org/10.1016/j.jacc.2009.12.055>
- Su, W., van Wijk, S. W., & Brundel, B. J. J. M. (2022). Desmin variants: Trigger for cardiac arrhythmias? *Frontiers in Cell and Developmental Biology*, 10(September), 1–11. <https://doi.org/10.3389/fcell.2022.986718>
- Sukhareva, K. S., Smolina, N. A., Churkina, A. I., Kalugina, K. K., Zhuk, S. V., Khudiakov, A. A., Khodot, A. A., Faggian, G., Luciani, G. B., Sejersen, T., & Kostareva, A. A. (2023). Desmin mutations impact the autophagy flux in C2C12 cell in mutation-specific manner. *Cell and Tissue Research*, 393(2), 357–375. <https://doi.org/10.1007/s00441-023-03790-6>
- Supek, F., Bošnjak, M., Škunca, N., & Šmuc, T. (2011). Revigo summarizes and visualizes long lists of gene ontology terms. *PLoS ONE*, 6(7). <https://doi.org/10.1371/journal.pone.0021800>

- Surova, O. V., Nagibin, V. S., & Tumanovskaya, L. V. (2009). *cell death and gene expression in neonatal rat*. 14(2), 57–61.
- Taegtmeyer, H., Sen, S., & Vela, D. (2010). Return to the fetal gene program: A suggested metabolic link to gene expression in the heart. *Annals of the New York Academy of Sciences*, 1188, 191–198. <https://doi.org/10.1111/j.1749-6632.2009.05100.x>
- Takahashi, K., Tanabe, K., Ohnuki, M., Narita, M., Ichisaka, T., Tomoda, K., & Yamanaka, S. (2007). Induction of Pluripotent Stem Cells from Adult Human Fibroblasts by Defined Factors. *Cell*, 131(5), 861–872. <https://doi.org/10.1016/j.cell.2007.11.019>
- Talkhabi, M., Aghdami, N., & Baharvand, H. (2016). Human cardiomyocyte generation from pluripotent stem cells: A state-of-art. *Life Sciences*, 145, 98–113. <https://doi.org/10.1016/j.lfs.2015.12.023>
- Tan, J., & Martin, S. E. (2016). Validation of synthetic CRISPR reagents as a tool for arrayed functional genomic screening. *PLoS ONE*, 11(12), 1–14. <https://doi.org/10.1371/journal.pone.0168968>
- Thornell, L.-E., Sjöström, M., & Andersson, K.-E. (1976). The relationship between mechanical stress and myofibrillar organization in heart Purkinje fibres. *Journal of Molecular and Cellular Cardiology*, 8(9), 689–695. [https://doi.org/https://doi.org/10.1016/0022-2828\(76\)90011-0](https://doi.org/https://doi.org/10.1016/0022-2828(76)90011-0)
- Tiburcy, M., Hudson, J. E., Balfanz, P., Schlick, S., Meyer, T., Liao, M. L. C., Levent, E., Raad, F., Zeidler, S., Wingender, E., Riegler, J., Wang, M., Gold, J. D., Kehat, I., Wettwer, E., Ravens, U., Dierickx, P., Van Laake, L. W., Goumans, M. J., ... Zimmermann, W. H. (2017). Defined engineered human myocardium with advanced maturation for applications in heart failure modeling and repair. *Circulation*, 135(19), 1832–1847. <https://doi.org/10.1161/CIRCULATIONAHA.116.024145>
- Tiburcy, M., Meyer, T., Liaw, N. Y., & Zimmermann, W.-H. (2020). Generation of Engineered Human Myocardium in a Multi-well Format. *STAR Protocols*, 1(1), 100032. <https://doi.org/10.1016/j.xpro.2020.100032>
- Tse, H.-F., Ho, J. C. Y., Choi, S.-W., Lee, Y.-K., Butler, A. W., Ng, K.-M., Siu, C.-W., Simpson, M. A., Lai, W.-H., Chan, Y.-C., Au, K.-W., Zhang, J., Lay, K. W. J., Esteban, M. A., Nicholls, J. M., Colman, A., & Sham, P. C. (2013). Patient-specific induced-pluripotent stem cells-derived cardiomyocytes recapitulate the pathogenic phenotypes of dilated cardiomyopathy due to a novel DES mutation identified by whole exome sequencing. *Human Molecular Genetics*, 22(7), 1395–1403. <https://doi.org/10.1093/hmg/ddt556>
- Tsikitis, M., Galata, Z., Mavroidis, M., Psarras, S., & Capetanaki, Y. (2018). Intermediate filaments in cardiomyopathy. *Biophysical Reviews*, 10(4), 1007–1031. <https://doi.org/10.1007/s12551-018-0443-2>
- Turkieh, A., El Masri, Y., Pinet, F., & Dubois-Deruy, E. (2022). Mitophagy Regulation following Myocardial Infarction. In *Cells* (Vol. 11, Issue 2). MDPI. <https://doi.org/10.3390/cells11020199>
- Utter, M. S., Ryba, D. M., Li, B. H., Wolska, B. M., & Solaro, R. J. (2015). Omecamtiv Mecarbil, a Cardiac Myosin Activator, Increases Ca²⁺ Sensitivity in Myofilaments With a Dilated Cardiomyopathy Mutant Tropomyosin E54K. *Journal of Cardiovascular Pharmacology*, 66(4), 347–353. <https://doi.org/10.1097/FJC.0000000000000286>
- Van Den Hoogenhof, M. M. G., Beqqali, A., Amin, A. S., Van Der Made, I., Aufiero, S., Khan, M. A. F., Schumacher, C. A., Jansweijer, J. A., Van Spaendonck-Zwarts, K. Y., Remme, C. A., Backs, J., Verkerk, A. O., Baartscheer, A., Pinto, Y. M., & Creemers, E. E. (2018). RBM20 mutations induce an arrhythmogenic dilated cardiomyopathy related to disturbed calcium handling. *Circulation*, 138(13), 1330–1342. <https://doi.org/10.1161/CIRCULATIONAHA.117.031947>

- van der Klooster, Z. J., Sepehrkhoy, S., Dooijes, D., te Rijdt, W. P., Schuringa, F. S. A. M., Lingeman, J., van Tintelen, J. P., Harakalova, M., Goldschmeding, R., Suurmeijer, A. J. H., Asselbergs, F. W., & Vink, A. (2021). P62-positive aggregates are homogenously distributed in the myocardium and associated with the type of mutation in genetic cardiomyopathy. *Journal of Cellular and Molecular Medicine*. <https://doi.org/10.1111/jcmm.16388>
- Van Spaendonck-Zwarts, K. Y., Van Hessem, L., Jongbloed, J. D. H., De Walle, H. E. K., Capetanaki, Y., Van der Kooi, A. J., Van Langen, I. M., Van den Berg, M. P., & Van Tintelen, J. P. (2011). Desmin-related myopathy. *Clinical Genetics*, 80(4), 354–366. <https://doi.org/10.1111/j.1399-0004.2010.01512.x>
- Veldhuizen, J., Migrino, R. Q., & Nikkhah, M. (2019). Three-dimensional microengineered models of human cardiac diseases. In *Journal of Biological Engineering* (Vol. 13, Issue 1). BioMed Central Ltd. <https://doi.org/10.1186/s13036-019-0155-6>
- Vučković, S., Dinani, R., Nollet, E. E., Kuster, D. W. D., Buikema, J. W., Houtkooper, R. H., Nabben, M., van der Velden, J., & Goversen, B. (2022). Characterization of cardiac metabolism in iPSC-derived cardiomyocytes: lessons from maturation and disease modeling. *Stem Cell Research and Therapy*, 13(1), 1–19. <https://doi.org/10.1186/s13287-022-03021-9>
- Wade, M. (2015). High-Throughput Silencing Using the CRISPR-Cas9 System: A Review of the Benefits and Challenges. *Journal of Biomolecular Screening*, 20(8), 1027–1039. <https://doi.org/10.1177/1087057115587916>
- Wahbi, K., Béhin, A., Charron, P., Dunand, M., Richard, P., Meune, C., Vicart, P., Laforêt, P., Stojkovic, T., Bécane, H. M., Kuntzer, T., & Duboc, D. (2012a). High cardiovascular morbidity and mortality in myofibrillar myopathies due to DES gene mutations: A 10-year longitudinal study. *Neuromuscular Disorders*, 22(3), 211–218. <https://doi.org/10.1016/j.nmd.2011.10.019>
- Wahbi, K., Béhin, A., Charron, P., Dunand, M., Richard, P., Meune, C., Vicart, P., Laforêt, P., Stojkovic, T., Bécane, H. M., Kuntzer, T., & Duboc, D. (2012b). High cardiovascular morbidity and mortality in myofibrillar myopathies due to DES gene mutations: a 10-year longitudinal study. *Neuromuscular Disorders*, 22(3), 211–218. <https://doi.org/10.1016/j.nmd.2011.10.019>
- Wang, L., Wada, Y., Ballan, N., Schmeckpeper, J., Huang, J., Rau, C. D., Wang, Y., Gepstein, L., & Knollmann, B. C. (2021). Triiodothyronine and dexamethasone alter potassium channel expression and promote electrophysiological maturation of human-induced pluripotent stem cell-derived cardiomyocytes. *Journal of Molecular and Cellular Cardiology*, 161(March), 130–138. <https://doi.org/10.1016/j.yjmcc.2021.08.005>
- Wang, T., Wei, J. J., Sabatini, D. M., & Lander, E. S. (2014). Genetic Screens in Human Cells Using the CRISPR-Cas9 System. *Science*, 343(6166), 80–84. <https://doi.org/10.1126/science.1246981>
- Wang, X., Osinska, H., Klevitsky, R., Gerdes, A. M., Nieman, M., Lorenz, J., Hewett, T., & Robbins, J. (2001). Expression of R120G- α B-crystallin causes aberrant desmin and α B-crystallin aggregation and cardiomyopathy in mice. *Circulation Research*, 89(1), 84–91. <https://doi.org/10.1161/hh1301.092688>
- Wang, X., & Robbins, J. (2014). Proteasomal and lysosomal protein degradation and heart disease. *Journal of Molecular and Cellular Cardiology*, 71, 16–24. <https://doi.org/10.1016/j.yjmcc.2013.11.006>
- Wang, X. X., Wan, R. Z., & Liu, Z. P. (2018). Recent advances in the discovery of potent and selective HDAC6 inhibitors. *European Journal of Medicinal Chemistry*, 143, 1406–1418. <https://doi.org/10.1016/j.ejmech.2017.10.040>
- Wang, Y. li. (2007). Computational Restoration of Fluorescence Images: Noise Reduction, Deconvolution, and Pattern Recognition. *Methods in Cell Biology*, 81(06), 435–445.

[https://doi.org/10.1016/S0091-679X\(06\)81020-4](https://doi.org/10.1016/S0091-679X(06)81020-4)

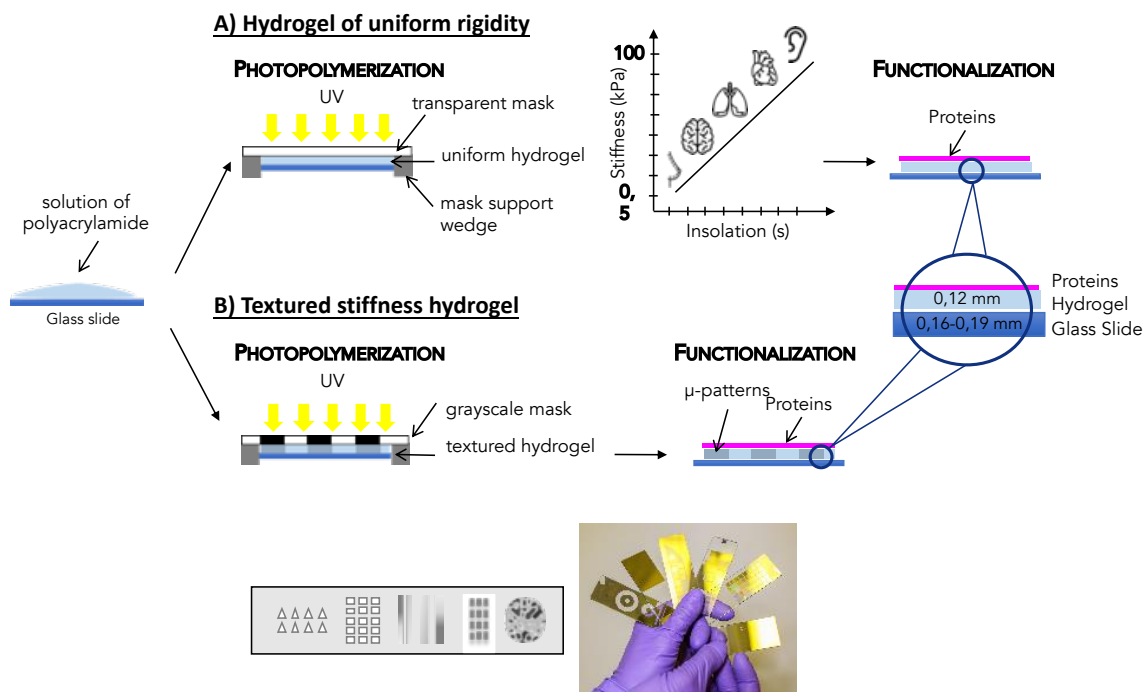
- Ware, J. S., & Cook, S. A. (2018). Role of titin in cardiomyopathy: From DNA variants to patient stratification. *Nature Reviews Cardiology*, 15(4), 241–252. <https://doi.org/10.1038/nrccardio.2017.190>
- Weisleder, N., Taffet, G. E., & Capetanaki, Y. (2004). Bcl-2 overexpression corrects mitochondrial defects and ameliorates inherited desmin null cardiomyopathy. *Proceedings of the National Academy of Sciences of the United States of America*, 101(3), 769–774. <https://doi.org/10.1073/pnas.0303202101>
- Wettstein, G., Bellaye, P. S., Micheau, O., & Bonniaud, P. (2012). Small heat shock proteins and the cytoskeleton: An essential interplay for cell integrity? *International Journal of Biochemistry and Cell Biology*, 44(10), 1680–1686. <https://doi.org/10.1016/j.biocel.2012.05.024>
- Wiersma, M., Henning, R. H., & Brundel, B. J. J. M. (2016). Derailed Proteostasis as a Determinant of Cardiac Aging. *Canadian Journal of Cardiology*, 32(9), 1166.e11-1166.e20. <https://doi.org/10.1016/j.cjca.2016.03.005>
- Wiersma, M., van Marion, D. M. S., Wüst, R. C. I., Houtkooper, R. H., Zhang, D., Groot, N. M. S. d., Henning, R. H., & Brundel, B. J. J. M. (2019). Mitochondrial Dysfunction Underlies Cardiomyocyte Remodeling in Experimental and Clinical Atrial Fibrillation. *Cells*, 8(10). <https://doi.org/10.3390/cells8101202>
- Willott, R. H., Gomes, A. V., Chang, A. N., Parvatiyar, M. S., Pinto, J. R., & Potter, J. D. (2010). Mutations in Troponin that cause HCM, DCM AND RCM: What can we learn about thin filament function? *Journal of Molecular and Cellular Cardiology*, 48(5), 882–892. <https://doi.org/10.1016/j.yjmcc.2009.10.031>
- Winter, D. L., Paulin, D., Mericskay, M., & Li, Z. (2014). Posttranslational modifications of desmin and their implication in biological processes and pathologies. *Histochemistry and Cell Biology*, 141(1), 1–16. <https://doi.org/10.1007/s00418-013-1148-z>
- Winter, L., Unger, A., Berwanger, C., Spörer, M., Türk, M., Chevessier, F., Strucksberg, K. H., Schlotzter-Schrehardt, U., Wittig, I., Goldmann, W. H., Marcus, K., Linke, W. A., Clemen, C. S., & Schröder, R. (2019). Imbalances in protein homeostasis caused by mutant desmin. *Neuropathology and Applied Neurobiology*, 45(5), 476–494. <https://doi.org/10.1111/nan.12516>
- Winter, Lilli, Staszewska, I., Mihailovska, E., Fischer, I., Goldmann, W. H., Schröder, R., & Wiche, G. (2014). Chemical chaperone ameliorates pathological protein aggregation in plectin-deficient muscle. *Journal of Clinical Investigation*, 124(3), 1144–1157. <https://doi.org/10.1172/JCI71919>
- Winter, Lilli, Wittig, I., Peeva, V., Eggers, B., Heidler, J., Chevessier, F., Kley, R. A., Barkovits, K., Strecker, V., Berwanger, C., Herrmann, H., Marcus, K., Kornblum, C., Kunz, W. S., Schröder, R., & Clemen, C. S. (2016). Mutant desmin substantially perturbs mitochondrial morphology, function and maintenance in skeletal muscle tissue. *Acta Neuropathologica*, 132(3), 453–473. <https://doi.org/10.1007/s00401-016-1592-7>
- Wippich, F., Bodenmiller, B., Trajkovska, M. G., Wanka, S., Aebersold, R., & Pelkmans, L. (2013). Dual specificity kinase DYRK3 couples stress granule condensation/ dissolution to mTORC1 signaling. *Cell*, 152(4), 791–805. <https://doi.org/10.1016/j.cell.2013.01.033>
- Wrobel, L., Topf, U., Bragoszewski, P., Wiese, S., Sztolsztener, M. E., Oeljeklaus, S., Varabyova, A., Lirsiki, M., Chroscicki, P., Mroczeck, S., Januszewicz, E., Dziembowski, A., Koblowska, M., Warscheid, B., & Chacinska, A. (2015). Mistargeted mitochondrial proteins activate a proteostatic response in the cytosol. *Nature*, 524(7566), 485–488. <https://doi.org/10.1038/nature14951>
- Wu, S. M. (2008). Mesp1 at the heart of mesoderm lineage specification. *Cell Stem Cell*, 3(1), 1–2.

<https://doi.org/10.1016/j.stem.2008.06.017>

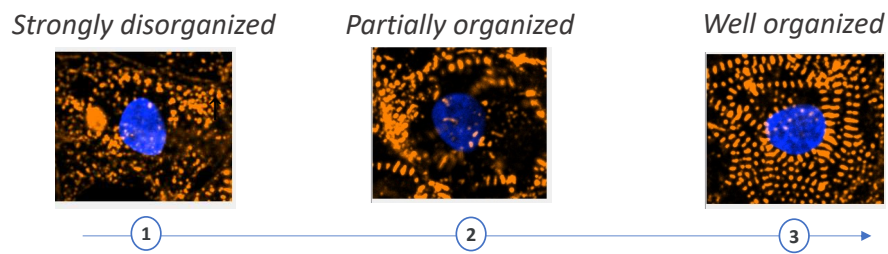
- Ya, J., Markman, M. W. M., Wagenaar, G. T. M., Blommaart, P. J. B., Moorman, A. F. M., & Lamers, W. H. (1997). Expression of the smooth-muscle proteins α -smooth-muscle actin and calponin, and of the intermediate filament protein desmin are parameters of cardiomyocyte maturation in the prenatal rat heart. *Anatomical Record*, 249(4), 495–505. [https://doi.org/10.1002/\(SICI\)1097-0185\(199712\)249:4<495::AID-AR9>3.0.CO;2-Q](https://doi.org/10.1002/(SICI)1097-0185(199712)249:4<495::AID-AR9>3.0.CO;2-Q)
- Yamanaka, S., & Takahashi, K. (2006). [Induction of pluripotent stem cells from mouse fibroblast cultures]. *Tanpakushitsu Kakusan Koso. Protein, Nucleic Acid, Enzyme*, 51(15), 2346–2351. <http://www.ncbi.nlm.nih.gov/pubmed/17154061>
- Yang, Jin, Grafton, F., Ranjbarvaziri, S., Budan, A., Farshidfar, F., Cho, M., Xu, E., Ho, J., Maddah, M., Loewke, K. E., Medina, J., Sperandio, D., Patel, S., Hoey, T., & Mandegar, M. A. (2022). Phenotypic screening with deep learning identifies HDAC6 inhibitors as cardioprotective in a BAG3 mouse model of dilated cardiomyopathy. In *Sci. Transl. Med* (Vol. 14). <https://www.science.org>
- Yang, Jing, He, J., Ismail, M., Tweeten, S., Zeng, F., Gao, L., Ballinger, S., Young, M., Prabhu, S. D., Rowe, G. C., Zhang, J., Zhou, L., & Xie, M. (2019). HDAC inhibition induces autophagy and mitochondrial biogenesis to maintain mitochondrial homeostasis during cardiac ischemia/reperfusion injury. *Journal of Molecular and Cellular Cardiology*, 130(August 2018), 36–48. <https://doi.org/10.1016/j.yjmcc.2019.03.008>
- Yang, X., Rodriguez, M. L., Leonard, A., Sun, L., Fischer, K. A., Wang, Y., Ritterhoff, J., Zhao, L., Kolwicz, S. C., Pabon, L., Reinecke, H., Sniadecki, N. J., Tian, R., Ruohola-Baker, H., Xu, H., & Murry, C. E. (2019). Fatty Acids Enhance the Maturation of Cardiomyocytes Derived from Human Pluripotent Stem Cells. *Stem Cell Reports*, 13(4), 657–668. <https://doi.org/10.1016/j.stemcr.2019.08.013>
- Yoshida, Y., & Yamanaka, S. (2017). Induced Pluripotent Stem Cells 10 Years Later. *Circulation Research*, 120(12), 1958–1968. <https://doi.org/10.1161/CIRCRESAHA.117.311080>
- Yoshii, S. R., & Mizushima, N. (2017). Monitoring and measuring autophagy. In *International Journal of Molecular Sciences* (Vol. 18, Issue 9). MDPI AG. <https://doi.org/10.3390/ijms18091865>
- Zeisberg, E. M., Ma, Q., Juraszek, A. L., Moses, K., Schwartz, R. J., Izumo, S., & Pu, W. T. (2005). Morphogenesis of the right ventricle requires myocardial expression of Gata4. *Journal of Clinical Investigation*, 115(6), 1522–1531. <https://doi.org/10.1172/JCI23769>
- Zhang, D., Hu, X., Henning, R. H., & Brundel, B. J. J. M. (2016). Keeping up the balance: Role of HDACs in cardiac proteostasis and therapeutic implications for atrial fibrillation. *Cardiovascular Research*, 109(4), 519–526. <https://doi.org/10.1093/cvr/cvv265>
- Zhang, R., Shen, Y., Zhou, L., Sangwung, P., Fujioka, H., Zhang, L., & Liao, X. (2017). Short-term administration of Nicotinamide Mononucleotide preserves cardiac mitochondrial homeostasis and prevents heart failure. *Journal of Molecular and Cellular Cardiology*, 112(September), 64–73. <https://doi.org/10.1016/j.yjmcc.2017.09.001>
- Zhao, R., Watt, A. J., Battle, M. A., Li, J., Bondow, B. J., & Duncan, S. A. (2008). Loss of both GATA4 and GATA6 blocks cardiac myocyte differentiation and results in acardia in mice. *Developmental Biology*, 317(2), 614–619. <https://doi.org/10.1016/j.ydbio.2008.03.013>
- Zheng, H., Tang, M., Zheng, Q., Kumarapeli, A. R. K., Horak, K. M., Tian, Z., & Wang, X. (2010). Doxycycline attenuates protein aggregation in cardiomyocytes and improves survival of a mouse model of cardiac proteinopathy. *Journal of the American College of Cardiology*, 56(17), 1418–1426. <https://doi.org/10.1016/j.jacc.2010.01.075>
- Zheng, Q., Su, H., Ranek, M. J., & Wang, X. (2011). Autophagy and p62 in cardiac proteinopathy. *Circulation Research*, 109(3), 296–308. <https://doi.org/10.1161/CIRCRESAHA.111.244707>

VIII. ANNEXES

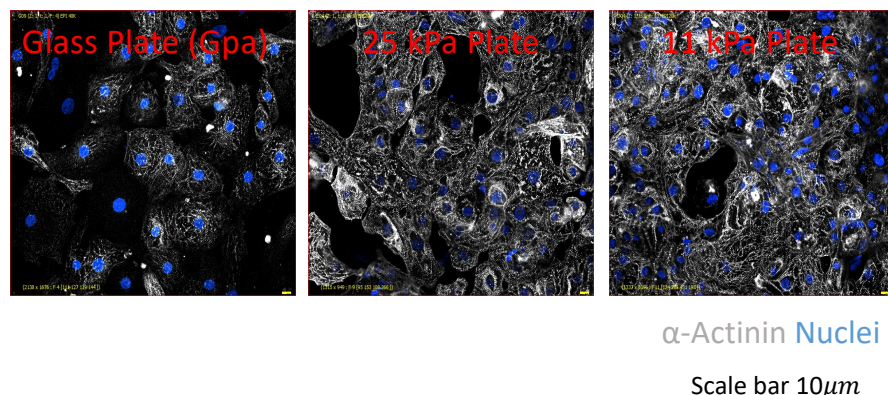
Annexe 1 : Cardiac modelling of desmin related myofibrillar myopathy *in vitro* on micropatterned soft hydrogels (Cell&Softs)



A.



B.



C.

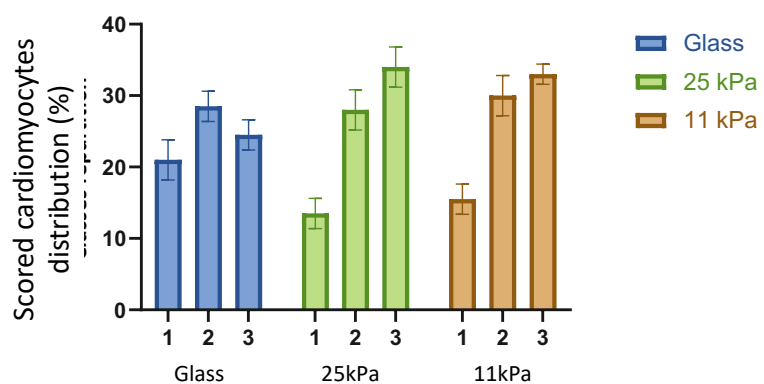
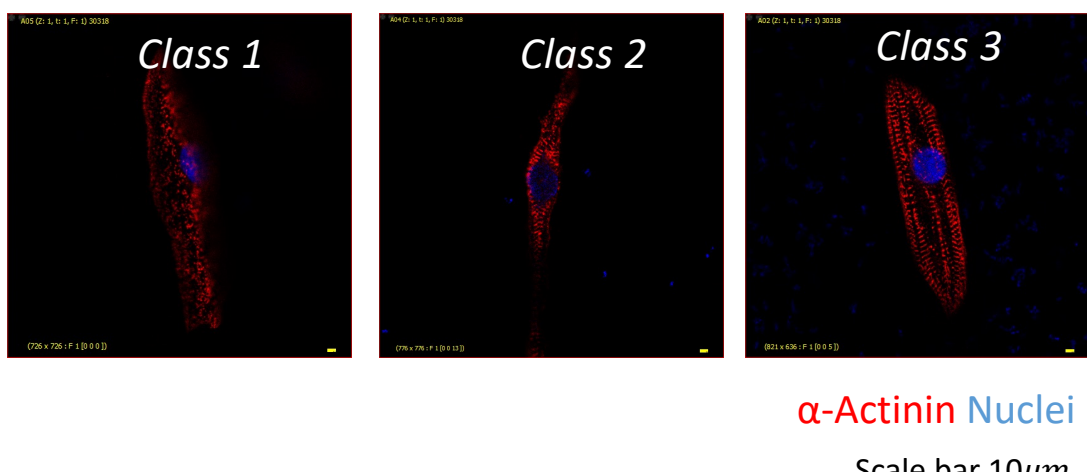


Figure 73 : Immunocytostaining of control cardiomyocyte cultured in different stiffness plates showing differences in the distribution of scored cardiomyocytes. These preliminary data suggest that cardiomyocyte cultures on 11 or 25kPa stiffness plates had a lower proportion of strongly

disorganized cardiomyocytes (score 1) than in glass plate cultures

A.



B.

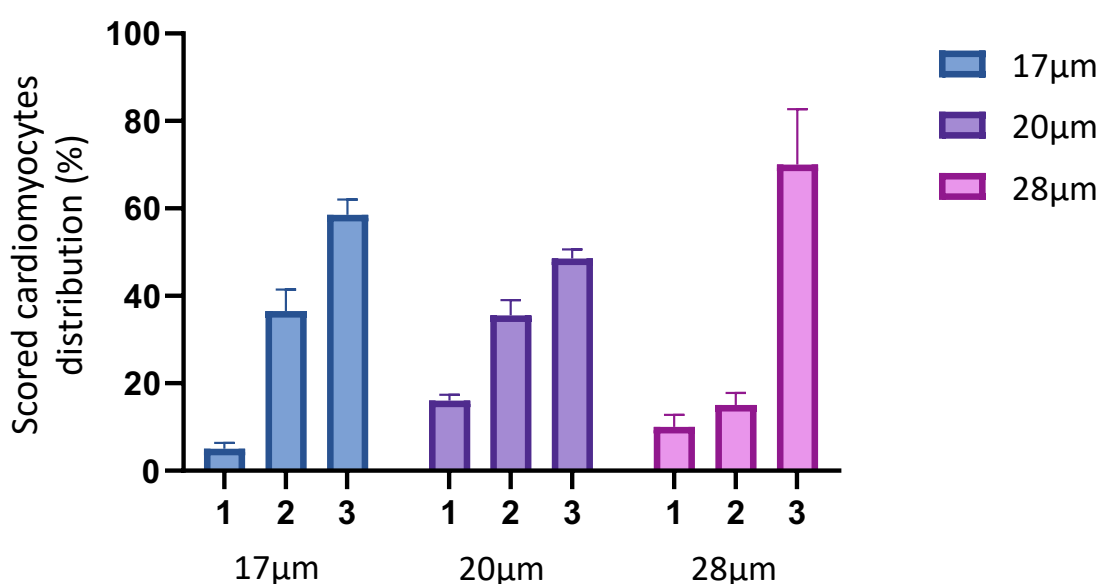


Figure 74 : Immunocytostaining of control cardiomyocyte cultured in 11kPa plates stiffness with different micropattern width showing differences in the distribution of scored cardiomyocytes. First, the micropattern appeared to reduce the proportion of strongly disorganized cardiomyocytes (score 1) compared with previous results. Secondly, the micropatterned cultures of cardiomyocytes at 28 μ m width seem to have a higher proportion of well organized cardiomyocytes (score 3).

Annexe 2: Analysis of the autophagic flux based on SQT M1/p62

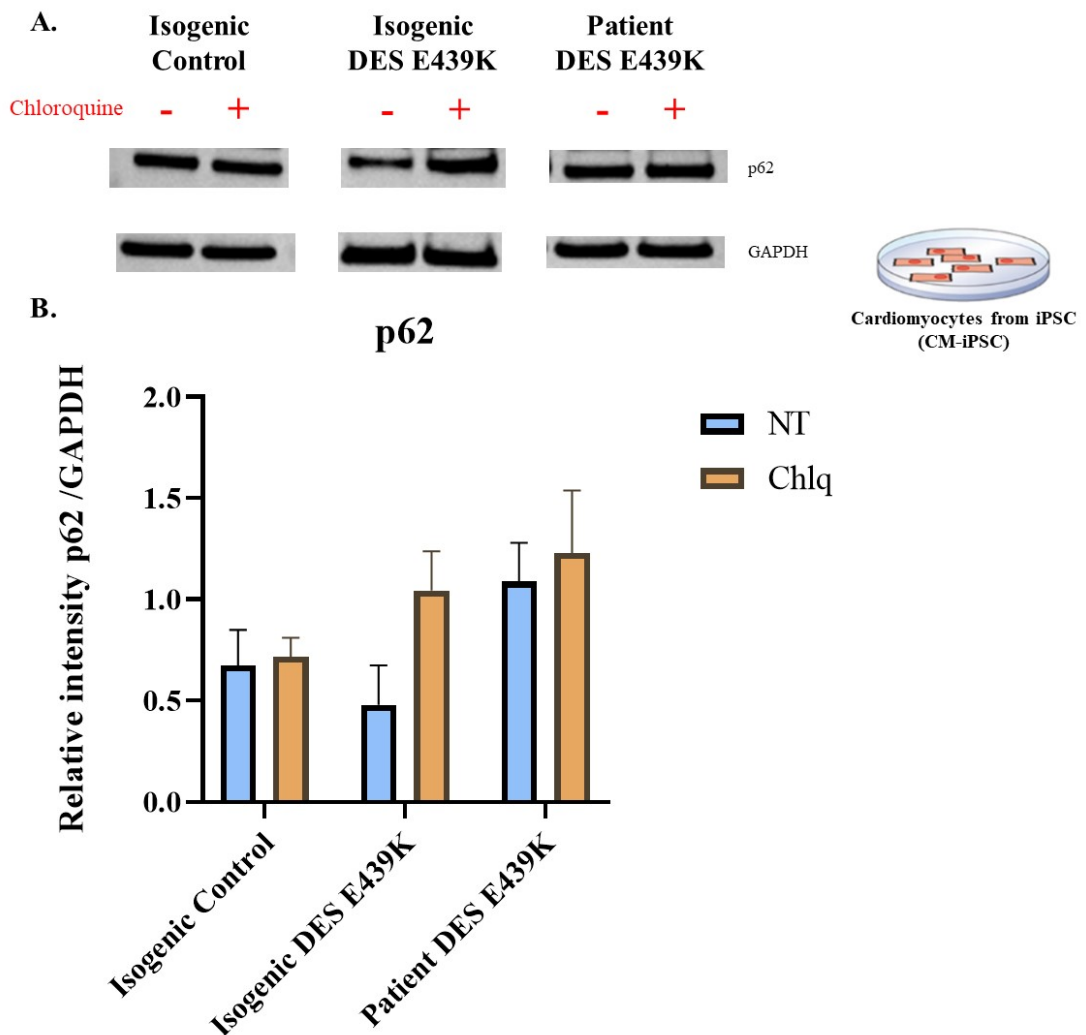


Figure 75: Western blot of Cardiomyocytes derived from iPSC (Isogenic control; Isogenic DES E439K; Patient DES E439K) in different condition +/- Chloroquine and staining of p62 (Autophagic flux marker) A. p62 protein levels were analyzed by performing Western blotting analysis, glyceraldehyde 3-phosphate dehydrogenase (GAPDH) was used as an internal control. B. Quantitative analysis of the results of Western blotting analysis, p62 levels normalized using the GAPDH levels.

Annexe 2 :

Critical contribution of mitochondria in the development of cardiomyopathy linked to desmin mutation

Yeranuhi Hovhannisyan¹, Zhenlin Li¹, Domitille Callon^{1,2}, Rodolphe Suspène³, Vivien Batoumeni¹, Alexis Canette⁴, Jocelyne Blanc¹, Hakim Hocini⁵, Cécile Lefebvre⁵, Nora El-Jahrani⁵, Aurore L'honoré¹, Ekaterini Kordeli¹, Paul Fornes², Jean-Paul Concorde⁶, Gérard Tachdjian⁷, Anne-Marie Rodriguez¹, Jean-Pierre Vartanian³, Anthony Béhin⁸, Karim Wahbi⁹, Pierre Joanne^{1*} & Onnik Agbulut^{1*}

¹ Sorbonne Université, Institut de Biologie Paris-Seine (IBPS), UMR CNRS 8256, INSERM U1164, Biological Adaptation and Ageing, Paris-France.

² Academic Hospital of Reims, Department of Pathology, Reims-France.

³ Virus and cellular stress Unit, Department of Virology, Institut Pasteur, Université Paris Cité, Paris-France.

⁴ Sorbonne Université, CNRS, Institut de Biologie Paris-Seine (IBPS), Service de microscopie électronique (IBPS-SME), Paris-France.

⁵ Université Paris-Est Créteil, INSERM U955, Equipe 16, Créteil-France.

⁶ Museum National d'Histoire Naturelle, INSERM U1154, CNRS UMR7196, Paris-France.

⁷ Université Paris Saclay, Hôpital Antoine Béclère, AP-HP, Service d'Histologie-Embryologie-Cytogénétique, Laboratoire de Cytogénétique, Clamart-France.

⁸ Sorbonne Université, Pitié-Salpêtrière Hospital, AP-HP, Reference Center for Muscle Diseases Paris-Est, Myology Institute, Paris-France.

⁹ Université Paris Cité, Cochin Hospital, AP-HP, Cardiology Department, Paris-France.

Short title: Mitochondria in desmin cardiomyopathy

Total word count: 14270

***Corresponding Authors:** Prof. Onnik Agbulut & Dr. Pierre Joanne. Sorbonne Université, Institut de Biologie Paris-Seine, UMR CNRS 8256, Inserm ERL U1164, 7, quai

St Bernard (case 256), F-75005 Paris-France. Email : onnik.agbulut@sorbonne-universite.fr & pierre.joanne@sorbonne-universite.fr

Abstract

Beyond the observed alterations in cellular structure and mitochondria, the cellular mechanisms linking genetic mutations to the development of heart failure in patients affected by desmin defects remain unclear due, in part, to the lack of relevant human cardiomyocyte models. We investigated the role of mitochondria using cardiomyocytes derived from human induced pluripotent stem cells carrying the heterozygous DES^{E439K} desmin mutation, that were either isolated from a patient or generated by gene editing. To increase physiological relevance, cells were either cultured on an anisotropic surface to obtain elongated and aligned cardiomyocytes, or as spheroids to create a micro-tissue. When applicable, results were confirmed with heart biopsies from the family harboring DES^{E439K} mutation. We show that mutant cardiomyocytes reproduce critical defects in mitochondrial architecture, respiratory capacity and metabolic activity as observed in patient's heart tissue. To challenge the pathological mechanism, normal mitochondria were transferred inside the mutant cardiomyocytes. This treatment restored mitochondrial and contractile functions. This work demonstrates the crucial role of mitochondrial abnormalities in the pathophysiology of desmin-related cardiomyopathy, and opens-up new potential therapeutic perspectives.

Key words: Desmin, Cardiomyocytes, Stem cells, Mitochondria, iPSC, Heart Failure, Dilated cardiomyopathy, Myofibrillar myopathy.

Abbreviations

- ATP5A, ATP synthase subunit alpha
COX, cytochrome c oxidase
CMs, Cardiomyocytes
Control-CMs, Control cardiomyocytes
Cx43, connexin-43
DCM, dilated cardiomyopathy
DEGs, differentially expressed genes
E439K-CMs, mutated cardiomyocytes
ECAR, extracellular acidification rate
EVs, extracellular vesicles
FCCP, Carbonyl cyanide-4 (trifluoromethoxy) phenylhydrazone
FDR, false discovery rate
FE-SEM, Field emission scanning electron microscopy
GSEA, gene set enrichment analysis
IF, intermediate filament
IFN α/β , Interferon alpha/beta
iPSC, induced pluripotent stem cells
iPSC-CM, cardiomyocytes derived from induced pluripotent stem cells
Iso-E439K-CMs, isogenic mutated cardiomyocytes
MFM, myofibrillar myopathy
MFM1, desmin-related myofibrillar myopathy
MT-COI, mitochondrial cytochrome c oxidase subunit I
mtDNA, mitochondrial DNA
NDUFB8, complex I NADH dehydrogenase (ubiquinone) 1 beta subcomplex subunit 8
OCR, oxygen consumption rate
PBMC, peripheral blood mononucleated cells
PCA, principal component analysis
PFA, paraformaldehyde

SEM, scanning electron microscopy

SDHB, complex II iron-sulfur protein subunit of succinate dehydrogenase

Td, denaturation temperature

TEM, transmission electron microscopy

VDAC, voltage-dependent anion channel

WGCNA, Weighted Gene Correlation Network Analysis

Introduction

Desmin-related myofibrillar myopathy (MFM1, OMIM:601419) represents a group of skeletal and cardiac muscle disorders caused by mutations in the desmin-encoding *DES* gene. Desmin is the major component of intermediate filaments (IFs) in striated and smooth muscle cells and tissues and plays an essential role in the tensile strength and integrity of muscle fibers^{1–4}. In humans, about a hundred mutations of the *DES* gene have been identified which usually disrupt the ability of desmin to form filamentous networks and/or to interact with partner proteins^{3,5}. Consequently, desmin mutations alter the mechanical properties of the desmin network, resulting in multiple functional and structural abnormalities in muscle cells, leading to progressive skeletal myopathy and cardiomyopathy, the most common clinical manifestations of MFM1⁶. Impairment of desmin network is also closely associated to the etiology of many striated muscle pathologies. It is worth to note that desmin IFs remodeling also occurs when proteostasis is disturbed, during inflammatory process, or during aging^{7–9}.

Beyond its role in muscle cell integrity and organization, several studies conducted with genetically modified cell lines carrying human desmin mutations or in desmin knockout mice indicated that desmin critically modulates mitochondria functions^{10–15}. Importantly, it has been noticed that mutated desmin leads to severe mitochondria abnormalities that directly contribute to MFM1 development. Consistent with this finding, abnormalities in the distribution and morphology of mitochondria as well as in their respiratory function have been reported with *DES* mutations using transiently transfected human or animal cells carrying human *DES* mutations^{15,16}, transgenic mouse hearts with *DES* mutations¹⁷ as well as human heart and skeletal biopsy samples of MFM1 patients^{18–20}. Moreover, several publications describe that *DES* mutations are associated with Cytochrome c oxidase (COX)-negative fibers and decreased activity of mitochondrial respiratory chain enzymes^{19,20}. Whether and how desmin regulates mitochondria network and function is far from being understood. Several reports indicated that desmin could mediate this effect through its physical interaction with mitochondria. Indeed, desmin can interact with mitochondria through either cytolinker proteins such as plectin isoform 1b^{21–23} or voltage-dependent anion channel (VDAC)^{24,25}, or directly through its N-terminal domain²⁶. Despite these previous studies pointing out that mitochondria are key players in the development of MFM1, none of them have used patient-derived cardiomyocytes or human cardiac organoids, at the best patient muscle biopsies or transgenic mice or transitory transfected cells carrying *DES* mutations have been used up to now. Therefore, knowledge in this field has been hampered by the lack of a suitable human cardiomyocyte experimental model to investigate the heart disease of MFM1.

To circumvent this limitation and address whether mitochondria is a critical target of desmin mutation in cardiomyocytes from MFM1 patients, we generated cardiomyocytes from induced pluripotent stem cells (iPSC) of a patient carrying heterozygous *DES*^{E439K} mutation. Using 2D and 3D models, we examined the structural and functional impairments

of cardiomyocytes generated from *DES*^{E439K} patient iPSC (E439K-CMs) and compared to cardiomyocytes generated from healthy donors (Control-CMs) as well as from an isogenic pair carrying the same mutation introduced in healthy iPSC by CRISPR/Cas9 (Iso-E439K-CMs). We then focused on investigation of mitochondrial abnormalities by oxygraphy measurement as well as immunolocalization, western-blot and electron microscopy analyses. Finally, we challenged the impact of mitochondrial abnormalities as a main mechanism in the emergence of desmin-related cardiomyopathy in *DES*^{E439K} patients by implementing a treatment with extracellular vesicles (EVs) containing healthy mitochondria. Here we show that this treatment was able to significantly restore mitochondrial respiration and increase contractility of E439K-CMs. In summary, our study highlights the deleterious effect of *DES*^{E439K} and the crucial role of mitochondrial abnormalities in pathophysiology of MFM1.

Methods

The study was conducted with samples from 2 patients (CII and CIII), from a French family with several members suffering myofibrillar myopathy (MFM1) (see **Figure-1**). Affected patients present a skeletal myopathy associated with arrhythmogenic DCM with complete atrioventricular block and atrial fibrillation. They have been diagnosed with a heterozygous pathogenic variant in the *DES* gene, namely a G-to-A transition at c.1315 (codon 439) in exon 8, which resulted in a substitution of glutamic acid by lysine in position 439 (*DES*^{E439K}) at the C-terminal end of desmin. Such replacement of a negatively charged amino acid by a positively charged one is considered as a pathological modification that can affect desmin structure and its interactome^{27,28}.

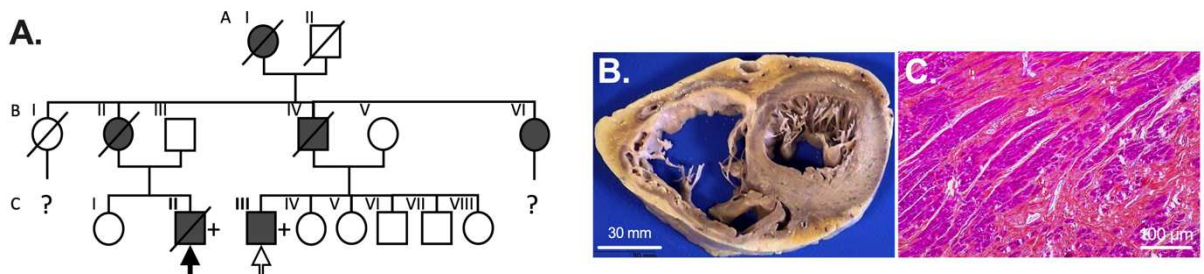


Figure 1. Familial myofibrillar myopathy with heterozygous *DES*^{E439K} variant. (A) Pedigree of the affected family. Circles and squares represent female and male subjects, respectively. Solid symbols show patients with myopathy and cardiomyopathy. Crossed-out symbols stand for deceased subjects. The + symbol represents patient with presence of the pathogenic heterozygous *DES* variant. Solid arrow indicates the family member whose cardiac biopsies were used for the histological and biochemical analysis. Empty arrow indicates the family member whose peripheral blood mononuclear cells were used to generate iPSC clones. (B) Biventricular transversal heart slice of cardiac samples of the Index case CII (solid arrow in A) showing dilation of both ventricles. (C) Hematoxylin-eosin safran staining of formalin fixed left ventricle section showing extensive fibrosis.

Human tissue samples. In addition to post-mortem heart samples of the index case CII (see **Figure-1A**) carrying a heterozygous c.1315G>A (E439K) desmin mutation²⁹,

post-mortem heart samples from five control healthy patients were obtained after anonymization by the Platform Center of Biological Resources of the Department of Pathology (Academic Hospital of Reims, France). For each patient, authorizations to perform autopsy and sampling were obtained from the French Biomedicine Agency. Blood samples from patient CIII were collected by Phenocell SAS (Grasse, France) and peripheral blood mononuclear cells (PBMC) were freshly collected using the SepMate (Stemcell Technologies) protocol. The generation of human iPSCs were performed with approval from the French Research Ministry in Phenocell SAS (agreement number: #AC-2013-1973). Formal informed consent was obtained from the different patients included in this study.

Generation and culture of iPSCs. PBMC of the patient CIII were reprogrammed into iPSCs using a non-integrative method (Epi5™ Episomal iPSC Reprogramming Kit, Thermo Fisher Scientific). Two clones (c2 and c15) were isolated and used in this study. Gibco Human Episomal iPSC clone (Control 1, Thermo Fisher Scientific) and CW30318 (Control 2, Fuji Cellular Dynamics) derived from healthy individuals without any cardiac pathology, were used as controls. All iPSC clones were cultured and amplified on Matrigel-coated (Corning Life Sciences) culture dishes with daily replacement of mTeSR1 (Stemcell Technologies) and passaged (1:30 ratio) when approximately 80% confluence using ReLeSR (Stemcell Technologies).

Generation of an isogenic pair. Control 1 iPSC cultured with mTesR1 was detached using Accutase® (Stemcell Technologies) and electroporated using the Neon® electroporation system (Thermo Fisher Scientific) with 3 different plasmids diluted in resuspension RB_buffer: (1) 1000 ng/µL of pCMV_AncBE4max_P2A_GFP³⁰, encoding a nucleus-targeted chimeric protein composed of a cytidine deaminase and a Cas9 nickase, 2x500 ng/µL of pBlueScript-U6sgRNA³¹ encoding single guide RNA specific for *DES* or encoding single guide RNA specific for *ATPIA1* (used for a positive selection of transformed clones)³². The sequence of guide RNAs for *DES* to generate E439K mutation was 5'-CTcAGAACCCCTTGCTC-3' and the sequence of guide RNAs for *ATPIA1* to generate point mutation to induce resistance to ouabain was 5'-cATCCAAGCTGCTACAGAAAGG-3'³³. Electroporation was performed at a voltage of 1300 V with 2 pulses on 150 000 cells resuspended in resuspension RBuffer for a 10 µl neon tip. After electroporation, the cells were transferred into pre-warmed mTeSR1 medium on Matrigel-coated plates, cultured for 3 days at which 1 µg/ml ouabain (Enzo Life Sciences) was added for clonal selection during 3 more days. The resistant cells were sequenced to confirm or deny the success of genomic editing. Single cell cloning was then performed using CloneR (Stem Cell Technologies) following the manufacturer's instructions. pCMV_AncBE4max_P2A_GFP was a gift from David Liu (Addgene plasmid #112100; <http://n2t.net/addgene:112100>; RRID:Addgene_112100) and pBluescript-U6sgRNA empty was a gift from Eugene Yeo (Addgene plasmid #74707; <http://n2t.net/addgene:74707>; RRID:Addgene_74707).

Generation of iPSC-derived human cardiomyocytes (iPSC-CM). Cardiac differentiation (**Figure-2A**) is based on the GiWi protocol published in 2012³⁴. At 80% confluence, iPSCs were detached with Accutase®, counted and then seeded at optimal density. Two days later, cardiac differentiation was initiated by replacing mTeSR1 with RPMI medium (Thermo Fisher Scientific) enriched with 2% insulin-free B27 supplement (Thermo Fisher Scientific) containing 9 µM CHIR99021 (Selleckchem). This medium was replaced with RPMI supplemented insulin-free B27 after 24 hours. Two days later, cells were treated with RPMI enriched with insulin-free B27 and 5 µM IWP2 (Tocris Bioscience) for 48 hours and then the medium was replaced with RPMI enriched with insulin-free B27. Two days later, the culture medium was replaced by RPMI enriched with 2% B27 supplement and was changed every two days. From day 12, 1µM dexamethasone (Merck) and 100nM triiodothyronine hormone (Merck) were added to the medium (maturation medium). At days 19-20 after initial detachment, cardiomyocytes were detached with TrypLE Select 1X (Thermo Fisher Scientific) (incubation at 37°C for 10 min), suspended in RPMI containing 20% fetal bovine serum (Thermo Fisher Scientific), filtered on a 70 µm cell strainer and then used for subsequent analysis or frozen in PSC Cryomedium (Life Technologies).

Generation of cardiac spheroids. 3D cardiac spheroid was generated using primary human cardiac fibroblasts (NHCFV, Lonza) cultured in FGM3 (Lonza) and iPSC-CM detached 19 days after the initiation of differentiation. Appropriate amounts of fibroblasts (1500/Spheroid) and iPSC-CM (8500/Spheroid) are mixed and seeded in 96-well spindle-shaped plate (S-BIO) in RPMI (Thermo Fisher Scientific) containing 20% of fetal bovine serum (Thermo Fisher Scientific). Medium was changed the day after, and every two days thereafter, with maturation medium. Spontaneously contractile spheroids were manually counted at day 7.

Immunostaining and morphological analysis. Frozen iPSC-CM were thawed, centrifuged at 200xg to remove freezing medium and directly seeded on the coverslips micropatterned with gelatin lines (see Supplemental methods). They were then cultured 20 days in maturation medium, washed with PBS, fixed with 4% PFA for 5 min and permeabilized in cold methanol (-20°C) or 0.1% Triton prior to immunostaining. Paraffin-embedded human tissue sections were deparaffinized in successive bathes of xylene and ethanol. Antigenic epitopes were unmasked in citrate buffer pH 6.0 at 95°C for 30 min. Sections were incubated with 1×TrueBlack Lipofuscin Autofluorescence Quencher (Biotium) in 70% ethanol for 30 s at room temperature. Primary antibodies were incubated overnight at 4°C and secondary for 1 hour at room temperature diluted in PBS containing 2% of bovine serum albumin (see Supplemental Table 1 and 2). Slides were mounted with mounting medium containing Mowiol (Merck). Experiments were performed 3 times for Control-CMs (Control 1 and 2), patient E439K-CMs (clones c2 and c15) and isoE439K-CMs. At least 15 desmin-positive cardiomyocytes were imaged from each experiment with an inverted confocal microscope (Leica TCS SP5 AOBS, IBPS imaging platform). All

images were acquired with a Z-step of 0.5 µm (image size 512x512, magnification 63x). The morphological analysis was performed using ImageJ and the 3D Manager plugin to measure length-to-width ratio and volumes of cells and nuclei.

Western Blot. Human frozen cardiac tissue samples or iPSC-CMs pellets were solubilized in RIPA buffer (10 mM Tris HCl pH 7.4, 0.5% sodium deoxycholate, 1% NP40, 0.1% sodium dodecyl sulfate, 150 mM NaCl) in the presence of Protease Inhibitor Cocktail (Thermo Fisher Scientific 78425), Phosphatase Inhibitor Cocktail 2 (Sigma P5726) and Phosphatase Inhibitor Cocktail 3 (Sigma P0044). Each sample was incubated on ice for 30 min and centrifuged at 13,000g for 30 min at 4°C. Soluble proteins were then dosed using the Bicinchoninic Acid Kit (Merck) and diluted in Laemmli protein sample buffer. Proteins migrated into 4% to 20% mini-PROTEAN TGX stain-free gels (Bio-Rad) and transferred on polyvinylidene fluoride membrane (0.45 µm pore size) (Bio-Rad). After blocking in 0.1% PBS-Tween containing 5% non-fat milk, membranes were incubated overnight at 4°C with mouse monoclonal Total OXPHOS rodent WB cocktail (1:500, Abcam) or Rabbit monoclonal COXIV (1:1000, Cell Signaling). After 3 washes, membranes were then incubated with goat anti-rabbit IgG-HRP (1:20000, Sigma) or Goat anti-mouse IgG-HRP (1:10000, Sigma) for 1 hour at room temperature. Immunoreactivity was revealed by using Chemiluminescent Western Blot Reagents (Thermo Fisher Scientific) according to the manufacturer's instruction. Images were acquired on a Bio-Rad Chemidoc system. Densitometry was normalized to the total protein loaded (stain free signal) for each lane using ImageJ.

Sample preparation for ultrastructural analysis. Spheroids were fixed 1h with 1.5% glutaraldehyde, 1% paraformaldehyde and 0.04% Ruthenium Red in 0.1M sodium cacodylate buffer (pH 7.4), washed with the same buffer, incubated 1h with 0.2% Oolong Tea Extract (OTE) in 0.1M cacodylate buffer, and washed again. Samples were postfixed 1h with 1% osmium tetroxide, 1.5% potassium ferrocyanide in 0.1M cacodylate buffer, washed with deionized water, and embedded with 4% low melting point agarose. Samples were dehydrated with increasing concentrations of ethanol then acetone, infiltrated with resin (Agar 100 kit), and polymerized in standing gelatin capsules for 48 h at 60°C. Blocks were cut with an ultramicrotome (Ultracut UCT, Leica microsystems) according to planes of maximum diameter for the spheroids. 500nm semithin sections were deposited on glass slide, stained with Toluidine blue and observed with a Leica DM1000 microscope equipped with a XCAM 1080PHA (Touptek). Following 70-80nm ultrathin sections were deposited on 5 mm square silicon wafers or 150 mesh copper grids and were contrasted 15 min with 2.5% uranyl acetate. Wafers were stuck on aluminum stubs and observed with a Field Emission Scanning Electron Microscope (GeminiSEM 500, Zeiss), operating in high vacuum, at 1.5kV with the high current mode and a 30µm aperture diameter, and around a 2mm working distance. Two in-column detectors were used to separately collect secondary and backscattered electrons (filtering grid at 600V). To obtain transmission electron microscope-like images, those 2 channels were mixed and LookUp Table was inverted.

Automated acquisitions were performed using Atlas 5 (Fibics), with a pixel dwell time of 6.4 μ s, a line average of 5, a pixel size of 8nm, an image definition of 5kx5k pixels, and an overlap of 15% between images forming a mosaic after stitching. Grids were observed at 80kV with a LaB₆ JEM 2100 HC transmission electron microscope (Jeol) equipped with a side mounted Veleta CCD camera driven by iTEM software (Olympus). Images were recorded with an exposure time of 750ms and an image definition of a 2kx2k pixels.

RNA sequencing. Frozen iPSC-CM from Control 1 and Clone c15 were thawed, centrifuged at 200xg to remove freezing medium and directly seeded on Matrigel-coated 12 well plates. They were then cultured 21 days in maturation medium, detached using TrypLE Select 1X, pelleted and flash frozen in liquid nitrogen. RNA was purified using Qiagen RNeasy microkits Plus (Qiagen). RNA was quantified using the Quant-iT RiboGreen RNA Assay Kit (Thermo Fisher Scientific) and quality control performed on a Bioanalyzer (Agilent), prior to mRNA library preparation using the Single Cell/Low Input RNA Library Prep Kit for Illumina® (New England Biolabs). Libraries were sequenced on an Illumina HiSeq 2500 V4 system. Sequencing quality control was performed using Sequence Analysis Viewer and FastQ files were generated on the Illumina BaseSpace Sequence Hub. Transcript reads were aligned to the hg18 human reference genome using Salmon v1.9.0³⁵. Import and summarize transcript-level abundance to gene-level was performed with tximport package³⁶. Quality control of the alignment was performed via MultiQC v1.4 . Finally, counts were normalized as counts per million. Differential gene expression analysis was performed with the DESeq2 R package³⁷. Principal Component Analysis (PCA) was performed with factorMineR package³⁸ and factoextra package³⁹. The differentially expressed genes with adjusted *p* values false discovery rate (FDR) \leq 0.05 were subjected to GSEA with GO database using the ClusterProfiler R package⁴⁰. The density plots were produced using the ggplot2 R package⁴¹. Weighted correlation network analysis (WGCNA) was applied on normalized data recovered from DESeq2 analysis. Pathways associated with each WGCNA modules were determined using METASCAPE web application⁴². WGCNA module genes were also submitted to protein-protein interactions using STRING web software (<https://string-db.org/>), and to MCODE analysis⁴³ using Cytoscape software⁴⁴. The heatmap was, performed with the R package pheatmap (version 1.0.12). All analysis was performed in R (v.4.2.0).

PCR, 3D-PCR, cloning and sequencing. For these experiments, iPSC-CMs monolayer was dissociated using TrypLE Select 1X. A fragment of *MT-COI* (mitochondrial cytochrome c oxidase subunit I) gene was amplified by PCR and by differential DNA denaturation polymerase chain reaction (3D-PCR). This technique relies on the fact that heat denaturation of AT-rich DNA occurs at a lower temperature compared to GC-rich DNA^{45,46}. Initial PCR conditions were a first cycle: 95 °C for 5 min, followed by 40 cycles (95 °C for 30 s, 60 °C for 30 s, and 72 °C for 2 min), and finally 10 min at 72 °C with the following primers, *MT-COI-ext5-5'-GCGGTTGACTATTCTACAAACCACAAA-3'* and *MT-COI-ext3-5'GGGGGTTTATATTGATAATTGTTGTGATGAAA-3'*. 3D-PCR

was performed with 1:50 of the first round PCR products. 3D-PCR was performed on an Eppendorf gradient Master S programmed to generate a 77-85°C gradient of denaturation temperature. The reaction parameters were a first cycle: 77 to 85 °C for 5 min, followed by 40 cycles: 77-85 °C for 30 s, 60 °C for 30 s, and 72 °C for 2 min, and finally 10 min at 72 °C. Primers used were *MT-COI-int5-5'-CGTTATCGTCACAGCCCATGCATTGTAA-3'* and *MT-COI-int3-5'-GAGGAGACACCTGCTAGGTGTAAGGTGAA-3'*. 3D-PCR products were purified from agarose gels (NucleoSpin Gel and PCR Clean-up, Macherey-Nagel) and ligated into the TOPO TA cloning vector (Invitrogen). About 100 colonies were sequenced.

Real-time PCR. All RNA was extracted from the cells using the RNeasy Plus minikit (Qiagen) and cDNA synthesis was performed using QuantiTect reverse transcription kit (Qiagen) from ~1 µg of RNA. Expression of APOBEC3 genes was assayed by real-time PCR based on TaqMan (Applied Biosystems) along with *RPL13A* as a reference gene. Primers used for the amplification of APOBEC3G were previously described⁴⁷.

Seahorse. 20 days after the initiation of differentiation, iPSC-CM were dissociated using TrypLE Select 1X, seeded (25,000-50,000 cells/well) on Matrigel coated test plates (Extracellular Flux Assay Kit, Agilent) and cultured 4 days in maturation medium prior to measurement. The assay was performed in test medium composed of bicarbonate-free RPMI (pH=7.4) supplemented with glucose (4.5 g/L), sodium pyruvate (100 µM) and glutamine (200 µM). Cells were washed twice and pre-incubated at 37°C without CO₂ in 500 µL of test medium for 1 h before measurement. For the Mito Stress test, 50µL of stock solution of each drug were injected sequentially during the experiment. Stock solutions of oligomycin (10 µM), FCCP (10 µM) and rotenone + antimycin A (1 µM) were prepared in DMSO, stored at -20°C and new aliquots were thawed extemporaneously for each experiment. For normalization, OCR values have been divided by the number of cardiomyocytes per well as counted after immunostaining for cardiac troponin T. Calibration to correct for the plate effect⁴⁸ has been done by dividing all the OCR values by the lowest OCR value of the plate after addition of Rotenone and Antimycin. Basal and ATP-linked respirations, Maximal and Reserve capacities and OCR/ECAR were calculated as described in⁴⁹. The experiment was performed 5 times with Control-CMs (Control 1 and Control 2), E439K-CMs (clones c2 and c15) and 2 times with Iso-E439K-CMs.

Isolation and transfer of extracellular vesicles containing mitochondria. The extracellular vesicles were obtained from Control-CMs-conditioned medium based on differential centrifugations. Floating cells, cell debris and apoptotic bodies were removed by centrifugation at 1,000xg for 10 min. Pelleted vesicles were obtained by centrifugation of the supernatant at 10,000xg for 30 min at 4 °C. The quantity of extracellular vesicles was evaluated by measuring the protein concentrations that were measured using Bicinchoninic Acid Kit (Sigma). Cardiomyocytes or spheroids were treated with pelleted vesicles corresponding to 0.1 mg of proteins per 25 000 cells every two days from day 10 until day 24 after the initiation of differentiation.

Statistical analysis. All experimental data are presented as mean ± standard error of the mean. Normality was verified using the test of Shapiro-Wilk and, when necessary, non-parametric tests were used. Statistical significance between two groups was determined using the Mann Whitney test. When multiple comparison was necessary, One-Way ANOVA combined with Dunnett's multiple comparison tests or Kruskal-Wallis test combined with Dunn's multiple comparison tests were used. A p-value of less than 0.05 was considered statistically significant. Data were analyzed and presented using GraphPad Prism 8. RNA-sequencing data that support the findings of this study have been deposited in Gene Expression Omnibus (GEO) repository with the accession codes XX.

Results

Morphological and mitochondrial alterations in iPSC-derived cardiomyocytes from the *DES*^{E439K} patient successfully recapitulate cellular defects of MFM1 hearts

To investigate the pathophysiological mechanisms of this heterozygous familial *DES*^{E439K} mutation, we generated two iPSC clones from the peripheral blood mononucleated cells (PBMC) of the patient CIII using a non-integrating episomal plasmid-based reprogramming strategy. Then, cardiomyocytes from *DES*^{E439K} iPSC (E439K-CMs) and two healthy control iPSC (Control-CMs) were generated using the biphasic activation/inhibition of the Wnt pathway differentiation protocol and detached or frozen at day 19 from first induction of cardiac differentiation (**Figure-2A**). Cardiomyocytes obtained from these iPSC clones were compared with cardiomyocytes from an isogenic pair carrying the same mutation which has been introduced by CRISPR/Cas9 (Iso-E439K-CMs) in one healthy iPSC clone (**Figure-S1**). In addition, when applicable, results from cardiomyocytes derived from iPSC (IPSC-CMs) were confirmed with heart biopsies of suddenly died Index case CII of the same family harboring *DES*^{E439K} mutation, and post-mortem heart samples from five control healthy patients. Since the diagnosis of MFM1 is most often made by the observation of structural perturbations, we first conducted a series of immunostaining on iPSC-CMs cultured on gelatin micro-patterns (20 µm-wide lines) (**Figure-2B**). After thawing, cardiomyocytes were cultured for 21 days in a medium containing T3 hormone and dexamethasone which are known to improve cardiac maturation of iPSC-CMs⁵⁰. In Control-CMs, sarcomeres, as visualized by troponin T staining, display an almost well-organized structure and are surrounded by a filamentous desmin network throughout the cytoplasm. In contrast, E439K-CMs as well as Iso-E439K-CMs are characterized by a strong disorganization of sarcomeres as well as accumulation and patchy aggregation of desmin within the cytoplasm (**Figure-2B**). These observations faithfully reproduce the structural defects of cardiomyocytes as detected in human cardiac biopsies of the *DES*^{E439K} patient after immunostaining for troponin T and desmin (**Figure-S2A**). To examine closely the morphological alterations of E439K-CMs and Iso-E439K-

CMs compared to Control-CMs, we measured cardiomyocyte length-to-width ratio, as well as nuclei and cardiomyocyte volumes. The length-to-width ratio is significantly lower in Control-CMs as compared to E439K-CMs and Iso-E439K-CMs (4.13 ± 0.14 , n=128 for Control-CMs vs 6.22 ± 0.32 , n=118 for E439K-CMs or 6.81 ± 0.70 , n=23 for Iso-E439K-CMs, p -value<0.001) (**Figure-2C**). Of note, high variability of length-to-width ratio was observed in mutant cardiomyocytes, which is consistent with the phenotype observed in DCM patients⁵¹. We validated the relevance of this parameter by showing that the length-to-width ratio of cardiomyocytes in biopsies was significantly higher in the heart of *DES*^{E439K} patient compared to healthy hearts (5.21 ± 0.14 for Control vs 7.00 ± 0.59 for *DES*^{E439K}, $p=0.003$) (**Figure-S2B**). No differences were found in the volumes of cells and nuclei between healthy and mutated cardiomyocytes, as calculated on the basis of the Troponin T and Hoechst staining respectively (**Figure-2D-E**), indicating that the change of cell shape is not due to a hypertrophic mechanism.

We pursued the investigation of cellular morphological alterations in mutant cardiomyocytes by ultrastructural analysis using electron microscopy. To increase the physiological relevance of our results, cardiac spheroids, providing a tissue-like 3D model⁵², were generated using primary cardiac fibroblasts and iPSC-issued cardiomyocytes. Seven days after detachment (see schematic protocol in **Figure-2A**), fibroblasts and cardiomyocytes were mixed in a ratio 1.5:8.5 and cultured 7 more days in PrimeSurface 96M plate to favor their self-aggregation to spheroids (**Figure-2F**). For a global analysis of the cardiomyocyte ultrastructure under the 3 experimental conditions, a full mapping of each spheroid (sectioned at its maximum diameter) was carried out using field emission scanning electron microscopy (FE-SEM) and automated image acquisition. Electron microscopy studies disclosed a particularly well-organized ultrastructure of Control-CMs in terms of sarcomere organization and Z-line alignment (**Figure-2G**). In contrast, *DES*^{E439K} mutation resulted in a strong disorganization of sarcomeres which are less abundant and often misaligned between each other (**Figure-2H-I**), as revealed by shifted Z-lines (white arrows).

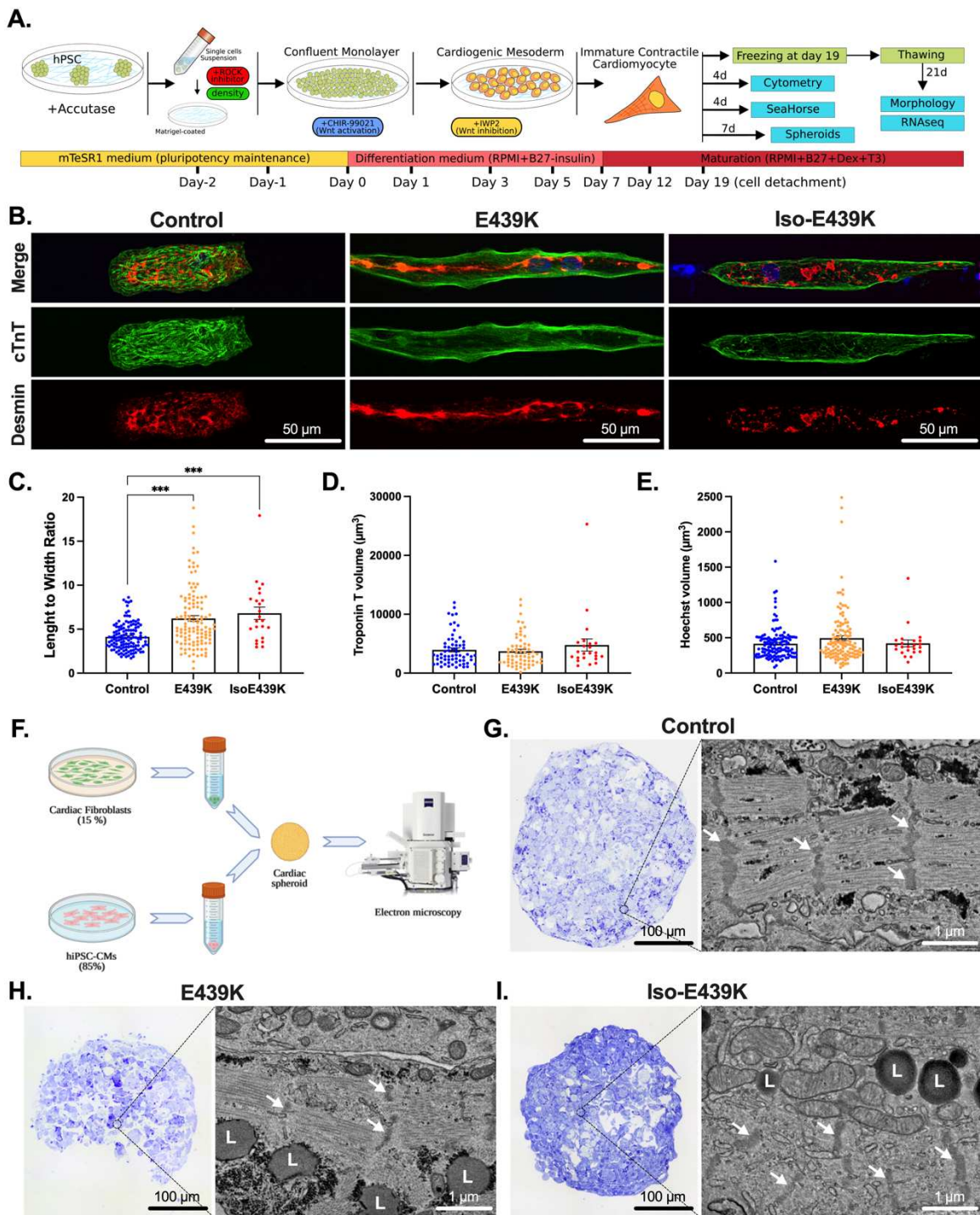


Figure 2. Morphological characterization of iPSC-derived cardiomyocytes carrying the DES^{E439K} mutation. (A) Schematic overview of the cardiac differentiation protocol from iPSC. After detachment or freezing at day 19, the cardiomyocytes are cultured for 4, 7 or 21 more days and analyzed. (B) Cardiac troponin T (Green) and Desmin (Red) immunostaining of cardiomyocytes cultured on gelatin micro-patterns (20 μm-wide lines) for 21 days after thawing. Nuclei were counterstained with Hoechst (blue). Note the marked disorganization of the sarcomeres and the accumulation of desmin in the cytoplasm of mutant cardiomyocytes. (C-E) Cardiomyocyte length-to-width ratio (C), cardiomyocyte volume (D, troponin T staining) and nuclei volume (E, Hoechst staining) were measured on cardiomyocytes after 21 days of culture on gelatin micro-patterns using ImageJ software. Values are given as means ± SEM. ***, p < 0.001. (F) Schematic representation of the production of a cardiac spheroid model used for electron microscopy analysis. (G-I) Bright-Field microscopy images of Toluidine blue-stained semithin sections and representative field emission scanning electron microscopy (FE-SEM) images from the full mapping of ultrathin sections of cardiac spheroids. White arrows indicate Z-lines; L, lipid droplets.

As shown in **Figure-2H-I**, we also noticed a strong cytoplasmic accumulation of lipid droplets in E439K-CMs and Iso-E439K-CMs as compared to Control-CMs, strongly suggesting that cellular metabolism may be affected in mutant cardiomyocytes. Following this observation, we investigated whether desmin mutated cardiomyocytes recapitulate mitochondrial abnormalities known to occur in hearts of MFM1 patients. For this, COXIV immunostaining was firstly assessed in E439K-CMs and Iso-E439K-CMs and compared to Control-CMs cultured on gelatin micro-patterns for 21 days after thawing. While COXIV-positive mitochondria were detected in Control-CMs, in particular at the extremities of cardiomyocytes and in the perinuclear area, this marker was not detectable in E439K-CMs and Iso-E439K-CMs (**Figure-3A**). Consistent with this observation, the expression of mitochondrial respiratory chain proteins, including respiratory complex I marker NDUFB8 and complex IV marker COXIV, was found decreased in mutated cardiomyocytes as compared to Control-CMs by Western blot analysis (**Figure-3B**). Once again, the mitochondrial defects detected in iPSC-derived mutated cardiomyocytes were confirmed in the heart of the desmin mutated patient since COXIV labeling (**Figure-S2A**) and Western blot analysis of NDUFB8 and COXIV markers (**Figure-S2C-E**) reveal similar decreased expression of these proteins in the diseased heart as compared to healthy ones. We then looked for an explanation for the decreased expression of respiratory mitochondrial proteins in desmin mutated cardiomyocytes. We first demonstrated that decreased expression was not due to a lower number of mitochondria in E439K-CMs. Microscopy and flow cytometry analysis of fluorescent MitoTracker-labeled mitochondria revealed no significant difference in their cytoplasmic distribution and quantity between mutated and control cardiomyocytes (**Figure-3C-D**). To determine whether this decrease was reflecting abnormal mitochondrial structure associated with the *DES^{E439K}* mutation, transmission electron microscopy (TEM) analysis was performed according to a classification of mitochondria into three types, *i.e.* normal, vesicular and swollen⁵³ (**Figure-3E**). Normal mitochondria are identified based on an appropriate architecture of cristae while vesicular mitochondria present enclosures of the internal membrane which creates several compartments within mitochondria. Finally, swollen mitochondria are identified by less dense staining of their matrix, expanded matrix space and fewer cristae. The quantification of mitochondria using this classification revealed a drastic increase of vesicular and swollen mitochondria in E439K-CMs compared to Control-CMs (**Figure-3F**), indicating important structural deficiencies in mitochondria of mutated cardiomyocytes that could explain the decrease in respiratory mitochondrial protein levels. Taken together, our results provide evidence that cardiomyocytes derived from iPSC of the *DES^{E439K}* patient successfully recapitulate crucial structural changes and mitochondrial alterations that are observed in biopsies of patients with the MFM1-related DCM, supporting the relevance of this cell model to study the pathology.

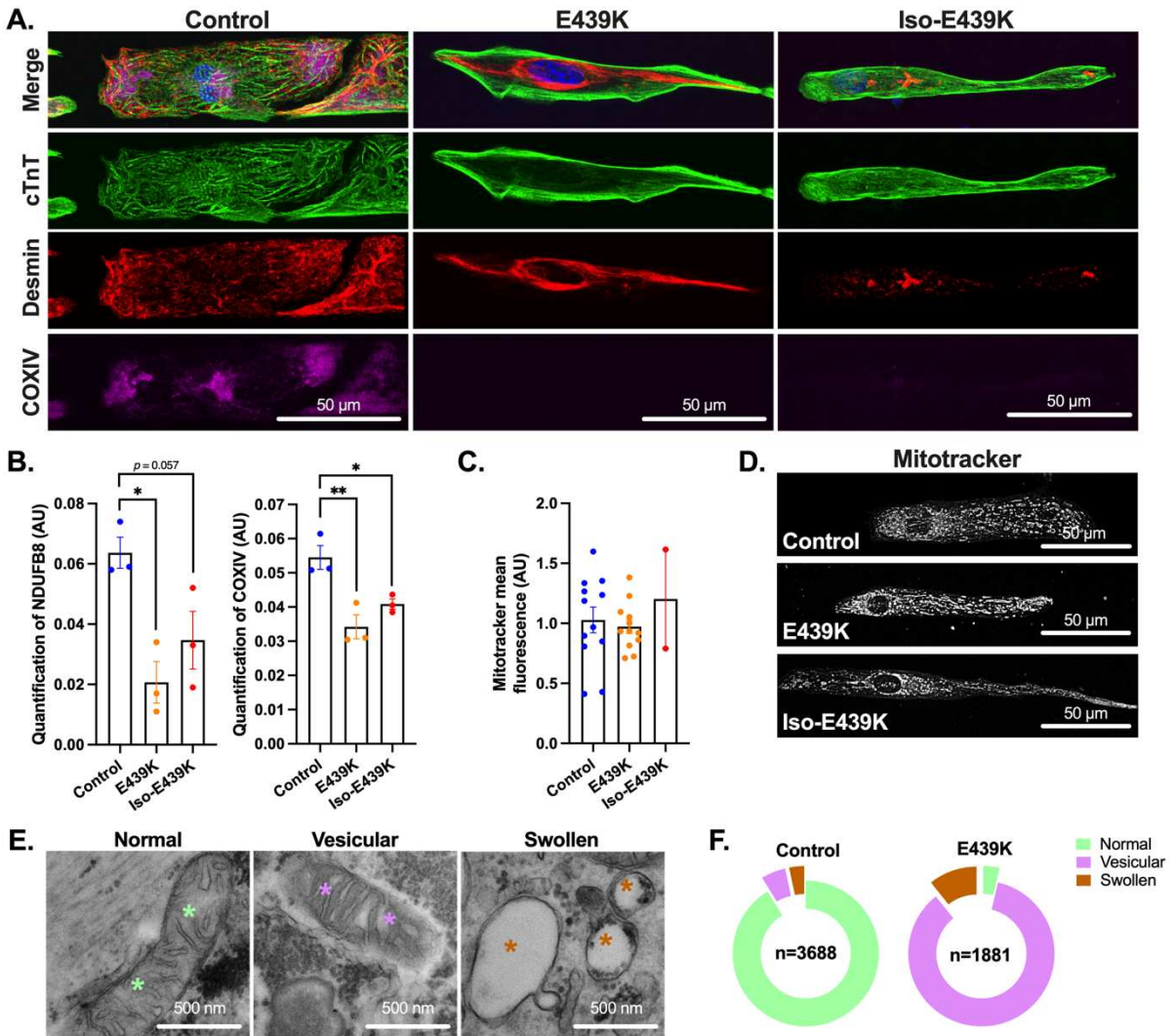


Figure 3. Structural and mitochondrial abnormalities in cardiomyocytes with the *DES*^{E439K} mutation. (A) Cardiac troponin T (Green), Desmin (Red) and COXIV (purple) immunostaining of cardiomyocytes cultured on gelatin micro-patterns (20 μm -width lines) for 21 days after thawing (see Figure 2A). Nuclei were counterstained with Hoechst (blue). Note the absence of COXIV labelling in E439K-CMs and Iso-E439K-CMs. (B) Quantitative analysis of Western Blot of NDUFB8 and COXIV showing the marked decrease of mitochondrial proteins in E439K-CMs and Iso-E439K-CMs compared to Control-CMs. Results are presented after normalizing to Stain-Free total protein profile. Results are expressed as mean values \pm SEM. *, $p < 0.05$, **, $p < 0.01$. (C) Quantification of mitochondria in cardiomyocytes by cytometry using MitoTracker, indicating close levels of mitochondria between mutant and control cardiomyocytes. Values are given as means \pm SEM. (D) Visualization of mitochondria using the mitochondria-specific fluorescent probe MitoTracker in iPSC-derived cardiomyocytes, indicating no significant differences in the cytoplasmic distribution of mitochondria in mutant cardiomyocytes. (E) Representative transmission electron microscopy (TEM) images of three types of mitochondria, *i.e.* normal (green asterisks), vesicular (purple asterisks) and swollen (brown asterisks), observed in iPSC-derived cardiomyocytes. (F) Ring chart showing the proportions of the 3 different types of mitochondria in E439K-CMs ($n=1881$: 3.6% normal, 85.8% vesicular and 10.6% swollen mitochondria) and Control-CMs ($n=3688$: 91% normal, 5.4% vesicular and 3.6% swollen mitochondria) revealing a switch of mitochondria from the normal to the vesicular type in E439K-CMs.

iPSC-derived cardiomyocytes from the *DES*^{E439K} patient suffer severe mitochondrial dysfunction

To investigate whether metabolism is altered in *DES*^{E439K} cardiomyocytes derived from iPSC, we first performed RNA sequencing to compare the transcriptional expression profiles of iPSC-derived E439K-CMs and Control-CMs cultured during 21 days after thawing. According to the principal component analysis (PCA), the samples of both groups are well segregated after the dimensionality reduction of gene expression (**Figure-4A**), indicating that desmin mutation induces strong changes in the transcriptome of the cardiomyocytes. To obtain a deeper insight into the impacted biological processes in cardiomyocytes carrying the *DES*^{E439K} mutation, a gene set enrichment analysis (GSEA) was performed to determine the sets of genes differently expressed between E439K-CMs and Control-CMs (**Figure-4B**). This analysis reveals that E439K-CMs are highly enriched in sets of up-regulated genes related to cell division, DNA repair and acute inflammation, consistent with an adaptive response of cardiac cells to DNA damage, inflammation and oxidative stress. In addition, E439K-CMs were found to exhibit less enrichment for a set of down-regulated genes related to the sarcomere organization, heart contraction, mitochondrial electron transport and respiratory chain complex I confirming the impact of the *DES*^{E439K} mutation on the sarcomeric structure and mitochondrial functionality in cardiomyocytes. To further analyze the RNAseq data, we performed a non-supervised Weighted Gene Correlation Network Analysis (WGCNA) to highlight clusters of highly correlated genes. Two clusters (Blue and Red) were determined as highly statistically significant (**Figures-4D** and **S3A** for blue, and **Figure-S3B-D** for red cluster). We decided to focus on the blue cluster because the enrichment analysis of the genes that are co-expressed in this cluster revealed several sets of genes related to mitochondria (*i.e.* oxidative phosphorylation, mitochondrial organization, mitochondrial gene expression, respiratory electron transport, proton transmembrane transport). The expression of the majority of genes within these sets (**Figure-4E-G**) are strongly downregulated in E439K-CMs, supporting that mitochondrial disruption is an important hallmark of the patient harboring the *DES*^{E439K} mutation.

We then investigated the impact of mitochondrial gene and protein alterations on the respiratory activity measured with the Seahorse metabolic analyzer in desmin mutated cardiomyocytes 4 days after thawing (**Figure-5A-F**). Using the mito stress test, we found strong, statistically significant differences between Control-CMs and cardiomyocytes carrying the *DES*^{E439K} mutation (E439K-CMs and Iso-E439K-CMs) in all examined parameters. The mito stress test allows to assess in real-time the oxygen consumption rate

(OCR) at the initial level as well as after the addition of inhibitors that target specific respiratory complexes (**Figure-5A**) to evaluate different parameters such as basal respiration, ATP-linked respiration, maximal respiration and reserve capacity (**Figure-5B-F**). Basal respiration is calculated from the OCR difference between the initial state and after complete blockage of the respiratory chain by addition of rotenone and antimycin A. As shown in **Figure 5B**, a decrease of basal respiration was detected in *DES^{E439K}* cardiomyocytes compared to Control-CMs. Addition of oligomycin, an ATP synthase inhibitor, allows to measure ATP-linked respiration, the consumption of oxygen specifically used for the biosynthesis of ATP. This parameter is lower in *DES^{E439K}* cardiomyocytes (**Figure-5C**), suggesting a lower involvement of mitochondria in ATP generation in the presence of the mutation.

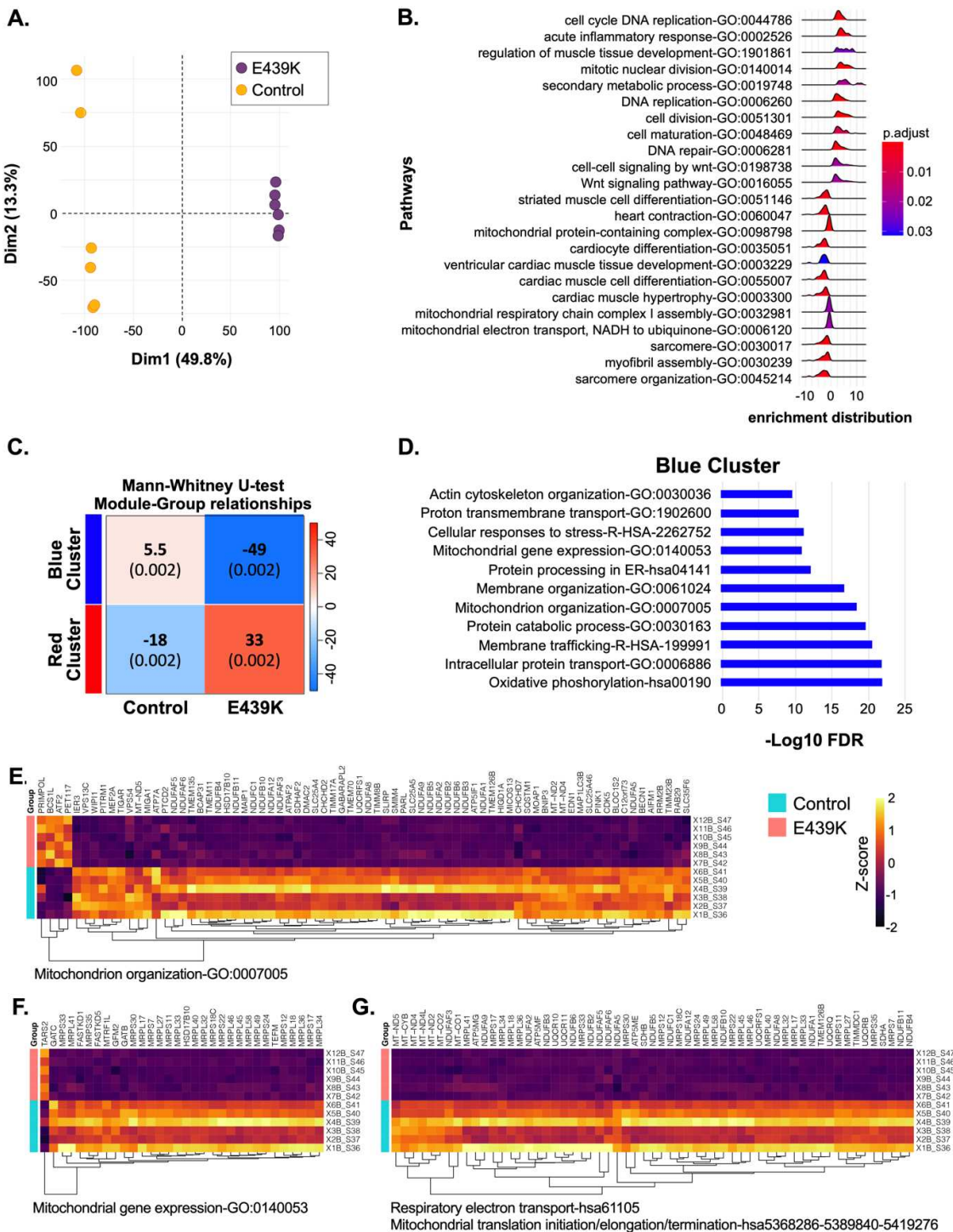


Figure 4. Transcriptomic analysis of E439K-CMs compared to Control-CMs reveals a strong signature of mitochondrial impairment. (A) Principal component analysis (PCA) of gene expression of the different samples from E439K-CMs (n=6) and Control-CMs (n=6). **(B)** Gene Set Enrichment Analysis (GSEA) of E439K-CMs compared to Control-CMs. **(C-G)** Non-supervised Weighted Gene Correlation Network Analysis (WGCNA) have detected two significant clusters of genes **(C)**. The molecular complex determination and enrichment analysis of the Blue cluster **(D)** reveals different sets of genes related to mitochondria **(E-G)**.

Carbonyl cyanide-4 (trifluoromethoxy) phenylhydrazone (FCCP) is an uncoupling agent that collapses the proton gradient and disrupts the mitochondrial membrane potential. Addition of FCCP results in uninhibited electron flow through the electron transport chain, allowing to measure the maximal oxygen consumption rate. As shown in **Figure-5D**, the maximal respiration is lower in *DES*^{E439K} cardiomyocytes, indicating a lower total mitochondrial activity. The reserve capacity, defined as the OCR difference between basal respiration and maximal respiration, is also lower in *DES*^{E439K} cardiomyocytes (**Figure-5E**). Finally, to evaluate the role of glycolysis in producing energy/metabolites in cardiomyocytes, initial OCR was normalized to the initial extracellular acidification rate (ECAR). The ratio of OCR to ECAR, which indicates cellular preference for oxidative phosphorylation versus glycolysis⁴⁹, was calculated for the different groups. As shown on **Figure-5F**, this ratio is lower in *DES*^{E439K} cardiomyocytes. Taken together, compared to Control-CMs, both types of mutant E439K-CMs have decreased mitochondrial respiration compensated by a higher glycolytic activity. In addition, electron microscopy analysis also revealed a strong cytoplasmic accumulation of lipid droplets in E439K-CMs and Iso-E439K-CMs as compared to Control-CMs (L, **Figure-5G**), that was confirmed by cytometry quantification of intracellular lipid using BODIPY, a fluorescent hydrophobic dye for lipids (**Figure-5H**). Taken in concert, these findings indicate that the metabolic activity of cardiomyocytes is altered when desmin is mutated.

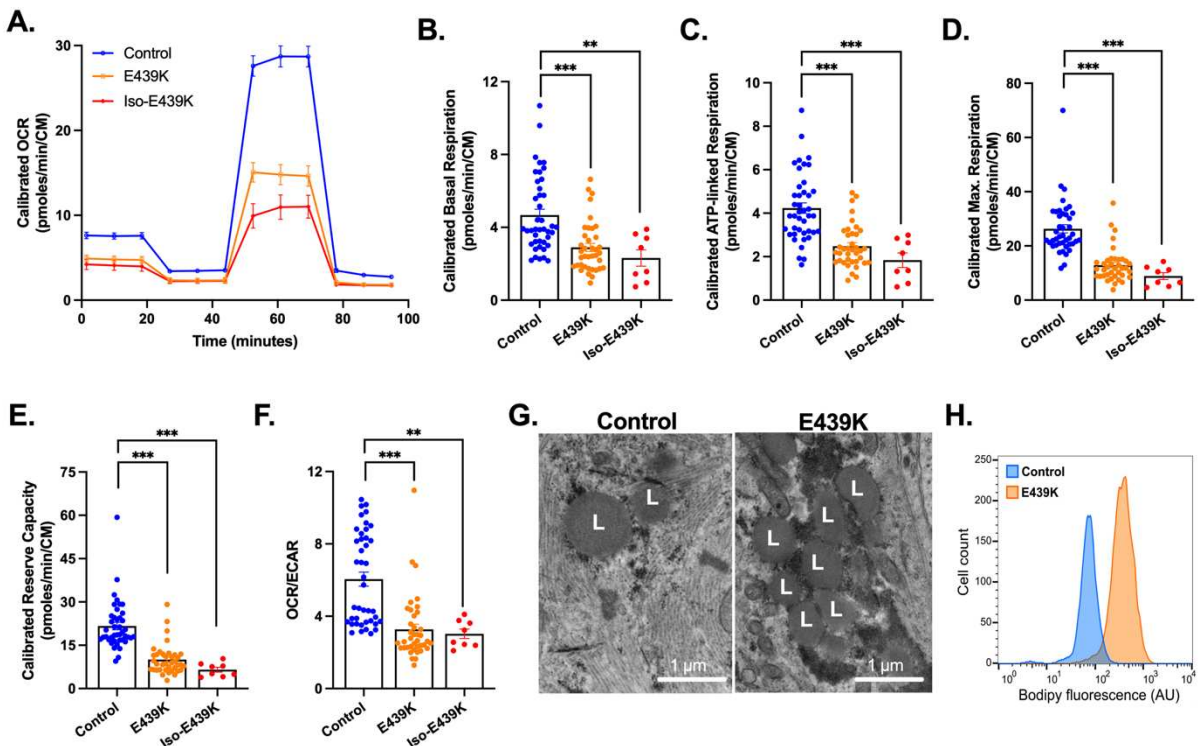


Figure 5. Decreased mitochondrial respiration and altered metabolic activity in cardiomyocytes with *DES*^{E439K} mutation. (A) Representative mitochondrial oxygen consumption rate (OCR) profiles in Control-CMs, E439K-CMs and Iso-E439K-CMs. OCR profiles are expressed as pmol O₂/min normalized to the number of cardiomyocytes and calibrated to the lowest value of the plate after addition of rotenone and antimycin A. (B) Quantification of basal respiration, (C) ATP-linked respiration, (D) maximal respiration and (E) reserve capacity of cardiomyocytes. (F) Ratio of OCR to ECAR in iPSC-derived cardiomyocytes.

Values are expressed as mean \pm SEM. **, $p<0.01$, ***, $p<0.001$. (G) Representative transmission electron microscopy images of lipid droplets (L) in iPSC-derived cardiomyocytes. (H) Flow cytometry analysis of cardiomyocytes after BODIPY staining demonstrating higher lipid levels in E439K-CMs.

APOBEC3G is up-regulated and involved in the editing of released mitochondrial DNA (mtDNA) in iPSC-derived cardiomyocytes from the *DES*^{E439K} patient

To further improve our understanding of the mitochondrial perturbation in cardiomyocytes with the *DES*^{E439K} mutation, the mitochondrial DNA (mtDNA) was analyzed. It is known that different stimuli and/or cellular stresses may induce the release into the cytoplasm of mtDNA which in turn triggers DNA sensor molecules to induce an inflammatory response^{54–56}, contributing to disease progression. We hypothesized a correlation between cell stress due to mitochondrial dysfunction and/or alteration of the cardiomyocyte structure, and the release of the mtDNA into the cytoplasm, where it gets edited. Using a differential DNA denaturation polymerase chain reaction (3D-PCR) we analyzed mtDNA editing on a fragment of mitochondria-specific *MT-COI* (mitochondrial cytochrome c oxidase subunit I) gene, in control (Control-CMs, n=5) and mutant cardiomyocytes (E439K-CMs, n=6 and Iso-E439K-CMs, n=2) (**Figure-6A**). A plasmid containing *MT-COI* DNA fragment and two cell lines (HeLa and 293T) were used as experimental controls (**Figure-6B**). 3D-PCR amplifies preferentially AT-rich DNA fragments that denature at a lower temperature than GC-rich DNA^{45,46}. 3D-PCR was performed with a 77–85°C gradient in the denaturation temperature (Td). Interestingly, 3D-PCR products were recovered at a Td as low as 79.7°C for E439K-CMs and Iso-E439K-CMs while *MT-COI* plasmid set the threshold Td at 85°C (**Figure-6A-B**). We also noted that *MT-COI* DNA isolated from HeLa and 293T cell lines were detected with a Td of 82.7°C, which far exceeded the Td of the plasmid containing *MT-COI* DNA fragment (**Figure-6B**). These cell lines are perpetually in balance between fission and fusion of mitochondria which results in the release of mtDNA in the cytoplasm followed by its editing⁵⁷. To explore editing at the molecular level, 3D-PCR products recovered at 79.7°C (E439K-CMs and Iso-E439K-CMs) and 80.7°C (Control-CMs) were cloned and sequenced. Extensive and monotonous G>A hyperediting was observed in *MT-COI* DNA from all three cardiomyocyte types (**Figure-6C**). Interestingly, the mutation frequency observed in E439K-CMs and in Iso-E439K-CMs (40–44 mutations in 248 bp; ~17%) was higher than Control-CMs (35–39 mutations in 248 bp; ~14%), demonstrating that the high mutation burden detected in mutant cardiomyocytes could be used as a marker for the detection of the mitochondrial network damage (**Figure-6D**).

The 5' dinucleotide context associated with editing was strongly in favor of 5'GpA and 5'GpG (**Figure-6E**), which is typical for polynucleotide cytidine A3 deaminases (APOBEC3), responsible for G>A (or C>U in the opposite DNA strand) editing. A3 enzymes (isoforms APOBEC3A to APOBEC3H) leave a telltale editing signature in DNA, namely they preferentially edit a cytidine residue in the context of 5'GpA (5'TpC in the opposite DNA strand) with the exception of APOBEC3G, which prefers 5'GpG

dinucleotides (5'CpC in the opposite DNA strand)^{46,58–60}. Therefore, at least APOBEC3G appears to be involved in mtDNA editing in iPSC-derived cardiomyocytes. Interestingly, our RNAseq data also showed an upregulation of the transcriptional expression of APOBEC3G in E439K-CMs compared to Control-CMs (Fold change is 3.95, adjusted *p* value=1.31x10⁻¹³).

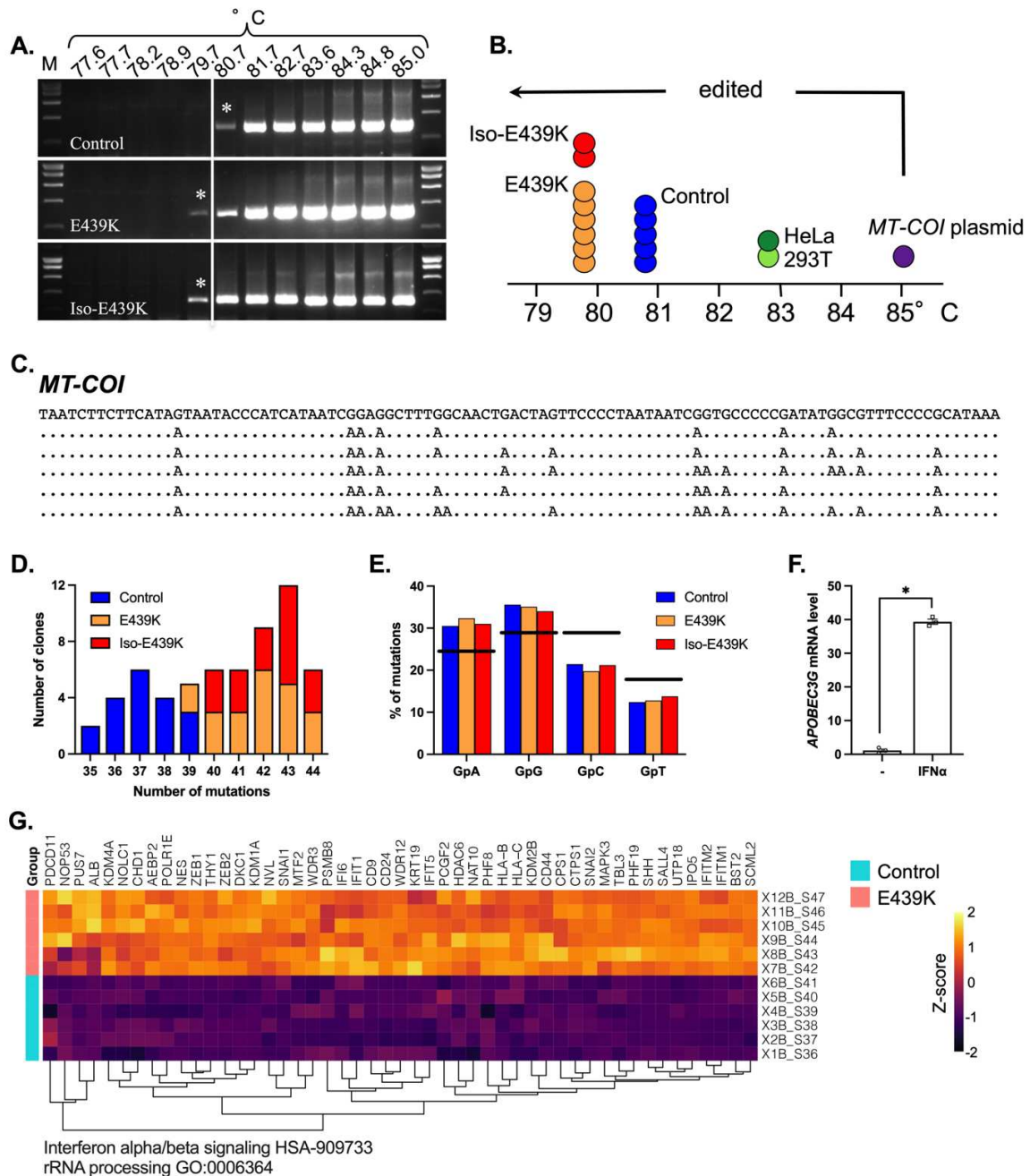


Figure 6. Editing of mtDNA in cardiomyocytes with the DES^{E439K} mutation using the MT-CO1 gene fragment. (A) mtDNA editing was analyzed using a denaturation temperature (Td) gradient across the heating block on first round PCR products. 3D-PCR recovered edited MT-CO1 DNA down to 79.7°C for E439K-CMs and Iso-E439K-CMs. The vertical white line indicates the threshold between Control-CMs, E439K-CMs and Iso-E439K-CMs 3D-PCR products in terms of the Td. M: molecular weight markers. Asterisks refer to the samples cloned and sequenced. (B) Schematic representation of the Td for the last positive 3D-PCR amplifications for 6 E439K-CMs samples (orange circles), 2 Iso-E439K-CMs samples (red circles), and 3 Control-CMs (blue circles). HeLa and 293T cell lines are shown as green circles, and a MT-CO1 plasmid is shown as a purple circle. (C) MT-CO1 sequence with mutations. The sequence is TAATCTTCTTCATAGTAATACCCATCATAATCGGAGGCTTGCAACTGACTAGTCCCCATAATAATCGTGCCCCGATATGGCGTTCCCCGATAAAA. Mutations are indicated by dots above the sequence. (D) Bar chart showing the number of clones versus the number of mutations for Control, E439K, and Iso-E439K samples. (E) Bar chart showing the percentage of mutations for GpA, GpG, GpC, and GpT across Control, E439K, and Iso-E439K samples. (F) Bar chart showing the APOBEC3G mRNA level for Control and E439K samples under basal (-) and IFNα conditions. (G) Heatmap showing Z-scores for various genes grouped by GO terms. The heatmap includes a color scale for Z-scores from -2 to 2. Genes include PDD11, NCF53, PUS7, ALB, KDM4A, NOLC1, CHD1, AEPBP2, POLR1E, NES, ZEB1, THY1, ZEB2, DKC1, KDM1A, SNAL1, MTF2, WDR3, PSMB8, IFIT1, IFIT15, PCGF2, HDAC6, NAT10, PHF8, HLA-B, HLA-C, KDM2B, CD44, CFB1, CTSPS1, SNAI2, MAPK3, TBL3, PIF19, SHL4, UTP18, IPO5, IFITM2, IFITM1, BST12, SCML2, X12B_S47, X11B_S46, X10B_S45, X9B_S44, X8B_S43, X7B_S42, X6B_S41, X5B_S40, X4B_S39, X3B_S38, X2B_S37, X1B_S36. The heatmap is centered on Interferon alpha/beta signaling HSA-909733 and rRNA processing GO:0006364.

circles), 5 Control-CMs samples (blue circles), non-transfected HeLa (dark green circle) and 293T (light green circle) cells and cells transfected with a plasmid containing *MT-COI* DNA fragment (purple circle). The arrow indicates the threshold T_d (85°C) at which the samples are hypermutated. (C) A selection of hypermutated G>A edited E439K-CMs and Iso-E439K-CMs samples ($T_d=79.7^{\circ}\text{C}$). The sequences are given with respect to the plus or coding strands. Only differences are shown. All sequences were unique, indicating that they corresponded to distinct molecular events. (D) Frequency analysis of edited *MT-COI* fragment gene as a function of the number of edits per sequence at 79.7°C and 80.7°C for the E439K-CMs and Iso-E439K-CMs-derived and for the control-CMs derived 3D-PCR products respectively. The size of the columns indicates the combined numbers of sequences analyzed across the three samples. (E) Bulk dinucleotide context of *MT-COI* gene fragment and compared to the expected values. The horizontal line represents the expected frequencies assuming that G>A transitions were independent of the dinucleotide context and correspond to the weighted mean dinucleotide composition of the reference sequence. The blue (Control-CMs), orange (E439K-CMs) and red (Iso-E439K-CMs) bars represent the percentage of G>A transitions occurring within 5'GpN dinucleotides for the hypermutated sequences. Preferential mutations in 5'GpA and 5'GpG contexts correspond to an APOBEC3G signature. (F) Gene expression quantification of APOBEC3G in Control-CMs evaluated by RT-qPCR after treatment with IFN α (1000U/ml). (G) Molecular complex detection of weighted gene correlation network analysis (WGCNA) from RNAseq data of E439K-CMs and Control-CMs have detected sets of genes related to IFN IFN α/β and rRNA processing.

Since some of these enzymes (APOBEC3A, APOBEC3G) could be up-regulated during inflammation⁶¹ we then verified by a supervised analysis of our RNAseq data, whether sets of genes related to inflammation are up or downregulated between Control-CMs and E439K-CMs. Interestingly, the red cluster of genes differently expressed in E439K-CMs (Figure-6C) is in particular characterized by the enrichment of the Interferon alpha/beta (IFN α/β) signaling set of genes (Figure-6G), suggesting that inflammation may be triggered in mutant cardiomyocytes. These data indirectly support that dysfunctional mitochondria of desmin-mutated cardiomyocytes could exacerbate deleterious inflammation processes by releasing their mtDNA in the cytosol. Finally, to confirm the RNA sequencing-based transcriptome analysis concerning the relation between inflammation signaling pathways and APOBEC3G, Control-CMs were incubated during 24 hours with IFN α . As a result, APOBEC3G transcripts were increased more than 34-fold in IFN α -treated iPSC-derived cardiomyocytes (Figure-6F). These data demonstrated that upregulation of APOBEC3G cytidine deaminase is possible in iPSC-derived cardiomyocytes under chronic inflammatory conditions. In addition, given that APOBEC3 enzymes are strictly cytoplasmic and do not localize within mitochondria⁵⁶, *MT-COI* DNA editing process could occur exclusively in the cytoplasm. Taken together, these results strongly suggest that the release of mtDNA into the cytoplasm possibly occurs, is more important in *DES*^{E439K} cardiomyocytes (E439K-CMs and Iso-E439K-CMs) compared to Control-CMs, and may induce stress responses that aggravate cellular defects.

Transfer of exogenous functional mitochondria restores the metabolism and contractile function in desmin-mutated cardiomyocytes

Given that mutant cardiomyocytes suffer from severe mitochondrial defects, we were prompted to test whether the transfer of exogenous healthy mitochondria could restore proper metabolism and contractile function in cardiomyocytes carrying the *DES*^{E439K} mutation. We expected that isolated mitochondria enter into targeted cells, integrate the

recipient's endogenous mitochondrial networks and restore functional defects in iPSC-derived mutant cardiomyocytes.

As a first attempt, mitochondria were isolated from Control-CMs and immediately transferred to E439K-CMs or Iso-E439K-CMs. To explore the efficacy of transfer, exogenous mitochondria were labeled with MitoTracker before isolation, and transferred mitochondria were measured by flow cytometry 24h after their addition to cardiomyocytes. These experiments confirmed that mitochondria were efficiently transferred to E439K-CMs as well as Iso-E439K-CMs as shown by the detected MitoTracker-positive cell population (**Figure-S4A**). We then investigated the consequences of this treatment in the metabolic activity of desmin-mutated cardiomyocytes. We found that uptake of exogenous mitochondria is accompanied by a general increase of the OCR profiles indicating the re-establishment of mitochondrial respiration in mutant cells (**Figures-S4B-C**). This phenomenon did not occur when the cells were treated with mitochondria previously inactivated with paraformaldehyde (PFA), supporting the metabolic role of exogenous mitochondria in recipient cells. Nevertheless, we found that 24h of treatment did not result in a significant improvement of mitochondrial respiration parameters (**Figures-S4B-C**), indicating that a short-term treatment may not be sufficient to restore cardiomyocyte bioenergetics. We therefore decided to evaluate the long-term effects of this treatment on mitochondrial respiration capacity as well as contractility of mutant cardiomyocytes (**Figure-7A**). In view of the high number of cells required for the isolation of mitochondria, we decided to simplify the protocol by switching from isolated mitochondria to the preparation of mitochondria-containing extracellular vesicles (EV) from the conditioned cell culture media, based on a recent publication by Ikeda et al.⁶². Flow cytometry analysis confirmed that mitochondria-containing EVs pre-treated with MitoTracker can effectively mediate the transfer of mitochondria into iPSC-CMs (**Figure-7D**). Cardiomyocytes carrying the *DES*^{E439K} mutation were treated with EVs every two days beginning day 10 up to day 20 of cardiac differentiation, and then their function in terms of respiration and contractility was evaluated. The beginning time of treatment (10 days of differentiation, see schematic protocol in **Figure-2A**) was chosen to test the hypothesis that the treatment may counteract the progressive accumulation of abnormalities in mutant cardiomyocytes. Indeed, mutant cardiomyocytes do not display any defects at the early time of differentiation neither in the expression profile of the different surrogate cardiomyocyte markers nor in mitochondrial respiration capacity (**Figure-S5A-C**). As shown in **Figure-7B-C**, this chronic treatment over 10 days results in an increase of OCR profiles of E439K-CMs and Iso-E439K-CMs compared to non-treated mutant cardiomyocytes. More interestingly, basal respiration, ATP-linked respiration and maximal respiratory capacity were all improved in both mutated iPSC-CMs compared to non-treated mutant cardiomyocytes. This functional improvement is also correlated to an increase in the percentage of spontaneously contractile spheroids (**Figure-7E**) monitored using MUSCLEMOTION⁶³. Essentially, spheroids derived from mutant cardiomyocytes did not

demonstrate any spontaneous beating if not treated with mitochondria. Taken in concert, these experiments, reveal that supply of mutant cardiomyocytes with functional mitochondria is sufficient to correct the functional defects of these cells and support the hypothesis that mitochondria abnormalities are the main responsible factor for the cellular defects behind the pathological symptoms found in the heart of desmin-mutated patients.

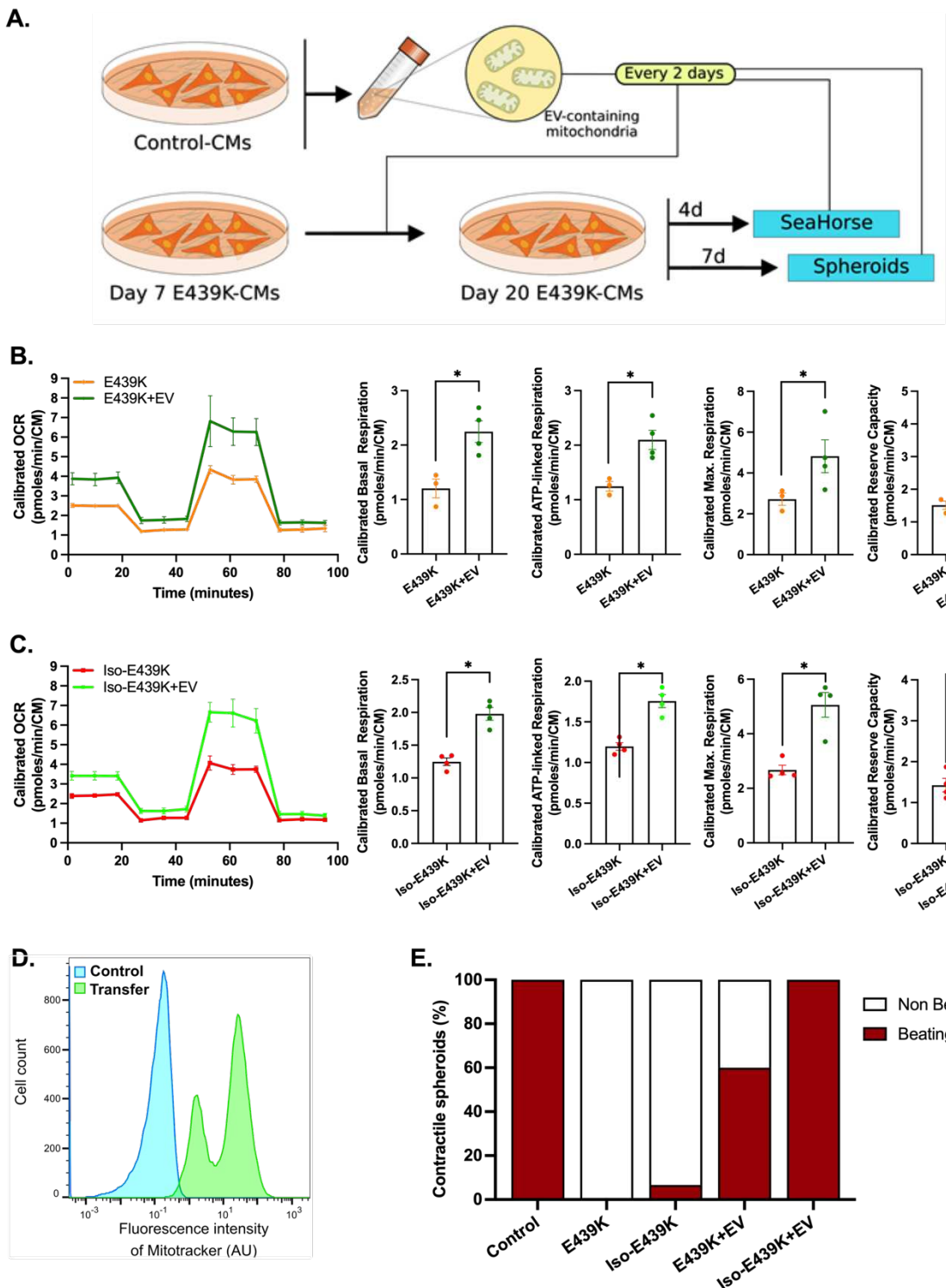


Figure 7. Long-term effects of the transfer of mitochondria on the function and respiration of cardiomyocytes with the DES^{E439K} mutation. (A) Experimental set-up. **(B-C)** Mitochondrial oxygen consumption rate (OCR) profiles and respiration parameters of the mito stress test of E439K-CMs (C) or Iso-E439K-CMs (D) untreated or treated with EVs-containing mitochondria (+EV). OCR profiles are expressed as pmol O₂/min normalized to the number of cardiomyocytes and calibrated to the lowest value of the plate after addition of R/A. **(D)** Flow cytometry analysis of Control-CMs untreated (Control) or treated (Transfer) with extracellular vesicles (EV) from Control-CMs previously incubated with MitoTracker. **(E)** Percentage of contractile spheroids assessed by video microscopy.

Discussion

Emergence of cardiac dysfunction in desmin-related myofibrillar myopathies has been associated with sarcomeric disorganization and mitochondrial abnormalities in cardiomyocytes. However, the pathophysiological mechanisms triggered by desmin mutations are far from being understood. Data are coming mostly either from transgenic animals, which in many pathological cases respond differently as compared to humans, or from transiently transfected cells carrying human *DES* mutations which provide useful information, but often artificial due to the expression levels of transfected DNA. Otherwise, human biopsies from patients provide valuable information but are difficult to obtain and allow only descriptive evidence. We believe that further progress in this field necessitates relevant human cellular or tissue models that faithfully reproduce cardiac disease.

Recent advances in iPSCs seem to be a very promising response to overcome the limitations of previously studied models. Thus, we generated cardiomyocytes using iPSCs from a patient carrying the heterozygous *DES*^{E439K} mutation and from healthy donors as a control. To complete our analysis, we also created an isogenic pair of these control iPSCs in which the same mutation has been introduced. In an effort to increase physiological relevance, cardiomyocytes were either cultured on an anisotropic micropatterned surface (2D cultures), to obtain elongated and aligned cardiomyocytes, or as a cardiac spheroid (3D cultures), to create a micro-tissue. Using these cardiomyocyte preparations, we were able to show that (i) cardiomyocytes derived from iPSC of a *DES*^{E439K} patient successfully recapitulate the crucial structural changes and mitochondrial alterations observed in heart biopsies from this MFM1 patient, highlighting the relevance of these cell models to study the pathology; (ii) the observed severe structural and functional mitochondrial abnormalities represent a primary mechanism in the emergence of desmin-related cardiomyopathy in *DES*^{E439K} patients, since transfer of exogenous healthy mitochondria restores the metabolism and contractile function in mutant cardiomyocytes. Based on these findings, we propose that in cardiomyocytes, the primary disruption of the desmin network due to desmin mutations induces mitochondrial defects which, in turn, contribute to a vicious circle leading to cardiomyocyte dysfunction and subsequently to DCM.

To the best of our knowledge, our study is the first that combines efficient protocols to generate cardiomyocytes from hiPSC and maturation techniques to study the pathological phenotypes and mechanisms of desmin-related MFM. To date only one publication has reported the characterization of cardiomyocytes derived from iPSC from patients with desmin mutations. In this work, Tse HF *et al.*⁶⁴ used for the first time iPSC-CMs derived from a *DES*^{A285V} patient affected by DCM. They showed that mutant iPSC-CMs displayed structural and functional abnormalities, namely a disorganized ultrastructure (alteration of intercalated discs, streaming of Z-disks, absence of I bands, accumulation of granulofilamentous material reminiscent of desmin aggregation) and an altered response to isoproterenol (lower rate of calcium re-uptake and a slower spontaneous beating rate). In this study the cardiomyocytes were obtained by a protocol based on the

co-culture of embryoid bodies with endoderm-like cells, dissected and dissociated 6 weeks after the initiation of differentiation and analyzed as single cells or cell clusters. This approach clearly limited the quantity and purity of obtained cardiomyocytes. These limitations did not affect the study since, according to authors, the model was mainly used to assess genetic basis of clinically observed DCM by providing histological and functional confirmation. However, this model would not be optimal for further analysis of pathological cell mechanisms. In parallel, Brodelh and collaborators published a series of studies where healthy hiPSC-CMs were transiently transfected with different mutants of desmin^{20,65–68}. Unfortunately, the mitochondrial function and/or phenotype was not characterized in these cardiomyocytes, probably because the efficiency of transient transfection was not sufficient to allow such analyses.

In our approach, after differentiation based on the monolayer GiWi protocol³⁴, hiPSC-CMs were 2D-seeded on a gelatin micropattern and treated with T3 and Dexamethasone, to improve maturation and analyze their morphology. Moreover, we generated a 3D spheroid model that is expected to better mimic the organization of the native cardiac tissue⁵². Our results were further validated through the generation of an isogenic pair by introducing the *DES*^{E439K} mutation into a control hiPSC clone, which rigorously establishes that this heterozygous desmin point mutation is at the origin of the observed pathogenic phenotype. Finally, by comparing with samples from a patient carrying the same mutation, we were able to show that our cellular models successfully mimic several features of the MFM cardiac phenotype, as discussed below. All these specificities of our study carry out an important step forward into the comprehension of the pathophysiological mechanisms that underlie desmin-related genetic-driven DCM.

This work highlights the structural and functional alteration of mitochondria as the hallmark and primary defect of *DES*^{E439K} cardiomyocytes. Even if the link between desmin and mitochondria is not perfectly understood, it is well established that one common trait in patients affected by MFM resides in defective mitochondria⁶⁹. At least 8 different mutations of desmin (*i.e.*, *DES*^{R16C}, *DES*^{E114del}, *DES*^{A213V}, *DES*^{K239fs242}, *DES*^{A357P}, *DES*^{E245D}, *DES*^{R350P} and *DES*^{K449T}) have been directly linked to mitochondrial dysfunctions in human tissue samples^{16,18,19,70,71}. In these studies, detrimental effects of desmin mutations on the mitochondrial content and biogenesis, morphology and maximal rate of respiration, have been observed. Moreover, alterations in mitochondrial organization and architecture also described with other genes related with MFM such as α-B-crystallin⁷², myotilin⁷¹ and ZASP⁷¹. Our study has strengthened the idea that mitochondrial disruption plays an important role in pathophysiology of desmin-related MFM. Indeed, our results show that the *DES*^{E439K} mutation is detrimental for proper mitochondria structure, respiratory capacity as well as mtDNA integrity. As shown in **Figure-3C-D**, the number of mitochondria was found similar between control and mutant cardiomyocytes in culture, suggesting that their biogenesis is not affected by desmin mutation. However, a remarkably high percentage (>90%) of abnormal vesicular and swollen mitochondria was observed in the *DES*^{E439K}

iPSC-derived cardiomyocytes compared to control cardiomyocytes which, in the contrary, displayed a normal mitochondrial morphology in their majority (>90%) (**Figure-3E-F**). This result is consistent with the idea that the desmin network playing an important role in the structural integrity of mitochondria¹¹. Recently, a direct interaction between desmin and mitochondrial proteins including VDAC, Mic60 (a component of the MICOS complex) and ATP synthase was demonstrated by Dayal and colleagues²⁶. The authors suggest that these interactions should participate in mito-protection at different levels. Desmin was also found tightly associated with plectin²¹ and appeared to regulate, at least indirectly, the function of VDAC²⁵. In desmin knockout mice, Kay et al.⁷³ described two populations of mitochondria with the emergence of often enlarged subsarcolemmal mitochondria disconnected from myofibrils. This is reminiscent of our observation regarding the change in proportions of different types of mitochondria between E439K-CMs and Control-CMs, suggesting that both loss and mutations of desmin lead to similar mitochondrial alterations. However, the question remains as to how the interaction between desmin and mitochondria regulates their structure and function, such as size or positioning, membrane potential, respiration and ATP production.

As we demonstrated in **Figure 3**, morphological alteration is accompanied by decreased expression of mitochondrial respiratory complex I marker NDUFB8 and complex IV marker COXIV, as evidenced by Western blot analysis. This phenotype is also described in skeletal muscles of hetero- and homozygous knock-in mice carrying the R349P desmin mutation¹⁹. Moreover, the presence of histochemically COX-negative (COX deficient) muscle fibers within muscle biopsies is considered to be a diagnostic hallmark of mitochondrial disease⁷⁴. Interestingly, at variance with Western blots, immunolocalization experiments showed the presence of completely COX-negative fibers in mutant cardiomyocytes. One explanation for this discrepancy could be a possible defect in the assembly of the complex IV in mutant cardiomyocytes; another possibility would be the masking of antibody's epitopes due to potential post-translational modification induced by pathological condition. RNA-seq data also confirmed in E439K-CMs the decreased expression of NDUFB8 and COXIV, as well as of many other genes related to mitochondria, *i.e.* involved in oxidative phosphorylation, mitochondrial organization, respiratory electron transport, proton transmembrane transport, and mitochondrial gene expression. Consistent with this observation, we demonstrated that *DES*^{E439K} induces a strong decrease of the mitochondrial respiratory function (see **Figure-5**). Basal and ATP-linked respirations, as well as maximal and reserve capacities are decreased in mutant cardiomyocytes. The overall decrease of these parameters, especially the maximal capacity, seems not to be related to a decrease in mitochondrial content, which was also observed previously in desmin knockout mice¹¹. It was stated that a change in basal respiration coupled to a change in ATP-linked respiration and maximal capacities can be due to an adaptation of mitochondria to altered ATP demand of the cardiomyocyte⁷⁵ rather than to an intrinsic dysfunction of mitochondria. Commonly, mitochondrial dysfunctions should

be determined if the decrease of basal and ATP-linked respiration is not coupled to a change in maximal capacity⁷⁵. Thus we cannot exclude that the observed changes in mitochondrial respiratory parameters may underlie changes in the global energetic characteristics of the cardiomyocyte⁴⁹. A change in the metabolic status could also explain the observed changes in the OCR/ECAR ratio that can be related to an increase in anaerobic glycolysis *versus* oxidative phosphorylation⁴⁹. In agreement with this hypothesis, we also observed increased expression of genes involved in lipid beta-oxidation and a strong increase in the presence of lipid droplets within the cytoplasm of cardiomyocytes (see **Figure-5G**). Indeed, neutral lipids can be accumulated in cardiomyocytes because of an alteration in β-oxidation⁷⁶. A recent publication highlighted a reconfiguration of the mitochondria-related metabolic pathways including fatty acid transport, activation, and catabolism⁷⁷ that is attributed, secondary, to defects in mitochondria. To test this hypothesis, the mito stress test could also be performed on isolated mitochondria instead on intact cells. Similar experiments have been performed on mitochondria isolated from the heart of control and desmin-null animals¹¹ and did not reveal any differences in respiration rates, while a significant difference in Vmax of oxygen consumption was noted in desmin-null intact cardiomyocytes.

Another interesting result was that the majority of the sets of genes displaying an increased expression in E439K-CMs are related to cell division, DNA repair and acute inflammation, indicating that an adaptive response to DNA damage and inflammation is possibly induced by desmin mutation. We further investigated this possibility. It is known that, while most damaged mitochondria following a cellular stress are removed by autophagy, some mtDNA fragments clearly find their way to the cytoplasm where they act as a danger signal and can trigger cytoplasmic DNA sensor molecules to induce inflammatory responses⁷⁸. In fact, it was recently reported that mtDNA induces Toll-like receptor 9-mediated inflammatory responses in cardiomyocytes leading to myocarditis⁷⁹. Similar mechanisms might play a role in other chronic inflammatory diseases or after severe bodily injury. On the other hand, APOBEC3 enzymes hypermutate (edit) and initiate catabolism of cytoplasmic mtDNA, acting as a mechanism for lowering the danger signal and preserving cells from chronic inflammation. By the way, expression of APOBEC3G was previously shown to be increased by IFNα^{80,81}. As shown in **Figure-6F**, we demonstrated that this regulatory mechanism exists also in cardiomyocytes. Interestingly, our 3D-PCR analysis of mtDNA editing revealed a higher rate of mtDNA mutations potentially related to APOBEC3G in E439K-CMs, which is an indirect indication for a more important release of mtDNA into the cytoplasm of mutant cardiomyocytes and/or a higher APOBEC3G activity. Moreover, the expression of the set of genes involved in IFNα/β signaling is increased in E439K-CMs.

Even though the causality between desmin network alterations, sarcomere abnormalities, mitochondrial dysfunctions and/or metabolic perturbations are not well established, it is clear that damages in both desmin and mitochondrial networks precede

left ventricular dysfunctions⁸². Our results clearly indicate that a primary effect of desmin E439K mutation in human cardiomyocytes is the mitochondrial abnormalities, which may contribute to the vicious circle leading to progressive dysfunction of cardiomyocytes. This hypothesis is further strengthened by several studies in cell and/or animal models. A comparative study of six pathogenic desmin mutations (S12F, A213V, L345P, A357P, L370P and D399Y) highlighted the role of mitochondrial dysfunction in the pathogenesis of desmin myopathies, independently from the position of the mutation on desmin¹⁵. Moreover, mitochondrial alterations seem to arise prior to any other observable defect such as loss of contractile material or myofibrillar alignment, according to a study of cardiac tissue from desmin knockout mice¹¹. Therefore, these data and our results strongly suggest that mitochondrial dysfunction could be a general mechanism to explain the pathogenesis of desmin-related cardiomyopathies.

It should be noted that mitochondrial dysfunction has been found in several cardiac diseases, *i.e.* dilated cardiomyopathy⁸³, hypertrophic cardiomyopathy⁸⁴, arrhythmogenic cardiomyopathy⁸⁵, viral myocarditis⁸⁶, ischemic heart disease⁸⁷ or rare cases of restrictive cardiomyopathy⁸⁸. This clearly suggests that defects in mitochondrial functions and/or structure may be a general trait of cardiac diseases. In that sense, treatments targeting mitochondria appear to be a potential novel approach to strengthen the treatment of this group of conditions as reviewed in⁸⁹. Despite the development of pharmacological molecules targeting key component of mitochondria (reviewed in^{90,91}), such as Elamipretide⁹², KL1333⁹³ and Idebenone⁹⁴, none of these drugs has yet been approved so far for the treatment of cardiac diseases. Novel research strategies which could lead to the development of innovative treatments are therefore strongly needed. One of the most exciting findings comes from our studies on the transfer of exogenous mitochondria into mutated cardiomyocytes. These experiments reveal that the delivery of functional healthy cardiac mitochondria alleviates the diseased phenotype of desmin-mutated cardiomyocytes. Similar therapeutic approaches have been envisioned to mitigate tissue injury in several cardiac diseases exhibiting dramatic mitochondrial dysfunctions, including ischemic heart diseases in mouse, rat, rabbit and pig models as well as in clinical trials with patients^{95–101}. In these settings, exogenous mitochondria have been shown to be internalized by stressed cardiomyocytes and to improve energy metabolism, viability and function of cardiomyocytes⁹⁶. However, despite these positive findings, numerous drawbacks pave the way for the application of mitochondrial transplantation as a regular treatment. In particular, it is difficult to control the integrity and functions of mitochondria in the extracellular space or the rate of delivery into cardiomyocytes. Consistent with these concerns, we found that the supply of exogenous functional mitochondria needs to be repeated along the differentiation process of cardiomyocytes to reverse the pathological phenotype indicating that the beneficial effects of these mitochondria are transient. These observations strongly suggest that the transferred mitochondria fail to integrate in the endogenous

mitochondrial network of mutant cardiomyocytes but rather they become rapidly defective and probably degraded in the mutant cardiomyocytes.

More recently, beneficial therapeutic effects have been observed in mouse infarcted myocardium following the delivery of mitochondria embedded in microvesicles released by cardiomyocytes derived from iPSCs⁶². The advantage of this approach is to allow a greater functional preservation of the mitochondria that have to be transferred to suffering cardiomyocytes. We applied this method in our study and demonstrated that such an approach is effective in alleviating the genetic defects of desmin-mutated cardiomyocytes as well. Our study raises the question of whether therapeutic efficacy can be influenced by the cellular origin of mitochondria to be transplanted. Consistent with this, only mitochondria isolated from cardiomyocytes have been found to restore contractile functions in a Duchenne muscular dystrophy-driven iPSC-CMs model¹⁰². This approach appears to be very challenging even if it could be an outstanding opportunity for patients with rare disease where mitochondria is affected. Whatever the fate of the exogenous mitochondria following their internalization in mutated cardiomyocytes, their metabolic effects and their consequences on cardiac function support the conclusion that mitochondrial defects observed in the heart of MFM1 patients critically contribute to the severe symptoms affecting cardiomyocytes. Moreover, our study emphasizes that mitochondria can be considered as a promising therapeutic tool to treat MFM1 myopathy not solely in cardiac muscle but also in all the organs affected by desmin mutations.

Acknowledgments

We acknowledge Alexandre Simon, Coline Rogue, Gaëlle Revet, Dorota Jeziorowska from CARTHÉ team for their help in the daily cell culture; Audrey Geeverding and Michaël Trichet from the IBPS electron microscopy core facility and all personnel from the IBPS photon microscopy core facility for helpful advice and technical assistance during microscopy preparation, image acquisition and analysis. The authors thank Brigitte Onteniente and Phenocell SAS (Grasse, France) to generate hiPSCs from MFM1 patient. The authors would also like to express their gratitude to Susanne Bolte from the IBPS photon microscopy core facility, who has sadly died recently.

Sources of Funding

This work was supported by funds from Sorbonne Université, the CNRS, the INSERM, the Agence Nationale de la Recherche (ANR-21-CE19-0027-MoHeDis) and the AFM-Téléthon (contract number: 22142). Y.H. and V.B. were supported by a Ph.D. fellowship from the AFM-Téléthon (contract number: 20479) and ANRT (contract number: 2020/0074), respectively.

Author contributions

Y.H., P.J. and O.A. designed and supervised research; Y.H., Z.L., D.C., R.S., V.B., A.C., J.B., C.L., N.E-J, J-P.V, P.J. and O.A. performed the experiments; Y.H., Z.L., D.C., H.H., A.L., E.K., P.F., J-P.C., G.T., A-M.R., J-P.V., P.J. and O.A. analyzed data; Y.H., P.J. and O.A. wrote the manuscript; all authors proofread the manuscript and approved the final version of this paper.

Disclosures

None.

References

1. Paulin, D., Huet, A., Khanamyrian, L. & Xue, Z. Desminopathies in muscle disease. *J. Pathol.* 204, 418–427 (2004).
2. Capetanaki, Y., Papathanasiou, S., Diokmetzidou, A., Vatsellas, G. & Tsikitis, M. Desmin related disease: a matter of cell survival failure. *Curr. Opin. Cell Biol.* 32, 113–120 (2015).
3. Brodehl, A., Gaertner-Rommel, A. & Milting, H. Molecular insights into cardiomyopathies associated with desmin (DES) mutations. *Biophys Rev* 10, 983–1006 (2018).
4. Agnelli, G., Herrmann, H. & Cohen, S. New roles for desmin in the maintenance of muscle homeostasis. *FEBS J* 289, 2755–2770 (2022).
5. Hnia, K., Ramspacher, C., Vermot, J. & Laporte, J. Desmin in muscle and associated diseases: beyond the structural function. *Cell and Tissue Research* 360, 591–608 (2015).
6. Béhin, A. et al. Myofibrillar myopathies: State of the art, present and future challenges. *Revue Neurologique* 171, 715–729 (2015).
7. Agnelli, G. et al. Desmin modifications associate with amyloid-like oligomers deposition in heart failure. *Cardiovasc. Res.* 102, 24–34 (2014).
8. Singh, S. R. & Robbins, J. Desmin and Cardiac Disease: An Unfolding Story. *Circ Res* 122, 1324–1326 (2018).
9. Rainer, P. P. et al. Desmin Phosphorylation Triggers Preamyloid Oligomers Formation and Myocyte Dysfunction in Acquired Heart Failure. *Circ Res* 122, e75–e83 (2018).
10. Milner, D. J., Weitzer, G., Tran, D., Bradley, A. & Capetanaki, Y. Disruption of muscle architecture and myocardial degeneration in mice lacking desmin. *J. Cell Biol.* 134, 1255–1270 (1996).
11. Milner, D. J., Mavroidis, M., Weisleder, N. & Capetanaki, Y. Desmin cytoskeleton linked to muscle mitochondrial distribution and respiratory function. *J. Cell Biol.* 150, 1283–1298 (2000).
12. Thornell, L., Carlsson, L., Li, Z., Mericskay, M. & Paulin, D. Null mutation in the desmin gene gives rise to a cardiomyopathy. *J. Mol. Cell. Cardiol.* 29, 2107–2124 (1997).
13. Lindén, M., Li, Z., Paulin, D., Gotow, T. & Leterrier, J. F. Effects of desmin gene knockout on mice heart mitochondria. *J. Bioenerg. Biomembr.* 33, 333–341 (2001).
14. Fountoulakis, M. et al. Alterations in the heart mitochondrial proteome in a desmin null heart failure model. *Journal of Molecular and Cellular Cardiology* 38, 461–474 (2005).
15. Smolina, N. et al. Desmin mutations result in mitochondrial dysfunction regardless of their aggregation properties. *Biochim Biophys Acta Mol Basis Dis* 1866, 165745 (2020).
16. Schröder, R. et al. On noxious desmin: functional effects of a novel heterozygous desmin insertion mutation on the extrasarcomeric desmin cytoskeleton and mitochondria. *Hum. Mol. Genet.* 12, 657–669 (2003).
17. Alam, S. et al. Aberrant mitochondrial fission is maladaptive in desmin mutation–Induced cardiac proteotoxicity. *Journal of the American Heart Association* 7, 1–22 (2018).

18. McCormick, E. M., Kenyon, L. & Falk, M. J. Desmin common mutation is associated with multi-systemic disease manifestations and depletion of mitochondria and mitochondrial DNA. *Front Genet* 6, 199 (2015).
19. Winter, L. et al. Mutant desmin substantially perturbs mitochondrial morphology, function and maintenance in skeletal muscle tissue. *Acta Neuropathologica* 132, 453–473 (2016).
20. Kubánek, M. et al. Desminopathy: Novel desmin variants, a new cardiac phenotype, and further evidence for secondary mitochondrial dysfunction. *Journal of Clinical Medicine* 9, (2020).
21. Reipert, S. et al. Association of mitochondria with plectin and desmin intermediate filaments in striated muscle. *Exp. Cell Res.* 252, 479–491 (1999).
22. Winter, L., Abrahamsberg, C. & Wiche, G. Plectin isoform 1b mediates mitochondrion-intermediate filament network linkage and controls organelle shape. *J Cell Biol* 181, 903–911 (2008).
23. Favre, B. et al. Plectin interacts with the rod domain of type III intermediate filament proteins desmin and vimentin. *Eur J Cell Biol* 90, 390–400 (2011).
24. Guzun, R. et al. Regulation of respiration in muscle cells *in vivo* by VDAC through interaction with the cytoskeleton and MtCK within Mitochondrial Interactosome. *Biochim Biophys Acta* 1818, 1545–1554 (2012).
25. Li, H. et al. Voltage-Dependent Anion Channel 1(VDAC1) Participates the Apoptosis of the Mitochondrial Dysfunction in Desminopathy. *PLoS One* 11, e0167908 (2016).
26. Dayal, A. A. et al. Desmin Interacts Directly with Mitochondria. *Int J Mol Sci* 21, 8122 (2020).
27. Chourbagi, O. et al. Desmin mutations in the terminal consensus motif prevent synemin-desmin heteropolymer filament assembly. *Exp. Cell Res.* 317, 886–897 (2011).
28. Joanne, P., Chourbagi, O. & Agbulut, O. [Desmin filaments and their disorganization associated with myofibrillar myopathies]. *Biol Aujourd’hui* 205, 163–177 (2011).
29. Fornès, P. & Callon, D. L'autopsie : indispensable pour la connaissance et la prévention de la mort subite cardiaque. *Annales de Pathologie* 41, 85–96 (2021).
30. Koblan, L. W. et al. Improving cytidine and adenine base editors by expression optimization and ancestral reconstruction. *Nat Biotechnol* 36, 843–846 (2018).
31. Nelles, D. A. et al. Programmable RNA Tracking in Live Cells with CRISPR/Cas9. *Cell* 165, 488–496 (2016).
32. Agudelo, D. et al. Marker-free coselection for CRISPR-driven genome editing in human cells. *Nat Methods* 14, 615–620 (2017).
33. Billon, P. et al. CRISPR-Mediated Base Editing Enables Efficient Disruption of Eukaryotic Genes through Induction of STOP Codons. *Mol Cell* 67, 1068-1079.e4 (2017).
34. Lian, X. et al. Robust cardiomyocyte differentiation from human pluripotent stem cells via temporal modulation of canonical Wnt signaling. *Proc. Natl. Acad. Sci. U.S.A.* 109, E1848-1857 (2012).

35. Patro, R., Duggal, G., Love, M. I., Irizarry, R. A. & Kingsford, C. Salmon provides fast and bias-aware quantification of transcript expression. *Nat Methods* 14, 417–419 (2017).
36. Soneson, C., Love, M. I. & Robinson, M. D. Differential analyses for RNA-seq: transcript-level estimates improve gene-level inferences. *F1000Res* 4, 1521 (2015).
37. Love, M. I., Huber, W. & Anders, S. Moderated estimation of fold change and dispersion for RNA-seq data with DESeq2. *Genome Biol* 15, 550 (2014).
38. Lê, S., Josse, J. & Husson, F. FactoMineR: An R Package for Multivariate Analysis. *Journal of Statistical Software* 25, 1–18 (2008).
39. Kassambara, A. & Mundt, F. factoextra: Extract and Visualize the Results of Multivariate Data Analyses. (2020).
40. Yu, G., Wang, L.-G., Han, Y. & He, Q.-Y. clusterProfiler: an R package for comparing biological themes among gene clusters. *OMICS* 16, 284–287 (2012).
41. Wickham, H. *ggplot2: elegant graphics for data analysis* New York. NY: Springer (2009).
42. Zhou, Y. et al. Metascape provides a biologist-oriented resource for the analysis of systems-level datasets. *Nat Commun* 10, 1523 (2019).
43. Bader, G. D. & Hogue, C. W. V. An automated method for finding molecular complexes in large protein interaction networks. *BMC Bioinformatics* 4, 2 (2003).
44. Shannon, P. et al. Cytoscape: a software environment for integrated models of biomolecular interaction networks. *Genome Res* 13, 2498–2504 (2003).
45. Suspène, R., Henry, M., Guillot, S., Wain-Hobson, S. & Vartanian, J.-P. Recovery of APOBEC3-edited human immunodeficiency virus G->A hypermutants by differential DNA denaturation PCR. *J Gen Virol* 86, 125–129 (2005).
46. Mussil, B. et al. Genotoxic stress increases cytoplasmic mitochondrial DNA editing by human APOBEC3 mutator enzymes at a single cell level. *Sci Rep* 9, 3109 (2019).
47. Stenglein, M. D., Burns, M. B., Li, M., Lengyel, J. & Harris, R. S. APOBEC3 proteins mediate the clearance of foreign DNA from human cells. *Nat Struct Mol Biol* 17, 222–229 (2010).
48. Yépez, V. A. et al. OCR-Stats: Robust estimation and statistical testing of mitochondrial respiration activities using Seahorse XF Analyzer. *PLoS One* 13, e0199938 (2018).
49. Schmidt, C. A., Fisher-Wellman, K. H. & Neufer, P. D. From OCR and ECAR to energy: Perspectives on the design and interpretation of bioenergetics studies. *J Biol Chem* 297, 101140 (2021).
50. Birket, M. J. et al. Contractile Defect Caused by Mutation in MYBPC3 Revealed under Conditions Optimized for Human PSC-Cardiomyocyte Function. *Cell Rep* 13, 733–745 (2015).
51. Pluess, M., Daeubler, G., dos Remedios, C. G. & Ehler, E. Adaptations of cytoarchitecture in human dilated cardiomyopathy. *Biophysical Reviews* 7, 25–32 (2015).
52. Giacomelli, E. et al. Human-iPSC-Derived Cardiac Stromal Cells Enhance Maturation in 3D Cardiac Microtissues and Reveal Non-cardiomyocyte Contributions to Heart Disease. *Cell Stem Cell* 26, 862-879.e11 (2020).

53. Sun, M. G. et al. Correlated three-dimensional light and electron microscopy reveals transformation of mitochondria during apoptosis. *Nat Cell Biol* 9, 1057–1065 (2007).
54. Suspène, R. et al. Self-cytoplasmic DNA upregulates the mutator enzyme APOBEC3A leading to chromosomal DNA damage. *Nucleic Acids Res* 45, 3231–3241 (2017).
55. Berry, N. et al. Herpes Simplex Virus Type 1 Infection Disturbs the Mitochondrial Network, Leading to Type I Interferon Production through the RNA Polymerase III/RIG-I Pathway. *mBio* 12, e0255721 (2021).
56. Khalfi, P. et al. Antagonism of ALAS1 by the Measles Virus V protein contributes to degradation of the mitochondrial network and promotes interferon response. *PLoS Pathog* 19, e1011170 (2023).
57. Meyer, J. N., Leuthner, T. C. & Luz, A. L. Mitochondrial fusion, fission, and mitochondrial toxicity Submitted for consideration for the Special Issue of Toxicology on “Chemical Mitochondrial Toxicity”. *Toxicology* 391, 42–53 (2017).
58. Beale, R. C. L. et al. Comparison of the differential context-dependence of DNA deamination by APOBEC enzymes: correlation with mutation spectra *in vivo*. *J Mol Biol* 337, 585–596 (2004).
59. Bishop, K. N. et al. Cytidine deamination of retroviral DNA by diverse APOBEC proteins. *Curr Biol* 14, 1392–1396 (2004).
60. Suspène, R. et al. APOBEC3G is a single-stranded DNA cytidine deaminase and functions independently of HIV reverse transcriptase. *Nucleic Acids Res* 32, 2421–2429 (2004).
61. Suspène, R. et al. Somatic hypermutation of human mitochondrial and nuclear DNA by APOBEC3 cytidine deaminases, a pathway for DNA catabolism. *Proceedings of the National Academy of Sciences* 108, 4858–4863 (2011).
62. Ikeda, G. et al. Mitochondria-Rich Extracellular Vesicles From Autologous Stem Cell-Derived Cardiomyocytes Restore Energetics of Ischemic Myocardium. *Journal of the American College of Cardiology* 77, 1073–1088 (2021).
63. van Meer, B. J. et al. Quantification of Muscle Contraction *In Vitro* and *In Vivo* Using MUSCLEMOTION Software: From Stem Cell-Derived Cardiomyocytes to Zebrafish and Human Hearts. *Curr Protoc Hum Genet* 99, e67 (2018).
64. Tse, H.-F. et al. Patient-specific induced-pluripotent stem cells-derived cardiomyocytes recapitulate the pathogenic phenotypes of dilated cardiomyopathy due to a novel DES mutation identified by whole exome sequencing. *Hum. Mol. Genet.* 22, 1395–1403 (2013).
65. Brodehl, A. et al. Restrictive Cardiomyopathy is Caused by a Novel Homozygous Desmin (DES) Mutation p.Y122H Leading to a Severe Filament Assembly Defect. *Genes (Basel)* 10, 918 (2019).
66. Brodehl, A., Holler, S., Gummert, J. & Milting, H. The N-Terminal Part of the 1A Domain of Desmin Is a Hot Spot Region for Putative Pathogenic DES Mutations Affecting Filament Assembly. *Cells* 11, 3906 (2022).
67. Kulikova, O. et al. The Desmin (DES) Mutation p.A337P Is Associated with Left-Ventricular Non-Compaction Cardiomyopathy. *Genes (Basel)* 12, 121 (2021).

68. Protonotarios, A. et al. The Novel Desmin Variant p.Leu115Ile Is Associated With a Unique Form of Biventricular Arrhythmogenic Cardiomyopathy. *Can J Cardiol* 37, 857–866 (2021).
69. Schwarz, N. & Leube, R. E. Intermediate Filaments as Organizers of Cellular Space: How They Affect Mitochondrial Structure and Function. *Cells* 5, 30 (2016).
70. Vrabie, A. et al. The enlarging spectrum of desminopathies: new morphological findings, eastward geographic spread, novel exon 3 desmin mutation. *Acta Neuropathol.* 109, 411–417 (2005).
71. Vincent, A. E. et al. Mitochondrial dysfunction in myofibrillar myopathy. *Neuromuscul Disord* 26, 691–701 (2016).
72. Maloyan, A. et al. Mitochondrial dysfunction and apoptosis underlie the pathogenic process in alpha-B-crystallin desmin-related cardiomyopathy. *Circulation* 112, 3451–3461 (2005).
73. Kay, L. et al. Study of regulation of mitochondrial respiration in vivo: An analysis of influence of ADP diffusion and possible role of cytoskeleton. *Biochimica et Biophysica Acta (BBA) - Bioenergetics* 1322, 41–59 (1997).
74. Barron, M. J. et al. Cytochrome c oxidase deficient muscle fibres: substantial variation in their proportions within skeletal muscles from patients with mitochondrial myopathy. *Neuromuscul Disord* 15, 768–774 (2005).
75. Brand, M. D. & Nicholls, D. G. Assessing mitochondrial dysfunction in cells. *Biochemical Journal* 435, 297–312 (2011).
76. Stanley, W. C., Recchia, F. A. & Lopaschuk, G. D. Myocardial substrate metabolism in the normal and failing heart. *Physiol Rev* 85, 1093–1129 (2005).
77. Elsnicova, B. et al. Desmin Knock-Out Cardiomyopathy: A Heart on the Verge of Metabolic Crisis. *International Journal of Molecular Sciences* 23, 12020 (2022).
78. Bryant, J. D., Lei, Y., VanPortfliet, J. J., Winters, A. D. & West, A. P. Assessing Mitochondrial DNA Release into the Cytosol and Subsequent Activation of Innate Immune-related Pathways in Mammalian Cells. *Curr Protoc* 2, e372 (2022).
79. Wu, B. et al. The Impact of Circulating Mitochondrial DNA on Cardiomyocyte Apoptosis and Myocardial Injury After TLR4 Activation in Experimental Autoimmune Myocarditis. *Cell Physiol Biochem* 42, 713–728 (2017).
80. Bonvin, M. et al. Interferon-inducible expression of APOBEC3 editing enzymes in human hepatocytes and inhibition of hepatitis B virus replication. *Hepatology* 43, 1364–1374 (2006).
81. Pautasso, S. et al. Strategy of Human Cytomegalovirus To Escape Interferon Beta-Induced APOBEC3G Editing Activity. *J Virol* 92, e01224-18 (2018).
82. Guichard, J. L. et al. Desmin loss and mitochondrial damage precede left ventricular systolic failure in volume overload heart failure. *American Journal of Physiology-Heart and Circulatory Physiology* 313, H32–H45 (2017).
83. Ramaccini, D. et al. Mitochondrial Function and Dysfunction in Dilated Cardiomyopathy. *Frontiers in Cell and Developmental Biology* 8, (2021).

84. Moore, J. et al. Multi-Omics Profiling of Hypertrophic Cardiomyopathy Reveals Altered Mechanisms in Mitochondrial Dynamics and Excitation–Contraction Coupling. *International Journal of Molecular Sciences* 24, 4724 (2023).
85. van Opbergen, C. J. M., den Braven, L., Delmar, M. & van Veen, T. A. B. Mitochondrial Dysfunction as Substrate for Arrhythmogenic Cardiomyopathy: A Search for New Disease Mechanisms. *Frontiers in Physiology* 10, (2019).
86. Mohamud, Y., Li, B., Bahreyni, A. & Luo, H. Mitochondria Dysfunction at the Heart of Viral Myocarditis: Mechanistic Insights and Therapeutic Implications. *Viruses* 15, 351 (2023).
87. Walters, A. M., Porter, G. A. & Brookes, P. S. Mitochondria as a Drug Target in Ischemic Heart Disease and Cardiomyopathy. *Circulation Research* 111, 1222–1236 (2012).
88. Thebault, C. et al. Mitochondriopathy: a rare aetiology of restrictive cardiomyopathy. *European Journal of Echocardiography* 9, 840–845 (2008).
89. Sabbah, H. N. Targeting the Mitochondria in Heart Failure: A Translational Perspective. *JACC: Basic to Translational Science* 5, 88–106 (2020).
90. Singh, A., Faccenda, D. & Campanella, M. Pharmacological advances in mitochondrial therapy. *eBioMedicine* 65, (2021).
91. Huang, X., Zeng, Z., Li, S., Xie, Y. & Tong, X. The Therapeutic Strategies Targeting Mitochondrial Metabolism in Cardiovascular Disease. *Pharmaceutics* 14, 2760 (2022).
92. Butler, J. et al. Effects of Elamipretide on Left Ventricular Function in Patients With Heart Failure With Reduced Ejection Fraction: The PROGRESS-HF Phase 2 Trial. *Journal of Cardiac Failure* 26, 429–437 (2020).
93. Seo, K.-S. et al. KL1333, a Novel NAD⁺ Modulator, Improves Energy Metabolism and Mitochondrial Dysfunction in MELAS Fibroblasts. *Frontiers in Neurology* 9, (2018).
94. Servais, L. et al. Long-term data with idebenone on respiratory function outcomes in patients with Duchenne muscular dystrophy. *Neuromuscular Disorders* 30, 5–16 (2020).
95. McCully, J. D. et al. Injection of isolated mitochondria during early reperfusion for cardioprotection. *Am J Physiol Heart Circ Physiol* 296, H94–H105 (2009).
96. Masuzawa, A. et al. Transplantation of autologously derived mitochondria protects the heart from ischemia-reperfusion injury. *Am J Physiol Heart Circ Physiol* 304, H966–H982 (2013).
97. Emani, S. M., Piekarski, B. L., Harrild, D., Del Nido, P. J. & McCully, J. D. Autologous mitochondrial transplantation for dysfunction after ischemia-reperfusion injury. *J Thorac Cardiovasc Surg* 154, 286–289 (2017).
98. Kaza, A. K. et al. Myocardial rescue with autologous mitochondrial transplantation in a porcine model of ischemia/reperfusion. *J Thorac Cardiovasc Surg* 153, 934–943 (2017).
99. Doulamis, I. P. et al. Mitochondrial transplantation for myocardial protection in diabetic hearts. *Eur J Cardiothorac Surg* 57, 836–845 (2020).
100. Yamada, Y. et al. Challenges in Promoting Mitochondrial Transplantation Therapy. *Int J Mol Sci* 21, 6365 (2020).

101. Vignais, M.-L. et al. Transfer of Cardiac Mitochondria Improves the Therapeutic Efficacy of Mesenchymal Stem Cells in a Preclinical Model of Ischemic Heart Disease. *Cells* 12, 582 (2023).

102. Zhang, A. et al. Delivery of mitochondria confers cardioprotection through mitochondria replenishment and metabolic compliance. *Molecular Therapy* 31, 1468–1479 (2023).

Supplementary Information

Critical contribution of mitochondria in the development of cardiomyopathy linked to desmin mutation

Yeranuhi Hovhannisyan¹, Zhenlin Li¹, Domitille Callon^{1,2}, Rodolphe Suspène³, Vivien Batoumeni¹, Alexis Canette⁴, Jocelyne Blanc¹, Hakim Hocini⁵, Cécile Lefebvre⁵, Nora El-Jahrani⁵, Aurore L'honoré¹, Ekaterini Kordeli¹, Paul Fornes², Jean-Paul Concordet⁶, Gérard Tachdjian⁷, Anne-Marie Rodriguez¹, Jean-Pierre Vartanian³, Anthony Béhin⁸, Karim Wahbi⁹, Pierre Joanne^{1*} & Onnik Agbulut^{1*}

¹ Sorbonne Université, Institut de Biologie Paris-Seine (IBPS), UMR CNRS 8256, INSERM U1164, Biological Adaptation and Ageing, Paris-France.

² Academic Hospital of Reims, Department of Pathology, Reims-France.

³ Virus and cellular stress Unit, Department of Virology, Institut Pasteur, Université Paris Cité, Paris-France.

⁴ Sorbonne Université, CNRS, Institut de Biologie Paris-Seine (IBPS), Service de microscopie électronique (IBPS-SME), Paris-France.

⁵ Université Paris-Est Créteil, INSERM U955, Equipe 16, Créteil-France.

⁶ Museum National d'Histoire Naturelle, INSERM U1154, CNRS UMR7196, Paris-France.

⁷ Université Paris Saclay, Hôpital Antoine Béclère, AP-HP, Service d'Histologie-Embryologie-Cytogénétique, Laboratoire de Cytogénétique, Clamart-France.

⁸ Sorbonne Université, Pitié-Salpêtrière Hospital, AP-HP, Reference Center for Muscle Diseases Paris-Est, Myology Institute, Paris-France.

⁹ Université Paris Cité, Cochin Hospital, AP-HP, Cardiology Department, Paris-France.

Short title: Mitochondria in desmin cardiomyopathy

***Corresponding Authors:** Prof. Onnik Agbulut & Dr. Pierre Joanne. Sorbonne Université, Institut de Biologie Paris-Seine, UMR CNRS 8256, Inserm ERL U1164, 7, quai St Bernard (case 256), F-75005 Paris-France. Email : onnik.agbulut@sorbonne-universite.fr & pierre.joanne@sorbonne-universite.fr

Supplemental Material and methods

Karyotyping. The absence of chromosomal aberration was verified by analyzing the karyotype of iPSC cells. Thus, standard chromosomal analyses were performed on cultured derived iPSC clones, by standard procedures [G-banding with trypsin using Giemsa (GTG); R-banding after heat denaturation and Giemsa (RHG)].

Cytometry. Cells cultured on Matrigel-coated plates were washed with PBS and detached using Accutase® (for pluripotent stem cells) or TrypLE Select 1X (for cardiomyocytes cultured 4 days after detachment). Immunostaining were performed after incubation in fixation (1% formaldehyde, 20 minutes at RT) and permeabilization (0.5% BSA + 0.1% TritonX-100, 10 minutes) buffers. Then they are stained 15 minutes with anti-Nanog-PE, anti-Sox2-APC and anti-Oct3/4-PerCP-Cy5.5 antibodies (1/100, Human Pluripotent Stem Cell Transcription Factor Analysis Kit, BD). Living cardiomyocytes were stained with MitoTracker Deep Red FM diluted in culture medium (500 nM, 20 min at 37 °C, 5% CO₂) or with BODIPY staining solution (2 µM in PBS, 15 min at 37 °C, 5% CO₂). Cells are then washed with PBS + 0.5% BSA, resuspended in the same buffer and immediately analyzed on a MACSQuant 10 cytometer. After acquisition, data analysis and figures were performed using FlowJo_v_10.8.1.

Sequencing. To confirm the presence of the mutation (or its absence in control iPSC lines) the DNA was extracted using the Genelute Mammalian Genomic DNA kit (Sigma). For PCR, 500 ng of cDNA obtained after extraction of genomic DNA was amplified with 1.5 µM of forward (5'-GAACTAGGAGGGATGGGAATGT-3') and reverse (5'-TAAAGACAGAGACCCTCTGCCA-3') primers, 1 µM of deoxinucleotide triphosphates, 0.2 µM of MgCl₂ and 2.5 units of Taq polymerase (One tas DNA polymerase, NEB). Amplification was performed in a thermal cycler according to the following protocol: 95 °C -30s, then 35 cycles (95 °C -30s, 60 C -30s, 72 °C -1 min) and 72 °C -10 min. Once amplified, electrophoresis of the DNA fragments was performed in a 1.5% agarose gel with TAE buffer and an electric field intensity of 100 V. To stain the DNA in the gel, 1:1000 of GelRED was added during agarose gel preparation. The size of the PCR products was determined by comparison with the size marker (GeneRuler 1 Kb, Thermo Scientific). After migration the DNA bands were purified using the NucleoSpin Gel and PCR clean-up kit (Macherey Nagel) following the manufacturer's instructions. Sequencing was performed by Eurofins Genomics using 5'-GCTGAAGGAAAGGTGTTAAAGTC-3' as forward primer and 5'-CAGCAGCAGCATGAAGTGC-3' as reverse primer.

Microcontact printing. A silicon master of the lines was obtained by photolithography techniques and PDMS stamps were fabricated by casting 1:10 PDMS onto the silicon master and baking at 60 °C during 2 hours. Gelatin was activated at room temperature for 30 minutes by incubation with 3.6 mg/mL sodium periodate diluted in in PBS-sodium acetate (50 mM) buffer. For inking, the PDMS stamps were incubated with 0.1% activated gelatin at room temperature for one hour. Then, the solution was aspirated, the stamps were

dried and carefully placed in close contact to the surface of a glass coverslip overnight to allow the transfer of protein patterns. The next day, the PDMS stamps were gently removed and the coverslip with the patterns was sterilized for one hour under UV. The coverslips are then immediately used for seeding iPSC-CM.

Mitochondria Isolation and transfer. Mitochondria were isolated from Control CMs cells using the Mitochondria Isolation Kit (Thermo Scientific, Waltham, MA, USA, Cat#89874) according to the manufacturer's instructions. The quantity of mitochondria was evaluated by measuring the protein concentration of pelleted mitochondria d using Bicinchoninic Acid Kit (Sigma 1003152319). To evaluate the acute effect of mitondria transfer, pelleted mitochondria corresponding to 0.2 mg per 25 000 cells of proteins were added into the culture medium of CMs for 24 h.

Supplemental Tables

Table S1. List of primary antibodies

Target	Antibody	Dilution factor	References
Nanog	Mouse monoclonal (IgG1), clone 1E6C4	1:50	Santa CruzBiotechnology ref # sc-293121 AC
TRA1-81	Mouse monoclonal (IgM)	1:100	Merck ref #MAB4381
Desmin	Mouse monoclonal (IgG1), clone D33	1:200	Agilent ref # M076029-2
Desmin	Rabbit monoclonal (IgG), clone Y66	1:200	Abcam ref #ab32362
Desmin	Goat Polyclonal (IgG)	1:200	R&D Systems ref #AF3844
Alpha-Actinin	Mouse monoclonal (IgG1), clone EA-53	1:200	Merck ref #A7811
Troponin T	Mouse monoclonal (IgG2a), clone 200805	1:1000	R&D Systems ref #MAB1874
COXIV	Rabbit monoclonal (IgG), clone 3E11	1:200	Cell Signaling ref #4850
VDAC1	Mouse monoclonal (IgG2b), clone 20B12AF2	1:200	Abcam ref #ab14734
Connexin 43	Rabbit monoclonal (IgG), clone F-7	1:500	Santa CruzBiotechnology ref # sc-271837

Table S2. List of secondary antibodies

Conjugate	Antibody	Dilution factor	References
Alexa 488	Goat-anti-Mouse IgG2a	1:1000	Life Technologies ref # A21131
Alexa 488	goat anti-Mouse IgG (H+L)	1:1000	Life Technologies ref # A11029
Alexa 555	goat anti mouse IgG1	1:1000	Life Technologies ref # A21127
Alexa 555	Donkey anti-Goat IgG (H+L)	1:1000	Life Technologies ref # A21432
Alexa 647	goat anti rabbit IgG (H+L)	1:1000	Life Technologies ref # A21245
Alexa 568	goat anti rabbit IgG (H+L)	1:10000	Life Technologies ref # A11036
Alexa 488	goat anti rabbit IgG (H+L)	1:1000	Life Technologies ref # A11034

Supplemental Figures with Figure Legends

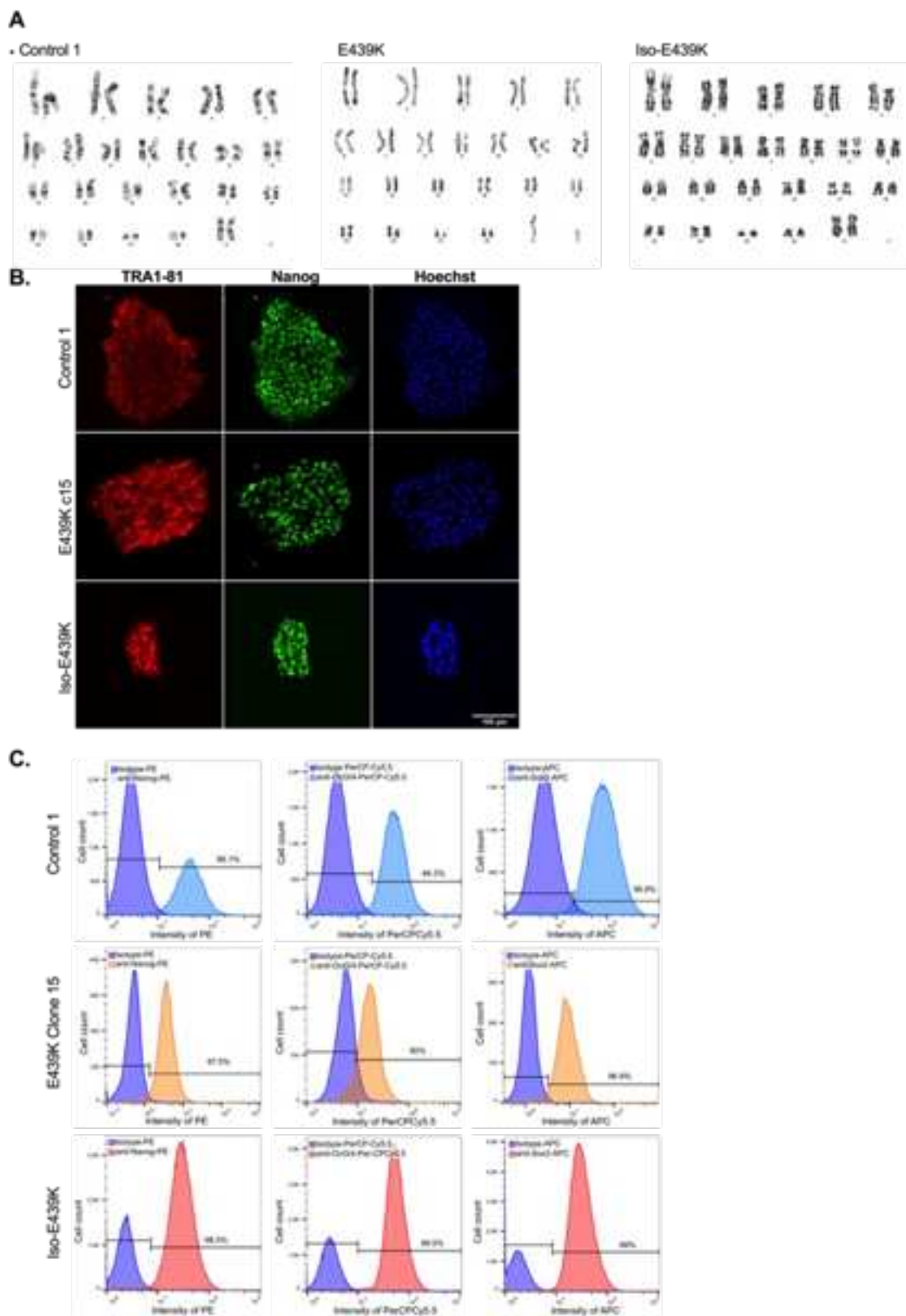


Figure-S1. Validation of induced pluripotent stem cell lines. (A) Karyotyping of a control (Control-1), a patient-derived (E439K, clone c15) and the isogenic mutant (Iso-E439K) induced pluripotent stem cell lines. The isogenic

mutant was obtained by introducing the point mutation G-to-A at c.1315 by gene editing using CRISPR-Cas9 (see Material and methods). No genomic abnormalities have been observed in the lines used in this study. **(B)** TRA-1-81 (red) and Nanog (green) immunostaining on growing colonies of a control (Control-1), a patient-derived (E439K, clone c15) and the isogenic mutant (Iso-E439K) induced pluripotent stem cell lines demonstrating correct expression and localization of these pluripotency markers. **(C)** Cytometry analysis of a control (Control-1), a patient-derived (E439K, clone c15) and the isogenic mutant (Iso-E439K) induced pluripotent stem cell lines demonstrating that more than 90% of cells are positive for the pluripotency markers Nanog, Oct3/4 and Sox2.

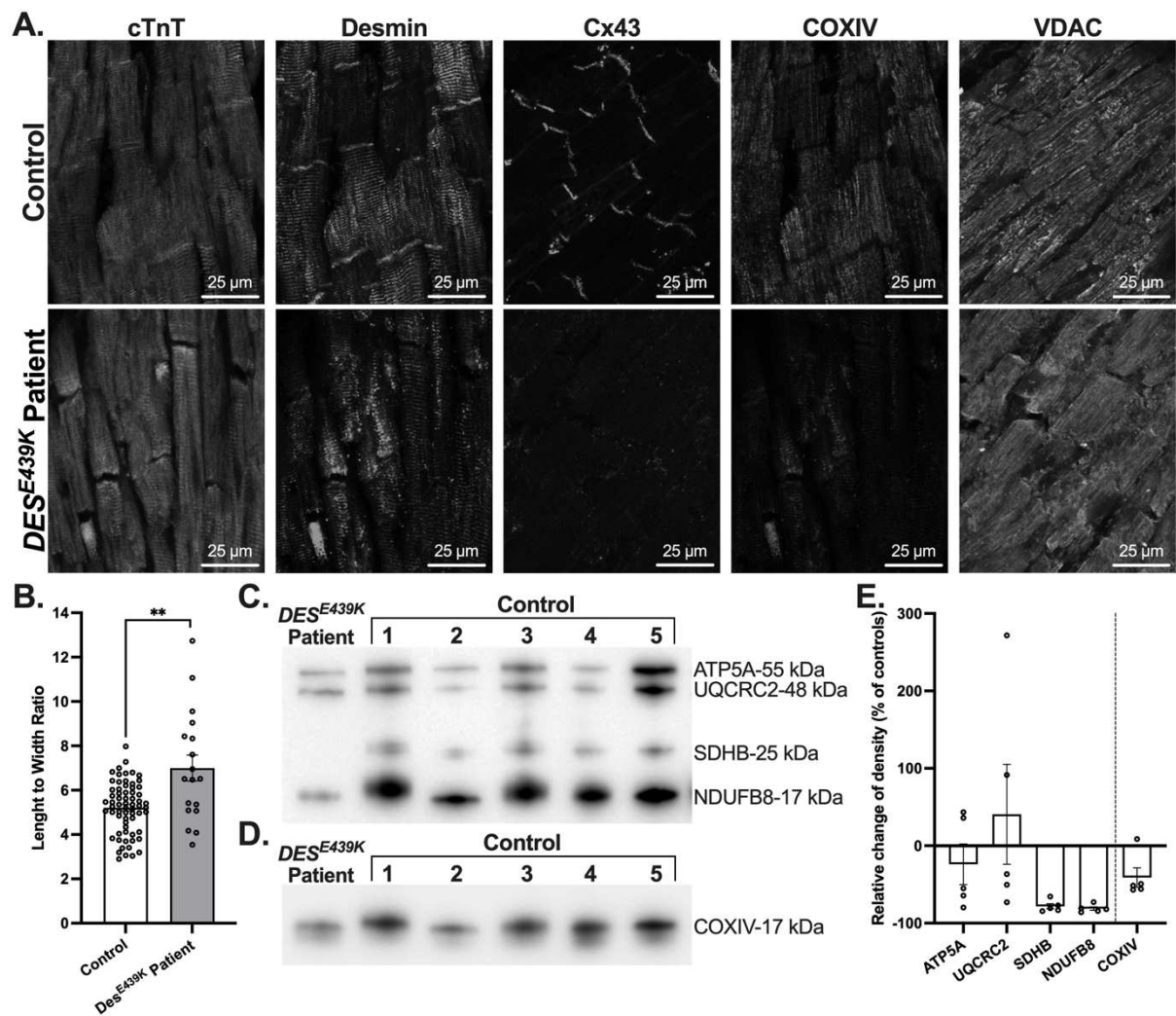


Figure-S2. Pathological patterns and biochemical analysis of cardiac samples of the Index case CII (see solid arrow in Figure-1A) carrying the *DES^{E439K}* mutation. (A) Cardiac troponin T (Green), desmin (Red), Connexin 43 (Cx43) (Gray), COXIV (Gray) and VDAC (Gray) immunostaining of formalin-fixed left ventricle sections demonstrating the strong disruption of the desmin network and intercalated discs, and a strong decrease of COXIV and Cx43 labelling in the patient's heart. **(B)** Cardiomyocyte length-to-width ratio was measured using ImageJ software. Values are given as means \pm SEM. **, $p < 0.01$. **(C-E)** Western blot analysis (C, D) and densitometry analysis (E) of mitochondrial proteins in control and patient cardiac tissue extracts using a cocktail of antibodies against OXPHOS proteins and COXIV. Note the marked decrease of mitochondrial proteins in the *DES^{E439K}* patient. Results are presented as percent of control density of detected protein bands after normalization to total protein band profile (stain free signal) per lane and are expressed as mean values \pm SEM. *, $p < 0.05$, **, $p < 0.01$, ***, $p < 0.001$.

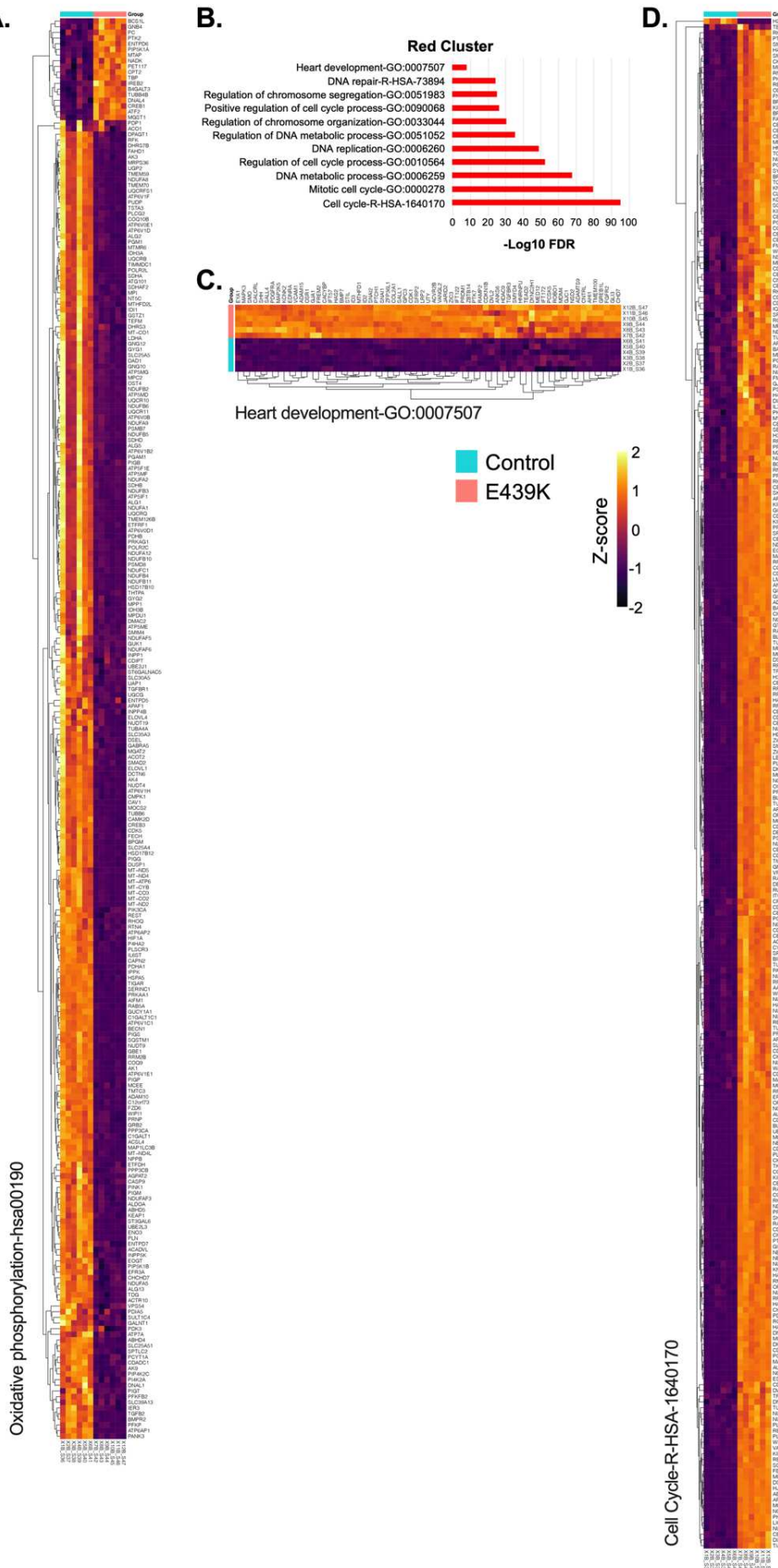


Figure-S3. Transcriptomic analysis of E439K-CMs compared to Control-CMs.

(A) Set of gene related to oxidative phosphorylation analyzed after gene set enrichment analysis of the genes of the Blue cluster determine by unsupervised WGCNA. Moreover, the enrichment analysis of the Red cluster **(B)** reveals different sets of genes related to heart development **(C)** and Cell Cycle **(D)**.

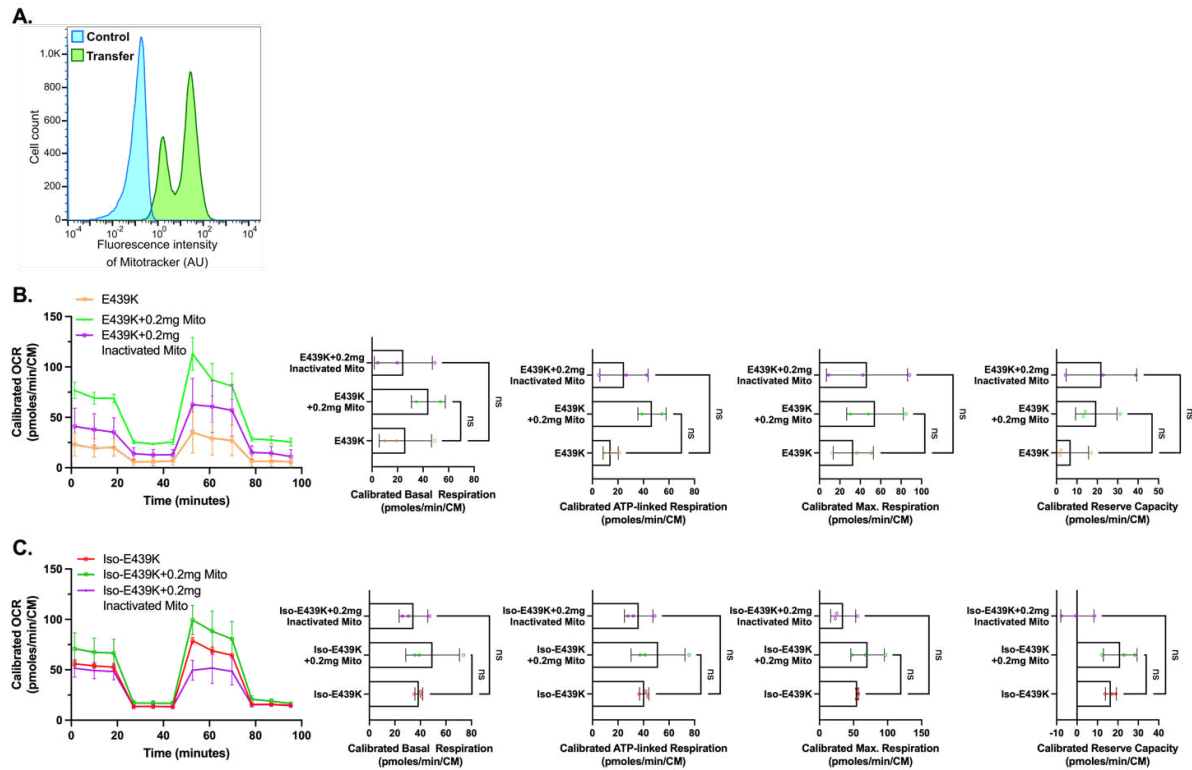


Figure-S4. Effect of acute treatment of cardiomyocytes with mitochondria purified from Control-CMs. (A) 24h after the treatment of Control-CMs derived mitochondria stained with MitoTracker®, cytometry analysis reveals that the mitochondria are effectively transferred into cardiomyocytes. **(B-C)** Representative mitochondrial oxygen consumption rate (OCR) profiles in E439K-CMs **(B)** or Iso-E439K-CMs **(C)** 24 hours after the transfer of mitochondria reveal that this treatment can modulate the respiration of mutant cardiomyocytes. OCR profiles are expressed as pmol O₂/min normalized to the number of cardiomyocytes and calibrated to the lowest value of the plate after addition of rotenone and antimycin. For each mutant line, quantification of basal respiration, ATP-linked respiration, maximal respiration and reserve capacity were calculated. Values are expressed as mean ± SEM. *, p < 0.05, **, p < 0.01, ***, p < 0.001.

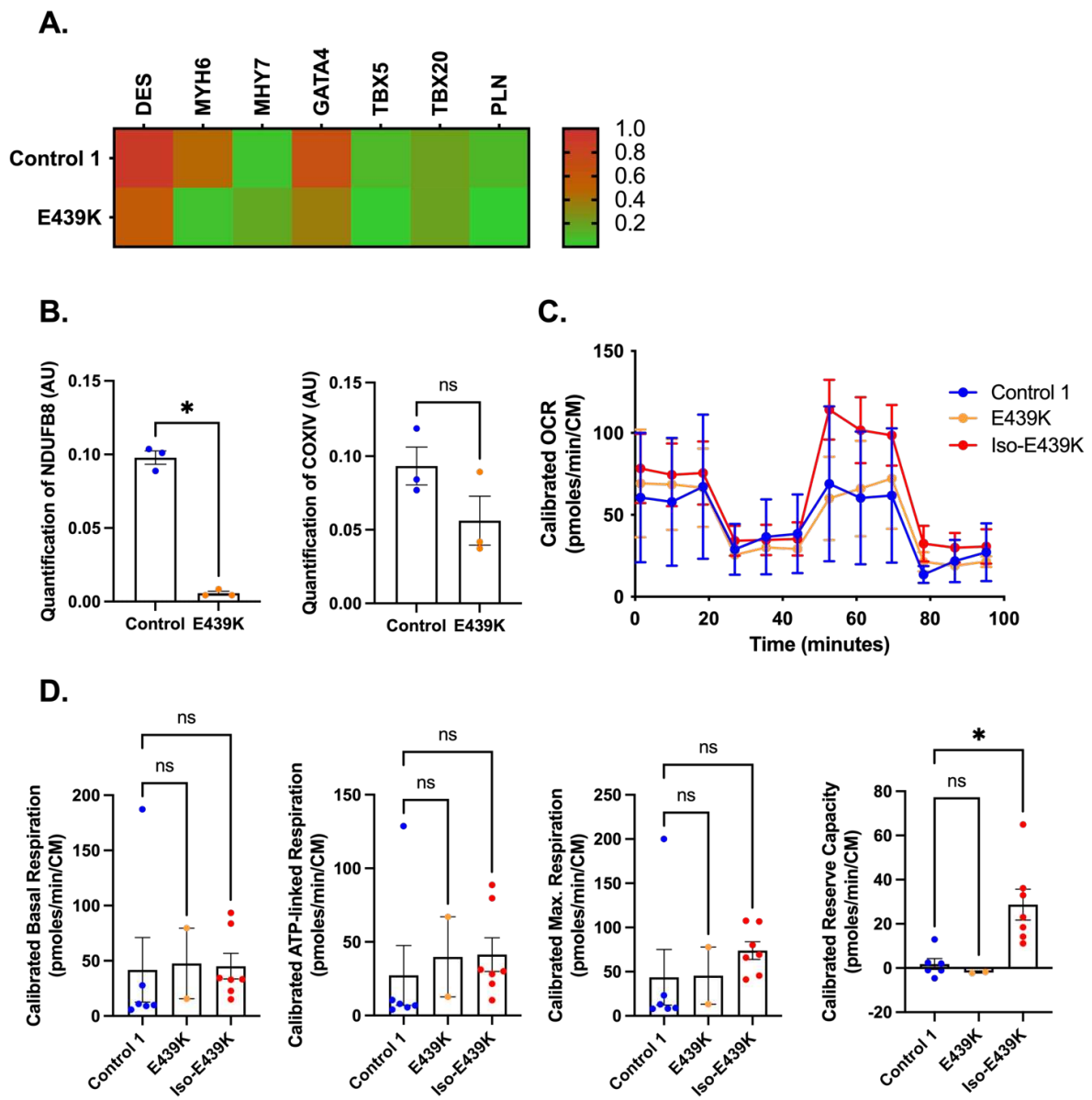


Figure-S5. Absence of strong differences at the beginning of differentiation in terms of genes and proteins expression as well as respiratory function.

(A) Heatmap op the gene expression 5 days after the initiation of cardiac differentiation of Control 1 and E439K iPSC lines revealing few differences in the expression of cardiomyocytes-related genes. (B) Quantitative analysis of Western Blot of NDUFB8 and COXIV showing a decrease of NDUFB8 mitochondrial protein but not COXIV in E439K-CMs compared to Control-CMs 7 days after the initiation of differentiation. Results are presented as fold change to control after normalizing to Stain-Free profile. (C) Representative mitochondrial oxygen consumption rate (OCR) profiles in Control-CMs, E439K-CMs and Iso-E439K-CMs 8 days after the initiation of differentiation. OCR profiles are expressed as pmol O₂/min normalized to the number of cardiomyocytes and calibrated to the lowest value of the plate after addition

of rotenone and antimycin A. **(D)** Quantification of basal respiration, ATP-linked respiration, maximal respiration and reserve capacity of cardiomyocytes. All values are expressed as mean \pm SEM. *, $p < 0.05$, **, $p < 0.01$, ***, $p < 0.001$.